Conversion of Biomass-Derived Oxygenated Compounds to Hydrocarbon Fuels and Commodity Chemicals using Solid Acid Catalysts

By

Dong Wang

A dissertation submitted in partial fulfillment
of the requirements for the degree of

Doctor of Philosophy
(Chemical Engineering)

at the

University of Wisconsin, Madison

2013

Date of final oral examination: 07/09/13

The dissertation is approved by the following members of the Final Oral Committee:

James A. Dumesic, Professor, Chemical and Biological Engineering
Manos Mavrikakis, Professor, Chemical and Biological Engineering
George W. Huber, Professor, Chemical and Biological Engineering
Brian F. Pfleger, Assistant Professor, Chemical and Biological Engineering
Dane Morgan, Associate Professor, Materials Science and Engineering

Conversion of Biomass-Derived Oxygenated Compounds to Hydrocarbon Fuels and Commodity Chemicals using Solid Acid Catalysts

Dong Wang

Under the supervision of Professor James A. Dumesic

at the University of Wisconsin-Madison

Due to the inevitable depletion of fossil fuel reserves, the development and utilization of renewable resources carry tremendous strategic significance in sustaining society's ever-growing needs for energy and materials in the long run. Amongst all forms of renewable energy resources, biomass assumes the unique position of being the only renewable source of carbon, from which liquid transportation fuels and organic chemicals are produced. The present thesis studies the catalytic conversion of key oxygenated platform molecules derived from the cellulose fraction of lignocellulosic biomass using solid acid catalysts to produce hydrocarbon fuels and commodity chemicals.

A catalytic route was first developed to convert an aqueous stream of gamma-valerolactone (GVL) over two solid acid catalysts into C_{8+} liquid alkenes with potential application as jet or diesel fuel precursors. In this process, GVL was nearly quantitatively decarboxylated into a stream of butene, which allowed for the use of well-established olefin oligomerization chemistry to produce C_{8+} hydrocarbons with overall yields greater than 60%. Kinetic studies on the interconversion between GVL and pentenoic acids (PEA) and their decarboxylation led to the development of a computerized model that satisfactorily captures experimental trends and thus can serve as a useful tool in reactor design and process optimization.

Experimental evidences obtained at short space times revealed that 1-butene was the primary decarboyxlation product. Based on this observation, γ-Al_2O_3 and WO_x-Al_2O_3 catalysts were used to achieve selective production of 1-butene via GVL decarboxylation by effectively suppressing isomerization of the terminal olefin. The approach also showed promise in producing higher linear alpha olefins from larger lactones.

Alternatively, GVL was converted into pentanoic acid by consecutive ring opening and hydrogenation over a bifunctional Pd/Nb_2O_5 catalyst. Pentanoic acid was further upgraded via ketonization reaction to form nonanone for use as diesel precursors. In this reaction, commercial niobic acid (Nb_2O_5) was found to crystallize and lose its surface area under hydrothermal conditions. Two niobia-silica composite materials were synthesized which showed significant improvement in hydrothermal stability.

Finally, a highly selective process was developed to convert furanics, including 2,5-dimethylfuran (DMF), 2-methylfuran (2-MF) and furan into *p*-xylene, toluene and benzene, respectively, through Diels-Alder type cycloaddtion with ethylene followed by dehydration. WO_x-ZrO_2 was identified as a highly efficient catalyst for this reaction due to its high Brønsted acidity.

Acknowledgements

Upon the completion of my PhD program, I would like to thank many wonderful people that have helped me tremendously through my 5 years in Madison. I am extremely grateful to my advisor, Professor James A Dumesic for his constant support, understanding, encouragement, and invaluable guidance in my scientific career as well as in life. Being a part of the Dumesic group has been a true privilege and education for me. Through day-to-day interaction, his deep knowledge in catalysis, infectious passion for research, uncompromising standards for scientific rigor, coupled with charisma, vision and very importantly, a witty sense of humor, sets an excellent example as a scholar and as a person. I also owe much gratitude to Professor Manos Mavrikakis and Professor Brian Pfleger for their kind support in my job search process. Throughout graduate school, I feel very fortunate to have had the opportunity to collaborate with excellent co-workers including Sikki, David, Jesse, Yomaira, Jean, Christian on different projects. I'm grateful for the help, instructions and friendship of my mentor in the lab, Juan Carlos Serrano-Ruiz. I would like to thank all current and former Dumesic group members, Jesse, David, Sikki, Brandon, Yomaira, Elif, Mei, Jean, Mark, Drew, Ed, Christian, Ryan, Tom, Max, Carrie and Ricardo for your constant willingness to help and enjoyable friendship. A special thank you goes to Judy Lewison, a tireless baking experimentalist who holds perhaps the highest success rate for experiments in our group. I'm grateful for the hard work she has done to feed us with delicious baked goods and keep our focus on research. I also greatly appreciate the expertise from John Cannon, Eric Codner and Joel Lord for equipment repairing and construction projects. I would like to thank Todd Ninman for IT assistance and Donna Bell and Kathy Heinzen for administrative support.

It is most difficult for me to put into words my gratitude to the most special person in my life, my beloved wife, Jieyi (Jenny), for her unconditional love, encouragement, understanding that have supported me through tough times in these five years and made me a better person. And finally, I am deeply indebted to my dear parents, who have really given their boy everything to support his pursuits in life.

TABLE OF CONTENTS

1. INTRODUCTION **1**

1.1 Energy Outlook: From 2011 to 2030 1
1.2 Liquid Transportation Fuels: Current Alternatives 4
1.3 The Petrochemical Industry 6
1.4 Lignocellulosic Biomass and Processing Options 7
1.4.1. Composition and Recalcitrance *7*
1.4.2 Thermochemical Conversion Technologies *9*
1.4.3 Aqueous-Phase Processing *10*
1.4.4 The HMF-LA-GVL Platform *12*
1.5 Research Directions 17
1.6 Overview of Chapters 20
1.7 References 22

2. EXPERIMENTAL TECHNIQUES **26**

2.1 Catalyst Synthesis 26
2.1.1 Commercial Catalysts *26*
2.1.2. Supported Catalysts *27*
2.1.3 SBA-15 Synthesis *28*
2.1.4 Silica-doped Niobia Catalysts *28*
2.1.5 Mesoporous Niobia by Atomic Layer Deposition *29*
2.2 Catalyst Characterization 30
2.2.1 CO Chemisorption *30*
2.2.2 Temperature Programmed Desorption *30*
2.2.3 N_2 Sorption *31*
2.2.4 X-Ray Diffraction *31*
2.2.5 Laser Raman Spectroscopy *32*
2.2.6 Fourier Transformed-Infrared Spectroscopy of adsorbed pyridine *32*
2.2.7 ICP-Atomic Emission Spectroscopy *33*
2.2.8 Thermogravimetric Analysis (TGA) *33*
2.2.9 Microcalorimetry *33*
2.3 Reactor setup for reaction studies 35
2.3.1 Flow reactor system *35*
2.3.2 Batch reactor system *36*
2.4 Definition and Data Analysis 38
2.5 References 38

3. INTEGRATED CONTINUOUS PROCESS FOR LIQUID OLEFIN PRODUCTION FROM BIOMASS-DERIVED Γ-VALEROLACTONE (GVL) **39**

3.1 Introduction 39
3.2 Process Description 43
3.3 Effect of Pressure, Temperature on Butene Formation from GVL and Catalyst Stability 44

3.4 Butene Oligomerization over Solid Acids: Effect of Water 47
3.5 Process Integration 50
3.6 Activation of Amberlyst-70 for Oligomerization 54
3.6.1 Activation of Amberlyst-70 for Oligomerization Reaction by Hydrophobic Media 54
3.6.2 Physical Characterization 56
3.6.3 Diffuse Reflectance Infrared Spectroscopy (DRIFT) 59
3.6.4 Microcalorimetric Study of Butene Adsorption on Amberlyst-70. 61
3.6.5 Temperature Programmed Desorption of Butene 66
3.7 Conversion of Raw Maple Wood to Jet Fuel Precursors at 1L Scale 68
3.7.1 Technology Overview 69
3.7.2 Levulinic Acid Production 72
3.7.3 GVL Production 74
3.7.4 GVL Conversion 78
3.8 Conclusion 80
3.9 References 81

4. KINETIC MODELING OF INTERCONVERSION BETWEEN Γ-VALEROLACTONE (GVL) AND PENTENOIC ACID (PEA) COMBINED WITH DECARBOXYLATION TO FORM BUTENE OVER AMORPHOUS SILICA/ALUMINA **83**

4.1 Introduction 83
4.2 Experimental Setup and Considerations for Kinetic Study 84
4.3 Reaction Model Development 89
4.4 Experimental Measurement of Kinetic Parameters 90
4.4.1 Catalyst Stability versus Time-On-Stream 90
4.4.2 Reaction Pathways 92
4.4.3 Thermochemistry and Effect of Reaction Temperature 95
4.4.4 Effect of GVL Partial Pressure 98
4.4.5 Effect of PEA Partial Pressure 100
4.4.6 Effect of Water Partial Pressure 101
4.5 Decarboxylation Pathways 102
4.6 Kinetic Model 106
4.7 Conclusion 116
4.8 References 116

5. SELECTIVE FORMATION OF ALPHA OLEFIN VIA DECARBOXYLATION OF LACTONES AND UNSATURATED ACIDS OVER SOLID LEWIS ACID CATALYSTS **118**

5.1 Introduction 118
5.2 Seletive 1-Butene Formation over Gamma-Alumina 122
5.3 Role of Basic Sites and Improved 1-Butene Yields over Tungstated-Alumina 126
5.4 Selective Production of Higher Linear Alpha Olefins 130
5.5 The Effect of Water: A Kinetic Phenomenon 132
5.6 Conclusion 134
5.7 References 135

6. BIFUNCTIONAL PD/NB_2O_5 CATALYST FOR THE CONVERSION OF Γ-VALEROLACTONE TO PENTANOIC ACID AND ITS KETONIZATION TO NONANONE **136**

6.1 INTRODUCTION 136
6.2 REACTION NETWORK 138
6.3 EFFECT OF PALLADIUM LOADING 139
6.4 INTEGRATED DUAL-BED REACTOR FOR UPGRADING Γ-VALEROLACTONE TO 5-NONANONE 140
6.5 INCREASING HYDROTHERMAL STABILITY OF NIOBIA: SILICA-MODIFIED NIOBIA 143
6.6 INCREASING HYDROTHERMAL STABILITY OF NIOBIA: ATOMIC LAYER DEPOSITION OF NIOBIA ON SBA-15 152
6.7 CONCLUSION 159
6.8 REFERENCES 160

7. SELECTIVE PRODUCTION OF AROMATICS FROM ALKYLFURANS OVER SOLID ACID CATALYSTS **161**

7.1 INTRODUCTION 161
7.2 *PARA*-XYLENE FORMATION FROM 2,5-DIMETHYLFURAN (DMF) AND ETHYLENE 162
7.2.1 Activities of Selected Solid Acid Catalysts for Para-xylene Formation from DMF and Ethylene *163*
7.2.2 Catalyst Stability for Para-xylene Production *166*
7.3 TOLUENE AND BENZENE PRODUCTION FROM 2-METHYLFURAN AND FURAN 167
7.4 EFFECT OF TUNGSTEN SURFACE DENSITY ON CATALYST ACTIVITY 173
7.5 PRODUCT ANALYSIS: ISOMERIC PURITY OF *PARA*-XYLENE 178
7.6 CONCLUSION 183
7.7 REFERENCES 184

8. CONCLUSIONS AND RECOMMENDATIONS **186**

8.1 SUMMARY OF CONCLUSIONS 186
8.2 RECOMMENDATIONS 190
8.2.1 Synthesis of Solid Lewis Acid Catalysts that Withstand Harsh Hydrothermal Conditions *190*
8.2.2. Tailor-Make Liquid Hydrocarbon Fuels that Meet Fuel Specifications *191*

List of Figures and Schemes

Figure 1.1 Primary energy consumption in the United States by source and sector in 2011 (all numbers in quadrillion BTU). Renewable energy include conventional hydroelectric power, geothermal, solar/photovoltaic, wind, and biomass. Taken from reference (2)

Figure 1.2 Projected primary energy consumption in North America in 2030. Renewables include wind power, biomass, solar/photovoltaic and geothermal energy; reconstructed from data in reference (3).

Figure 1.3 Molecules that can be efficiently synthesized from 5-hydroxymethylfurfural (HMF)

Figure 1.4 Molecules that can be efficiently synthesized from levulinic acid (LA)

Figure 1.5 Molecules that can be efficiently synthesized from γ-valerolactone (GVL)

Figure 2.1 Schematic of the calorimeter connected to a vacuum system as used in Chapter 3

Figure 2.2 Schematic of fixed-bed flow reactor setup

Figure 2.3 Schematic of batch reactor setup

Figure 3.1 Synthesis of valeric biofuels (12).

Figure 3.2 Reaction pathways the integrated conversion of GVL to a liquid stream of alkenes for use in transportation fuels and a gaseous stream rich in CO_2 that is appropriate for further processing options.

Figure 3.3 Yield of butene versus time on stream for conversion of 30wt% GVL in water at 36 bar and WHSV= 0.9 h^{-1} over SiO_2/Al_2O_3 at 648K (●) and 673K (○).

Figure 3.4 Yield of butene versus time on stream for conversion of GVL at 648 K, 36 bar and WHSV= 0.9 h^{-1} over SiO_2/Al_2O_3 at various GVL concentrations. 30 wt% (■), 60 wt% (○), 80 wt% (▲).

Figure 3.5 Yield of butene from GVL in reactor 1, butene conversion in reactor 2, and overall yield of liquid C_{8+} alkenes from GVL in the integrated process versus the time on stream. First reactor operated at 36 bar, 648 K and 0.18 h^{-1}. First separator operated at 36 bar and 383 K. Second reactor operated at 36 bar 443 K and 3 g Amberlyst-70. Second separator operated at 36 bar and 298 K. Butene yield (●), butene conversion (▷), yield to C_{8+} alkenes (■)

Figure 3.6 Optical microscopy images. a) Dry Amberlyst-70. b) Amberlyst-70 after contact with water

Figure 3.7 Optical microscopy images. a) Dry Amberlyst-70. b) Amberlyst-70 after contact with 5-nonanone.

Figure 3.8 DRIFT spectra recorded at 433 K. a) Pure Amberlyst-70 (black line) and Amberlyst-70 after treatment with 5-nonanone (red line). b) DRIFT spectra after adsorption of ammonia over Amberlyst-70 dried (black line) and treated with 5-nonanone (red line)

Figure 3.9 Differential heats of butene adsorption at 302 K for dry Amberlyst-70 (■) and Amberlyst-70 treated with 5-nonanone (○).

Figure 3.10 Integrated heat evolution following a dose of butene versus time. Dry Amberlyst-70 (■) Amberlyst-70 treated with 5-nonanone (○)

Figure 3.11 Schematic diagram for butene adsorption/desorption.

Figure 3.12 TPD of butene for dry Amberlyst-70 (continuous line) and Amberlyst-70 treated with 5-nonanone (dashed line), and TPD of 5-nonanone for Amberlyst-70 (dotted line)

Figure 3.13. Process flow diagram of proposed technology for the production of furfural, jet fuels, formic acid, and acetic acid from lignocellulose.

Figure 3.14. Chemical reactions in the acid catalyzed hydrolysis of cellulose leading to the formation of levulinic and formic acids.

Figure 3.15. Proposed catalytic routes to convert levulinic and formic acid into C_{8+} alkenes via GVL and butenes

Figure 4.1: Pathways for inter-conversion between GVL and PEA and their decarboxylation over acid catalysts.

Figure 4.2 Rate of butene production from GVL as a function of time on stream. WHSV = 3.7 h^{-1}, P = 1 bar, T = 623 K.

Figure 4.3 Molar ratio of butene isomers as a function of GVL WHSV at 613 K and 1 bar using a feed of 60 wt% GVL in water

Figure 4.4 Proposed mechanism of decarboxylation through an intermediate bearing a carbenium ion at the beta carbon.

Figure 4.5 Calculated thermochemistry for ring-opening of γ-valerolactone to pentenoic acids and subsequent decarboxylation to butene. ΔG^o and ΔH^o (in brackets) are presented in kJ/mol for each reaction illustrated at standard conditions.Adapted from reference (9)

Figure 4.6 Rates of reaction for ring opening (Δ) and decarboxylation (□) of gamma-valerolactone at various reaction temperatures; feed is 10 wt% GVL in water, WHSV = 15 h^{-1}, P = 1 bar.

Figure 4.7 Rates of reaction for ring closure (○) and decarboxylation (□) of trans-2-PEA at various reaction temperatures; feed is 10 wt% trans-2-pentenoic acid in water, WHSV = 15 h^{-1}, and P = 1 bar

Figure 4.8 Rates of reaction for ring opening (Δ) and decarboxylation (□) of gamma-valerolactone at various partial pressures of GVL; T = 623 K, WHSV = 10 h^{-1}

Figure 4.9 Rates of reaction for ring closure (○) and decarboxylation (□) of trans-2-pentenoic acid at various partial pressures of PEA; T = 623 K, WHSV = 10 h^{-1}.

Figure 4.10 Rates of reaction for ring opening (Δ) and decarboxylation (□) of GVL at various partial pressures of water; T = 623 K, WHSV = 10 h^{-1}.

Figure 4.11 Summary of reaction kinetics data obtained at short space times. a) Outlet GVL (○), PEA (Δ), and butene (or CO_2) (■) partial pressures as a function of space time (1/WHSV). Butene (or CO_2) partial pressure (■) is plotted on the right hand axis. b) Extrapolation of PEA partial pressure (Δ) to the zero space time limit. c) Rates of ring opening (Δ) and decarboxylation (■) as a function of space time (1/WHSV). The decarboxylation rate is plotted on the right hand axis. d) Extrapolation of the decarboxylation rate to the zero space time limit. The solid line represents a linear regression of the measured data while the dashed line is included to illustrate the requisite decarboxylation trend in the absence of a direct pathway for GVL decarboxylation. Experimental conditions for a) – d) 10 wt% GVL in water, 633 K, WHSV of 36 to 240 h^{-1}

Figure 4.12 Comparison between model predicted trends (solid lines) and experimentally observed molar flow rates of GVL (○), PEA (Δ), and butene(or CO_2) (□) in the effluent of plug flow reactors operating at various conditions. a) describes the trends observed in the effluent molar flow rates versus the GVL partial pressure. b) describes the trends observed in the effluent molar flow rates versus the PEA partial pressure. c) describes the trends observed in the effluent molar flow rates versus the water partial pressure. d) describes the trends observed in the rates of GVL ring opening and decarboxylation at various reaction

temperatures.e) describes trends observed in the rates of PEA cyclization and decarboxylation at various reaction temperatures.

Figure 5.1 Distribution of isomeric n-butenes at equilibrium at various temperatures. (6)

Figure 5.2 Butene production by decarboxylation of GVL over SiO_2-Al_2O_3. Reaction conditions: 30 wt% GVL in water, 648K, 1 bar at various WHSV.

Figure 5.3 Butene production by decarboxylation of GVL over γ-Al_2O_3. Reaction conditions: 30 wt% GVL in water, 648K, 1 bar at various WHSV.

Figure 5.4 Pathway of gamma-valerolactone decarboxylation over γ-Al_2O_3 and SiO_2-Al_2O_3

Figure 5.5 Effect of water concentration on the selectivity to acetic acid (a), pentenoic acids (b) and butenes (c) for GVL decarboxylation over γ-Al_2O_3. Reaction conditions: 648K, 1 bar, varying WHSV to achieve desired conversion levels.

Figure 5.6. Schematic representation of partially dehydroxylated γ-Al_2O_3 surface

Figure 6.1. Catalytic approach used to upgrade levulinic acid by dehydration, hydrogenation and C-C coupling reactions.

Figure 6.2. GVL conversion as a function of time on stream for a 50 wt% GVL in water feed at 573 K, 35 bar, WHSV=3.1 hr^{-1} and co-feed of both H_2 and He at 25 ml/min for the three niobia-supported Pd catalysts: (●) Pd(1%)/HY-340; (○) Pd(1%)/Nb-Si Oxide_ANO; (□) Pd(1%)/ Nb-Si Oxide_ETO.

Figure 6.3. HAADF image a) and HRTEM image b) of 1 wt% Pd/HY-340, as-prepared, with well-dispersed Pd nanoparticles (not visible). After GVL reaction, HAADF image c) and HRTEM image d) show that Pd nanoparticles have sintered to form larger particles and the support has transformed from mesoporous, amorphous niobia into crystalline Nb_2O_5

Figure 6.4. a) HAADF image and b) HRTEM image of 1 wt% Pd/ETO, as-prepared, with well-dispersed Pd nanoparticles (not visible). After GVL reaction, c) and e) HAADF image, d) and f) HRTEM images show the presence of Pd nanoparticles and two morphologies of niobia: mesoporous amorphous niobia (c-d) and crystalline niobia (e-f).

Figure 6.5. a) HAADF image b) HRTEM image of 1 wt% Pd/ANO, as-prepared, with small, dispersed Pd nanoparticles. After GVL reaction, c) and e) HAADF image, d) and f) HRTEM images show the presence of Pd nanoparticles and two morphologies of niobia: mesoporous amorphous niobia (c-d) and crystalline niobia (e-f).

Figure 6.6 Pd particle size distributions for the three niobia-supported Pd catalysts after GVL reaction.

Figure 6.7. FTIR spectra of (a) SBA-15, (b) SBA-15-ALD-1, (c) SBA-15-ALD-10, (d) SBA-15-ALD-19 and (e) SBA-15-ALD-30.

Figure 6.8. X-ray diffraction for (a) SBA-15, (b) SBA-15-ALD-1, (c) SBA-15-ALD-10, (d) SBA-15-ALD-19 and (e) SBA-15-ALD-30.

Figure 6.9. (A) GVL conversion as a function of time-on-stream for (▲) Pd/ HY-340 at 573 K and 35 bar, WHSV 3 h^{-1} and (○) Pd/ SBA-15-ALD-19 at 573 K and 35 bar, WHSV 17 h^{-1}. (B) Estimation of deactivation rate constants assuming pseudo first-order reaction (with a rate constant, k) and first-order deactivation for (▲) Pd/ HY-340 and (○) Pd/ SBA-15-ALD-19.

Scheme 7.1 Reaction scheme and thermochemistry (at 523K) for the conversion of 2,5-dimethylfuran (DMF) and ethylene to *p*-xylene

Figure 7.1 (a) Selectivity towards *p*-xylene, calculated at 60% DMF conversion, in the reaction with ethylene. (b)Turnover frequency (TOF) defined as the number of *p*-xylene

molecules formed per Brønsted acid site (except for γ-Al_2O_3 and TiO_2) per second. TOF values are calculated at 25~30% DMF conversion.

Figure 7.2 Stability of catalysts for *p*-xylene production in three consecutive recycle runs. Fresh: all three catalysts were subjected to 60% DMF conversion; Washed: catalysts were washed with isopropanol and dried before reuse; Calcined: catalysts were washed with isopropanol, dried and calcined in air for 3 hours at 923 K. The same reaction time was allowed in three runs for the same catalyst.

Scheme 7.2. Reaction network for the conversion of furanoic substrates to aromatics, where R_1 and R_2 are either -H or -CH_3.

Figure 7.3 Formation rates of aromatics, cyclohexenone and benzofuran type compounds from different furanoic substrates. Left panel: rates for benzene, toluene and *p*-xylene formation; middle panel: rates for cyclohexenone type compunds; right panel: rates for benzofuran type compounds. (Reaction conditions: 10 wt% dienes in anhydrous hexadecane, 0.15 g catalyst, 523 K, 20 bar ethylene charged at 298 K in 50 mL batch reactor)

Figure 7.4 Effect of reaction temperature on the rates of p-xylene (○) and dimethylcyclohexenone (▲) formation over WO_X-ZrO_2-923. (Reaction conditions; 10 wt% DMF in anhydrous hexadecane, 0.15 g catalyst, 453 to 548 K,20 bar ethylene charged at 298 K in 50 mL batch reactor, DMF conversions < 35%)

Scheme 7.3 Proposed reaction mechanism for the formation of a bicyclic adduct from DMF and ethylene catalyzed by Brønsted acids.

Figure 7.5 Effect of calcination temperature on conversion of DMF and selectivity to *p*-xylene. (Δ *p*-xylene selectivity ■ DMF conversion, reaction conditions: 10 wt% dienes in anhydrous hexadecane, 0.15 g catalyst, 523 K, 20 bar ethylene charged at 298 K in 50 mL batch reactor)

Figure 7.6 In situ Raman spectra of WOx-ZrO2 catalysts calcined at different temperatures acquired under dehydrated conditions

Figure 7.7 Amoco PX crystallization process

Figure 7.8 Equilibrium concentrations for C_8 aromatic compounds.

Figure 7.9 Chromatogram showing the relative concentrations of three xylene isomers.

List of Tables

Table 1.1 Composition for a variety of typical lignocellulosic biomass feedstock. Adapted from reference (40).

Table 3.1. GVL conversion and butene yield at different reaction conditions over a SiO_2/Al_2O_3 catalyst operating at a weight hourly space velocity (WHSV) equal to 0.9 h^{-1}.

Table 3.2 Butene conversion, selectivity, and yield to liquid C_8-C_{16} and C_{8+} alkenes over HZSM-5 and Amberlyst-70 catalysts.

Table 3.3 Performance of integrated catalytic system consisting of two flow reactors in series with an inter-reactor separator: GVL conversion and butene yield from first reactor containing SiO_2/Al_2O_3; butene conversion and selectivities to liquid C_8-C_{16} and C_{8+} alkenes from the second reactor containing HZSM-5/Amberlyst-70 as catalyst at 36 bar.

Table 3.4 Volume changes of Amberlyst-70 after swelling in different solvents for 24 h.

Table 3.5 Particle dimensions calculated by optical microscopy.

Table 3.6. Representative composition of cellulose hydrolysates obtained by treatment with H_2SO_4 at 473K for 60 minutes in a 4L steam gun

Table 3.7. Summary of the performance of the two-reactor GVL decarboxylation system employed for the production of alkene oligomers from commercial and lignocellulose-derived GVL. For both studies, the first reactor contained SiO_2/Al_2O_3 and operated at 648K and 35 bar with a GVL WHSV of 0.18 h-1. The second reactor contained Amberlyst 70 and operated at 343K and 35bar with a GVL WHSV of 0.15 h^{-1}.

Table 4.1 Summary of kinetic parameters estimated by nonlinear least squares. (†) Parameter value fixed.

Table 5.1 Physiochemical properties and catalytic activities of solid catalysts for GVL (30 wt% in water) decarboxylation at 648 K, 1bar.

Table 5.2 Production of LAO from various lactones on 4 wt % WO_x-Al_2O_3

Table 5.3. Kinetic data on decarboxylation of 2-pentenoic acid and 1-butene isomerization reaction in the presence and in the absence of water

Table 6.1. Carbon distributions and carbon selectivities for levulinic acid and GVL conversion over different catalysts.

Table 6.2. Surface area and acid sites density of niobia-supported Pd catalysts (determined by NH_3-TPD)

Table 6.3. CO chemisorption for the niobia-supported Pd catalysts

Table 6.4. Chemical composition, surface area and porosity properties of SBA-15 and SBA-15-ALD-y materials.

Table 7.1 Physiochemical properties and activity of catalysts.

Table 7.2 Physiochemical and catalytic properties of WO_x-ZrO_2 with varying W surface densities for *p*-xylene production

Table 7.3 Physical properties of xylene isomers

Table 7.4 Comparison between specifications of commercial *p*-xylene product and *p*-xylene stream obtained in this work

1. Introduction

1.1 Energy Outlook: From 2011 to 2030

The wide use of fossil fuels is the underpinning of the modern world. Our high-energy civilization relies on the consumption of vast quantity of coal, oil and natural gas to power modern industry, commercial activities and modes of transportation. In year 2011, approximately 1 billion tons of coal, 7 billion barrels of petroleum and 24 trillion cubic meters of natural gas (1) were consumed in the United States to generate enormous amount of electricity that went into our grid, to provide liquid fuels that drove our vehicles, to heat our homes, cook our food or to produce commodity chemicals that met the immense demand of materials of our society. Figure 1.1 summarizes primary energy consumption in the United States by source and sector as reported in the latest Annual Energy Review (2) published by U.S. Energy Information Administration. In year 2011, the total energy consumption in the United States was 97.3 quadrillion BTU (1 quadrillion BTU = 1.055×10^{18} J), of which 36% was derived from petroleum, 26% from natural gas and 20% from coal, while renewable resources including conventional hydroelectric power, geothermal, solar/photovoltaic, wind, and biomass accounted for a mere 9% of total energy consumed.

Through technological innovation and more stringent efficiency mandates, the world's energy intensity (the amount of energy consumed per unit of economic output) has been on a steady decreasing trend in all regions globally.(3) Despite this, the global energy demand is still projected to increase by 36% between 2011 and 2030 as income rises and population expands,

especially in emerging economies.(3) Undoubtedly, fossil fuels will continue to assume dominant positions in the energy landscape in 2030 and probably a few decades beyond.

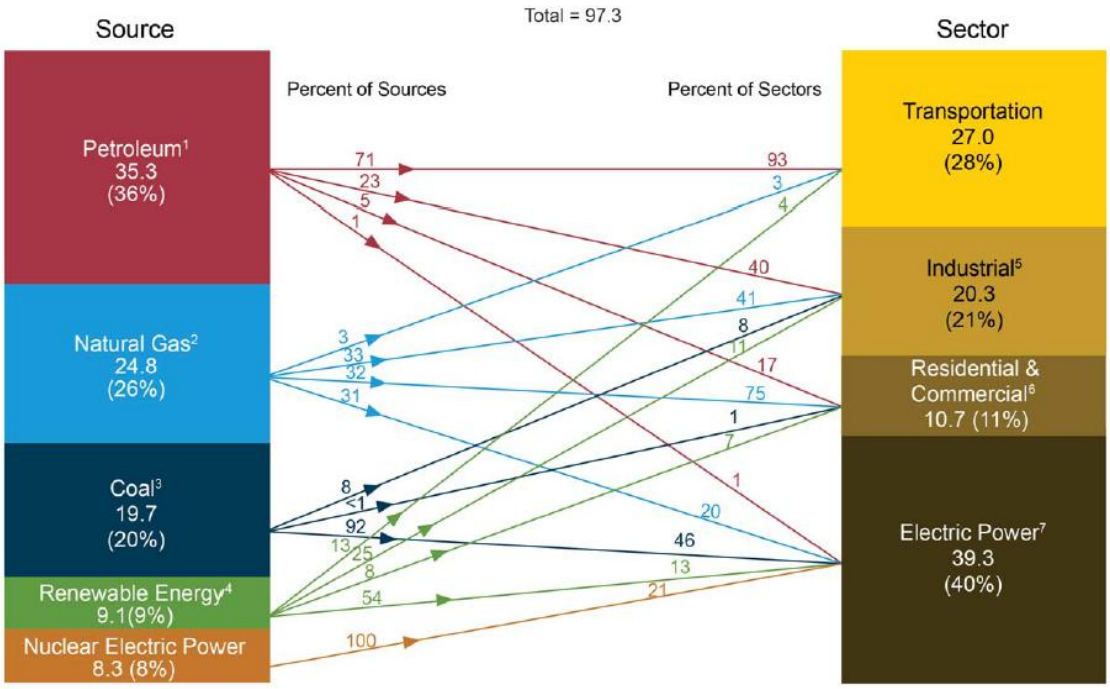

Figure 1.1 Primary energy consumption in the United States by source and sector in 2011 (all numbers in quadrillion BTU). Renewable energy include conventional hydroelectric power, geothermal, solar/photovoltaic, wind, and biomass. Taken from reference (2)

Figure 1.2 presents the primary energy supply in North America in year 2030 as predicted in the BP Energy Outlook of 2030.(3) It is projected that in year 2030, 32% of energy use will be supplied by oil, 32% by natural gas and 16% by coal. Much of the capacity increase will come from conventional fossil fuel sources. On the other hand, high energy prices driven by strong energy demand also provides strong economic incentives to unlock vast unconventional fossil resources via technological innovation, such as the boom of shale gas and shale oil in the past 5 years in North America powered by horizontal drilling and hydraulic fracturing technologies. (4)

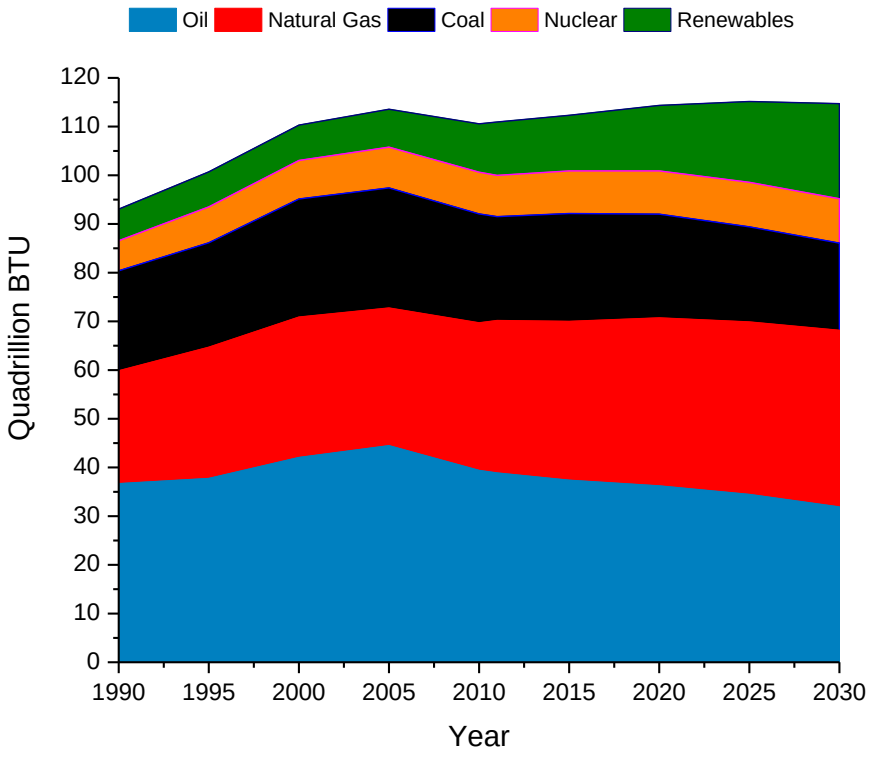

Figure 1.2 Projected primary energy consumption in North America in 2030. Renewables include wind power, biomass, solar/photovoltaic and geothermal energy; reconstructed from data in reference (3).

In the meantime, high prices for fossil fuels also support the expansion of non-fossil energy resources.(5) By the estimate shown in Figure 1.2, the consumption of renewable energy more than doubles from 2011 to 2030 (9.5 qudrillion BTU in 2011 versus 19.5 qudrillion BTU in 2030), accounting for 17% of the total energy use. Compared to unconventional fossil fuels, the development and deployment of renewable energy sources carries strategic significances in the long run due to concerns about global climate change associated with anthropogenic greenhouse gas emissions and perhaps more importantly the fundamentally unsustainable nature of coal, oil and gas. (6, 7)

1.2 Liquid Transportation Fuels: Current Alternatives

While the share of fossil fuel in generating heat and electricity for stationery applications can be substituted by the use of renewable resources such as hydroelectric power, nuclear power, geothermal, wind and solar energy, the choices are very limited in the transportation sector.(8) (9)The need for efficient mobility requires abundant, inexpensive, clean-burning-liquid fuels with high energy density for convenient onboard storage to power internal combustion engines and jet turbines.(6, 9) As can be seen in Figure 1.1, this need is currently met almost exclusively (93%) by crude oil, from which gasoline, diesel and jet fuel are derived.

Amongst all forms of renewable resources, only biomass can be used for the production of liquid transportation fuels. Today, the most widely used biofuels are bioethanol produced from corn starch or sugarcane and biodiesel produced from oil crops such as soybean and canola or waste grease and cooking oil. (10, 11)

Ethanol currently dominates the biofuel landscape, accounting for approximately 93% of total biofuel consumption in the United States in 2011.(12) The production of bioethanol involves the fermentation of biomass-derived carbohydrates to produce an aqueous solution of ethanol. The concentration of ethanol in the fermentation broth is often limited to a low level due to the toxicity of ethanol on the fermenting microorganism.(13) Consequently, the separation of ethanol from water by distillation becomes a very energy intensive process. (14) While ethanol is currently blended at low concentrations (5%-15%) into gasoline used in spark ignition engines, the use of ethanol-rich mixtures (85% to 100%) requires additional engine modifications.(15) A number of limitations further impede a full-scale adoption of ethanol as a major fuel component.

These include low energy density, high volatility, and contamination by the absorption of water from the atmosphere during transportation and storage.(15)

Biodiesel production in the United States emerged around year 2000 and it is now the second most abundant renewable liquid fuel used in the nation.(16, 17) Biodiesel are mono-alkyl esters of fatty acids usually produced via trans-esterification of lipids (triglycerides) with an alcohol (often methanol or ethanol) (18, 19) In contrast to bioethanol, the high energy density and combustion properties allow biodiesel to be used in current diesel engines with a wide range of blending ratios with petrol-diesel or as a pure fuel. However, biodiesel is still not completely compatible with current infrastructure due to concerns about accelerated engine wear, higher viscosity and higher NOx emission compared to conventional diesel. (20-22)

One challenge common to potential large-scale fuel ethanol and biodiesel production is the over-consumption of edible biomass feedstocks that can otherwise be used as food supplies. Currently, most of the ethanol plants in the United States rely on corn as feedstock, while the main feedstocks for biodiesel are soybean and canola oil.(23, 24) The use of scarce food source for fuel and chemical production not only raises ethic issues, it also drives up the prices of these crops and hence the manufacturing costs of the products.(25) The experience of the corn ethanol industry has exemplied this mechanism. In the early years of the rapid growth in corn starch ethanol production, the price of corn was less than 2 dollars per bushel, making it a very economical feedstock. But with increasing demand, supplies became tight and corn price increased sharply and profit margins of many ethanol plants was depressed**.** (25) Similar risks could occur in the biodiesel industry. In that regard, lingocellulose is the only viable source of

biomass that has the potential to meet long-term feedstock demand without affecting food supply. (26, 27)

1.3 The Petrochemical Industry

The eventual depletion of fossil mass reserves also has far-reaching repercussions on modern petrochemical industry.(28, 29) (30)The foundation of the U.S petrochemical industry has been based on inexpensive and widely available organic carbon-rich feedstocks in the form of petroleum-derived naphtha and natural gas liquids (mainly ethane, propane and butane). Currently, more than 54 million metric tons of primary chemicals are produced in the United States each year which are further manufactured into materials that help maintain our standard of living.(31) Compared to the energy industry, the feedstock for the chemical industry is rather restricted. While energy can be generally transformed from a variety of resources, most materials, especially polymer-based materials, can only be derived from carbon-based feedstocks.(28, 31) Hence biomass, in particular lignocellulose, also holds the long-term strategic position of being the only form of renewable organic carbon that can be used as feedstock for the chemical industry. (28, 30)

Over the past five decades, the petroleum refinery has greatly improved its efficiency through scientific and technological developments. Today refineries around the world equipped with highly optimized and efficient technologies produce large quantities of fuels and a handful of highly pure key intermediates, including methanol, ethylene, propylene, butylenes, benzene, toluene, and the xylenes, from which families of derivatives are then produced.(31, 32) By the same token, it is critical that in a “biorefinery”, the production of high-volume, low-value transportation fuels be integrated with the production of value-added commodity chemicals,

leading to favorable overall economics and optimal valorization of renewable feedstocks. (30, 33, 34)

1.4 Lignocellulosic Biomass and Processing Options

1.4.1. Composition and Recalcitrance

Lignocellulosic biomass represents the most abundant form of biomass on earth.(35) Common sources of lignocellulose include sawdust, corn stover, sugarcane bagasse, municipal waste and pulp sludge that are currently deemed as low-value waste. However, energy crops dedicated to fuel and chemical production will need to be grown on a large scale to meet the vast demand for feedstock.(36-38) Various types of fast-growing grasses and trees have thus been identified as promising feedstocks with switchgrass, Miscanthus, poplar and eucalyptus being prominent examples.(36) The portion of the lignocellulosic biomass from which carbohydrates are derived is the plant cell wall, which comprises of three major structural components, namely, cellulose, hemicellulose and lignin.(39) The relative amounts of these components vary with source of waste biomass, crop harvest time and environmental factors such as stress during growth, leading to considerable composition diversity of lignocellulosic biomass, as shown in Table 1.1.(40)

Table 1.1 Composition for a variety of typical lignocellulosic biomass feedstock. Adapted from reference (40).

Feedstock	Cellulose	Hemicellulose	Lignin
Corn stover	36.4	22.6	16.6
Wheat straw	38.2	24.7	23.4
Switchgrass	31.0	24.4	17.6
Poplar	49.9	25.1	18.1

Cellulose is the primary component of the plant cell wall. It is a polysaccharide consisting of a linear chain of several hundred to over ten thousand D-glucose units linked together by β-1,4 glycosidic bonds.(39) Long linear strands of glucose are tightly packed together through numerous inter- and intra molecular hydrogen bonds into microfibrils that resembles steel beams. These microfibrils further form crystalline conformations that are highly rigid. On the other hand, hemicelluloses are amorphous, branched, single-chain polymers composed primarily of five different sugar monomers: xylose, arabinose, galactose, glucose, and mannose, with xylose being the most abundant component.(39, 41) The third major component of the plane cell wall is lignin, which is also an amorphous polymer comprises of highly cross-linked hydroxylated and methoxylated phenylpropane monomers such as coumaryl alcohol, coniferyl alcohol and sinapyl alcohol.(41, 42) An interesting analogy likens the structure of lignocellulose to reinforced concrete.(43) Multiple crystalline cellulose fibrils (steel rods) are thought to tangle with chains of hemicellulose (wire mesh or cable) to provide additional strength and linkages. Lignin then acts like the cement to hold everything tightly in place. Consequently, this highly complex, composite structure renders lignocellulose very resistant to mechanical, chemical and biological decay.(27) This recalcitrance barrier blocks access to the carbohydrate monomers and poses a major challenge that needs to be overcome in order to realize the production of fuels and chemicals from lignocellulose.

In so far, three main conversion strategies, namely, thermochemical conversion, enzymatic digestion and aqueous-phase processing have been developed to break lignocellulose into chemical platforms that are more amenable to further upgrading with established chemical and biological processes. Pretreating lignocellulose with dilute acid or base followed by

enzymatic digestion falls beyond the scope of this thesis and will not be detailed herein. We shall briefly discuss thermochemical conversion technologies and fractionation combined with aqueous-phase processing of lignocellulose in the following sections. To distinguish from dilute acid pretreatment commonly used to prepare biomass for subsequent enzymatic production of fermentable sugars, in this thesis aqueous-phase processing refers to those conversion technologies carried out to produce less-oxygenated platform molecules compared to sugars in the feedstock. These platform molecules are further converted into wide ranges of chemicals and fuel precursors via chemical catalytic processes.

1.4.2 Thermochemical Conversion Technologies

Depending on the form of desirable products, thermochemical conversions can be further divided into gasification, direct pyrolysis and liquefaction. In gasification, biomass is partially oxidized at high temperatures (600–900 ^{o}C) by oxygen or steam in the presence of catalysts.(44) Syngas (CO and H_2) is the major product from the gasifier, accompanied by impurities such as tars, ammonia, hydrogen sulfide, and particulates. These impurities can have an adverse effect on downstream processing, and they must be removed by different chemical and physical treatments. Three distinct types of catalytic materials have been used for biomass gasification, namely, dolomite catalysts (a magnesium ore with the general formula $MgCO_3 \bullet CaCO_3$), alkali metal and nickel catalysts.(44) As an important biomass conversion technology, the merits of gasification lie in its ability to convert all three components of lignocellulose into a simple, yet flexible platform that can be further processed by proven technologies such as Fischer–Tropsch synthesis (FTS) (45) and methanol synthesis (46) into versatile products. The purification of the syngas stream, however, coupled with the economies of scale limit the feasibility of this option

to large centralized processing facilities which in turn increases costs associated with transporting large quantities of biomass feedstock.(45) The main challenges and opportunities in the catalysis-related research of gasification are the development of novel catalysts that further increase the efficiency of gasification by minimizing the amount of impurities such as tars and reducing energy input. (44)

Both pyrolysis and liquefaction yield a complex mixture of water and oxygenated hydrocarbons called bio-oil. Bio-oils are currently the cheapest form of liquid fuels that can be made from lignocellulosic biomass.(9, 47) Bio-oils are composed of polar organics (ca. 75–80 wt%) and water (ca. 20–25 wt%).(48) The organic phase consists of water soluble and insoluble functionalities. The water soluble phase has very high oxygen content, originating from cellulose and hemicellulose fractions of biomass.(48) The water insoluble phase derives from the lignin fraction of biomass which is mainly aromatics, and has lower oxygen content and high viscosity. Crude bio-oils have low heating value (16–19 MJ/kg; less than half that of petroleum-derived fuels), strong corrosiveness (pH of 2–3), high viscosity (35–1000 cP at 40 ^{o}C), and poor chemical stability (viscosity and phase change with time).(48) Bio-oil can contain hundreds of different chemical components that require further separation and processing to produce consumable fuels and chemicals.(49)

1.4.3 Aqueous-Phase Processing

One distinct feature of all the abovementioned thermochemical conversion technologies is that all three major components of lignocellulose are processed simultaneously. Gasification breaks all carbonecous feedstock into its most basic units, CO and H_2, leading to complete destruction of functionalities and C-C bonds which need to be reconstructed from scratch to

produce long-chain hydrocarbons or functionalized molecules. Pyrolysis/ liquefaction serves as a great option for rapid biomass densification and potentially allows for the transportation of biomass over longer distances, but it is quite challenging to upgrade and valorize the complex bio-oil, which is still highly oxygenated.(49) Meanwhile, based on their different chemical and physical properties, it is not surprising that the optimum conditions for efficiently processing cellulose, hemicellulose and lignin are different. (50) Therefore, a third strategy for lignocellulose conversion is to first fractionate it into its three constituents, and the resultant cellulose, hemicellulose and lignin streams are further converted by separate processes, often in aqueous-phase, that specifically designed to maximize conversion efficiency for each fraction.(50) Compared to thermochemical decomposition, this approach allows for the conversion of each biomass fraction into a handful of simple platform molecules with high yields, thus leading to highly efficient feedstock utilization. (51) Oxygen content in each fraction is only reduced by carefully controlled reactions, which prevents formation of product streams with complex compositions that require significant efforts to separate. Limited functional groups preserved in these platform molecules also lend themselves to a versatile tool kit of organic chemistry for further transformation into a wide range of chemicals and fuel precursors, which is critical to increase the flexibility of utilizing biomass feedstock towards establishing biomass-based chemical and fuel industries. (31)

The efficient utilization of biomass feedstock is likely to build on the strengths and synergies of all the aforementioned conversion technologies, as will be briefly discussed in Chapter 3 of the thesis. However, work in this thesis mainly focuses on the conversion of several platform molecules derived from the cellulose fraction of lignocellulosic biomass via aqueous-

phase processing into hydrocarbon fuel precursors and a variety of important commodity chemicals by efficient catalytic processes.

1.4.4 The HMF-LA-GVL Platform

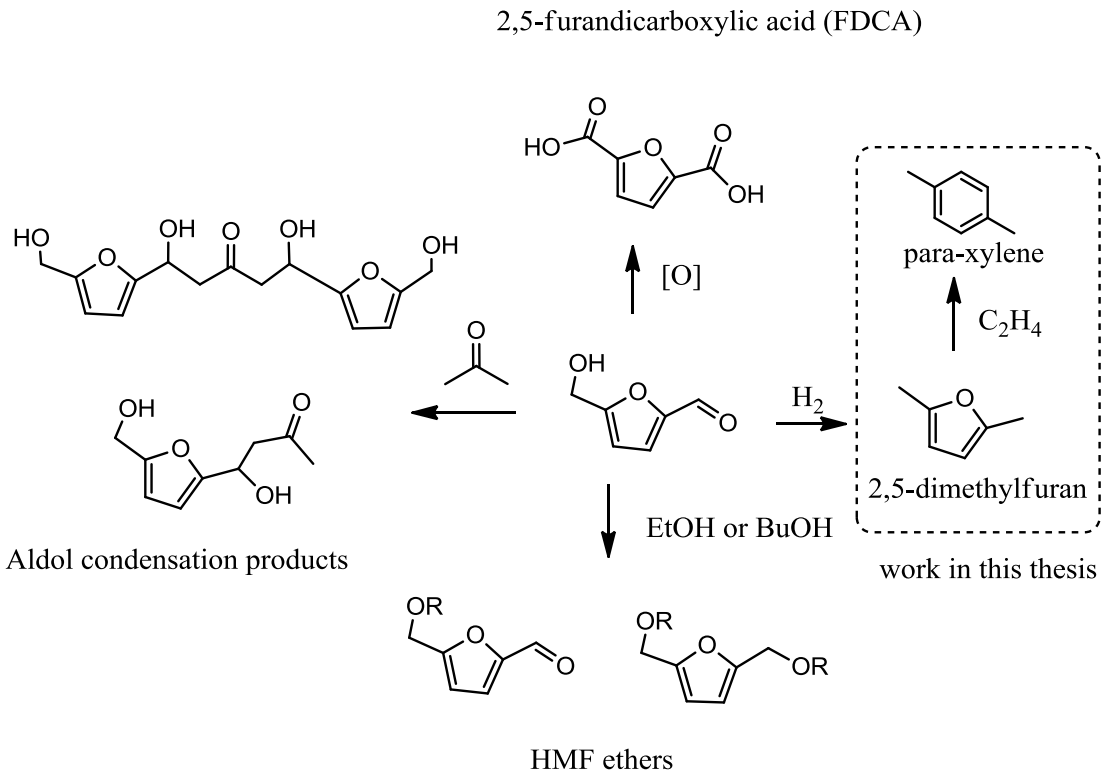

Figure 1.3 Molecules that can be efficiently synthesized from 5-hydroxymethylfurfural (HMF)

5-Hydroxymethylfurfural (HMF), levulinic acid (LA) and γ-valerolactone (GVL) represent arguably the three most important platform molecules derived from the cellulose fraction of lignocellulosic biomass.(41) These three molecules occupy closely interdependent positions on the value chain. HMF is the dehydration product of glucose and fructose which can be hydrolyzed to form LA.(52) LA can in turn be converted to GVL via dehydration/hydrogenation reactions.(53) HMF, LA and GVL are all versatile molecules and

each serves as an entry point to a long list of valuable chemicals and fuels precursors. Any technological breakthrough or new application with any of these three molecules or their derivatives is likely to have a significant impact on the rest. Therefore, it is advisable to take a holistic approach and treat HMF-LA-GVL as a single grand platform.

Figure 1.3 summarizes valuable molecules that can be derived from HMF with high yields as reported in literature. Pioneer work in converting HMF to fuel precursors conducted by Huber et al.(54) focused on coupling HMF with one or two molecules of acetone through efficient aldol condensation reaction with the carbonyl group of HMF. Upon dehydration/hydrogenation over bifunctional catalysts, these molecules were converted into liquid alkanes with carbon numbers ranging from C_7 to C_{15} which are suitable as transportation fuel components. In another study by Roman-Leshkov et al,(55) HMF is converted into 2,5-dimethylfuran (DMF) by hydrogenolysis over a copper-ruthenium (Cu-Ru/C) catalyst with over 70% yield. DMF has been proposed as a good gasoline additive Recently, Balakrishnan and co-workers(56) reported the one-pot reductive etherification of HMF to form 5-(alkoxymethyl)furfurals and 2,5-bis(alkoxymethyl)furans which are promising bio-diesel candidates. An important route of using HMF for chemical application involves oxidizing both the methylhydroxyl and the carbonyl group of HMF to form 2,5-furandicarboxylic acid (FDCA).(57, 58) FDCA has received a great deal of attention because it is a promising candidate to replace terephthalic acid in polyester production and is claimed to offer better product properties including superior barrier properties against oxygen, CO_2 and water permeation, and improved thermal properties as compared to PET bottles.(59) As will be shown in this thesis

(Chapter 7), another promising route to use HMF for chemical purposes involves converting the derivative DMF for the production of a key commodity chemical, para-xylene.

Levulinic acid (LA, 4-oxopentanoic acid) is another attractive platform molecule that can be derived from HMF. (60) Levulinic acid can be obtained by direct hydrolysis of glucose or raw cellulose through dilute sulfuric acid treatment via the intermediate HMF.(61-63) Equimolar amount of formic acid is formed together with levulinic acid. Although levulinic acid production by hydrolysis of cellulose has been reported using different processes, including using various mineral acids,(64, 65) solid acids (66) and ionic liquids,(67) hydrolysis using dilute sulfuric acid appears to be the most promising route in terms of process cost, levulinic acid yield and scalability. In fact, the Biofine process (Biofine Renewables, LLC),(68, 69) which is a patented technology that has been demonstrataed at pilot scale, produces levulinic acid, furfural, formic acid and lignin char from lignocellulose by dilute sulfuric acid hydrolysis. The process consists of a continuous two-stage reactor system operated at optimized conditions to produce levulinic acid at 70-80% theoretical yields, which corresponds to 50% mass yield on C_6 sugars basis. Formic acid is a co-product accounting for 20% of the mass yield while water-insoluble solid residues (humins) accounts for the rest of the product mass.

Being a bifunctional gamma-keto-carboxylic acid, levulinic acid has a rich chemistry and can be converted into a wide range of derivatives with applications as polymer precursors, pharmaceutical precursors as well as fuel additives.(60, 70) Figure 1.4 summarizes notable levulinic acid derivatives that can be prepared with high yields as reported in literature. Methyltetrahydrofuran (MTHF) is a promising fuel extender that is produced from levulinic acid via 1,4-pentanediol (PDO). MTHF is miscible with gasoline at all proportions and has favorable

oxygenate and vapor pressure properties (52). δ-aminolevulinic acid is a biodegradable, versatile herbicide that can be synthesized from levulinic acid via the amination of the C_5 carbon.(52) Synthetic route utilizing the ketone group has also received much attention. One example is the production of diphenolic acid (DPA)(71) by reacting one mole of levulinic acid with two moles of phenol, as shown in Figure 1.4. DPA can be used in many applications to substitute bisphenol A (BPA).(68) Another startup company Segetis, Inc, has developed technologies that react diols with levulinic acid to produce a novel class of ketals which can be potentially used as solvents, surfactants as plasticizers.(72) DuPont has also patented a number of levulinic acid derivatives with applications ranging from Nylon intermediates, ionic liquids, to biofuel addititves.(72)

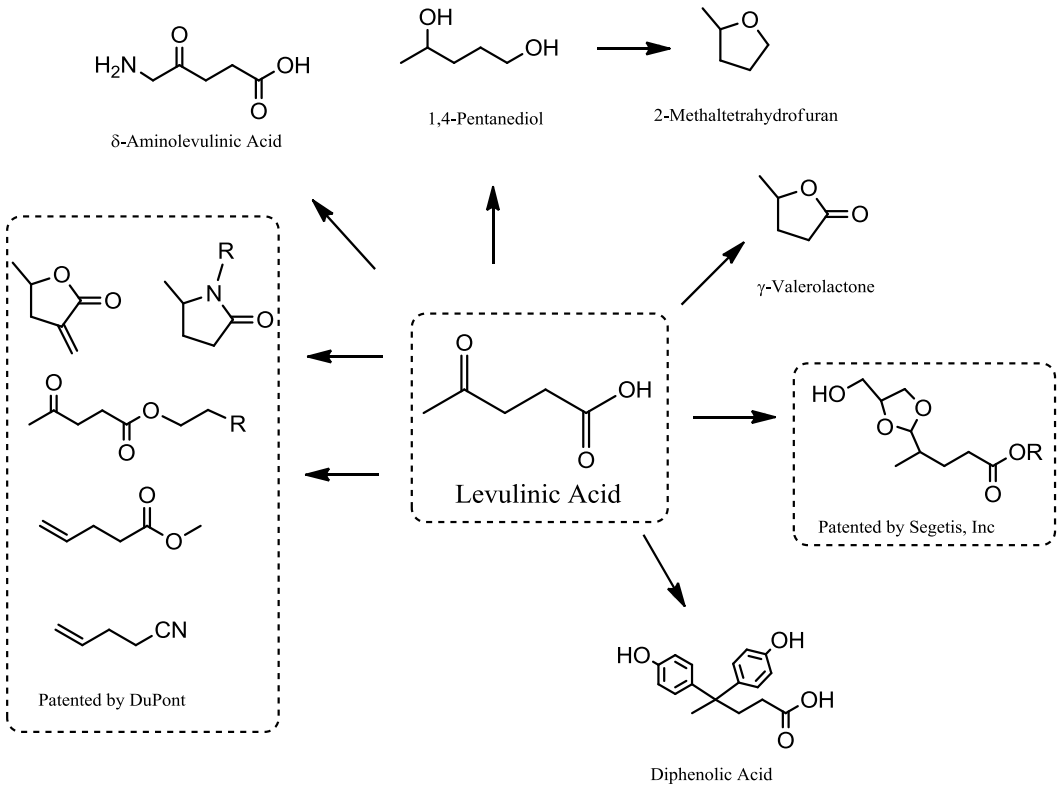

Figure 1.4 Molecules that can be efficiently synthesized from levulinic acid (LA)

γ-valerolactone (GVL) is produced from levulinic acid by dehydration/hydrogenation reactions via the cyclic pseudo-levulinic acid or angelica lactone intermediates.(60) Almost quantitative yields of GVL (95-97%) can be obtained using a Raney Nickel(73) or Ru/C (74, 75) catalyst in the presence of molecular H_2. Recently, hydrogentation of levulinic acid to form GVL using H_2 generated in situ from formic acid decomposition has been demonstrated over a Au/ZrO_2 catalyst, (76, 77) which eliminates the need to separate formic acid and consumption of external molecular hydrogen.

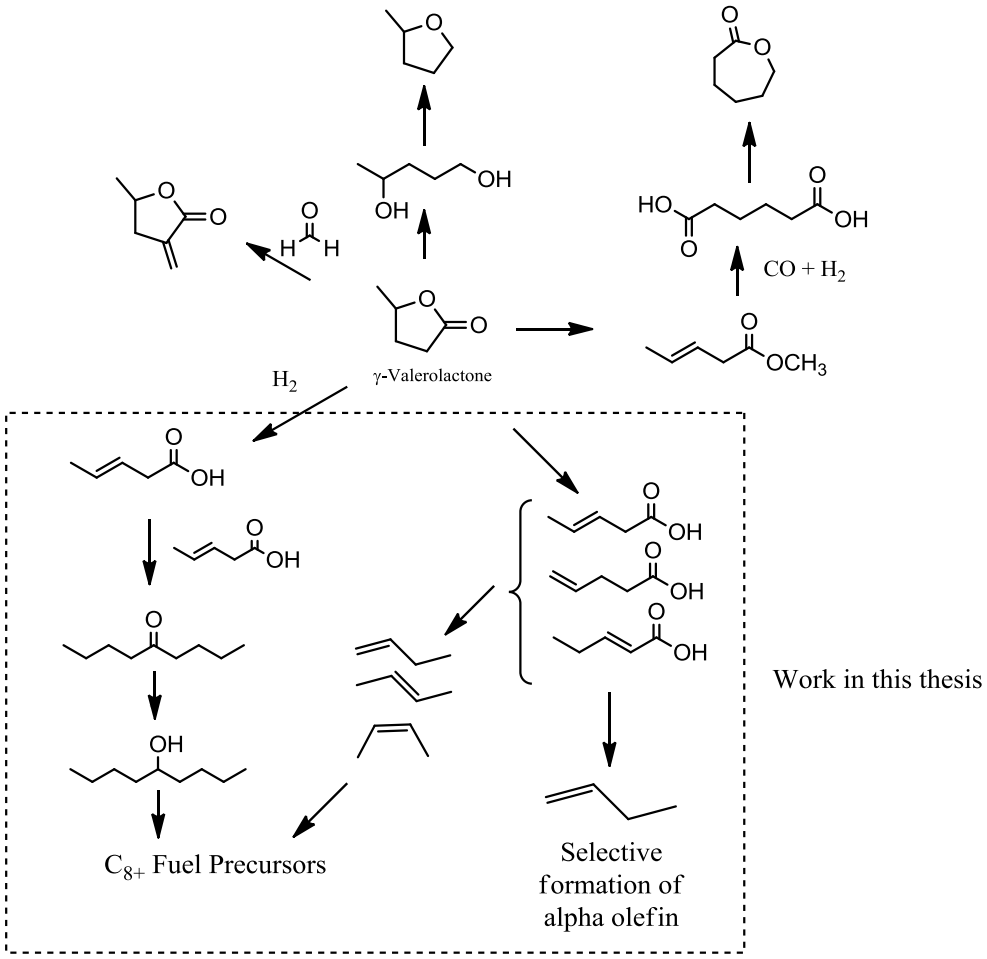

Figure 1.5 Molecules that can be efficiently synthesized from γ-valerolactone (GVL)

Like levulinic acid, GVL itself is also a versatile platform molecule and converting levulinic acid to GVL opens up access to a new collection of valuable molecules (Figure 1.5).(53) Some examples include α-methylene-γ-valerolactone,(78) adipic acid(79) and caprolactone,(79) which can be used as monomers for polymer synthesis. A unique application of GVL is its direct use as a green solvent for biomass processing, as first proposed by Horvath and coworkers.(80-82) Recently, Horvath et al. reported the use of GVL as solvent to produce HMF, LA, and GVL, from fructose.(83) Alonso et al. employed an aqueous phase modifier, such as salt or sugars to create a biphasic system with GVL as the organic layer in the production of LA from cellulose.(84) The most remarkable advantage of using GVL as the solvent is that GVL solubilizes both the feedstock and the humins formed during reaction, thus preventing accumulation of solids in the reactor.(41, 53) The higher extent of cellulose solubilization in GVL (with small amount of water as co-solvent) allowed for the use of significantly less amount of sulfuric acid or even solid acids (85) to achieve remarkable LA yields. Because GVL also solubilizes the post-reaction solid residues, continuous processes for raw biomass digestion can in principle be implemented based on flow reactors designs. Finally, as will be extensively demonstrated in this thesis (Chapter 3, 4, 5 and 6), GVL can also be converted into commodity chemicals and hydrocarbon fuels with highly efficient catalytic processes developed in this thesis

1.5 Research Directions

As illustrated by the HMF-LA-GVL platform above, a key requirement for the successful implementation of the aqueous-phase processing strategy is the availability of an array of highly efficient downstream processing technologies (catalytic or biological) that convert platform molecules into families of valuable derivatives. The discovery and development of catalytic

materials, reaction conditions and separation technologies to meet this requirement is an on-going quest involving both academic and industrial efforts.(86) From the chemical perspective, lignocellulose-derived molecules are over-functionalized compared to hydrocarbons found in fossil feedstock and hence need to be de-functionalized selectively to produce existing commodity chemicals and hydrocarbon fuels.(31, 51, 87) However, the current understanding of catalysis has been largely focused on increasing the functionality of feedstock molecules to manipulate chemical reactivity towards the desired transformation.(88) Therefore, a fundamental task of catalysis research in this field is to acquire knowledge and understandings and to develop catalysts, chemistry and processes that enable selective removal of functionalities without activating large reaction networks that lead to undesirable competing reactions such as polymerization. (86)

Oxygen atoms in biomass-derived molecules are ultimately removed as H_2O, CO_2 or CO and these selective oxygen-removal steps rely heavily on acid-catalyzed reactions such as dehydration, decarboxylation and decarbonylation.(89) In that regard, solid acid catalysts have served as important functional materials for modern oil refining and chemical industry. According to a comprehensive statistical survey by Tanabe and Hölderic(90) in 1999, about 103 different kinds of solid acid catalysts were then involved in 127 industrially important processes, spanning a wide spectrum of reactions such as alkylation, acylation, isomerization, oligomerization, dehydration, hydration, esterificaiton, cracking, amination and etc. Materials used include zeolites, heteropoly acids, oxides (mixed oxides and sulfated oxides), phosphates and ion-exchange resins.(90) In particular, the application of various zeolites is credited to have the greatest contribution to modern petroleum refining and chemical industry.(91, 92) Solid acid

catalysts possess many clear advantages over their homogeneous counterparts in that they are more environmentally friendly with respect to corrosiveness, safety, waste disposal and ease of separation and catalyst recovery. (91, 92)

The wealth of existing solid acid catalysts is the starting point in the development of new catalytic processes involving acid-catalyzed reactions. Years of research motivated by petroleum chemistry has advanced our understanding of solid acid catalysts to a point where the nature of the active sites are known at the atomic level in favorable cases and their chemical behaviors are elucidated in many cases by means of existing theories and a plethora of characterization techniques.(93) General principles based on these fundamental insights help guide the synthesis of solid acids to achieve optimum combination of the type, number and strengths of acid sites.(91, 92) For instance, despite the varying nature of acid sites, solid acids can be generally described in terms of their Brønsted/Lewis acidity, the concentration, strength and accessbility of these sites. Favorable product selectivity depends on the fine-tuning of these traits.(94-97) Due to the high oxygen to carbon stoichiometry, carbohydrates and their many derivatives are often very soluble in water, making water, the most environmentally friendly solvent, an attractive processing medium.(50) However, the hydrolytic power of water destructs the structural integrity of some conventional solid acids and hydrothermal stability becomes a concern, especially at elevated temperatures.(88, 98) Clearly, in such cases, synthesis of more water-tolerant solid acid catalysts would be a necessary endeavor. When the catalyst is structurally stable under the hydrothermal reaction conditions, water can also act as a reagent that participates in the reaction network or affects the reaction kinetics by strongly coordinating to acid sites.(99, 100) Hence, elucidating the effect of water on reaction pathway and kinetics within a reaction network

represents an important task in developing efficient processes for biomass conversion. On the other hand, water also has potential positive effects such as mitigating coke formation (Chapter 3) and in one interesting case presented in this thesis (Chapter 5), its inhibitory effect is used to positively influence product selectivity.

1.6 Overview of Chapters

The work presented in this thesis falls within the scope of the grand effort that is aimed at searching for efficient strategies of utilizing lignocellulosic biomass to meet our society's needs for liquid hydrocarbon fuels and commodity chemicals. We focus on the important HMF-LA-GVL platform and strive to expand the pool of products that can be efficiently derived from this platform. We achieve so by developing catalytic processes that use inexpensive, robust catalysts (with focus on solid acids) that offer high activity and selectivity to desired products. A constant effort is made to understand the structural and compositional properties of these solid acids that lead to efficient/inefficient catalysis. Understanding of this kind then helps guide further design and modification of catalysts with improved activity, selectivity or stability.

Chapter 2 presents the experimental and analytical techniques used throughout the thesis. Chapter 3 details a novel process where an aqueous stream of GVL is first decarboxylated into a stream of butene mixture, which is then oligomerized to produce liquid hydrocarbons with molecular weights suitable as jet and diesel fuel precursors. The acidic resin used for the oligomerization reaction, Amberlyst-70, displays an unexpected activation behavior upon contact with a C_9 ketone, whereby the activity increases by a factor of 5. Detailed characterization work is carried out therein to elucidate the origin of this interesting behavior. Using the process describes therein, the last part of Chapter 3 explores the production of oligomer fuel at 1 liter

scale using raw maple wood as part of a multi-university collaborative project aimed at producing liquid hydrocarbons for jet fuel application. Chapter 4 explores the reaction kinetics for the inter-conversion between GVL and pentenoic acid (PEA) and their decarboxylation to form equimolar quantities of butene and CO_2 over the SiO_2-Al_2O_3 catalyst, these steps being key components for the process described in Chapter 3. A kinetic model is built which provides satisfactory description of experimental data including the inhibitory effect of water. Detailed kinetic study carried out in this chapter also confirms that although a mixture consisting of butene isomers (1-butene, *trans*- and *cis*-2-butene) is produced using the SiO_2-Al_2O_3 catalyst in Chapter 3, 1-butene is in fact the primary decarboxylation product of GVL. Based on this observation, in Chapter 5, Lewis-acid based catalysts are then studied and further modified to achieve selective production of 1-butene as well as other higher alpha olefins, which are value-added chemical building blocks with wide commercial applications. In chapter 5, we find that water is essential for the selective production of alpha olefins, which represents an interesting case where the high water content commonly encountered in biomass processing can be utilized to positively influence product selectivity. Chapter 6 demonstrates that over a bifunctional Pd supported on niobia (Nb_2O_5) catalyst, GVL can be efficently converted via combined ring opening and hydrogenation to produce pentanoic acid, which can then be further upgraded into a C_9 ketone via ketonization reaction. Since the commercial Nb_2O_5 catalyst crystallizes and leads to loss of activity, two strategies are used to synthesize Nb_2O_5 materials with improved hydrothermal stability. Chapter 7 mainly demonstrates a highly selective route to produce a key commodity chemical para-xylene from 2,5-dimethylfuran, which is readily derived from HMF. Finally, Chapter 8 summarizes the findings of all chapters and proposes future research directions.

1.7 References

1. U.S. Energy Information Administration http://tonto.eia.doe.gov/energyexplained/index.cfm
2. U.S. Energy Information Administration / Annual Energy Review 2011, Figure 1.0 Energy Flow, 2011
3. BP Statistical Review of World Energy (2013)
4. T. C. Kinnaman, *Ecological Economics*, 2011, **70**, 1243-1249.
5. I. Dincer, *Renewable and Sustainable Energy Reviews*, 2000, **4**, 157-175.
6. A. J. Ragauskas, C. K. Williams, B. H. Davison, G. Britovsek, J. Cairney, C. A. Eckert, W. J. Frederick, J. P. Hallett, D. J. Leak, C. L. Liotta, J. R. Mielenz, R. Murphy, R. Templer and T. Tschaplinski, *Science*, 2006, **311**, 484-489.
7. S. E. Koonin, *Science*, 2006, **311**, 435.
8. V. Smil, *Energy at the Crossroads: Global Perspectives and Uncertainties*, The MIT Press, 2005.
9. G. W. Huber, S. Iborra and A. Corma, *Chemical Reviews*, 2006, **106**, 4044-4098.
10. H. Fukuda, A. Kondo and H. Noda, *Journal of Bioscience and Bioengineering*, 2001, **92**, 405-416.
11. A. E. Farrell, R. J. Plevin, B. T. Turner, A. D. Jones, M. O'Hare and D. M. Kammen, *Science*, 2006, **311**, 506-508.
12. U.S. Energy Information Administration / Annual Energy Review 2011, Figure 10.3 Fuel Ethanol Overview
13. Y. Sun and J. Cheng, *Bioresource Technology*, 2002, **83**, 1-11.
14. J. Hill, E. Nelson, D. Tilman, S. Polasky and D. Tiffany, *Proceedings of the National Academy of Sciences*, 2006, **103**, 11206-11210.
15. A. K. Agarwal, *Progress in Energy and Combustion Science*, 2007, **33**, 233-271.
16. L. C. Meher, D. Vidya Sagar and S. N. Naik, *Renewable and Sustainable Energy Reviews*, 2006, **10**, 248-268.
17. A. Demirbas, *Energy Policy*, 2007, **35**, 4661-4670.
18. S. A. Basha, K. R. Gopal and S. Jebaraj, *Renewable and Sustainable Energy Reviews*, 2009, **13**, 1628-1634.
19. D. Y. C. Leung, X. Wu and M. K. H. Leung, *Applied Energy*, **87**, 1083-1095.
20. M. n. Lapuerta, O. Armas and J. RodrÃ-guez-FernÃ¡ndez, *Progress in Energy and Combustion Science*, 2008, **34**, 198-223.
21. R. L. McCormick, M. S. Graboski, T. L. Alleman, A. M. Herring and K. S. Tyson, *Environmental Science & Technology*, 2001, **35**, 1742-1747.
22. W. G. Wang, D. W. Lyons, N. N. Clark, M. Gautam and P. M. Norton, *Environmental Science & Technology*, 2000, **34**, 933-939.
23. P. Schenk, S. Thomas-Hall, E. Stephens, U. Marx, J. Mussgnug, C. Posten, O. Kruse and B. Hankamer, *BioEnergy Research*, 2008, **1**, 20-43.
24. Y. Zhang, M. A. Dubra, D. D. McLean and M. Kates, *Bioresource Technology*, 2003, **90**, 229-240.
25. Mitchell, D. A note on rising food prices in World Bank Policy Research Working Paper Series, 2008
26. N. Mosier, C. Wyman, B. Dale, R. Elander, Y. Y. Lee, M. Holtzapple and M. Ladisch, *Bioresource Technology*, 2005, **96**, 673-686.
27. M. E. Himmel, S.-Y. Ding, D. K. Johnson, W. S. Adney, M. R. Nimlos, J. W. Brady and T. D. Foust, *Science*, 2007, **315**, 804-807.
28. P. N. R. Vennestrøm, C. M. Osmundsen, C. H. Christensen and E. Taarning, *Angewandte Chemie International Edition*, **50**, 10502-10509.
29. J. v. Haveren, E. L. Scott and J. Sanders, *Biofuels, Bioproducts and Biorefining*, 2008, **2**, 41-57.

30. C. H. Christensen, J. Rass-Hansen, C. C. Marsden, E. Taarning and K. Egeblad, *ChemSusChem*, 2008, **1**, 283-289.
31. E. S. Lipinsky, *Science*, 1981, **212**, 1465-1471.
32. F. J. Soday, *The Analysts Journal*, 1951, **7**, 17-24.
33. G. W. Huber and J. A. Dumesic, *Catalysis Today*, 2006, **111**, 119-132.
34. J. J. Bozell and G. R. Petersen, *Green Chemistry*, **12**, 539-554.
35. J.-P. Lange, in *Catalysis for Renewables*, Wiley-VCH Verlag GmbH & Co. KGaA, 2007, pp. 21-51.
36. R. E. H. Sims, A. Hastings, B. Schlamadinger, G. Taylor and P. Smith, *Global Change Biology*, 2006, **12**, 2054-2076.
37. I. Lewandowski, J. C. Clifton-Brown, J. M. O. Scurlock and W. Huisman, *Biomass and Bioenergy*, 2000, **19**, 209-227.
38. I. Lewandowski, J. M. O. Scurlock, E. Lindvall and M. Christou, *Biomass and Bioenergy*, 2003, **25**, 335-361.
39. R. Rinaldi and F. Schüth, *ChemSusChem*, 2009, **2**, 1096-1107.
40. Charles Wyman, Handbook on Bioethanol: Production and Utilization, CRC Press, 1996
41. S. G. Wettstein, D. M. Alonso, E. I. Gurbuz and J. A. Dumesic, *Current Opinion in Chemical Engineering*, **1**, 218-224.
42. E. Adler, *Wood Science and Technology*, 1977, **11**, 169-218.
43. C. E. Wyman, B. E. Dale, R. T. Elander, M. Holtzapple, M. R. Ladisch and Y. Y. Lee, *Bioresource Technology*, 2005, **96**, 1959-1966.
44. D. Sutton, B. Kelleher and J. R. H. Ross, *Fuel Processing Technology*, 2001, **73**, 155-173.
45. H. Schulz, *Applied Catalysis A: General*, 1999, **186**, 3-12.
46. X. Yin, D. Y. C. Leung, J. Chang, J. Wang, Y. Fu and C. Wu, *Energy & Fuels*, 2004, **19**, 305-310.
47. T. R. Carlson, T. P. Vispute and G. W. Huber, *ChemSusChem*, 2008, **1**, 397-400.
48. D. Mohan, C. U. Pittman and P. H. Steele, *Energy & Fuels*, 2006, **20**, 848-889.
49. T. P. Vispute, H. Zhang, A. Sanna, R. Xiao and G. W. Huber, *Science*, **330**, 1222-1227.
50. C. E. Wyman, ed., *Aqueous Pretreatment of Plant Biomass for Biological and Chemical Conversion to Fuels and Chemicals*, Wiley Series in Renewable Resources, 2013.
51. J. N. Chheda, G. W. Huber and J. A. Dumesic, *Angewandte Chemie International Edition*, 2007, **46**, 7164-7183.
52. J. J. Bozell, L. Moens, D. C. Elliott, Y. Wang, G. G. Neuenscwander, S. W. Fitzpatrick, R. J. Bilski and J. L. Jarnefeld, *Resources, Conservation and Recycling*, 2000, **28**, 227-239.
53. D. M. Alonso, S. G. Wettstein and J. A. Dumesic, *Green Chemistry*, **15**, 584-595.
54. G. W. Huber, J. N. Chheda, C. J. Barrett and J. A. Dumesic, *Science*, 2005, **308**, 1446-1450.
55. C. J. B. Yuriy Román-Leshkov, Zhen Y. Liu & James A. Dumesic, *Nature*, 2007, **447, 21 June 2007**, 982-986.
56. M. Balakrishnan, E. R. Sacia and A. T. Bell, *Green Chemistry*, **14**, 1626-1634.
57. S. E. Davis, L. R. Houk, E. C. Tamargo, A. K. Datye and R. J. Davis, *Catalysis Today*, **160**, 55-60.
58. S. E. Davis, B. N. Zope and R. J. Davis, *Green Chemistry*, **14**, 143-147.
59. A. J. J. E. Eerhart, A. P. C. Faaij and M. K. Patel, *Energy & Environmental Science*, **5**, 6407-6422.
60. R. H. Leonard, *Industrial & Engineering Chemistry*, 1956, **48**, 1330-1341.
61. B. Girisuta, L. P. B. M. Janssen and H. J. Heeres, *Chemical Engineering Research and Design*, 2006, **84**, 339-349.
62. B. Girisuta, L. P. B. M. Janssen and H. J. Heeres, *Industrial & Engineering Chemistry Research*, 2007, **46**, 1696-1708.
63. B. Girisuta, L. P. B. M. Janssen and H. J. Heeres, *Green Chemistry*, 2006, **8**, 701-709.

64. J. C. Serrano-Ruiz, D. J. Braden, R. M. West and J. A. Dumesic, *Applied Catalysis B: Environmental*, **100**, 184-189.
65. M. Mascal and E. B. Nikitin, *Green Chemistry*, **12**, 370-373.
66. J. Hegner, K. C. Pereira, B. DeBoef and B. L. Lucht, *Tetrahedron Letters*, **51**, 2356-2358.
67. F. Tao, H. Song and L. Chou, *Carbohydrate Research*, **346**, 58-63.
68. S. W. Fitzpatrick, in *Feedstocks for the Future*, ACS Symposium Series, Vol. 921, 2006.
69. S. W. Fitzpatrick, *Biofine Incorporated* US Patent 5608105, 1997.
70. B. V. Timokhin, V. A. Baransky and G. D. Eliseeva, *Russian Chemical Reviews*, 1999, **68**, 73-84.
71. Isoda Y and A. M., *Honshu Chemical Ind.*, Japanese patent 08053390, 1996.
72. L. E. Manzer, in *Catalysis for the Conversion of Biomass and Its Derivatives*, eds. M. Behrens and A. K. Datye, 2013.
73. R. V. Christian, H. D. Brown and R. M. Hixon, *Journal of the American Chemical Society*, 1947, **69**, 1961-1963.
74. Z.-p. Yan, L. Lin and S. Liu, *Energy & Fuels*, 2009, **23**, 3853-3858.
75. J. C. Serrano-Ruiz, D. Wang and J. A. Dumesic, *Green Chemistry*, **12**, 574-577.
76. X.-L. Du, L. He, S. Zhao, Y.-M. Liu, Y. Cao, H.-Y. He and K.-N. Fan, *Angewandte Chemie*, **123**, 7961-7965.
77. Q.-Y. Bi, X.-L. Du, Y.-M. Liu, Y. Cao, H.-Y. He and K.-N. Fan, *Journal of the American Chemical Society*, **134**, 8926-8933.
78. L. E. Manzer, *Applied Catalysis A: General*, 2004, **272**, 249-256.
79. J.-P. Lange, J. Z. Vestering and R. J. Haan, *Chemical Communications*, 2007, 3488-3490.
80. D. n. Fegyverneki, L. s. Orha, G. z. Lang and I. n. T. Horvath, *Tetrahedron*, **66**, 1078-1081.
81. I. T. Horvath, H. Mehdi, V. Fabos, L. Boda and L. T. Mika, *Green Chemistry*, 2008, **10**, 238-242.
82. I. T. Horvath, *Green Chemistry*, 2008, **10**, 1024-1028.
83. L. Qi and I. n. T. HorvÃ¡th, *ACS Catalysis*, **2**, 2247-2249.
84. S. G. Wettstein, D. M. Alonso, Y. Chong and J. A. Dumesic, *Energy & Environmental Science*, **5**, 8199-8203.
85. D. M. Alonso, J. M. R. Gallo, M. A. Mellmer, S. G. Wettstein and J. A. Dumesic, *Catalysis Science & Technology*, **3**, 927-931.
86. M. Behrens and A. K. Datye, eds., *Catalysis for the Conversion of Biomass and Its Derivatives*, 2013.
87. D. A. Simonetti and J. A. Dumesic, *ChemSusChem*, 2008, **1**, 725-733.
88. T. Okuhara, *Chemical Reviews*, 2002, **102**, 3641-3666.
89. E. L. Kunkes, D. A. Simonetti, R. M. West, J. C. Serrano-Ruiz, C. A. GÃ¤rtner and J. A. Dumesic, *Science*, 2008, **322**, 417-421.
90. K. Tanabe and W. F. Halderich, *Applied Catalysis A: General*, 1999, **181**, 399-434.
91. A. Corma, *Chemical Reviews*, 1995, **95**, 559-614.
92. A. Corma, *Current Opinion in Solid State and Materials Science*, 1997, **2**, 63-75.
93. W. E. Farneth and R. J. Gorte, *Chemical Reviews*, 1995, **95**, 615-635.
94. S. Telalovic, J. F. Ng, R. Maheswari, A. Ramanathan, G. K. Chuah and U. Hanefeld, *Chemical Communications*, 2008, **0**, 4631-4633.
95. K.-i. Shimizu, H. Furukawa, N. Kobayashi, Y. Itaya and A. Satsuma, *Green Chemistry*, 2009, **11**, 1627-1632.
96. A. Corma, S. B. A. Hamid, S. Iborra and A. Velty, *Journal of Catalysis*, 2005, **234**, 340-347.
97. J. G. Santiesteban, J. C. Vartuli, S. Han, R. D. Bastian and C. D. Chang, *Journal of Catalysis*, 1997, **168**, 431-441.
98. T. Okuhara, M. Kimura, T. Kawai, Z. Xu and T. Nakato, *Catalysis Today*, 1998, **45**, 73-77.
99. Y. RomÃ¡n-Leshkov and M. E. Davis, *ACS Catalysis*, **1**, 1566-1580.

100. L. Smith, A. K. Cheetham, R. E. Morris, L. Marchese, J. M. Thomas, P. A. Wright and J. Chen, *Science*, 1996, **271**, 799-802.

2. Experimental Techniques

2.1 Catalyst Synthesis

2.1.1 Commercial Catalysts

For several studies presented in this thesis, catalysts were purchased from catalyst suppliers and used as received or were pretreated as described below. Amorphous SiO_2/Al_2O_3 (**Chapter 3, 4, 5 and 7**) was obtained from Grace-Davison/Davicat (SIAL 3113, Si/Al=3.40). Prior to reaction kinetics studies, the SiO_2/Al_2O_3 catalyst was dried in situ at 723 K (heating rate of 3 K min^{-1}, followed by 4 h hold) in flowing air (Airgas, Medical Grade 50 cm^3(STP)/min). H-ZSM-5 (Si:Al = 14) used in the oligomerization of butene (**Chapter 3**) was obtained from Engelhard/BASF and conditioned via thermal calcination at 773 K under flowing air prior the catalytic experiments. Zeolite H-Y (Zeolyst, CBV400, Si/Al=2.55, S.A.=730 m^2/g) was calcined at 823 K for 4 hours before use. Niobic acid (CBMM, HY-340, S.A. 118 m^2/g) was used without further pretreatment. Amberlyst-70 used in the oligomerization of butene (**Chapter 3**) was obtained from Rohm and Haas (Dow Chemical). Prior to reaction, it was rinsed with de-ionized water until the effluent showed no signs of residual acidity, dried overnight at 393 K and ground to fine powders. γ-Al_2O_3 (**Chapter 5 and 7**) was obtained from STREM Chemicals and was pre-treated at 648 K in 60 cm^3 (STP) min^{-1} helium (Airgas, industrial grade) for 3 hours before use. The Magnesium Oxide (MgO) catalyst (**Chapter 5**) was obtained from NanoScale Materials, Inc. and was activated at 500K under 60 cm^3 (STP) min^{-1} helium (Airgas, industrial grade) for 3 hours before reaction studies. Niobic acid ($Nb_2O_5\,xH_2O$, HY-340) was purchased from CBMM

and was used as received (**Chapter 6 and 7**). 5 wt% Ru/C catalyst (Sigma–Aldrich) was used as received.

2.1.2. Supported Catalysts

Supported catalysts used in this thesis were generally prepared by incipient wetness impregnation technique as described herein. Catalysts consisting of Pd nanoparticles supported on niobia, including commercial niobia HY-340, silica-modified niobia and mesoporous niobia (**Chapter 6**) were prepared by impregnating an aqueous solution of $Pd(NO_3)_2$ xH2O (Aldrich). Catalysts were dried in air at 380 K overnight, followed by calcination at 538 K (1 K min^{-1} ramp) in flowing air (250 cm^3 (STP) min^{-1}) for 2h. The zirconia supported tungsten oxide (WO_x-ZrO_2, **Chapter 7**) catalysts were prepared by calcining commercial tungstated zirconium hydroxide (15 wt% WO_3 loading, MEL Chemicals, XZO1251/01) precursors at temperatures from 723 to 1223 K for 3 hours in static air before use. A sample calcined at temperature T is denoted as WO_x-ZrO_2-T, e.g., WO_x-ZrO_2-923 being the sample calcined at 923 K. γ-Al_2O_3 supported tungsten oxide (WO_x-Al_2O_3, **Chapter 5**) were prepared by impregnation of γ-Al_2O_3 with an aqueous solution of ammonium metatungstate (Sigma-Aldrich, 99.99% trace metals basis). After impregnation, the material was dried at 383 K overnight followed by calcination at 723 K for 5 hours in static air. Before reaction studies, the catalysts were further pre-treated at 648 K in 60 cm^3 (STP) min^{-1} helium (Airgas, industrial grade) for 3 hours. Catalyst containing 4 wt% WO_3 (calculated value) is denoted as 4W-Al. The RuSn/C catalysts (**Chapter 3**)were prepared by impregnating the commercial 5 wt% Ru/C (Sigma-Aldrich) with an aqueous solution of $SnCl_2$ $2H_2O$, followed by calcination in air at 353 K for 2 h. Prior to reactions studies, catalyst samples

were reduced in situ for 3 h at 723 K (1 K min^{-1}), else catalysts were reduced as described above, and subsequently passivated in 2% O_2 in He (50 cm3 min^{-1}, Airgas) at 298 K for 60 minutes.

2.1.3 SBA-15 Synthesis

Mesoporous silica, SBA-15 (**Chapter 6**), was synthesized following the procedure of Zhao, et al.(1) In a typical synthesis, 4.0 g of Pluronic P123 (Aldrich) was dissolved in 120 g of 2 M HCl solution and 30 g of deionized H_2O while stirring at 308 K. Once dissolved, 8.50 g of tetraethoxysilane (TEOS, Aldrich) was added to the solution, followed by stirring for 20 h at 308 K. The resulting mixture was maintained at 373 K under static conditions for 24 h. The solid product was filtered, washed, and air-dried at room temperature. Template removal (P123) was accomplished by calcination in air at 773 K (ramp 1 K min^{-1}) for 6 h.

2.1.4 Silica-doped Niobia Catalysts

Silica-doped niobia catalysts (**Chapter 6**) were synthesized by collaborators at University of New Mexico using the following procedure. 95 wt% Nb-Si oxide_ANO was prepared using Ammonium Niobium Oxalate (ANO) with a molar ratio of CTAB:H_2O = 1:284 and a molar ratio of SiO_2:ANO = 0.1:1. CTAB was dissolved in water followed by the addition of ANO. Sodium silicate was added dropwise to the solution in order to obtain a homogeneous mixture. The pH was then slowly adjusted to 7 by adding 1M NH_4OH. The mixture was heated at 353 K for 7 hr in a water bath, cooled to ambient temperature, and then kept at ambient temperature overnight. The mixture was filtered, washed with water, vacuum dried, and calcined in air at 773 K for 12 hr to remove the CTAB template.

95 wt% Nb-Si oxide_ETO was prepared using tetraethyl orthosilicate (TEOS) as the silica precursor. For this preparation, tetradecylamine (1.7 g, 7.9 mmol) was dissolved in a mixture of niobium(V) ethoxide ($Nb(EtO)_5$) (ETO) (4.2 g, 13.3 mmol) and tetraethyl orthosilicate (0.28 g, 1.32 mmol) in the absence of water. The solution was stirred until homogeneous, then 5 mL of ethanol and 15 mL of water were added to the mixture; this causing the precipitation of a white solid. The mixture was left at ambient temperature for 1 day and then aged at 353 K, 373 K, and 453 K for 1, 1, and 7 days respectively. The product was filtered and washed with 500 mL of water and 500 mL of ethanol. After drying of the product, the surfactant was removed by an acid reflux treatment with 70% nitric acid at pH 0.5 in a 4:1 (v:v) mixture of isopropanol and water for 24 hr. The product was filtered, washed and dried in a vacuum oven at 353 K overnight.

2.1.5 Mesoporous Niobia by Atomic Layer Deposition

These materials (**Chapter 6**) were synthesized by collaborators at Argonne National Laboratory using the following procedure. Niobia was deposited by atomic layer deposition (ALD) in a viscous flow reactor at a temperature of 473 K.(2) Synthesized SBA-15 was placed in a shallow tray in a layer approximately 1mm deep and covered with a tight fitting wire cloth lid to contain the SBA-15 while allowing access to the ALD precursor vapors. The loaded tray was first heated in air at 473 K for 30 min to remove physisorbed moisture, weighed, and then inserted into the viscous flow ALD reactor. Ultrahigh purity (99.999%) nitrogen carrier gas was continuously passed through the reactor at a mass flow rate of 190 cm3 (STP) min^{-1} and a pressure of 1.1 Torr. The ALD of Nb_2O_5 was performed using alternating exposures to niobium(V) ethoxide ($Nb(OCH_2CH_3)_5$) (Aldrich) and deionized H_2O. The $Nb(OCH_2CH_3)_5$ was

held in a stainless steel bubbler heated to 408 K through which 100 cm3 (STP) min^{-1} of nitrogen carrier gas was diverted for a period of 8 min. The H_2O was held in a stainless steel reservoir at room temperature, and the H_2O vapor was injected onto the flowing nitrogen at a rate of 25 cm^3 (STP) min^{-1} for a period of 4min. Purge periods of 2 min were used between exposures to the ALD reactants. The trays were immediately weighed upon removal from the reactor and then allowed to cool in the laboratory air environment. Samples are denoted as SBA-15-ALD-y, where y corresponds to the number of niobia cycles performed (e.g., 1, 10, 19, and 30).

2.2 Catalyst Characterization

2.2.1 CO Chemisorption

CO adsorption (**Chapter 6**) isotherms were collected using a Micromeritics ASAP 2020 apparatus. Prior to chemisorption measurements, the catalysts were reduced in flowing H_2 (100 cm^3 (STP) min^{-1}) for 3 hr at 538 K (1.5 K min^{-1}). The samples were then purged with UHP helium to clean the metallic surface (200 cm^3 (STP) min^{-1}) for 1 hr at 538 K. After cooling the samples to 300 K subsequently, small amounts of CO were dosed onto the catalysts. Two isotherms were collected and irreversible probe molecule uptake was calculated by subtracting the reversible uptake from the total uptake measured in the first isotherm. Pd dispersions were calculated on the basis of a Pd/CO stoichiometry of 2:1.

2.2.2 Temperature Programmed Desorption

Temperature-programmed desorption of NH_3 (**Chapter 5, 6 and 7**) was used to determine the total acid site density by loading 100-200 mg of catalyst in a glass flow-through cell. Before NH_3 adsorption, samples were held at 538 K for 1 h under flowing helium (120 cm^3

(STP) min^{-1}) to remove adsorbed moisture. NH_3 was then adsorbed by exposing the sample to a flowing gas mixture of 1 mol% NH_3 in He (100 cm^3 (STP) min^{-1}) at 423 K for ca. 45 min. Physisorbed NH_3 was removed by holding the sample at 423 K under flow helium (120 cm^3 (STP) min^{-1}) for 45 min. Temperature-programmed desorption was performed using a temperature ramp of 10 K min^{-1} from room temperature to 1073 K under flowing He (40 cm^3 (STP) min^{-1}). In the case of CO_2 adsorption (**Chapter 5**), 10 mol% CO_2 in He (Airgas, 100 cm^3 (STP) min^{-1}) was then passed through the sample at 298K for ca. 45 min. Physisorbed CO_2 was removed by holding the sample at 298 K under flow helium (120 cm^3 (STP) min^{-1}) for 45 min. The desorbed NH_3 or CO_2 was quantified by an online mass spectrometer (OmniStar).

2.2.3 N_2 Sorption

Nitrogen adsorption-desorption isotherms were measured at 77 K using a Micromeritics ASAP 2020 analyzer. The samples were degassed at 423K for 5 hours prior to analysis. The specific surface areas of the materials were determined using the BET approach. Pore size distribution was determined by the BJH method of the desorption branch of the isotherm (**Chapter 5, 6 7**). Pore volumes were determined from the adsorption branch of the N_2 isotherm at P/P0 = 0.97 single point.

2.2.4 X-Ray Diffraction

XRD analyses (**Chapter 6**) were carried out using a Siemens STOE diffractometer (Cu Kα, λ = 1.5406 Å) at 25 mA and 40 kV. Diffraction patterns were collected in a continuous mode with a step width of 0.02 degrees and with an acquisition time of 10 seconds per step.

2.2.5 Laser Raman Spectroscopy

Raman spectroscopy (**Chapter 7**) was performed with a visible laser (532 nm) excitation on a LabRAM Aramis Horiba Jobin Yvon Raman spectrometer. The spectrometer was equipped with an in situ treatment cell (Linkam, THMS 600) which allowed for control of both temperature and atmosphere within the cell chamber. The catalyst samples, in the form of loose powder (10-20 mg), were loaded into the cell chamber. The WO_x-ZrO_2 samples were dehydrated at 723 K for 1 h in flowing dry air (Airgas, Dry Grade, 50 mL min^{-1}) to desorb moisture and then cooled to 393 K.(3) Spectra were taken at 393 K with 10 scans of 10 s/scan, for a total acquisition time of 4 min. per spectrum. System alignment was verified using the characteristic 520 cm^{-1} band from a silicon reference standard.

2.2.6 Fourier Transformed-Infrared Spectroscopy of adsorbed pyridine

The ratio of Brönsted and Lewis acid sites on the solid acid catalysts studied was determined from infrared spectroscopic measurements of adsorbed pyridine (**Chapter 5 and 7**). Approximately 10 mg of catalyst was placed in a 1.2 cm die and pressed into a self-supporting wafer, which was placed in a treatment/sampling cell where it was heated to 648 K under flowing dry helium (Airgas, industrial grade) for 2 h. A reference spectrum of the catalyst was then taken. Pyridine was introduced into the cell through a bubbler for 30 min at room temperature, followed by purging under flowing helium for 1 h before another spectrum was taken. The areas of the pyridine peaks at 1455, and 1540 cm^{-1}, assigned to Lewis and Brönsted acid sites, respectively, (4, 5)were determined by subtracting the spectra of the sample before and after pyridine exposure. The Brönsted/Lewis acid ratios were obtained by normalizing the

areas with integrated molar extinction coefficients reported in the literature: 1.67 cm μmol^{-1} for Brönsted sites and 2.22 cm μmol^{-1} for Lewis sites.(5)

2.2.7 ICP-Atomic Emission Spectroscopy

In **Chapter 6**, the niobium content of each sample was measured by inductively coupled plasma-atomic emission spectrometry (ICP) analysis using a Perkin-Elmer Plasma 400 ICP emission spectrometer after dissolving the sample in 5 wt% aqueous hydrofluoric acid (HF) solution. Standard solutions of niobium (Aldrich) were used to obtain a calibration curve.

2.2.8 Thermogravimetric Analysis (TGA)

Thermogravimetric Analysis (TGA) was carried out using a Thermogravimetric Analyzer Q500 in oxygen atmosphere (50 cm^3 (STP) min^{-1}) with a rate of 20 K min^{-1} to 973 K. The temperature was maintained at 973 K for 10 minutes for each experiment. Approximately 42 mg of sample was used in each experiment. (**Chapter 5**)

2.2.9 Microcalorimetry

Microcalorimetric experiments (**Chapter 3**) were carried out using a glass high-vacuum system and custom-built calorimetry cells, as described in detail elsewhere.(6) Heats of adsorption were measured at 302 K using a BT-2.15D Tian-Calvet heat flux microcalorimeter (Setaram), and butene uptake was determined volumetrically by monitoring system pressure using MKS Baritron capacitance manometers. The sample cell was loaded with 2.0 g of crushed Amberlyst-70 resin and outgassed under vacuum using an externally heated furnace to control the cell temperature, which was ramped from 298 to 373 K at a rate of 1.25 K min^{-1}, held at 373

K for 60min, ramped to 433 K at a rate of 3 K min^{-1}, and held at 433 K for 180 min, after which no further outgassing was observed. 1-Butene (Airgas, CP grade) was introduced into the dosing manifold and subsequently to the sample cell.

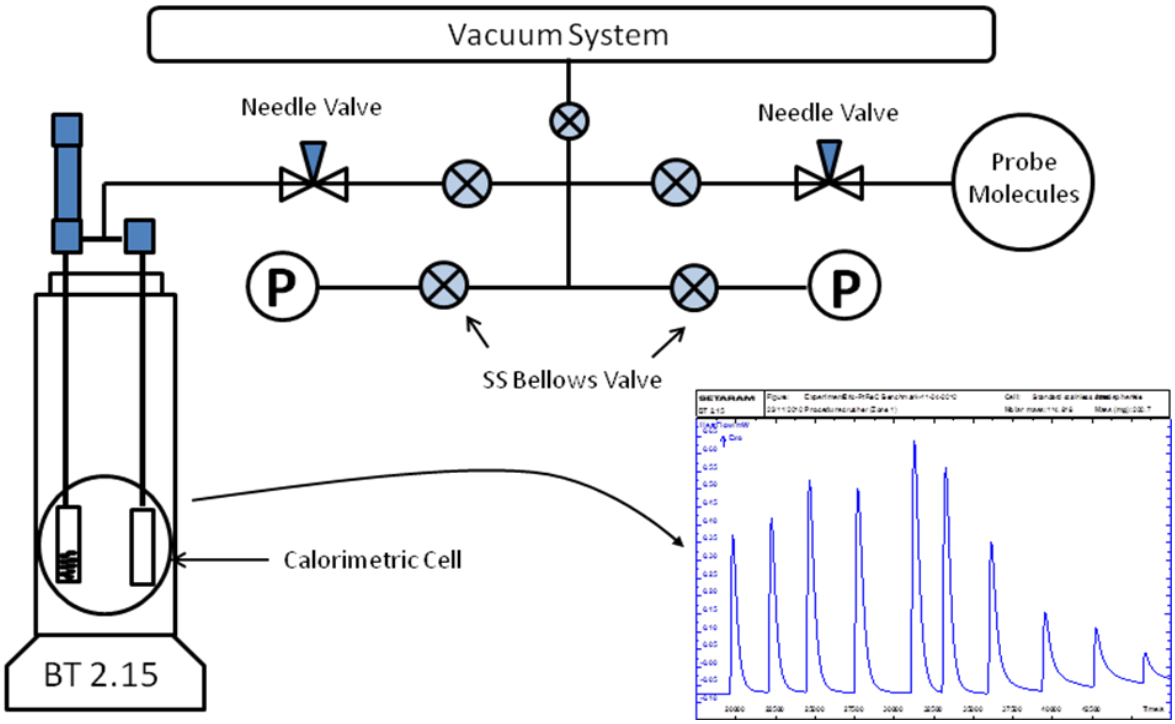

Figure 2.1 Schematic of the calorimeter connected to a vacuum system used in Chapter 3

Typically, times of 60 – 90 min were allowed between doses to allow a return to thermal equilibrium in the microcalorimeter. A second experiment to elucidate the effect of 5-nonanone on catalytic activity was designed similarly; however, after the initial outgassing step, the Amberlyst was sealed under 500 Torr of Nitrogen and transferred into a glove box held in a nitrogen atmosphere, where 5-nonanone was introduced into the sample cell (1.0 g of nonanone per gram of Amberlyst-70). The calorimetry cells were again isolated under nitrogen and re-connected to the vacuum system, where they were repeatedly evacuated for time intervals of 5 to 10 seconds to purge residual nitrogen and retain only liquid 5-nonanone and Amberlyst resin in

the sample cell. Ultimately, the cell pressure equilibrated at approximately 0.65 Torr, which is the vapor pressure of 5-nonanone at 302 K. Prior to microcalorimetric measurements, a total site count was estimated by volumetric adsorption of butene using the same apparatus at 298 K.

2.3 Reactor setup for reaction studies

2.3.1 Flow reactor system

Reaction studies were conducted in a fixed-bed, up-flow reactor comprises of 6.4 mm (0.25 inch, wall thickness = 0.028 inch) outer-diameter stainless steel tube (**Chapter 3, 4 5, 6**). The reactor set up is illustrated in Figure 2.2.

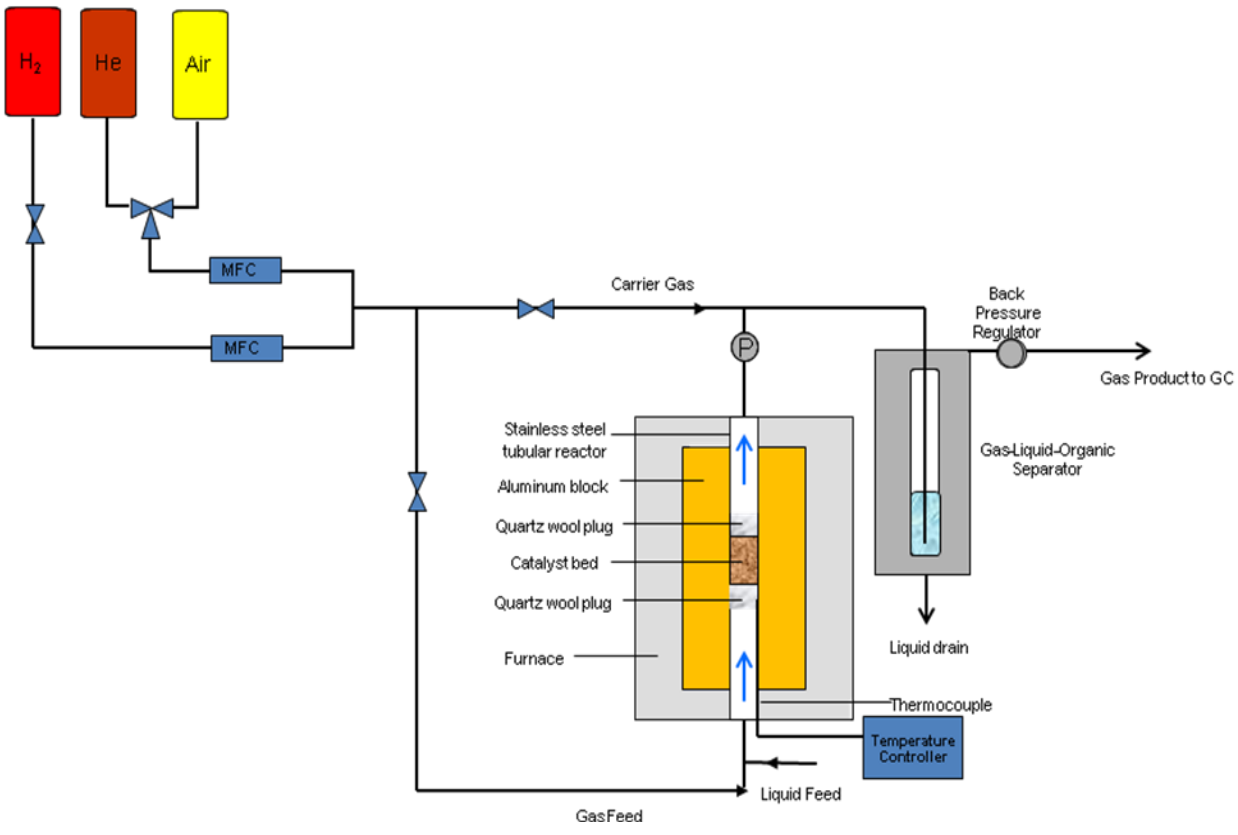

Figure 2.2 Schematic of fixed-bed flow reactor setup

The reactor was packed with 100 mg ~ 2g of catalyst diluted with fine fused silica powder (Sigma-Aldrich). Two quartz wool plugs were used to seal both ends of the reactor. The reactor was heated by an insulated furnace (Applied Test Systems Series 3210), and temperature was monitored using a K type thermocouple (Omega) and was controlled with a PID temperature controller (Love Controls, Series 16A). An HPLC pump (Lab Alliance Series I) was used to deliver aqueous solution to the reactor. In cases where the reactants have low solubility in water, two syringe pumps were used to deliver water and reactant to the reactor. Gas flow was regulated using a mass flow controller (Brooks 5850 model), and the system pressure was maintained by a back-pressure regulator (GO BP-60). The effluent liquid was collected in a gas-liquid separator (Jerguson Gage and Valve) maintained at room temperature and was drained periodically for quantitative analysis by High-Performance Liquid Chromatography (Waters e2695 HPLC system, equipped with a 2998 PDA UV detector and a 2414 refractive index detector), or Gas Chromatography (Shimadzu GC-2010 with FID detector). The effluent gas was analyzed by two online GCs equipped with an FID detector (Shimadzu, 2010 for hydrocarbon detection) and a TCD detector (Shimadzu GC-8A for Cox detection), respectively. Products were identified using a gas chromatograph/mass spectrometer system (Shimadzu GCQP-2010).

2.3.2 Batch reactor system

Batch reaction kinetics studies (**Chapter 7**) were conducted in a 50 mL, high pressure hastelloy Parr reactor (Parr instrument) furnished with graphite gaskets and tapes (see Figure 2.3). The reactor was heated to 523 K by a homemade furnace controlled by a 16A series programmable temperature controller (Love controls), and stirring was provided by a high temperature SmCo (29 MGO) magnetic stir bar (V&P scientific Inc.). The reactor was charged

with 0.15 g of catalyst and 2 g of diene (99%, Sigma-Aldrich) dissolved in 18 g of hexadecane (anhydrous grade, Sigma-Aldrich). The reactor was purged at room temperature with argon twice before it was pressurized with ethylene (Praxair) to 20 bar (300 psi) under vigorous stirring to ensure that the liquid was saturated with ethylene. It was estimated from solubility data (7) that an excess of ethylene was present in the reactor (ethylene/diene > 2), and thus the conversion was not limited by ethylene. The reactor was brought to the reaction temperature and maintained for the desired reaction time (approx. 1.5-6 h) before liquid samples were collected. Products were identified using a gas chromatograph/mass spectrometer system (Shimazu GCQP-2010) and quantifications were performed using a gas chromatograph (Shimazu GC-2010) equipped with a flame ionization detector. Spent catalysts were recovered by centrifugation. They were washed with 300 mL of isopropanol to remove residual solvents and then dried in an oven (373 K) for 3 hours before reuse. When regeneration was needed, catalysts were calcined under flowing air for 3 hours at 923 K.

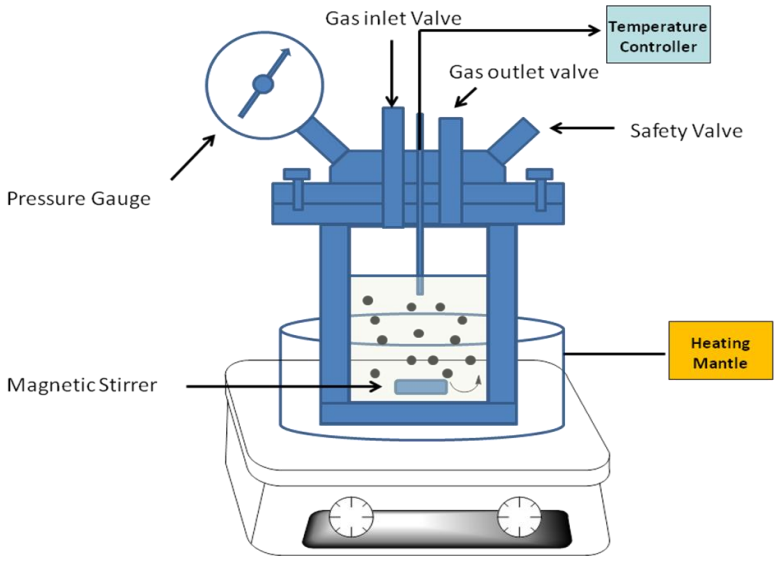

Figure 2.3 Schematic of batch reactor setup

2.4 Definition and Data Analysis

In this thesis, conversion, selectivity, yield and weight hourly space velocity (WHSV) were defined as:

$$\text{Conversion (\%)} = \frac{\text{moles of lactones converted}}{\text{moles of lactones fed}} \times 100\%$$

$$\text{Selectivity (\%)} = \frac{\text{moles of product}}{\text{moles of lactones converted}} \times 100\%$$

$$\text{Yield (\%)} = \frac{\text{moles of product}}{\text{moles of lactones fed}} \times 100\%$$

$$\text{WHSV}(h^{-1}) = \frac{\text{hourly mass flowrate of reactant}}{\text{mass of catalyst}}$$

2.5 References

1. D. Zhao, Q. Huo, J. Feng, B. F. Chmelka and G. D. Stucky, *J. Am. Chem. Soc.*, 1998, **120**, 6024-6036.
2. J. W. Elam, M. D. Groner and S. M. George, *Rev. Sci. Instrum.*, 2002, **73**, 2981-2987.
3. E. I. Ross-Medgaarden, W. V. Knowles, T. Kim, M. S. Wong, W. Zhou, C. J. Kiely and I. E. Wachs, *J. Catal.*, 2008, **256**, 108-125.
4. E. P. Parry, *J. Catal.*, 1963, **2**, 371-379.
5. C. A. Emeis, *J. Catal.*, 1993, **141**, 347-354.
6. B. E. Spiewak and J. A. Dumesic, *Thermochim. Acta*, 1997, **290**, 43-53.
7. A. Sahgal, H. M. La and W. Hayduk, *Can. J. Chem. Eng.*, 1978, **56**, 354-357.

3. Integrated Continuous Process for Liquid Olefin Production from Biomass-derived γ-Valerolactone (GVL)

3.1 Introduction

As described in Chapter 1, diminishing fossil fuel reserves and increasing levels of atmospheric CO_2 require the development and implementation of technologies for converting renewable feedstocks to meet the societal need for materials and transportation fuels in a sustainable manner(*1-4*). Within this context, a continued supply of liquid fuels is a primary challenge since the transportation sector is the largest single consumer of crude oil reserves (Figure 1.1). Such research has been on-going for decades, and, at present, biodiesel production from triglycerides and ethanol production from starches are mature technologies. However, the true potential of bioenergy will not be unlocked until lignocellulosic biomass can be cost-effectively converted into fuels with comparable properties with existing hydrocarbon fuels and are thus compatible with current infrastructures. In this respect, gamma-valerolactone (GVL) has been identified as a promising molecule (5) with potential for impact as a feedstock in the production of both energy (5, 6) and chemicals (7). GVL is produced by hydrogenation of levulinic acid, the latter of which can be produced, potentially at low cost, from agricultural waste (*3*) using processes already established on a commercial scale (8). Recently, researchers have minimized the demand for an external source of hydrogen in this process by utilizing the formic acid formed in equi-molar amounts with levulinic acid from cellulose (6) and C_6 sugars (9). GVL retains 97% of the energy content of glucose and performs comparably to ethanol

when used as a blending agent (10% v/v) in conventional gasoline (5). It has also been applied as a renewable co-solvent in splash blendable Diesel fuel (10).

However, as with other oxygenated molecules, direct application of GVL as a fuel additive still suffers from several limitations for widespread use in the transportation sector, such as high water solubility, blending limits for use in conventional combustion engines, possible corrosiveness in storage and lower energy density compared to petroleum-derived fuels. These limitations can be partially alleviated by reduction of GVL with an external source of hydrogen to produce methyltetrahydrofuran (MeTHF) (11), which can be blended up to 70% in gasoline. Another effort made by a group of researches at Shell Global Solutions studied the conversion of glucose-derived GVL to the so-called valeric biofuels, which consists of alkyl (mono/di) valerate esters. The 4-step manufacturing process of valeric fuels are summarized in Figure 3.1.(12) GVL is obtained by the hydrolysis of cellulose using dilute sulfuric acid to form levulinic acid, followed by its hydrogenation and ring closing over a Pt/TiO_2 catalyst. Using a bifunctional catalyst, Pt/ZSM-5, GVL is then ring opened and hydrogenated to produce valeric acid (or pentanoic acid), which are then esterified with an alcohol to produce alkyl valerate esters.

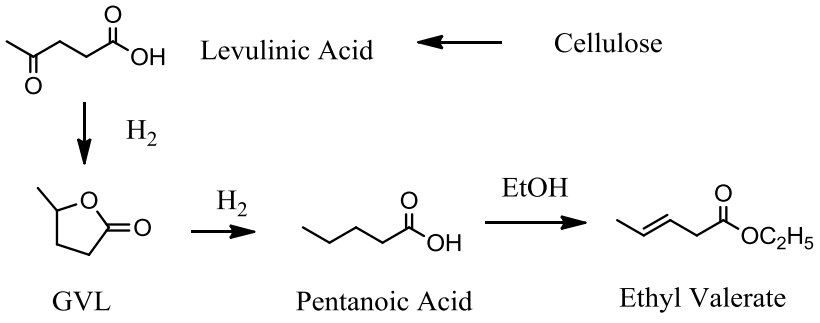

Figure 3.1 Synthesis of valeric biofuels (12).

It is reported that these valerate esters have acceptable energy densities and more suitable polarities than current biofuel molecules, including ethanol, n-butanol, GVL and MeTHF) for gasoline applications. While the valerate esters potentially offer a good platform of cellulosic biofuel that can be blended into gasoline with ratios higher than competing candidates such as ethanol or n-butanol, some of the aforementioned limitations of oxygenated fuel still restrict its application on a large scale. On the other hand, these limitations would be completely eliminated by converting GVL to liquid alkenes (or alkanes) with molecular weights targeted for direct use as transportation fuels.

Generally, in the United States, the majority of gasoline internal combustion engines can accommodate oxygenate blending at 10 – 15 vol%. Oxygenate inclusion is more severely restricted in distillate fuels, particularly those intended for aviation, which have a high demand for volumetric energy density. Although near-term production of oxygenates will aid in meeting renewable fuel mandates through gasoline blending, it is essential to shift biofuel production toward liquid alkanes in the long term. This will permit lignocellulosic carbon to supply energy-dense hydrocarbons to essential jet- and diesel markets in the long-term, particularly as technological advances enable increasing use of alternative power supplies for light-duty transportation. (13, 14)

As shown in the stoichiometric relations below, the conversion of GVL to alkenes and CO_2 does not require an external source of hydrogen:

$$C_5O_2H_8 \longrightarrow C_4H_8 + CO_2$$
$$n(C_4H_8) \longrightarrow C_{4n}H_{8n}$$

$$n(C_5O_2H_8) \longrightarrow C_{4n}H_{8n} + nCO_2$$

The hydrogenation of an alkene to an alkane requires one equivalent of H_2; however, the amount of H_2 required for the overall conversion of GVL to an alkane decreases as the molecular weight of the alkane increases. While the combustion of biomass-derived alkenes is equivalent to the combustion of GVL in terms of energy, the combustion of alkenes would lead to a net decrease in the level of CO_2 in the atmosphere by cycles of biomass growth and bio-fuel combustion, provided that the CO_2 formed during the conversion of GVL to alkenes could be utilized effectively. The same argument can be used to describe the conversion of glucose to ethanol, as indicated in the stoichiometric relation below:

$$C_6O_6H_{12} \longrightarrow 2C_2OH_6 + 2CO_2$$

However, an important difference between these two approaches for the production of bio-fuels is that the production of CO_2 during the conversion of GVL to alkenes can be accomplished at elevated pressure (e.g., 36 bar, as demonstrated in this report), appropriate for sequestration (15, 16), conversion to methanol (17, 18) upon reaction with a renewable source of hydrogen (19, 20), or utilized for polycarbonate production via co-polymerization with epoxides (21, 22). In contrast, the production of CO_2 during fermentation of glucose to ethanol is carried out at atmospheric pressure (23).

In this chapter, I describe an integrated continuous process that converts biomass-derived GVL into liquid olefins with chain lengths suitable for jet and diesel fuel applications. The effect

of process parameters as well as the effect of water on the solid acid catalysts used for this transformation will be discussed. Also included in this chapter is an effort to scale up this process to deliver liter quantities of jet fuel components directly from lignocellulose (maple wood in this case), which is part of a concerted, multi-university research program supported by the U.S. Defense Advanced Research Projects Agency (BAA 08-48, Surface Catalysts for Energy (SurfCAT) program). The outcome of this project is an efficient process of converting whole lignocellulose to C_8 and larger hydrocarbon fuels with an overall carbon yield of 80% or higher using stable catalytic processes operating at short residence times (<1 hour) for extended operation (200 hours on stream).

3.2 Process Description

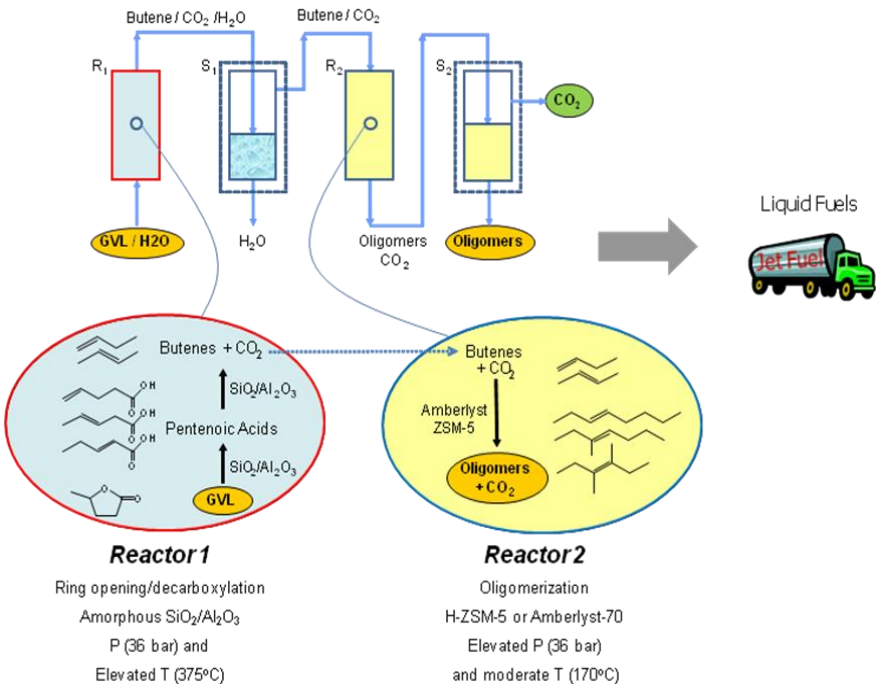

Figure 3.2 Reaction pathways the integrated conversion of GVL to a liquid stream of alkenes for use in transportation fuels and a gaseous stream rich in CO_2 that is appropriate for further processing options.

Figure 3.2 shows our integrated approach to convert an aqueous solution of GVL to liquid alkenes with molecular weights appropriate for transportation fuels, involving the catalytic decarboxylation of GVL to butene and CO_2, combined with the oligomerization of butene at elevated pressures, using a single catalytic system involving two tubular flow reactors connected in series with an inter-reactor separator (24). The first step is the ring opening of GVL to produce an isomeric mixture of unsaturated pentenoic acids, which can then undergo decarboxylation to produce butene isomers and a stoichiometric quantity of CO_2. It is demonstrated herein that both of these transformations can be carried out over a solid acid catalyst, SiO_2/Al_2O_3, in the presence of water in a single, fixed bed reactor. Moreover, these reactions can be carried out at pressures ranging from ambient to 36 bar. After a separation step in which water is condensed to the liquid state, the butene/CO_2 gas stream is upgraded in a second reactor to higher molecular weight alkenes through acid-catalyzed oligomerization (25, 26). This oligomerization process is favored at elevated pressures and can be tuned to yield alkenes with a targeted range of molecular weights and varied degrees of branching in the product stream (27, 28). In a second separation step, the alkenes are condensed to form a liquid product stream, while CO_2 remains as a high pressure gas. This approach does not require an external source of hydrogen as is necessary, for example, in the catalytic upgrading of bio-oils produced by pyrolysis of biomass (29).

3.3 Effect of Pressure, Temperature on Butene Formation from GVL and Catalyst Stability

Table 3.1 summarizes effects of pressure, temperature, and feed composition for the conversion of aqueous solutions of GVL to butene and CO_2 over a SiO_2/Al_2O_3 catalyst (24). For a given temperature (entries 1 – 3), the conversion of GVL is approximately constant at pressures

ranging from 1 to 36 bar; however, the yield of butenes decreases at higher pressures, caused by the appearance of higher levels of pentenoic acid, which is a reactive intermediate. Butene selectivity can be improved by operating the reactor at higher temperatures, and good yields of butene (60%) were observed at 673 K and 36 bar (entry 4); however, higher temperature leads to coke formation, which causes catalyst deactivation with time on stream. Increasing the concentration of GVL in the feed has a positive effect on butene yield (entries 5, 6), although coke formation eventually becomes problematic, leading to catalyst deactivation at GVL concentrations higher than 80 wt%.

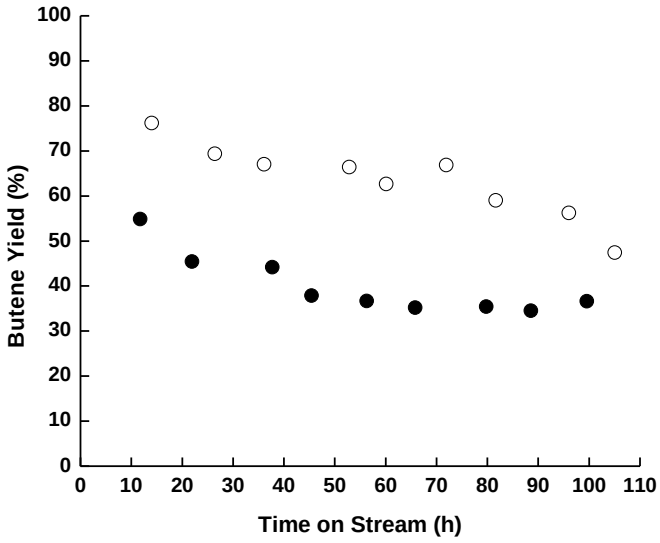

Figure 3.3 Yield of butene versus time on stream for conversion of 30wt% GVL in water at 36 bar and WHSV= 0.9 h^{-1} over SiO_2/Al_2O_3 at 648K (●) and 673K (○).

Figure 3.3 illustrates the yield of butene from GVL over SiO_2/Al_2O_3 at 648 K and 673 K plotted versus time on stream. At both temperatures, the reactor was operated at 36 bar and a WHSV of 0.9 h^{-1}. The catalyst initially shows higher activity at 648 K, which decreases to a stable yield after 40 hours of time on stream. At 673 K the catalyst shows continued deactivation.

The activity can be restored by calcination in air at 723 K. Figure 3.4 illustrates the yield of butene from GVL over SiO_2/Al_2O_3 at feed concentrations of 30, 60, and 80 wt% GVL versus time on stream. Reaction temperature, pressure, and WHSV were constant at 648 K, 36 bar, and 0.9 h^{-1} respectively. For feeds containing 30 and 60 wt% GVL, the catalyst initially shows a loss of activity, but achieves stable catalytic activity after 40 hours of time on stream. At 80 wt% GVL, a steady decline in the butene yield is observed. Experiments conducted using a pure GVL feed led to extensive formation of coking/polymerization products in the reactor, indicating that small amounts of water in the GVL feed are beneficial for achieving stable catalyst performance.

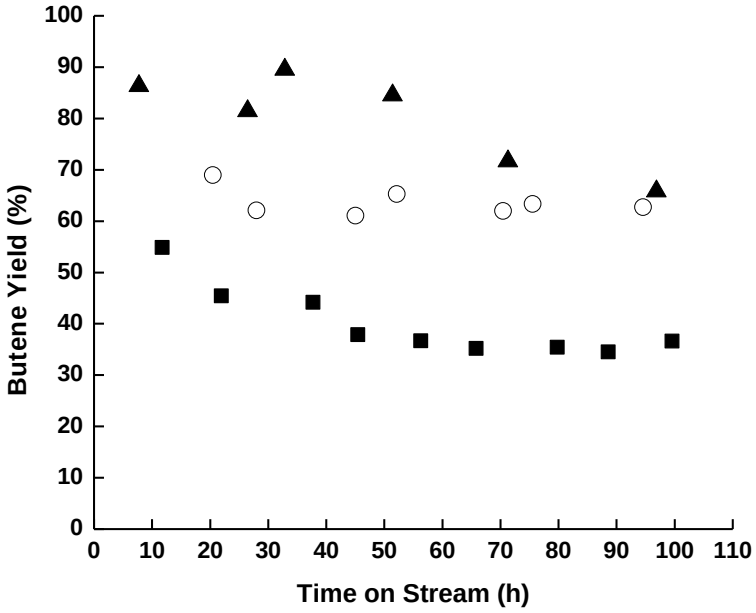

Figure 3.4 Yield of butene versus time on stream for conversion of GVL at 648 K, 36 bar and WHSV= 0.9 h^{-1} over SiO_2/Al_2O_3 at various GVL concentrations. 30 wt% (■), 60 wt% (○), 80 wt% (▲).

Deactivation of SiO_2/Al_2O_3 is reversible, and catalytic activity can be regenerated by calcination at 723 K. An appropriate compromise between obtaining a high rate of GVL

conversion and maintaining stable catalyst operation is achieved using an aqueous feed solution containing 60 wt% GVL at 648 K and at a pressure of 36 bar, at which conditions catalytic activity remains constant for over 100 hours of time on stream (supporting online text). The butene yield at these conditions (60%) is limited by formation of the intermediate product pentenoic acid, and yields in excess of 90% are achieved using a 60 wt% feed at lower space velocities (Table 3.1, entry 7).

Table 3.1. GVL conversion and butene yield at different reaction conditions over a SiO_2/Al_2O_3 catalyst operating at a weight hourly space velocity (WHSV) equal to 0.9 h^{-1}.

Entry	T(K)	P(bar)	Feed GVL	GVL conv (%)	Butene Yield (%)
1	648	1	30 wt%	97	75
2	648	18	30 wt%	94	65
3	648	36	30 wt%	70	35
4	673	36	30 wt%	95	60
5	648	36	60 wt%	87	65
6	648	36	80 wt%	99	96
7	648[a]	36	60 wt%	99	93

[a] WHSV = 0.18 h^{-1}

3.4 Butene Oligomerization over Solid Acids: Effect of Water

The effluent from the GVL decarboxylation reactor is a mixture of butene, CO_2, and water at elevated temperature and pressure that must subsequently be passed to the butene oligomerization reactor operating at lower temperature and high pressure which are conditions that favor alkene oligomerization and minimize cracking reactions.

Table 3.2 Butene conversion, selectivity, and yield to liquid C_8-C_{16} and C_{8+} alkenes over HZSM-5 and Amberlyst-70 catalysts.

Entry	Catalyst	Feed Composition	T (K)	P (bar)	Butene Conversion (%)	Liquid selectivity ($C_8 - C_{16}$)/ C_{8+} alkenes (%)	Liquid yield ($C_8 - C_{16}$)/ C_{8+} alkenes (%)
1[a]	HZSM-5	Butene	523	1	51	77/80	40/41
2[a]	HZSM-5	Butene	573	1	87	50/55	43/48
3[a]	HZSM-5	Butene	523	17	90	59/73	53/66
4[a]	HZSM-5	Butene	498	17	64	78/88	50/56
5[a]	HZSM-5	Butene	473	17	38	89/91	34/35
6[a]	HZSM-5	Butene	498	36	87	82/88	71/77
7[a]	HZSM-5	Butene/CO_2 50:50	498	36	64	77/85	49/54
8[a]	HZSM-5	Butene	498	36	90	80/89	72/80
9[b]	HZSM-5	Butene/CO_2 50:/50	498	17	90	65/88	58/79
10[b]	HZSM-5	Butene/CO_2/H_2O 47.5/47.5/5	498	17	82	72/89	59/73
11[b]	HZSM-5	Butene/CO_2/H_2O 45/45/10	498	17	72	72/86	52/62
12[b]	HZSM-5	Butene/CO_2/H_2O 33/33/33	498	17	47	79/89	37/42
13[b]	HZSM-5	Butene/CO_2 50:50	498	17	86	78/93	67/80
14[c]	Amberlyst 70	Butene	443	17	99	72/96	71/95
15[c]	Amberlyst 70	Butene/CO_2 50:50	443	17	93	69/95	64/88
16[c]	Amberlyst 70	Butene/CO_2/H_2O 47.5/47.5/5	443	17	90	74/95	66/86
17[c]	Amberlyst 70	Butene/CO_2/H_2O 45/45/10	443	17	50	85/92	43/46
18[c]	Amberlyst 70	Butene/CO_2/H_2O 33/33/33	443	17	0	---	---
19[c]	Amberlyst 70	Butene/CO_2 50:50	443	17	93	58/93	54/87

[a] WHSV equal to 0.11 h^{-1}. [b] WHSV equal to 0.09 h^{-1}. [c] WHSV equal to 0.63 h^{-1}

Although the oligomerization of alkenes is practiced widely in the petrochemical industry (25, 26, 30), the processing of butene/CO_2 mixtures, in the presence of water, at elevated pressures has not been reported in the literature, thus necessitating studies to identify catalysts and reaction conditions for our integrated catalytic process. Table 3.2 summarizes experimental results for butene oligomerization using HZSM-5 and Amberlyst-70 as catalysts (24). The conversion of butene over HZSM-5 is approximately 50% at ambient pressure and moderate temperature (523 K, entry 1). Higher conversions are achieved by increasing the reaction temperature to 573 K (entry 2); however, a larger fraction of the products observed are low molecular weight alkenes, produced via cracking, such that the selectivity for desired products (C_{8+} alkenes for jet fuel applications) decreases from 80% to 55 %. Increasing the pressure to 17 bar leads to an increase in the conversion of butene accompanied by a decrease in selectivity for C_{8+} alkenes (entry 3). Higher selectivities (>88%) can be achieved at elevated pressure (17 bar) by decreasing the temperature to 498 K (entry 4). A further decrease in temperature to 473 K leads to minimal improvement in selectivity but causes a decrease in butene conversion (entry 5). An increase in pressure to 36 bar at 498 K allows for high overall yields of C_{8+} alkenes (77%) at high butene conversion (87%) (entry 6.)

The addition of an equi-molar co-feed of CO_2 to the butene oligomerization reactor leads to a decrease in butene conversion (entry 7), while the selectivity to C_{8+} alkenes remains unchanged. This decrease in butene conversion is caused by the corresponding decrease in butene partial pressure in the reactor, as the initial activity is restored upon removal of CO_2 from the feed (entry 8). Entry 9 shows that it is possible to increase the conversion of butene to 90% in the presence of an equi-molar amount of CO_2 , without modifying the selectivity to C_{8+} olefins,

by decreasing the weight hourly space velocity (WHSV) to 0.09 h^{-1}. Entries 10 to 12 document the effect of co-feeding water to the oligomerization reactor using HZSM-5 as the catalyst. Low levels of water in the feed decrease the conversion of butene from 90% to 82% (entry 10). As the concentration of water in the oligomerization feed increases, inhibition becomes more pronounced, and only 47% of the butene is converted when equi-molar quantities of butene, CO_2, and water are fed to the reactor. When the water co-feed is stopped, 96% of the initial activity is recovered indicating that the effect of water is reversible. In all experiments reported using HZSM-5 at 498 K, the selectivity to C_{8+} olefins is higher than 85%, indicating minimal extent of cracking.

It is possible to achieve complete butene conversion over Amberlyst-70 with high selectivity to C_{8+} oligomers at elevated space velocities (0.63 h^{-1}, entry 14). The conversion of butene decreases upon introducing an equi-molar co-feed of CO_2 (entry 15), as found for HZSM-5. The inhibiting effect of water is minimal at low feed concentrations (entry 16). As the concentration of water in the feed increases, inhibition becomes more pronounced and complete loss of activity is observed at high amounts of water (entries 17,18). When the co-feed of water is stopped, Amberlyst-70 regains 100% of its initial activity.

3.5 Process Integration

Results from Tables 3.1 and 3.2 suggest that it should be possible to couple GVL decarboxylation with butene oligomerization in a single system at elevated pressures, thereby reducing the overall capital expenditure that would be required to separate, purify and pressurize the butene obtained from GVL.

Table 3.3 Performance of integrated catalytic system consisting of two flow reactors in series with an inter-reactor separator: GVL conversion and butene yield from first reactor containing SiO_2/Al_2O_3; butene conversion and selectivities to liquid C_8-C_{16} and C_{8+} alkenes from the second reactor containing HZSM-5/Amberlyst-70 as catalyst at 36 bar.

	Reactor 1 (GVL to butene)				Reactor 2 (Butene to alkenes)				
Entry	T (K)	GVL conversion (%)	Butene yield (%)	Butene out 1st separator (%)	Catalyst	T (K)	Butene conversion (%)	Liquid selectivity to C_8-C_{16}/C_{8+} (%)	GVL to liquid C_8-C_{16} /C_{8+}(%)
1[a]	648	63	37	75	HZSM-5	498	95	63/90	17/24
2[b]	648	98	91	90	HZSM-5	498	44	76/86	28/31
3[b]	648	99	92	88	Amberlyst	443	92	74/94	50/62
4[c]	648	99	90	89	Amberlyst	443	94	64/93	48/66
5[d]	648	99	94	93	Amberlyst	443	81	79/94	53/63

[a] Reactor 1: 2.7 g SiO_2-Al_2O_3.WHSV equal to 0.68 h^{-1}. First separator at 373 K. Reactor 2 : 14 g HZSM-5 [b] Reactor 1: 10g SiO_2-Al_2O_3.WHSV equal to 0.18 h^{-1}. First separator at 383 K. Reactor 2: 3 g Amberlyst-70 [c] Reactor 1: 10 g SiO_2-Al_2O_3.WHSV equal to 0.18 h^{-1}. First separator at 388 K. Reactor 2 : 4 g Amberlyst-70 [d] Reactor 1: 10 g SiO_2-Al_2O_3.WHSV equal to 0.22 h^{-1}. First separator at 398 K. Reactor 2 : 4 g Amberlyst-70

However, because water has a strong negative effect on oligomerization, the reaction system depicted in Figure 3.2 was designed to carry out the desired conversion of GVL to liquid alkenes by including a separation unit between the GVL decarboxylation reactor and the butene oligomerization reactor to remove most of the water carried downstream. This system allows for the delivery of a high pressure stream of gaseous butene from the first separator to the inlet of the oligomerization reactor, while achieving removal of >98% of the water in the effluent from the

first reactor as a liquid. The total pressure of the system is set at 36 bar, a value that is appropriate for GVL conversion (Table 3.1) as well as for butene oligomerization (Table 3.2), and the temperature of the inter-reactor separator is set at a value (e.g., 373 - 398 K) that is sufficiently low to liquefy most of the water for removal but sufficiently high to maintain butene in the gaseous state for transfer to the oligomerization reactor. The products from the second reactor are collected in a second phase separator operating at ambient temperature, producing a liquid effluent stream of C_{8+} alkenes and unreacted butene, and a gaseous effluent stream of CO_2 with trace quantities of organic compounds.

Table 3.3 shows results for the conversions of GVL and butene in the integrated catalytic system depicted in Figure 3.2 (24). Entry 1 shows that the values for the conversion of GVL and yield of butene in the first reactor, and butene conversion and selectivity to liquid C_{8+} alkenes in the second reactor of this integrated system are similar to those values obtained for the isolated processes operating at similar conditions. This experiment was carried out for over 100 hours while operating the inter-reactor separator (first separator) at 373 K and a pressure of 36 bar, at which conditions no aqueous phase was observed in the effluent from the oligomerization reactor, and the overall yield from GVL to C_{8+} alkenes was 24%. This overall yield was limited by the decarboxylation of GVL and loss of butene in the first separation step.

To increase the total yield of GVL to liquid alkenes, experiments were carried out at lower space velocity of GVL (entry 2) and higher separator temperature (383 K). At these conditions, GVL is almost quantitatively converted into butene with the formation of minimal side products such as C_{8+} alkenes and aromatics. Operating the separator at higher temperature increases the extent of both butene and water vaporization and subsequent delivery to the

oligomerization reactor. The increased WHSV of butene in the second reactor combined with the inhibiting effect of water cause a decrease in butene oligomerization, although total yield of C_{8+} oligomers is improved to 31%.

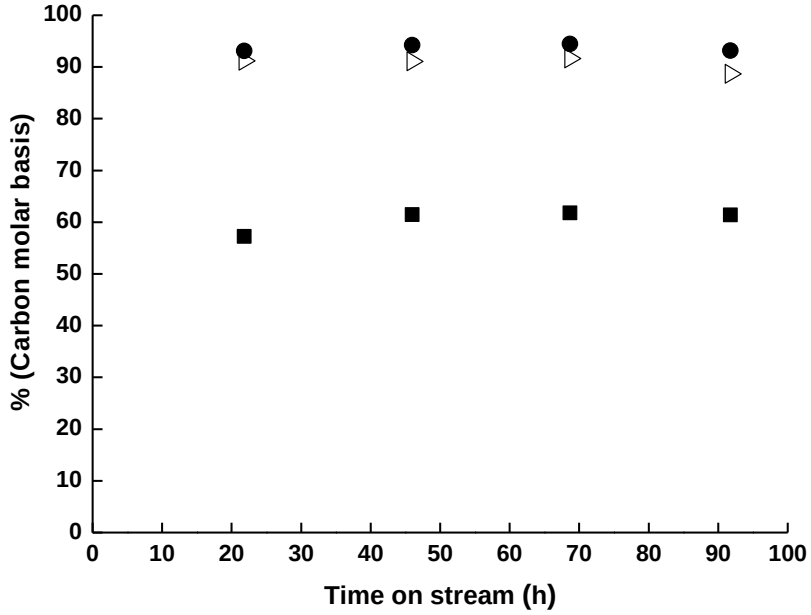

Figure 3.5. Yield of butene from GVL in reactor 1, butene conversion in reactor 2, and overall yield of liquid C_{8+} alkenes from GVL in the integrated process versus the time on stream. First reactor operated at 36 bar, 648 K and 0.18 h^{-1}. First separator operated at 36 bar and 383 K. Second reactor operated at 36 bar 443 K and 3 g Amberlyst-70. Second separator operated at 36 bar and 298 K. Butene yield (●), butene conversion (▷), yield to C_{8+} alkenes (■)

Amberlyst-70 was identified to be a more active oligomerization catalyst than HZSM-5, and it can be used at lower temperatures to reduce the extent of cracking reactions and to improve the oligomerization selectivity to C_{8+} alkenes. Using Amberlyst-70 in the second reactor, the conversion of butene increases to 92%, with 94% selectivity to C_{8+} alkenes. At these conditions the total yield of C_{8+} alkenes from GVL increases to 62%. As seen in Figure 3.5, the

integrated catalytic system operates for more than 100 hours on stream with high conversions of GVL and butene in the first and second reactors, respectively, and with a high overall yield to C_{8+} alkenes (>60%).

The total yield to C_{8+} alkenes can be increased by reducing the WHSV in the second reactor to increase butene conversion (entry 4). To maximize the amount of butene delivered to the second reactor the WHSV was increased from 0.18 h^{-1} to 0.22 h^{-1} , which reduces decarboxylation by-products such as higher olefins and aromatics and increases butene yield to 94%. Additionally, by operating the initial separator at 398 K, 94% of the butene formed is delivered to the oligomerization reactor (entry 5). The higher separator temperature increases the amount of water in the second reactor, which inhibits butene oligomerization (81% conversion) and results in an overall yield of C_{8+} olefins equal to 63%.

The integrated system herein for conversion of GVL to liquid alkenes in the transportation fuel range consists of two flow reactors, two phase separators, and a simple pumping system for delivery of an aqueous solution of GVL, thereby minimizing secondary processing steps and equipment (e.g., purification of feeds, compression and pumping of gases). In addition, this approach does not require an external source of hydrogen, and it does not require the use of precious metal catalysts, further decreasing capital costs.

3.6 Activation of Amberlyst-70 for Oligomerization

3.6.1 Activation of Amberlyst-70 for Oligomerization Reaction by Hydrophobic Media

In the C-C bond formation strategy outlined above, Amberlyst-70 was used as an acid catalyst for alkene coupling, which shows higher activity and selectivity to C_{8+} products than

HZSM-5 and can be used at lower temperatures to reduce the extent of cracking reactions and to improve the oligomerization selectivity to C_{8+} alkenes. Of the polystyrene/sulfonic acid catalysts commercially available, only Amberlyst-70 can withstand temperatures necessary to achieve high rates of coupling (463 K), particularly with large, non-terminal alkenes, which are less reactive than the more thoroughly studied short chain-alkenes. (31)While Amberlyst-70 has demonstrated potential as an alkene oligomerization catalyst, its physical properties can limit its application. Specifically, Amberlyst-70 is a macroreticular resin which is swelled by polar solvents. Typically, the highest rates of reaction reported for Amberlyst-70 are achieved using water or alcohols as solvents. It has been reported previously that the introduction of trace quantities of alcohol can improve the activity of Amberlyst-70 in the oligomerization of nonene, which can be attributed to swelling of the resin by the alcohol itself or by the water produced by alcohol dehydration. (31)However, increasing the percentage of alcohol in the feed leads to a decrease in oligomerization activity, which can be attributed to inhibition by water. For example, it was observed above that the introduction of an equi-molar quantity of water is sufficient to completely suppress butene oligomerization. Thus, activation of the catalyst through swelling in aqueous media is not an appropriate strategy in alkene oligomerization.

Previous studies (32) show that Amberlyst-70 achieves higher activity for alkene oligomerization upon pretreatment with a mixture of nonenes that were prepared from 5-nonanone. This section studies the effect of this activation procedure and presents a strategy by which the activity of Amberlyst-70 can be enhanced up to 5 times for use in hydrophobic media. We have carried out experimental studies, including optical microscopy, microcalorimetry, and temperature programmed desorption, to identify the mechanism for enhancement of catalytic

activity. In particular, we attribute the observed enhancement to alleviation of transport limitations present in non-swelled Amberlyst-70.

3.6.2 Physical Characterization

This enhancement in catalytic activity of ion-exchange resins, such as Amberlyst-70, is typically attributed to a physical swelling of the solid resin in polar media, which results in increased surface area and pore dimensions and facilitates pore diffusion and active site accessibility. For example, in water, the surface area of Amberlyst-70 is reported to increase from 0.0181 to 30 m^2 g^{-1} in the dry state to 176 m^2 g^{-1} upon hydration. (33)The differences observed when measuring the area in the dry state illustrate the difficulty in characterizing Amberlyst-70. However, the swelling of Amberlyst-70 in larger alcohols and ketones has not been as extensively documented. To investigate the role of swelling, we have measured the increment in the volume of Amberlyst-70 upon exposure to several solvents. Considering a bulk sample of Amberlyst-70 as being comprised of spherical beads that are homogenously dispersed with a constant packing factor, the swelling properties of the resin can be estimated as the increase in height in a packed column.

Table 3.4 Volume changes of Amberlyst-70 after swelling in different solvents for 24 h.

Solvent	Initial height (mm)	Final height (mm)	Swelling (%)
Water	100	250	150%
5-nonanol	100	170	70%
5-nonanone	100	100	---
2- butanone	100	240	140%

Table 3.5 Particle dimensions calculated by optical microscopy.

Swelling Agent	Initial diameter (μm)	Final diameter (μm)	Volume Increase (%)
Water	231	308	137%
5-nonanone	198	196	-3%

Table 3.4 indicates the initial height of a column of dried Amberlyst-70 before and after contact with different solvents, as well as the extent to which Amberlyst- 70 swells in each. The swelling of Amberlyst-70 in water has been previously demonstrated, and in this study we observed a rapid expansion with the spheres ultimately swelling to a 150% increment of their initial volume, implying an increase in the surface area as result of the low extent of cross-linking typical in these resins, which has been described elsewhere. (33)In the presence of 5-nonanol, the swelling was not evident initially, but after 16 h in contact with Amberlyst-70, a 70% increase in the volume was observed. Interestingly, we have observed that the volume of Amberlyst-70 increases dramatically in 2-butanone, with the catalyst sample achieving a final volume comparable to that when swelled in water. Thus, it appears that polar aprotic ketone groups are appropriate for swelling Amberlyst-70. However, no swelling is observed when Amberlyst-70 is exposed to 5-nonanone. Similar results indicate that Amberlyst-70 swells visibly and rapidly in water, whereas swelling is less evident in alcohols and non-polar solvents such as ethers. This result suggests that catalyst swelling is not involved to an appreciable extent in the rate enhancement achieved through pretreatment with 5-nonanone. However, as the surface area of dried Amberlyst-70 is reported to be exceedingly low, it is possible that even microscopic

physical changes could contribute significantly to the observed rate enhancement despite being macroscopically invisible.

To better describe the extent of swelling upon exposure to 5-nonanone, Amberlyst-70 beads were imaged through optical microscopy before and after exposure to water and 5-nonanone. The particle diameters were then measured digitally, and the resultant volume calculated assuming a spherical particle. Sphere dimensions are summarized in Table 3.5. Figure 6 shows a particle of Amberlyst-70 before (Fig. 3.6a) and after (Fig. 3.6b) contact with water, and it is observed that the diameter of the particle increases by 33% (140% increase in volume). The swelling of individual particles occurs rapidly in the presence of water and thus accounts for the increase in the column height reported macroscopically. Figure 3.7 shows a second particle of Amberlyst-70 before (Fig.3.7a) and after contact with 5-nonanone (Fig.3.7b). In this case we do not observe an increase in particle diameter or external volume. This result suggests that particle swelling does not contribute to the observed rate enhancement upon pretreatment in 5-nonanone.

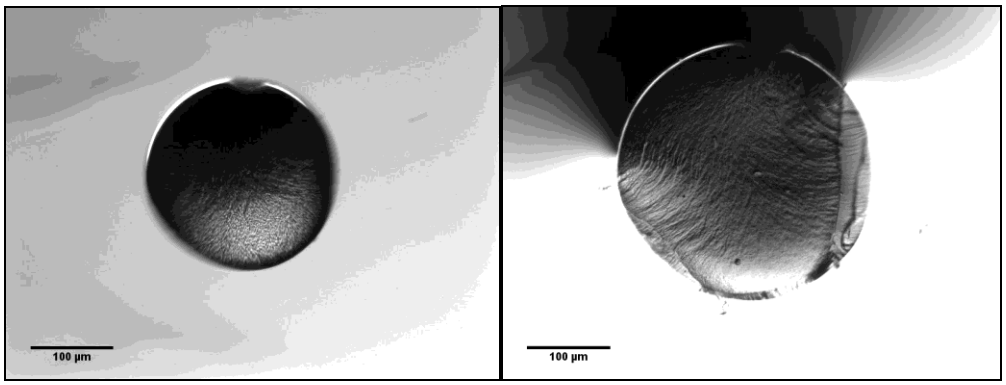

Figure 3.6 Optical microscopy images. a) Dry Amberlyst-70. b) Amberlyst-70 after contact with water

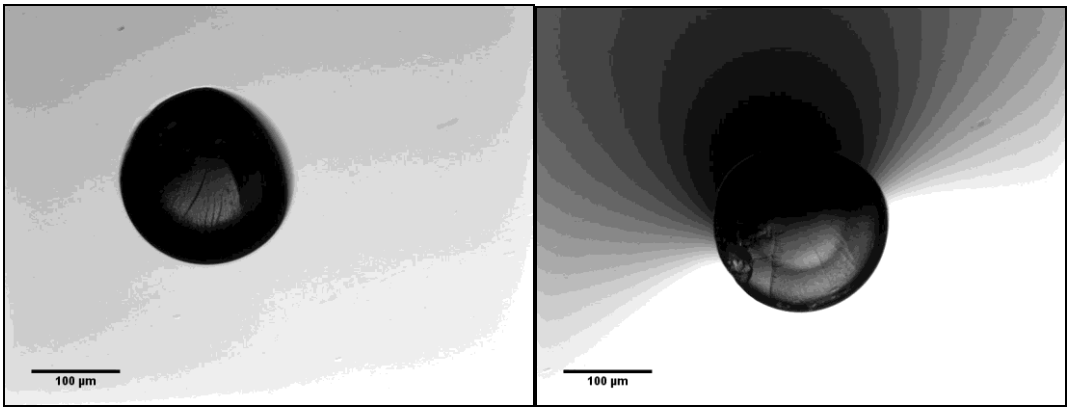

Figure 3.7. Optical microscopy images. a) Dry Amberlyst-70. b) Amberlyst-70 after contact with 5-nonanone.

3.6.3 Diffuse Reflectance Infrared Spectroscopy (DRIFT)

Amberlyst-70 was characterized by DRIFTS to discern surface interactions between 5-nonanone and Amberlyst-70. Spectra were acquired before and after treatment with 5-nonanone, and perturbations in the nature of the active sites were subsequently assessed by ammonia adsorption.

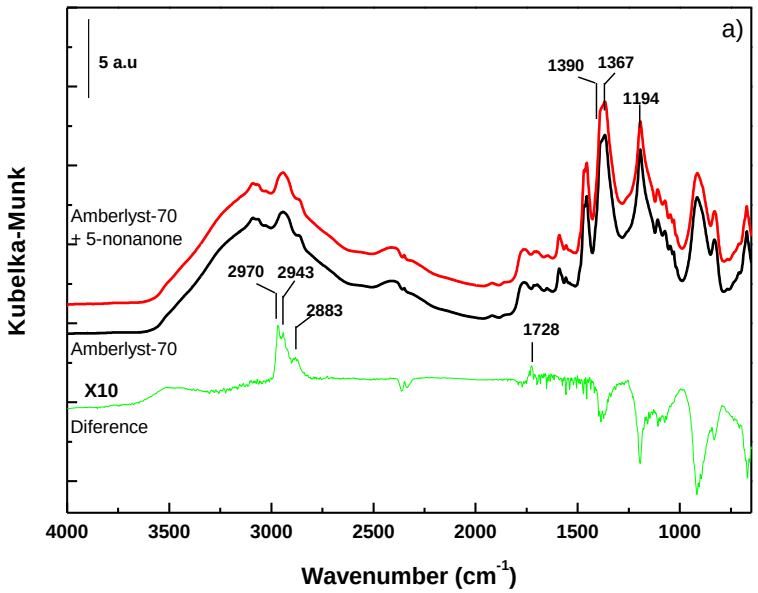

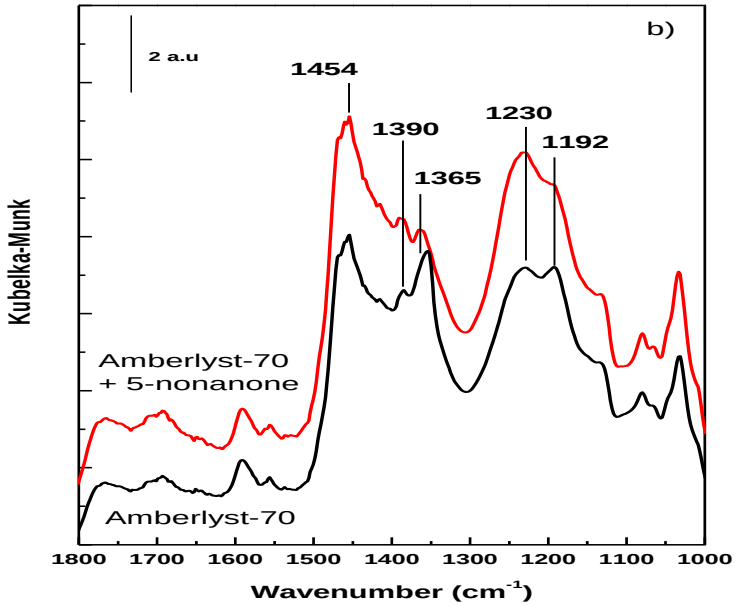

Figure 3.8 DRIFT spectra recorded at 433 K. a) Pure Amberlyst-70 (black line) and Amberlyst-70 after treatment with 5-nonanone (red line). b) DRIFT spectra after adsorption of ammonia over Amberlyst-70 dried (black line) and treated with 5-nonanone (red line)

Figure 3.8a shows the spectrum of Amberlyst-70 before and after exposure to 5-nonanone. Both spectra are similar, indicating that the presence of 5-nonanone does not modify the catalyst significantly. The main differences occur at 2970, 2943, 2883 and 1728 cm-1 where bands appear corresponding to ketone moieties. In addition, the bands corresponding to the sulfonic acid groups, 1390–1367 and 1194 cm-1 are slightly less intense after exposure to 5-nonanone indicating that there is a direct interaction between 5-nonanone and the sulfonic acid groups of Amberlyst-70 and suggesting some uptake upon exposure.

Figure 3.8b shows DRIFTS spectra of ammonia adsorbed on Amberlyst-70 before and after exposure to 5-nonanone, with focus given to wavenumbers from 1000–1800 cm-1. The spectra show no significant differences, suggesting that the total number of acid sites does not

change upon pretreatment with 5-nonanone. The main change is observed in the relative intensity of the band at 1365 cm-1, which increases in intensity, indicating that there is an interaction between sulfonic groups and the 5-nonanone.

3.6.4 Microcalorimetric Study of Butene Adsorption on Amberlyst-70.

We have employed microcalorimetry to assess differences in the binding energies of butene on dry and nonanone-treated Amberlyst-70. Differential heats are plotted against surface coverage in Figure 3.9. In the case of dry Amberlyst-70, the differential heat of adsorption in initial doses (1.0–5.0 Torr) was estimated to be approximately 30 kJ mol^{-1}. Differential heats of this magnitude are indicative of 1-butene physisorption, which has been reported to liberate 38 and 44–48 kJ mol^{-1} upon adsorption on gmelinite (34) and phosphotungstic acid,(35) respectively, while the chemisorption of 1-butene on solid acids has been reported to liberate 59 kJ mol^{-1} on zeolites(34) and 88–103 kJ mol^{-1} on heteropoly acids.(35) Differential heats observed for butene adsorption on dried Amberlyst-70 suggest that chemisorption is not favored on the dry sample, particularly at the low butene pressures of our calorimetric study. It has been previously reported that steric factors in porous catalysts can lead to lower heats of adsorption for olefins of increasing chain length in zeolites.(34) It is possible that such steric effects may be important in the uptake of butene on Amberlyst-70, suggesting that transport limitations may govern the adsorption of 1-butene on Amberlyst-70, particularly at low partial pressures.

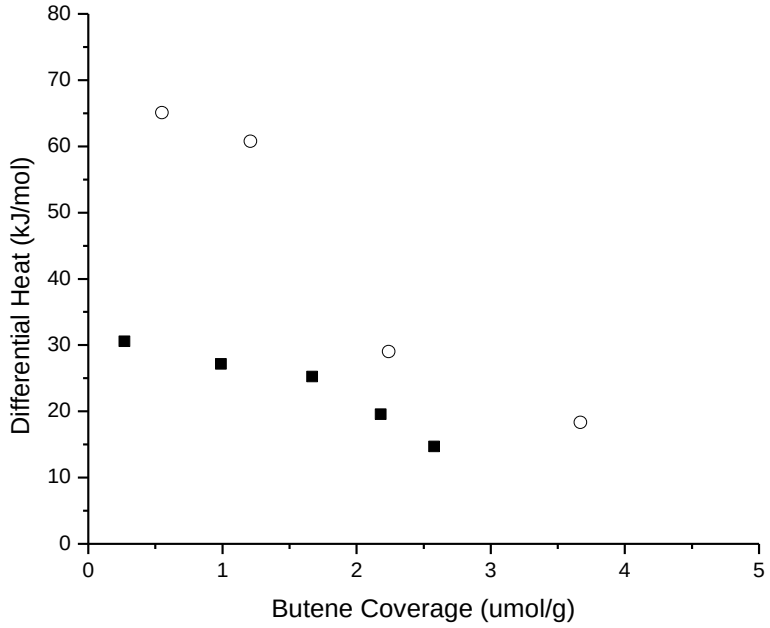

Figure 3.9. Differential heats of butene adsorption at 302 K for dry Amberlyst-70 (■) and Amberlyst-70 treated with 5-nonanone (○).

For samples of Amberlyst-70 treated with nonanone, the differential heat of adsorption was estimated in initial doses to be 60–70 kJ mol^{-1}, which is higher than that measured on dry Amberlyst-70 and in accord with previously reported estimates for the adsorption of 1-butene on solid acids. As described above, DRIFTS spectra showed little modification of the sulfonic acid sites of Amberlyst-70 upon treatment with 5-nonanone. Thus, we expect that if butene adsorption occurs on acid sites of Amberlyst-70 treated with 5-nonanone (which we observe in microcalorimetric measurements), then it should also take place on identical sites in dried Amberlyst-70. This conclusion supports the notion of active site inaccessibility in the dried sample, where butene adsorption occurs very slowly. Accordingly, the presence of 5-nonanone may serve to reduce transport limitations such that butene adsorption occurs on a time scale that is more readily observed via microcalorimetry.

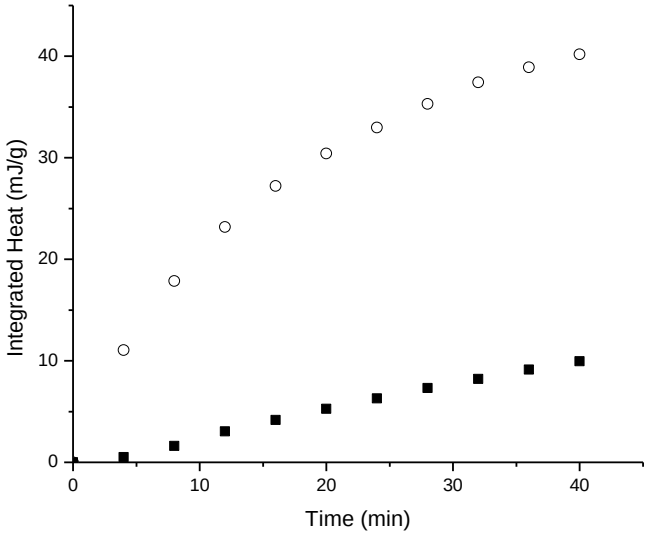

Figure 3.10. Integrated heat evolution following a dose of butene versus time. Dry Amberlyst-70 (■) Amberlyst-70 treated with 5-nonanone (○)

In both treated and un-treated samples, the total butene uptake observed is low (<5 micromol g^{-1}) but comparable, and we cannot attribute the substantial enhancement in catalytic activity (500%) to an enhanced capacity for adsorption (30–40%). These observations are in accord with estimates obtained by volumetric adsorption of butene (5–6 micromol g^{-1} on dry Amberlyst-70) and agree well with minimal uptakes reported for various olefins on heteropoly acids, which have shown a sorption capacity of 1.9, 9.4, and 10.5 micromol g^{-1} of ethylene, propylene, and isobutylene (34) despite a relatively high acid site density as indicated by capacity for ammonia adsorption (e.g., 1000 micromol g^{-1}).(36)

A more detailed analysis of the heat signal from butene adsorption reveals a significant difference in the rate at which butene is adsorbed on dry and 5-nonanone saturated Amberlyst-70. For this analysis, we have considered comparable 5 Torr doses of butene on both catalyst samples, corresponding to approximately 2.2 micromol of butene per gram of Amberlyst-70.

After a 5 Torr dose of 1-butene, dry Amberlyst-70 adsorbed approximately 0.40–0.45 micromol g^{-1} and released 12.6 mJ g^{-1} of energy measured over 90 min, and extrapolation of the heat signal to 140 min increases the estimate to 20.4 mJ g^{-1} of total heat evolved. Upon a comparable dose, Amberlyst-70 saturated with 5-nonanone adsorbs approximately 0.65–0.7 micromol g^{-1} and releases 43.8 mJ g^{-1} of energy in 60 min. In Figuire 3.10, the total heat evolved is plotted against the time elapsed from the start of the dose for the first 40 min of data acquisition. A significant difference is evident in the rate of heat released from each sample. In the case of dry Amberlyst-70, approximately 9.9 mJ g^{-1} of heat is measured in the first 40 min of equilibration, corresponding to only half of the total heat evolved. In contrast, the nonanone-treated Amberlyst-70 sample liberates 40.2 mJ g^{-1}, 92% of the total heat flux measured within 40 min. More revealing is the initial rate of heat evolution, estimated from the first 8 min of data acquisition. The initial rates of heat evolution are 0.23 mJ min^{-1} g^{-1} and 2.3 mJ min^{-1} g^{-1} for dry and 5-nonanone-treated samples, respectively. The degree of uncertainty in the initial rate of heat flux is lower than that for differential heat and butene uptake estimates. This measurement was performed at high butene pressures (5 Torr) relative to the vapor pressure of 5-nonanone (0.65 Torr), minimizing the extent of nonanone vaporization. Additionally, it relies only upon thermal measurements which are less susceptible than pressure readings to errors introduced by the presence of the condensable 5-nonanone. That the nonanone treated sample evolves heat at a substantially elevated rate suggests that butene uptake occurs far more rapidly when 5-nonanone is present on the catalyst surface.

To aid in the interpretation of the calorimetric results, we describe the adsorption phenomena with a simple model, as illustrated in the energy diagram of Figure 3.11, where the

activation barrier for adsorption is given by E_A, the binding energy (a negative number equal to ΔH_{ads}) is given by the enthalpy difference between adsorbed and gas phase butene, and the activation barrier for desorption can be expressed as E_A- ΔH_{ads}. In addition, we presume that the rate of heat evolution scales directly with the net rate of butene adsorption. Accordingly, we can express the rates of adsorption, desorption, and net butene uptake as in Equations (1)–(3), where preexponential factors are taken to be 10^6 s^{-1} atm^{-1} and 10^{13} s^{-1} for adsorption and desorption, respectively.

$$r_{ads} = A_{ads} \cdot e^{\left(\frac{-E_A}{RT}\right)} \cdot p_{butene} \cdot \theta_v \quad (1)$$

$$r_{des} = A \cdot e^{\left(\frac{-(E_A - \Delta H_{ads})}{RT}\right)} \cdot \theta_* \quad (2)$$

$$r_{net} = r_{ads} - r_{des} \quad (3)$$

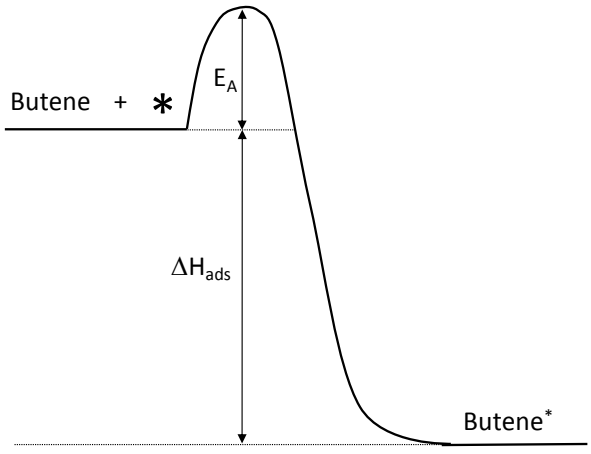

Figure 3.11.Schematic diagram for butene adsorption/desorption.

In this model, we consider the case where the presence of 5-nonanone reduces the barrier for adsorption directly, and we calculate that a modest decrease of 5–6 kJ mol^{-1} in the adsorption barrier can yield the observed ten-fold enhancement in the rate of butene uptake at 302 K, despite simultaneously deceasing the desorption barrier by the same amount. The presence of the hydrophobic 5-nonanone in the Amberlyst-70 sample, as revealed by DRIFTS spectra, thus appears to alleviate transport limitations, thereby enhancing butene adsorption and yielding the observed differences in heat evolution. Modification of surface polarity to enhance catalytic activity by facilitating transport, has been extensively studied by functionalization of polar surfaces with non-polar compounds.(37, 38) In this case, the weak interaction between the carbonyl group of 5-nonanone and the Amberlyst surface could sufficiently modify surface polarity to improve diffusion despite leading to no observation of physical swelling.

3.6.5 Temperature Programmed Desorption of Butene

Temperature programmed desorption of butene is included to provide complementary insights to those discussed in the preceding section. Figure 3.12 shows the desorption of 1-butene from Amberlyst-70 with and without a 5-nonanone pretreatment. In the untreated sample, we observe a single, broad peak with maximum intensity at 376 K. In this sample, the integrated area reveals the desorption of 3.6 micromol butene per gram of Amberlyst-70. In contrast, the butene evolution from Amberlyst-70 pretreated with 5-nonanone occurs more rapidly, resulting in a narrower peak centered at a slightly lower temperature (360 K). A small shoulder is observed at approximately 325 K, which can possibly be attributed to the onset of outgassing of dissolved butene from liquid nonanone retained on the catalyst surface. An upward drift is observed in the butene signal beginning at approximately 425 K, which is likely attributed to

increased nonanone vaporization (boiling point of 460 K) rather than to more strongly bound butene species. 5-Nonanone and butene have similar fragmentation patterns, and as the concentration of 5-nonanone increased, we observe a decrease in the quality of the butene signal detected by mass spectrometry. Integration of the main peak (360 K) indicates desorption of 3.2 micromol butene per gram of Amberlyst-70, suggesting a comparable, if not slightly reduced capacity for butene adsorption in Amberlyst-70 samples treated with 5-nonanone. The total quantity of butene desorbed in each case is similar to that obtained volumetrically through butene chemisorption on a dry Amberlyst-70 sample (5–6 micromol g^{-1} at 10 Torr butene) in our lab.

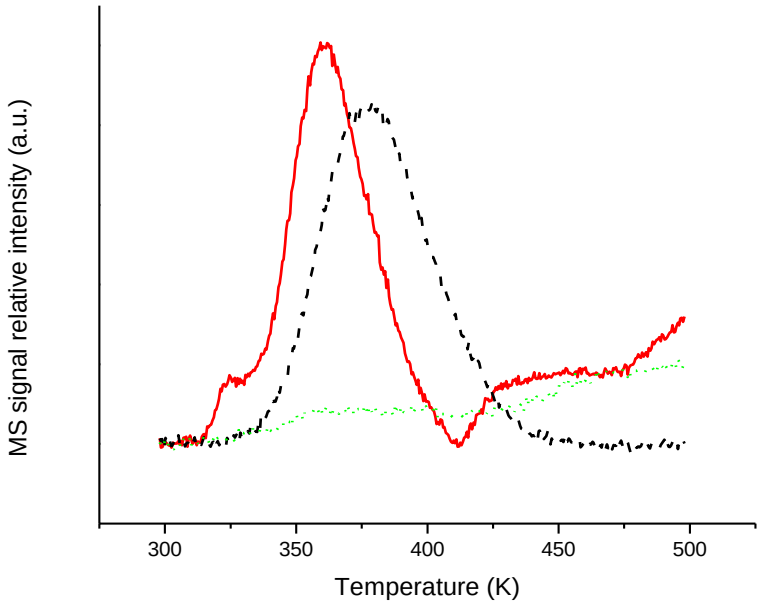

Figure 3.12. TPD of butene for dry Amberlyst-70 (dashed line) and Amberlyst-70 treated with 5-nonanone (continuous line), and TPD of 5-nonanone for Amberlyst-70 (dotted line)

Even though the total uptake of butene is similar in treated and untreated catalysts, we observe a difference in the temperatures at which maximum rates of desorption occur. This result can be explained by the kinetic model of adsorption presented in section 3.6.4. For a qualitative

assessment of peak differences, we have assumed a maximum butene uptake of 5 micromol per gram of catalyst, and that surface coverage is near butene saturation at the start of the temperature ramp ($\theta = 0.9$). Other kinetic parameters are equal to those described in section 3.6.4. We predict that a binding energy of approximately 65–70 kJ mol^{-1} will result in maximum desorption in the range of 360–380 K, as observed in the two samples. Further, a 5–6 kJ mol^{-1} decrease in the activation barrier for adsorption—which simultaneously reduces the desorption barrier—is sufficient to the shift the peak maximum from 376 to 360 K, as observed upon treatment with 5-nonanone, a conclusion which reconciles with insights from microcalorimetry.

The value of 65–70 kJ mol^{-1} estimated by TPD for the binding energy of butene is reasonable compared to the values estimated through microcalorimetry of 5-nonanone treated samples and expectations from the literature. (34-36) These values are substantially higher than the differential heats measured for 1-butene adsorption on dry Amberlyst-70, again suggesting that adsorption of butene on the dry sample is slow on the time scale of the microcalorimetric measurements. The clear observation of chemisorbed butene in the TPD of dry Amberlyst-70 samples (compared to that observed by microcalorimetry) can be explained by a higher rate of adsorption conferred by an increase in butene partial pressure from 5 Torr in the microcalorimetric experiments to 760–1000 Torr in the butene pretreatments for TPD experiments.

3.7 Conversion of Raw Maple Wood to Jet Fuel Precursors at 1L Scale

In the preceding sections, we have demonstrated the catalytic production of liquid alkene fuels from cellulose-derived GVL at bench-scale (using 0.25 OD tubular reactors, reactor volume approximately 10 cm^3). The feedstocks used thus far are commercially available reagent grade

GVL, free of impurities that might be encountered when produced directly from raw biomass. These impurities may be detrimental to the catalyst life or can cause difficulty in operation. To explore practical issues in the scaling up of this process, it is essential to start from raw biomass and integrate research efforts in biomass pretreatment, catalyst design, and lignocellulose conversion. Meanwhile, it is also desirable to utilize all three fractions of the parent biomass. Frequently, minor components are underutilized, decreasing the industrial viability of lignocellulose feedstocks. This section presents a concerted approach for the production of jet fuel components from hardwood (maple wood) feedstocks. Work in this section represents part of a three-year, multi-university research program supported by the U.S. Defense Advanced Research Projects Agency (BAA 08-48, Surface Catalysts for Energy (SurfCAT) program). The stated objective of this research was to convert whole lignocellulose to C_8 and larger hydrocarbon fuels with an overall carbon yield of 80% or higher using stable catalytic processes operating at short residence times (<1 hour) for extended operation (200 hours on stream). The final technology was employed to deliver liter quantities of jet fuel components directly from lignocellulose.

3.7.1 Technology Overview

Figure 3.13 summarizes the integrated, catalytic process developed through this program. Both direct, thermochemical conversion of whole biomass and hydrolytic fractionation were employed as required for production of a hydrocarbon mixture intended to match the specifications of JP-8 aviation-grade fuel. Fractionation by two-stage hydrolysis allows for separate processing of C_5 and C_6 sugars to produce linear and branched alkanes, while pyrolysis allows facile production of monoaromatics. Importantly, all cellulose, hemicellulose, and lignin

are used to target fuel production, commodity chemicals, or combined heat and power. Though these studies were performed with red maple or mixed hardwoods, the overall process is adaptable to any lignocellulose feedstock (e.g, miscanthus, switchgrass, and poplar). The remainder of this section provides a general description of the technology.

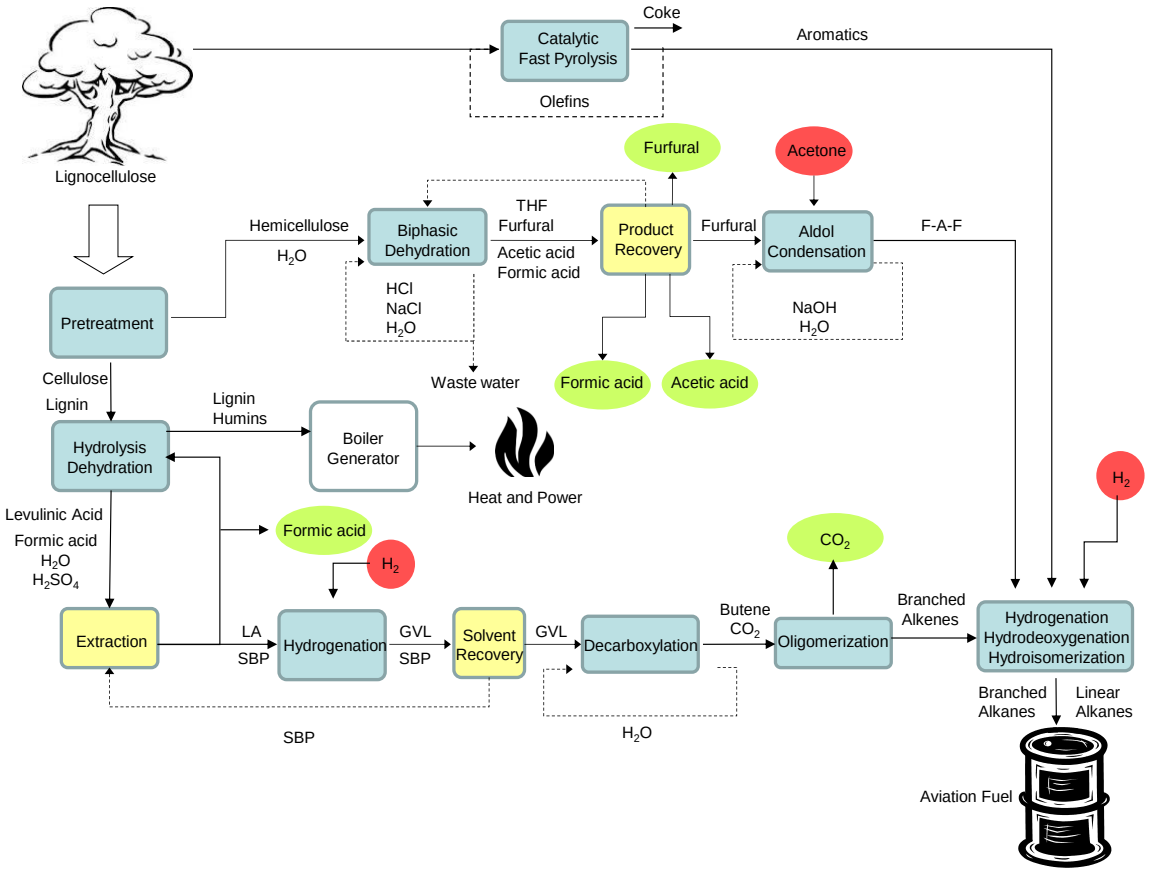

Figure 3.13. Process flow diagram of proposed technology for the production of furfural, jet fuels, formic acid, and acetic acid from lignocellulose.

A portion of the total quantity of the lignocellulose fed to the process is upgraded directly by catalytic fast pyrolysis to yield monoaromatic hydrocarbons, such as ethylbenzene and toluene. Using a fluidized bed reactor, hardwood feeds are rapidly heated to (873 K) in the presence of an H-ZSM-5 catalyst. In this manner, minimally processed wood samples are

thermally depolymerized into a mixture of light oxygenates and olefins, which couple and ultimately form aromatics over the ZSM-5 catalyst.(39, 40) The remaining lignocellulose is pretreated using hot water autohydrolysis, which extracts hemicellulose. During pretreatment, 85% of hemicellulose sugars are recovered as an aqueous solution of xylooligomers, which are subsequently introduced to a two-stage, biphasic reactor along with HCl and tetrahydrofuran. In the initial stage, hemicellulose oligomers are hydrolyzed to form a mixture of sugars—predominately xylose—as well as acetic and formic acids. In the second stage, sugars are dehydrated to form furans. Primarily, furfural is produced via xylose and arabinose dehydration in excess of 90% yield. Dehydration products are recovered in the THF extracting phase alongside acetic and formic acids. The organic acids are easily recovered and can be sold in commodity markets, while furfural can be either sold in chemical markets or used as a platform for the production of long-chain alkanes.(41) If targeting jet fuel production, furfural monomers can be condensed in basic media, with an acetone co-feed, to produce high molecular weight oxygenates (C_7 – C_{31}) in good yields (>90%). These oxygenates are then processed over bifunctional catalysts, along with an H_2 cofeed, to fully remove oxygen and saturate any C=C bonds, improving energy density and stability. The end product of furfural upgrading is thus a blend of straight-chain and branched alkanes that retain the entire carbon content of the parent sugar molecules.

Pretreated solids, comprised of cellulose and lignin, are recovered from hot water autohydrolysis and are subsequently treated with dilute aqueous sulfuric acid (H_2SO_4) using a steam-gun. In this manner, cellulose is converted to equimolar quantities of levulinic (LA) and formic acids (75% yield), which are recovered in aqueous solution along with the sulfuric acid

catalyst. Residual solids from this step contain lignin and solid degradation products, which form during hydrolysis through parallel reaction pathways. Solids, recovered by filtration, are then used as feed to a boiler for heat and power production. LA is recovered from the dilute H_2SO_4 hydrolysis product via extraction using 2-secbutylphenol and is subsequently converted, without separation, to γ-valerolactone (GVL) by hydrogenation over RuSn/C catalysts (>95% yield.(42, 43) Multiple extraction/hydrogenation cycles can be optionally employed to increase the GVL concentration and improve the energy efficiency of GVL recovery. GVL is then further converted to branched, $C_8 - C_{16}$ alkanes in a two-reactor system. In the first reactor, GVL undergoes decarboxylation over SiO_2/Al_2O_3 to form butene isomers and CO_2. In the second reactor, butenes are oligomerized to a mixture of C_8, C_{12}, and C_{16} alkenes over a solid acid catalyst. This mixture is then hydrogenated to produce a branched alkane product for inclusion in final jet fuel blends.

3.7.2 Levulinic Acid Production

Cellulose is the dominant carbohydrate in lignocellulosic biomass, comprising roughly 42% in representative hardwood samples considered in this research program. (44) In acidic media, cellulose will hydrolyze, forming glucose, which subsequently dehydrates to yield 5-HMF. In parallel, HMF can condense with other HMF monomers or glucose, leading to humin formation and reducing product yields. Ultimately, in acidic aqueous solutions, HMF will hydrate to form levulinic acid (LA) and formic acid (FA). A summary of the various acid-catalyzed steps and products formed is given in Figure 3.14.

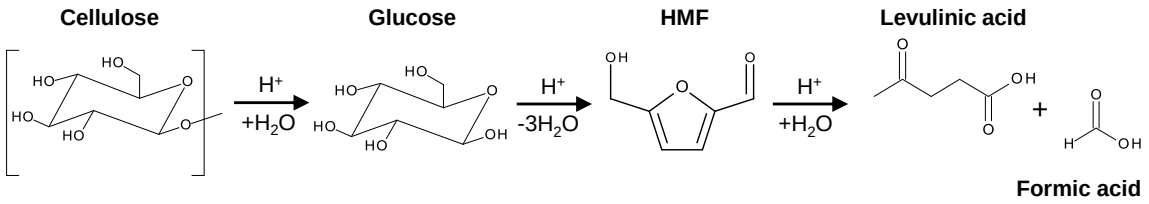

Figure 3.14. Chemical reactions in the acid catalyzed hydrolysis of cellulose leading to the formation of levulinic and formic acids.

Pretreated cellulose-lignin residuals were hydrolyzed in aqueous mineral acids (HCl or H_2SO_4) from 453 to 493 K over a range of residence times. The highest levulinic acid yield observed in this project was obtained through sulfuric acid hydrolysis (1.5 wt% H_2SO_4) of pretreated cellulose (10 wt % solids loading) in a stirred tank reactor at 473K. At these conditions, a 45 minute residence time delivered 75.5% of the maximum theoretical yield of LA and FA. Comparable yields were observed when operating at 50 wt% solids loadings in a 4L steam gun; however, operating conditions were modified slightly to account for the higher solids loading. Specifically, the steam gun required longer residence times (60 minutes) to achieve complete cellulose conversion at 473K. The steam gun was employed for supplying project collaborators with unrefined LA feedstocks, and a representative composition of these hydrolysates is summarized in Table 3.6. Viable LA yields were observed only using HCl and H_2SO_4 as catalysts. Total LA yields were slightly higher (10%) when employing H_2SO_4 as compared to HCl, indicating that it is slightly more selective. However, HCl appears more intrinsically active such that higher acid loadings or longer residence times are required when using H_2SO_4. For the process described here, H_2SO_4 was preferred for its lower cost, reduced corrosiveness, and improved LA selectivity. Further, residual sulfates are more easily separable and had less impact upon downstream LA processing than residual chlorides.

Table 3.6. Representative composition of cellulose hydrolysates obtained by treatment with H_2SO_4 at 473K for 60 minutes in a 4L steam gun

	Concentration	
	g/ L	mol / L
Sulfuric acid	15.2	0.155
Levulinic acid	53.8	0.460
Formic acid	10.1	0.220
5-HMF	1.85	0.015
Glucose	13.3	0.075
Xylose	1.00	0.007

3.7.3 GVL Production

Levulinic acid can be used for production of specialty or commodity chemicals, or it can be upgraded to jet fuel through intermediate formation of GVL, a strategy which is summarized in Figure 3.15. GVL is prepared by hydrogenation of LA, and numerous studies have reported the suitability of both homogeneous (6, 45)and heterogeneous (46, 47) Ru-based catalysts for this reaction. Further, FA dehydrogenation over Ru,(45, 48) Pd(49, 50) or Au can supply in-situ H_2 for LA reduction.(45, 51) The majority of LA hydrogenation studies have been carried out using model aqueous LA feedstocks, and limited consideration has been given to the implications of acid or biomass residuals on catalytic hydrogenation. Through this program, we have observed that typical heterogeneous catalysts used in reducing LA are susceptible to such impurities and have determined that GVL production strategies will depend strongly upon the extent to which raw cellulose hydrolyzates are purified prior to hydrogenation.

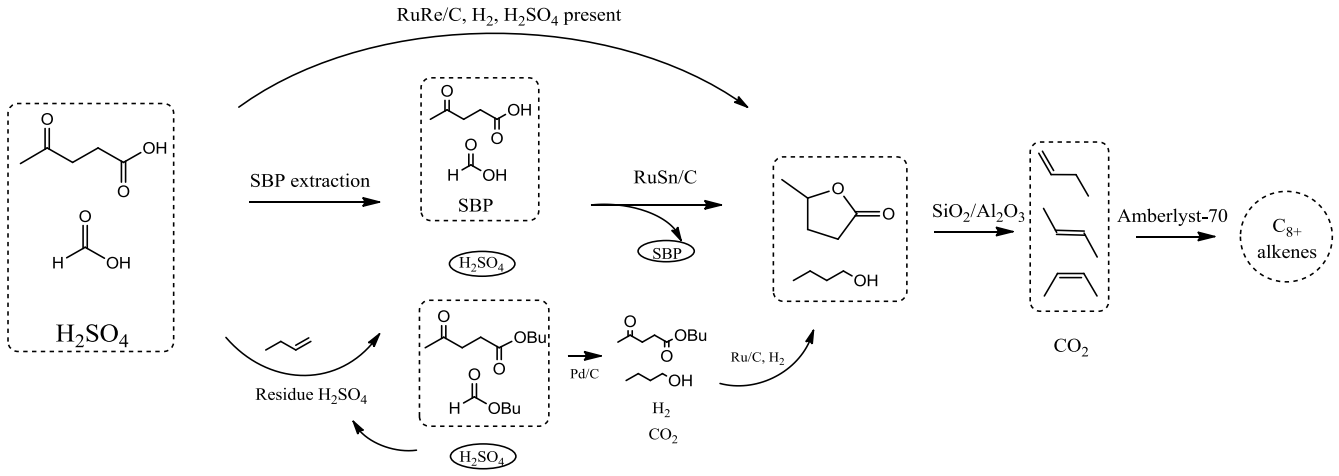

Figure 3.15. Proposed catalytic routes to convert levulinic and formic acid into C_{8+} alkenes via GVL and butenes

Residual H_2SO_4 critically impairs the activity of Ru/C during LA reduction (36) and its management is central to achieving high hydrogenation rates. A straightforward option for H_2SO_4 removal is precipitation of gypsum from raw LA hydrolysates via addition of $Ca(OH)_2$, and neutralization does enable the use of Ru/C in model systems; however, with lignocellulose-derived LA feedstocks, it was necessary to carry out hydrogenations under alkaline conditions (pH = 11) to achieve high GVL yields. Though this effect was not characterized in detail, we believe that alkaline conditions facilitate precipitation of biomass-derived impurities, such as acid-soluble lignin, which inhibit catalytic activity if retained in solution. It is important to note that, under these conditions, levulinic acid and formic acid exist primarily as calcium levulinate and calcium formate, though both are highly soluble in water and are thus not removed along with gypsum during filtration. Though superficially simple, neutralization presented a number of processing challenges that may hinder the scalability of the approach. For example, the requirement of highly alkaline conditions increases $Ca(OH)_2$ consumption, adding to raw material costs. Further, gypsum retains a significant portion of the aqueous hydrolysate during

filtration and requires extensive washing to recover more than 90% of the levulinate and formate salts. Repeated washings result in low filtrate concentrations such that a portion of the water needs to be evaporated prior to hydrogenation to concentrate the salts, improve reaction rates, and reduce reactor sizes.

Bimetallic catalysts (e.g., RuRe/C) permit direct hydrogenation of LA in the presence of H_2SO_4, eliminating the need for acid neutralization or inter-stage separations.(36) Operating at 423K and 35 bar H_2 in 0.5M H_2SO_4, comparably high selectivity and GVL yields (>99%) were observed over both Ru/C and RuRe/C; however, the bimetallic system offered improved stability, with the addition of Re preventing catalyst deactivation. An advantage of this approach is that GVL is more hydrophobic than LA and can therefore be extracted using low-boiling solvents, such as ethyl or butyl acetate, establishing relatively facile downstream recovery of both GVL and the extracting solvent. (36) (52) Some drawbacks of the approach, however, are the requirement of specialty alloy in the construction of the hydrogenation reactor to accommodate dilute H_2SO_4 at high temperatures. Further, in the presence of H_2SO_4, overall GVL production rates are low (0.005 mmol GVL $min^{-1}g^{-1}$), necessitating potentially impractical residence times, reactor sizes, and catalyst loadings.

Another strategy for acid management and GVL production was based upon esterification of levulinic and formic acids using either butene or butanol in the presence of catalytic H_2SO_4 retained in cellulose hydrolysates.(50) This step results in the formation of hydrophobic butyl esters, which separate spontaneously from the acidic aqueous phase. Butyl formate and butyl levulinate can subsequently be processed along with a water co-feed using a single reactor in which butyl formate is first converted to H_2, CO_2, and 1-butanol over a first bed

of Pd/C and butyl levulinate is subsequently converted to GVL, and 1-butanol via hydrogenation over a second bed of Ru/C. Operating at 443K and 35 bar of H_2, GVL yields of over 95% can be achieved in this manner. This strategy is attractive because it utilizes internally produced butene as an extracting agent for LA and FA recovery. Further, the 2 equivalents of butanol co-produced alongside GVL can be dehydrated over SiO_2/Al_2O_3 in parallel to GVL decarboxylation to regenerate the equivalents of butene required for extraction. (50) Finally, quantitative recovery of H_2SO_4 in the aqueous phase was observed such that the acid catalyst is easily reused in subsequent hydrolysis cycles. A potential constraint with this approach is that concentrated solutions of LA and FA (over 6M) are required to establish favorable esterification equilibrium in water. (50) As raw hydrolysates are generally available at 0.5M LA and FA, water evaporation represents a significant energy input and may limit practical implementations.

At present, the preferred method for LA recovery is the use of alkylphenol solvents (specifically, 2-secbutylphenol, SBP) since they efficiently partition LA from dilute H_2SO_4 with minimal solvent volumes. Additionally, they have no affinity for sulfuric acid or water and permit quantitative recovery of the acidic aqueous phase for subsequent cycles of cellulose hydrolysis. We have observed that solvent aromaticity is critical to effective partitioning of LA, and that LA can be hydrogenated selectively in the presence of SBP without intermediate distillation.(31) For this catalytic step, it was important to reduce only the carbonyl group of LA as opposed to the aromatic ring in SBP, and we observed that the addition of Sn to Ru/C facilitated the requisite selectivity. In addition, RuSn/C does not allow for deep-hydrogenation of GVL to form products such as pentanediol or MTHF.(53) Further, Sn-promotion conferred stability to the catalysts and eliminated irreversible deactivation observed over monometallic

analogs. Importantly, SBP has an exceptionally high partition coefficient for GVL—on the order of 20. Considering this alongside the exclusive selectivity of RuSn/C, GVL/SBP effluents from the hydrogenation step can be used for multiple cycles of LA extraction and hydrogenation. In this manner, GVL concentrations in the SBP extracting phase can be increased fourfold, substantially improving the energy efficiency of GVL distillation. (43)

3.7.4 GVL Conversion

Once formed, GVL is processed in the aforementioned (section 3.2) integrated catalytic strategy that converts the aqueous stream of GVL into liquid alkenes in a molecular weight range appropriate for inclusion in jet fuels. The major difficulties associated with scale-up of this technology are deactivation of SiO_2/Al_2O_3 during the initial 24 hours on stream and a profound water inhibition during butene oligomerization. (36) In the decarboxylation reactor, catalyst stability can be managed through introduction of water by maintaining GVL concentrations below 60 wt% (6M) in the feed. As such, a water co-feed to the decarboxylation reactor is required for stable catalytic activity; however, this must be balanced with the demand for a relatively dry oligomerization feed. Specifically, over Amberlyst-70 at 17 bar and 443K, introducing 10 mol% water into an equimolar butene/CO_2 feed decreases butene conversion by 50%, while increasing to an equimolar quantity of water completely suppresses butene conversion.(36) In integrated strategies, water was removed from the process stream using a simple, inter-reactor phase separator that was temperature controlled between 373K and 398K and maintained at reactor pressure (35 bar). Under these conditions, over 98% of the water in the process stream is condensed while butene and CO_2 are transferred downstream in the vapor

phase. (36) Preliminary conditions outlined for high yields in this system scaled well to larger reactors (1 inch OD) employed for liter-scale production in the SurfCAT program.

Table 3.7. Summary of the performance of the two-reactor GVL decarboxylation system employed for the production of alkene oligomers from commercial and lignocellulose-derived GVL. For both studies, the first reactor contained SiO_2/Al_2O_3 and operated at 648K and 35 bar with a GVL WHSV of 0.18 h-1. The second reactor contained Amberlyst 70 and operated at 343K and 35bar with a GVL WHSV of 0.15 h^{-1}.

		Maple wood GVL	Commercial GVL
Si-Al reactor	GVL conversion (%)	98	99
	Butene yield (%)	97	98
Amberlyst 70	Butene conversion (%)	95	94
Final oligomers composition (%)	C8-	9	13
	C8	21	24
	C12	22	24
	C16	23	22
	C20	14	12
	C20+	10	6

Importantly, we have observed that the process is sufficiently robust to accommodate lignocellulose-derived GVL prepared from LA hydrolysates after neutralization with $Ca(OH)_2$. To benchmark stability of the system, maple-derived GVL was fed to the reactor continuously for 200 h, and no significant loss of activity was observed. After 200h, the feed was changed to a 6M solution of commercial GVL (Sigma Aldrich, >98%) in deionized water and operated continuously for another 300 h at identical conditions. Overall yields for the production of C8+ oligomers (from lignocellulose-derived GVL) were >78% with 99% GVL conversion and >97% butene yields in the first reactor. The overall composition of the olefin oligomer product derived from Maple-sourced and commercial GVL is presented in Table 3.7. These results indicate that the performance of maple-derived GVL is comparable to that observed using model compounds.

3.8 Conclusion

This chapter develops a novel catalytic process that converts an aqueous stream of gamma-valerolactone (GVL) into a stream of butene mixture, which is then oligomerized to produce liquid hydrocarbons with molecular weights suitable as jet and diesel fuel precursors. The decarboxylation chemistry over solid acids discovered herein serves to expand the GVL platform by allowing unique access to a simple alkene, a completely deoxygenated molecule that creates a convenient route to form larger hydrocarbons using well-established olefin chemistry. The present two-reactor process utilizes only inexpensive, robust commercial solid acid catalysts, operates continuously, demands no external hydrogen source for oxygen removal and requires minimum product separation, thus providing an excellent example to demonstrate design principles in developing efficient catalytic strategies for biomass conversion. We further demonstrate the use of a multitude of characterization techniques to acquire fundamental understanding of the structural properties of Amberlyst-70, which help elucidate the origin of its intriguing catalytic behavior in the oligomerization of butene. The last part of this chapter presents a concerted effort that converts raw lignocellulosic biomass to produces C_8 and higher hydrocarbon fuels in liter quantities. In this manner, common practical issues encountered in process scaling up including sulfuric acid management, solid residue (e.g., gypsum) removal and catalyst stability have been explored, which provides guidance for future design and development of catalytic routes for biomass conversion. Notably, we demonstrate that the two-reactor process is sufficiently robust to handle GVL derived from maple wood over extended time on stream.

3.9 References

1. E. L. Kunkes, D. A. Simonetti, R. M. West, J. C. Serrano-Ruiz, C. A. Gartner and J. A. Dumesic, *Science*, 2008, **322**, 417-421.
2. A. J. Ragauskas, C. K. Williams, B. H. Davison, G. Britovsek, J. Cairney, C. A. Eckert, W. J. Frederick, J. P. Hallett, D. J. Leak, C. L. Liotta, J. R. Mielenz, R. Murphy, R. Templer and T. Tschaplinski, *Science*, 2006, **311**, 484-489.
3. G. W. Huber, S. Iborra and A. Corma, *Chemical Reviews*, 2006, **106**, 4044-4098.
4. D. A. Simonetti, J. Rass-Hansen, E. L. Kunkes, R. R. Soares and J. A. Dumesic, *Green Chemistry*, 2007, **9**, 1073-1083.
5. I. T. Horvath, H. Mehdi, V. Fabos, L. Boda and L. T. Mika, *Green Chemistry*, 2008, **10**, 238-242.
6. H. Mehdi, V. Fabos, R. Tuba, A. Bodor, L. T. Mika and I. T. Horvath, *Topics in Catalysis*, 2008, **48**, 49-54.
7. L. E. Manzer, *Applied Catalysis a-General*, 2004, **272**, 249-256.
8. S. W. Fitzpatrick, *Final Technical Report Commercialization of the Biofine Technology for LeVulinic Acid Production from Paper Sludge* DOE/CE/41178, BioMetics, Inc, Washington, DC, 2002.
9. H. Heeres, R. Handana, D. Chunai, C. B. Rasrendra, B. Girisuta and H. J. Heeres, *Green Chemistry*, 2009, **11**, 1247-1255.
10. I. Ahmed, *United States Patent.*, 6,190,427, 2001.
11. D. C. Elliott and J. G. Frye, *Battelle Memorial Institute (Richland, WA) United States Patent.*, 5,883,266, 1999.
12. J.-P. Lange, R. Price, P. M. Ayoub, J. Louis, L. Petrus, L. Clarke and H. Gosselink, *Angewandte Chemie International Edition*, **49**, 4479-4483.
13. P. N. R. Vennestrøm, C. M. Osmundsen, C. H. Christensen and E. Taarning, *Angewandte Chemie International Edition*, **50**, 10502-10509.
14. J. R. Regalbuto, *Biofuels, Bioproducts and Biorefining*, **5**, 495-504.
15. P. Goldberg, Z. Chen, W. O'Connor, R. Walters and H. Ziock.
16. K. S. Lackner, *Science*, 2003, **300**, 1677-1678.
17. H. Sakurai and M. Haruta, *Catalysis Today*, 1996, **29**, 361-365.
18. J. Toyir, P. R. de la Piscina, J. L. G. Fierro and N. Homs, *Applied Catalysis B-Environmental*, 2001, **34**, 255-266.
19. S. Koppatz, C. Pfeifer, R. Rauch, H. Hofbauer, T. Marquard-Moellenstedt and M. Specht, *Fuel Processing Technology*, 2009, **90**, 914-921.
20. R. D. Cortright, R. R. Davda and J. A. Dumesic, *Nature*, 2002, **418**, 964-967.
21. D. J. Darensbourg, *Chemical Reviews*, 2007, **107**, 2388-2410.
22. G. W. Coates and D. R. Moore, *Angewandte Chemie-International Edition*, 2004, **43**, 6618-6639.
23. M. Wick and J. M. Lebeault, *Applied Microbiology and Biotechnology*, 2001, **56**, 687-692.
24. D. M. Alonso, J. Q. Bond, J. C. Serrano-Ruiz and J. A. Dumesic, *Green Chem*, 2010, **12**, 992-999
25. S. Matar and L. F. Hatch, *Chemistry of Petrochemical Processes*, second edn., Houston, 2000.
26. J. Cejka, H. Van Bekkum, A. Corma and F. Schuth, *Introduction to Zeolite Science and Practice*, 3rd edn., Elsevier, Amsterdam, 2007.
27. A. Mantilla, F. Tzompantzi, G. Ferrat, A. Lopez-Ortega, S. Alfaro, R. Gomez and M. Torres, *Catalysis Today*, 2005, **107-08**, 707-712.
28. R. J. Quann, L. A. Green, S. A. Tabak and F. J. Krambeck, *Industrial & Engineering Chemistry Research*, 1988, **27**, 565-570.
29. G. Centi and R. Van Santen, *Catalysis for Renewables: From Feedstock to Energy Production*, Wiley-VCH, Wienheim, 2007.

30. J. Skupinska, *Chemical Reviews*, 1991, **91**, 613-648.
31. D. M. Alonso, J. Q. Bond and J. A. Dumesic, *Green Chemistry*, 2010, **12**, 1493-1513.
32. J. Q. Bond, D. M. Alonso, D. Wang, R. M. West and J. A. Dumesic, *Science*, **327**, 1110-1114.
33. R. Bringue, M. Iborra, J. Tejero, J. F. Izquierdo, F. Cunill, C. FitÃ© and V. J. Cruz, *Journal of Catalysis*, 2006, **244**, 33-42.
34. L. Benco, J. Hafner, F. Hutschka and H. Toulhoat, *The Journal of Physical Chemistry B*, 2003, **107**, 9756-9762.
35. K. A. Campbell, M. J. Janik, R. J. Davis and M. Neurock, *Langmuir*, 2005, **21**, 4738-4745.
36. B. B. Bardin, S. V. Bordawekar, M. Neurock and R. J. Davis, *The Journal of Physical Chemistry B*, 1998, **102**, 10817-10825.
37. I. K. Mbaraka and B. H. Shanks, *Journal of Catalysis*, 2005, **229**, 365-373.
38. W. Shen, Y. Gu, H. Xu, D. Dube and S. Kaliaguine, *Applied Catalysis A: General*, **377**, 1-8.
39. T. R. Carlson, Y.-T. Cheng, J. Jae and G. W. Huber, *Energy & Environmental Science*, **4**, 145-161.
40. A. J. Foster, J. Jae, Y.-T. Cheng, G. W. Huber and R. F. Lobo, *Applied Catalysis A: General*, **423-424**, 154-161.
41. R. Xing, W. Qi and G. W. Huber, *Energy & Environmental Science*, **4**, 2193-2205.
42. S. G. Wettstein, J. Q. Bond, D. M. Alonso, H. N. Pham, A. K. Datye and J. A. Dumesic, *Applied Catalysis B: Environmental*, **117-118**, 321-329.
43. D. M. Alonso, S. G. Wettstein, J. Q. Bond, T. W. Root and J. A. Dumesic, *ChemSusChem*, 2011, **4**, 1078-1081.
44. N. Mosier, C. Wyman, B. Dale, R. Elander, Y. Y. Lee, M. Holtzapple and M. Ladisch, *Bioresource Technology*, 2005, **96**, 673-686.
45. L. Deng, J. Li, D.-M. Lai, Y. Fu and Q.-X. Guo, *Angewandte Chemie International Edition*, 2009, **48**, 6529-6532.
46. Z.-p. Yan, L. Lin and S. Liu, *Energy & Fuels*, 2009, **23**, 3853-3858.
47. J. C. Serrano-Ruiz, D. Wang and J. A. Dumesic, *Green Chemistry*, **12**, 574-577.
48. L. Deng, Y. Zhao, J. Li, Y. Fu, B. Liao and Q.-X. Guo, *ChemSusChem*, 2010, **3**, 1172-1175.
49. B. J. O'Neill, E. I. Guburz and J. A. Dumesic, *Journal of Catalysis*, **290**, 193-201.
50. E. I. Gürbüz, D. M. Alonso, J. Q. Bond and J. A. Dumesic, *ChemSusChem*, 2011, **4**, 357-361.
51. H. Heeres, R. Handana, D. Chunai, C. Borromeus Rasrendra, B. Girisuta and H. Jan Heeres, *Green Chemistry*, 2009, **11**, 1247-1255.
52. S. Murat Sen, C. A. Henao, D. J. Braden, J. A. Dumesic and C. T. Maravelias, *Chemical Engineering Science*, 2012, **67**, 57-67.
53. H. Mehdi, V. r. Fabos, R. b. Tuba, A. Bodor, L. s. T. Mika and I. n. HorvÃ¡th, *Topics in Catalysis*, 2008, **48**, 49-54.

4. Kinetic Modeling of Interconversion between γ-Valerolactone (GVL) and Pentenoic Acid (PEA) combined with Decarboxylation to form Butene over Amorphous Silica/Alumina

4.1 Introduction

In this chapter, we explore the reaction kinetics for the inter-conversion between gamma-valerolactone (GVL) and pentenoic acid (PEA) and their decarboxylation to form equimolar quantities of butene and CO_2 over the silica/alumina catalyst, these steps being key components for the aformentioned strategy for the conversion of lignocellulosic biomass to liquid alkenes with molecular weights appropriate for gasoline and/or jet fuel.

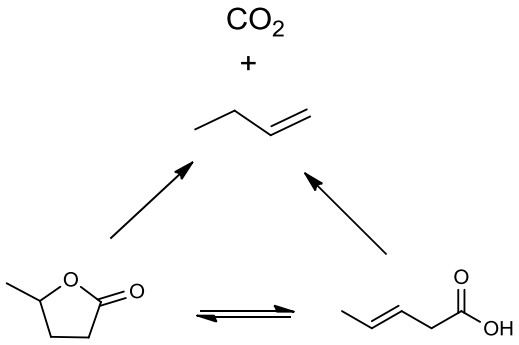

Figure 4.1: Pathways for inter-conversion between GVL and PEA and their decarboxylation over acid catalysts.

We find that the ring opening of GVL to PEA is a reversible reaction over silica/alumina over a wide range of reaction conditions, i.e., at pressures from 1 to 35 bars and temperatures from 523 to 648 K. We also consider the possibility that decarboxylation may occur either directly from GVL or indirectly from PEA produced by ring opening of GVL, and both of these pathways should be irreversible under typical reaction conditions given the favorable

thermodynamics for the formation of CO_2. The overall reaction scheme can thus be written as illustrated in Figure 4.1.

To explore the significance of each pathway in Figure 4.1, we have collected reaction kinetics data for different partial pressures of GVL and PEA at various temperatures. In addition, we have studied the effect of water on the reaction kinetics for conversion of GVL and PEA. Water is typically present in biomass-derived sources of GVL, and addition of water to GVL has been shown previously to be advantageous for achieving stable catalytic activity versus time-on-stream, although water reversibly inhibits the downstream oligomerization reaction. Further, to aid in the development of a representative kinetic model, we have attempted to quantify the extent to which direct GVL decarboxylation may contribute to the net rate of butene production via analysis of reaction kinetics at short space times. Finally, we have developed a simple kinetic model, accounting for adsorption and unimolecular surface reactions of GVL and PEA on silica/alumina, to describe experimentally observed reactivity trends. Insights gained from this study will guide the development of new catalysts and optimal processing strategies for the production of cellulosic biofuels using the continuous process described in Chapter 3.

4.2 Experimental Setup and Considerations for Kinetic Study

The ring opening of GVL, cyclization of PEA, and the decarboxylation of both reagents were studied in a fixed bed catalytic reactor operating in an up-flow configuration with pressures varied from atmospheric to 36 bar and temperatures from 548 to 648 K. The catalyst (SiO_2/Al_2O_3) was physically mixed with crushed quartz granules to maintain a consistent bed length for different experiments. The mixture was loaded into a stainless steel tubular reactor (6.35 mm OD) and held between two end-plugs of quartz granules and quartz wool. Typically,

GVL was introduced into the reactor in an aqueous solution (10 – 60 wt% GVL) using an HPLC pump (Lab Alliance Series I). PEA is sparingly soluble in water (~2 wt%) and was thus introduced using a high pressure syringe pump (Harvard Apparatus, PHD 2000) along with a co-feed of water from an HPLC pump. The co-feed setup was also used in experiments designed to test the effect of GVL concentration. Helium was used to pressurize the reactor and separator at the reactor effluent, and air was introduced as necessary for periodic catalyst regeneration. Gas feed rates were controlled by mass flow controller (Brooks Instruments, 5850S). The tubular reactor was fitted inside of an aluminum cylinder and placed within a well insulated furnace (Applied Test Systems). Bed temperature was monitored at the reactor wall using a Type K thermocouple (Omega) and controlled using a 16A series programmable temperature controller (Love Controls). Reactor pressure was controlled using a back pressure regulator (GO BP-60). The reactor effluent was diverted to a vapor-liquid separator wherein the liquid product was collected. For quantification of gas phase species, the separator volume was purged by bubbling a helium sweep gas (10 – 50 cm^3(STP)/min) through the liquid product.

Gas phase products were analyzed using an in-line pair of gas chromatographs. A GC-2014 (Shimadzu) equipped with an FID detector was used for analysis of hydrocarbon products , while CO and CO_2 were quantified using a GC-8A (Shimadzu) with a TCD detector using helium as a carrier/reference. Liquid samples were drained from the separator, and organic species were identified by GC-MS (Shimadzu GCQP-2010). To ensure accurate quantification of aqueous and organic product portions, the liquid product—commonly an emulsion of PEA, GVL, and water—was dissolved in ethanol and analyzed by HPLC using an RI detector (Waters).

Individual experiments were designed such that contributions to the rate of key species (GVL, PEA, water) could be isolated. To this end, studies were carried out wherein feed concentration, feed flow rate, and system pressure were modulated such that all reaction parameters other than the partial pressures of interest were held constant. Reaction conditions (catalyst loading, weight hourly space velocity (WHSV), temperature) were selected such that total conversion of the feed molecule was maintained below 20% and therefore, the reactor can be treated as a differential reactor for data analysis.

Rates of GVL ring opening and PEA ring closure were respectively given by the observed production rates of PEA and GVL, with concentrations measured by HPLC. The rate of decarboxylation reported for various experiments is given as the average production rate of butene and CO_2. Butene and CO_2 concentrations were independently measured by GC-FID and GC-TCD. In all instances of decarboxylation, the molar ratio of butene to CO_2 was measured (within experimental error) to be 1.0, in accord with the mechanism proposed herein. Generally, total carbon balances closed to within 5%.

To ensure that the reactions described herein are catalytic, we have examined the extent of inter-conversion and decarboxylation of both GVL and PEA in the absence of catalyst (SiO_2/Al_2O_3). No decarboxylation products are observed from either GVL or PEA at the highest temperature reported in this study (648 K). Similarly, the inter-conversion between GVL and PEA does not occur at temperatures at or below 648 K. The onset of decarboxylation from GVL begins, in the absence of a solid acid catalyst, at roughly 873 K. Thus, the reactions considered here occur catalytically over SiO_2/Al_2O_3.

In this study, we have addressed the possible influence of both intra-particle and external transport limitations in controlling observed rates of reaction. Regarding external mass transfer limitations, we consider the relationship given by Equation 1, which indicates that external transport limitations are not governing provided that the dimensionless group on the left hand side of the inequality is less than 0.15 for a first order reaction (1). In this expression, *Rate* is the total rate of reaction (ring opening/ring closure plus decarboxylation) per unit volume of catalyst, R_p is the radius of a representative particle of SiO_2/Al_2O_3, C_b is the bulk concentration of GVL or PEA in the reactor feed, k_c is the mass transfer coefficient between the catalyst and bulk phases, and n is the reaction order (taken to be 1 for this system).

$$\frac{Rate \cdot R_p}{C_b \cdot k_c} < \frac{0.15}{n} \quad (1)$$

Reaction rates and bulk oxygenate concentrations were taken from representative reaction kinetics measurements reported in this work. The particle radius was estimated using a graduated series of standard mesh screens (40 – 230). The powdered SiO_2/Al_2O_3 used in this study was observed to pass through a 230 mesh screen, indicating a maximum particle diameter of 0.063 mm. Mass transfer coefficients were obtained using standard correlations for gas flow through packed beds (2). At the conditions of this study, the dimensionless group was generally estimated to be on the order of 0.001. For 4 of the 79 data points considered, experimental conditions were particularly demanding, leading to an elevated rate of reaction at a temperature of 648 K and a low oxygenate partial pressure of roughly 0.02 bar. In this case, we estimate that the dimensionless group increases by an order of magnitude to 0.01. Importantly, the value in

this limiting case remains below the threshold suggested in Equation 1. As such, we do not consider inter-phase transport to limit the rate of reaction at the conditions reported herein.

To probe the extent of transport control within catalyst particles, we have estimated the Weisz-Prater number as given by Equation 2(3):

$$N_{W-P} = \frac{Rate \cdot R_p^{\,2}}{C_s D_{eff}} \qquad (2)$$

Rate and R_p are defined as in the preceding paragraph, and C_s is the reactant concentration at the catalyst surface. In the absence of external transport limitations, we consider C_s to be equal to the bulk oxygenate concentration. D_{eff} is estimated by Equation 3 as the product of the porosity (p) and the Knudsen diffusivity (D_{Kn}).

$$D_{eff} = p \cdot D_{Kn} \qquad (3)$$

The porosity was taken to be 0.5 for SiO_2/Al_2O_3 and the Knudsen diffusivity was estimated as per Vannice(3). According to the Weisz-Prater criteria, rate control by intra-particle transport becomes significant at values of $N_{W\text{-}P}$ greater than 0.3. We have observed that, at temperatures below 600 K, values of the Weisz-Prater number were typically on the order of 0.005 and clearly in the kinetically controlled regime. The value of $N_{W\text{-}P}$ increases to 0.08 at the highest temperature considered in this study (648 K), suggesting that intra-particle diffusion is not rate limiting, even under the most demanding conditions tested.

As a final consideration, we observe that the apparent activation energy in Arrhenius plots is constant as experimental conditions transition from low to high temperatures. The clearly demonstrated absence of transport limitations at the lower temperatures combined with a constant apparent activation barrier over the entire range of temperatures indicate that the experimental data are kinetically controlled and free from both internal and external transport limitations throughout this study.

4.3 Reaction Model Development

Linearized models of experimental data were used to describe observed trends, for instance in Arrhenius plots to estimate apparent activation energies. Estimation of the slope was achieved using linear least squares, and confidence intervals on estimates were calculated at 95% confidence. Kinetic models were developed according to observations from studies designed to elucidate the effects of temperature and concentrations of relevant species, and parameters were assessed for sensitivity by measuring the change in predicted rates of reaction produced for a 10% perturbation in initial parameter values. Insensitive parameters were lumped where possible to reduce the total number of variable parameters. Robust nonlinear least squares analysis was carried out using MATLAB (nlinfit) and resulted in optimized parameter estimates and ranges of confidence intervals. The inclusion of a parameter governing a direct pathway for GVL decarboxylation is considered according to the Akaike Information Criteria, as presented in section 4.6.

To decouple the effects of interconversion of GVL and PEA, reactor feeds in this study were comprised of GVL or PEA in isolation rather than mixtures of the two. In this manner, we have quantified adsorption thermodynamics for each species separately prior to generalizing

these results in a model which accounts for adsorption of both species. Importantly, as GVL and PEA interconversion occurs rapidly, we have observed that this model is effective in reactivity trends under conditions where both GVL and PEA are present in significant quantities. This treatment, though derived using single-reagent feed solutions, is appropriate for capturing reactivity trends under conditions where competitive adsorption of each species is significant.

4.4 Experimental Measurement of Kinetic Parameters

4.4.1 Catalyst Stability versus Time-On-Stream

Figure 4.2 shows a plot of catalytic activity for GVL conversion to butene as a function of time-on-stream. The data presented show the natural logarithm of the rate of decarboxylation (r) normalized by the initial rate of decarboxylation (r_0), which was obtained by linear extrapolation of the trend observed in the initial data points to zero time-on-stream.

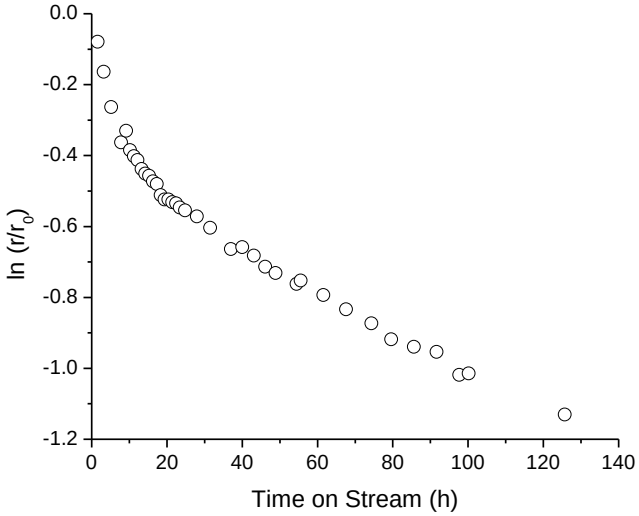

Figure 4.2 Rate of butene production from GVL as a function of time on stream. WHSV = 3.7 h^{-1}, P = 1 bar, T = 623 K.

In Figure 4.2, we observe that the rate decreases by about 50% within the initial 24 hours on stream. Afterwards, the system stabilizes and a lower rate of deactivation is observed, with the activity decreasing by roughly 0.4 – 0.5% per hour on stream. Accordingly, experiments designed to elucidate the effects of temperature and changes in the concentrations of GVL, PEA, and water were carried out after the system reached conditions at which the rate of deactivation did not significantly affect trends in data. Thus, reaction kinetics experiments were standardized to a common state of deactivation by collecting data after an initial 72 hour period of time-on-stream at a baseline condition. After this period of time, the loss of activity stabilizes to a rate which does not significantly alter trends (0.4% loss in activity per hour). Each set of experimental data was then collected within a period of 24 hours, typically within 10 hours. The maximal loss of catalytic activity is predicted to be roughly 10% over 24 hours for a feed containing 60 wt% GVL at 623 K. With the exception of data points at high oxygenate partial pressures, reaction kinetics studies were carried out using more dilute feeds, leading to a slower rate of deactivation. In addition, for each experimental data set, reaction conditions were varied in a random fashion to avoid superposition of catalyst deactivation onto trends in reaction kinetics data. In representative experiments, data were first collected at baseline reaction conditions; data were then collected by randomly varying a specific variable (e.g., temperature, partial pressure); and the data set was completed by returning to the baseline reaction conditions and measuring catalytic activity. By this method, we verified that significant deactivation (>5%) does not take place over the course of a single data set. In modeling trends in reactivity, initial rate data were estimated at a common time-on-stream using the deactivation constant reported herein.

Because the initial activity of the catalyst can be regenerated by calcination, catalyst deactivation is likely caused by deposition of coke. To test this hypothesis, we have carried out temperature programmed oxidation of catalysts that have been exposed to baseline reaction conditions for a period of 72 hours on stream. Indeed, these TPO studies show the formation of CO and CO_2 upon oxidation of spent SiO_2/Al_2O_3, leading to complete restoration of initial catalytic activity. We suggest that coke formation arises from polymerization of either GVL or PEA, which are demonstrated to interact strongly with SiO_2/Al_2O_3, rather than by polymerization of the butene product. We did not observe expected products of butene oligomerization (e.g., octene, dodecene) or cracking (e.g., ethylene, propylene), and the extent of butene isomerization at the elevated space velocities studied is minimal. Rather, we observed equimolar quantities of butene and CO_2 in the reactor effluent. These observations suggest minimal interaction of butene with the catalyst surface in the presence of feed oxygenates and water. In Chapter 3, we have observed severe competitive inhibition by water in butene oligomerization over solid acids(4), supporting a preferential coordination of water and a minimal involvement of the butene product in catalyst deactivation.

4.4.2 Reaction Pathways

Variation in the space time has a pronounced effect on the distribution of butene isomers measured in the reactor effluent, suggesting that 1-butene is the primary product of the decarboxylation reaction and 1-butene isomerization is not sufficiently rapid to become equilibrated. The trend in the observed ratio of 1-butene:2-butene as a function of space time (1/WHSV) is presented in Figure 4.3.

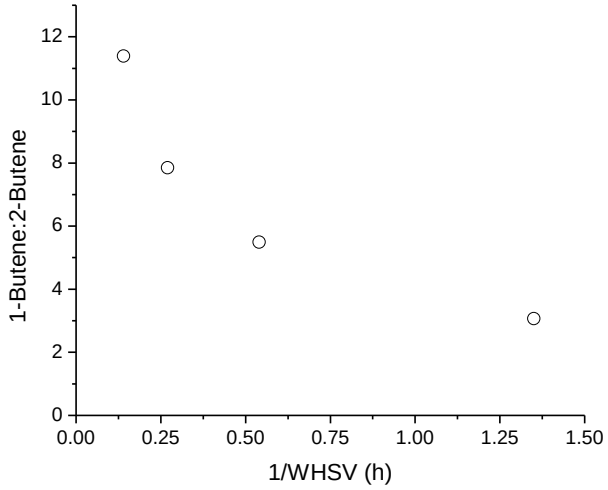

Figure 4.3 Molar ratio of butene isomers as a function of GVL WHSV at 613 K and 1 bar using a feed of 60 wt% GVL in water

We observe that 1-butene is the dominant product at 613 K, and the molar ratio of 1-butene:2-butene present in the reactor effluent increases as the reactor space time decreases (higher WHSV), a result which can be attributed to a decrease in the extent of butene isomerization at short residence times. For comparison, prior studies indicate that the molar ratio of 1-butene:2-butene at equilibrium is expected to be approximately 0.2 – 0.3 in the range of 604 – 623 K (5, 6). These results support the pathway where decarboxylation is proposed to occur preferentially through intermediates bearing carbenium ions beta to the carboxyl group, and C-C bond cleavage occurs between the beta- and carbonyl carbons to produce 1-butene and CO_2, as shown in Figure 4.4.

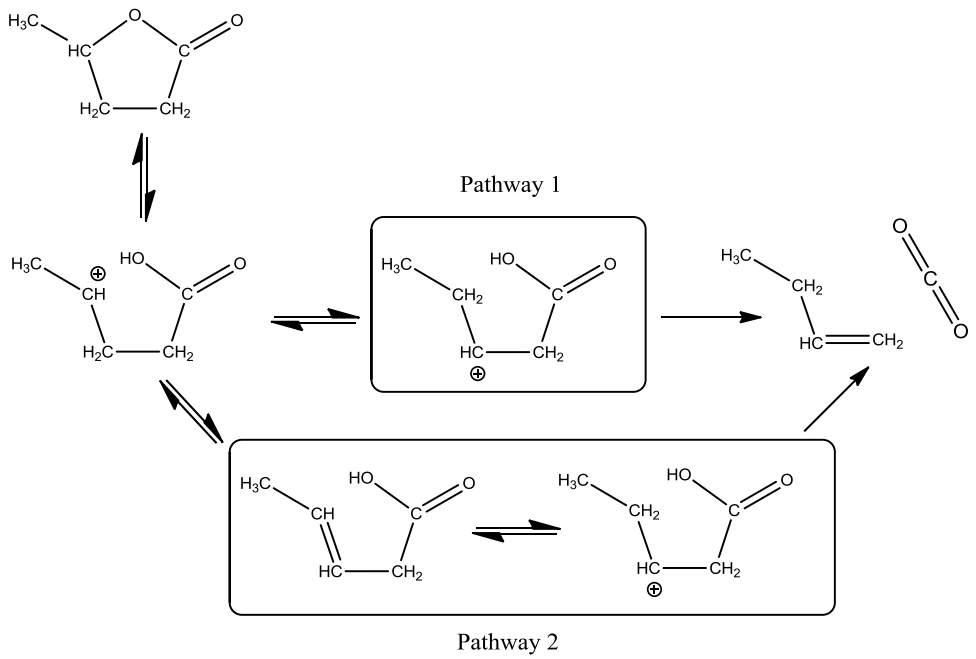

Figure 4.4 Proposed mechanism of decarboxylation through an intermediate bearing a carbenium ion at the beta carbon.

This pathway is consistent with that suggested by Noyce et. al. (7), who similarly proposed an initial activation of the beta-carbon of beta-phenylcinnamic acid via hydration in aqueous sulfuric acid, followed by dehydration/beta-scission to yield diphenylethylene, water, and CO_2. In a related study(8), the authors observed similar selectivity toward decarboxylation products from beta-lactones, supporting selective cleavage of the bond between the carboxyl group and the alpha-carbon over other possible beta-scission pathways. In contrast to these prior reports, we suggest that a hydrated intermediate (hydroxy-pentanoic acid in this case) is not requisite because we have observed decarboxylation of GVL over SiO_2/Al_2O_3 in the absence of water. Additionally, under the conditions studied, we have not observed hydroxy-pentanoic acid by GC-MS analysis, suggesting that hydration is unfavorable at the temperatures reported over SiO_2/Al_2O_3. Subsequent to decarboxylation, isomerization of 1-butene occurs over acidic sites to

yield cis-2 and trans-2 butene, which are the predominate products under conditions of high butene yield.

4.4.3 Thermochemistry and Effect of Reaction Temperature

As indicated in Figure 4.1, the net rate of butene production from GVL is potentially dependent on the reversible ring opening of GVL, combined with both direct and/or indirect decarboxylation pathways--of GVL and PEA respectively--both of which are irreversible. Experimental evidence from a prior study from our group(9) shows that higher concentrations of PEA are favored by equilibrium at higher reaction temperatures. Theoretical calculations in Figure 4.5 outline the thermochemistry of the inter-conversion between GVL and PEA as well as their decarboxylation to form butene. ΔG^o and ΔH^o (in brackets) values are included in kJ/mol for each reaction illustrated at standard conditions. The ΔH^o of reaction for the ring-opening of GVL to form 4-pentenoic acid was estimated to be 36 kJ/mol. Calculated ΔH^o associated with the production of other pentenoic acid isomers are lower than the estimate included for 4-pentenoic acid. The ΔH^o for the production of 2-trans, 3-trans, 2-cis, and 3-cis pentenoic acids are estimated to be 17, 25, 26, 32 kJ/mol, respectively. Similarly, changes in standard Gibbs free energy are estimated to be 19, 16, 14, 8, and 25 kJ/mol for 3-cis, 2-cis, 3-trans, 2-trans, and 4-pentenoic acids, respectively. This trend is expected since the conjugation of the C=C with the C=O of the carboxyl group provides additional stabilization of the molecule.

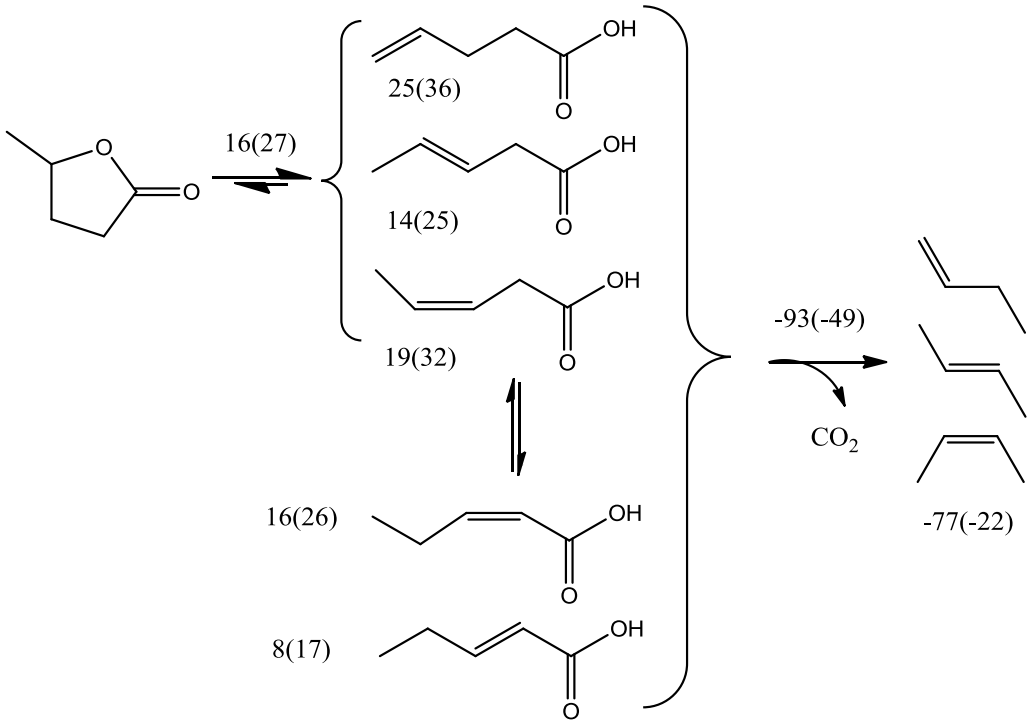

Figure 4.5 Calculated thermochemistry for ring-opening of γ-valerolactone to pentenoic acids and subsequent decarboxylation to butene. ΔG^o and ΔH^o (in brackets) are presented in kJ/mol for each reaction illustrated at standard conditions.Adapted from reference (9)

Figure 4.6 summarizes the observed effect of reaction temperature on the rate of GVL ring opening and on the overall rate of decarboxylation. From this figure, we estimate that the apparent activation energies for ring opening and decarboxylation are equal to 85 +/- 19kJ/mol and 175 +/- 20 kJ/mol, respectively (95% confidence intervals) when the feed to the reactor is comprised of GVL and water.

Additional experiments, plotted in Figure 4.7, were carried out at analogous conditions with a feed of trans-2-pentenoic acid and water to observe the temperature dependencies of cyclization (to form GVL) and decarboxylation of PEA, which we propose to be an intermediate in the decarboxylation of GVL. Similarly, we observe stronger temperature dependence in the

rate of decarboxylation, and apparent activation energies for cyclization and decarboxylation are estimated to be 58 +/- 24 kJ/mol and 142 +/- 11 kJ/mol, respectively (95% confidence intervals).

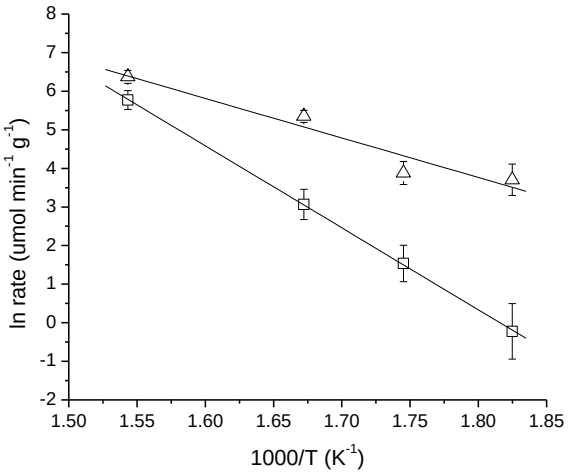

Figure 4.6 Rates of reaction for ring opening (Δ) and decarboxylation (□) of gamma-valerolactone at various reaction temperatures; feed is 10 wt% GVL in water, WHSV = 15 h^{-1}, P = 1 bar.

Comparing the rates of reaction of both GVL and PEA, we see that the activation barriers to ring opening (of GVL) and ring closure (of PEA) are relatively small and comparable for each reaction. Thus, a rapid inter-conversion between GVL and PEA is expected under typical reaction conditions, achieving equilibrium ratios of GVL and PEA at longer space times, as reported previously(9). We observe a difference of 33 kJ/mol in the apparent activation barriers for decarboxylation of GVL and PEA, suggesting that C-C bond cleavage occurs more readily from PEA than directly from GVL and that butene production occurs predominately through the PEA intermediate. It is possible, however, that a pathway for direct decarboxylation

of GVL exists, especially at short space times for which the partial pressure of PEA is low, as will be explored later in this chapter.

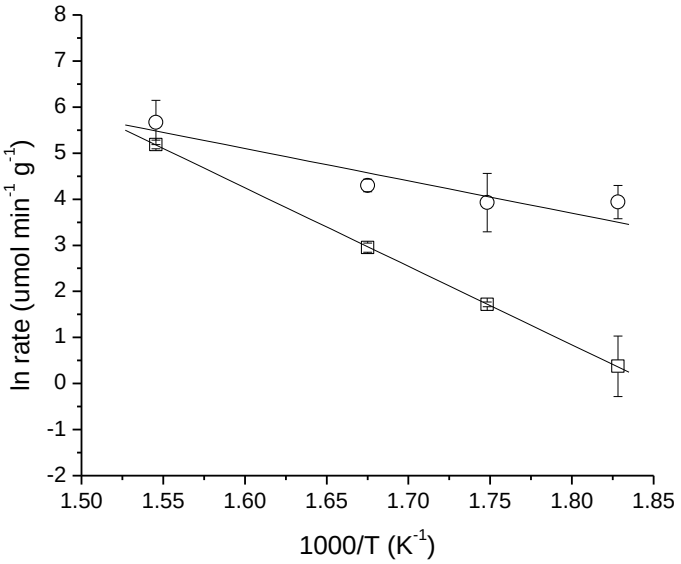

Figure 4.7 Rates of reaction for ring closure (○) and decarboxylation (□) of trans-2-PEA at various reaction temperatures; feed is 10 wt% trans-2-pentenoic acid in water, WHSV = 15 h^{-1}, and P = 1 bar

4.4.4 Effect of GVL Partial Pressure

Figure 4.8 shows results for the dependence of the rates of ring opening and decarboxylation on the partial pressure of GVL, from which we calculate apparent reaction orders of 0.16 +/- 0.03 and 0.42 +/- 0.09 for ring opening and decarboxylation of GVL, respectively. The observed trend in both ring opening and decarboxylation is an apparent fractional order dependence on GVL partial pressure, although a less pronounced dependence is observed in the rate of ring opening than that of decarboxylation.

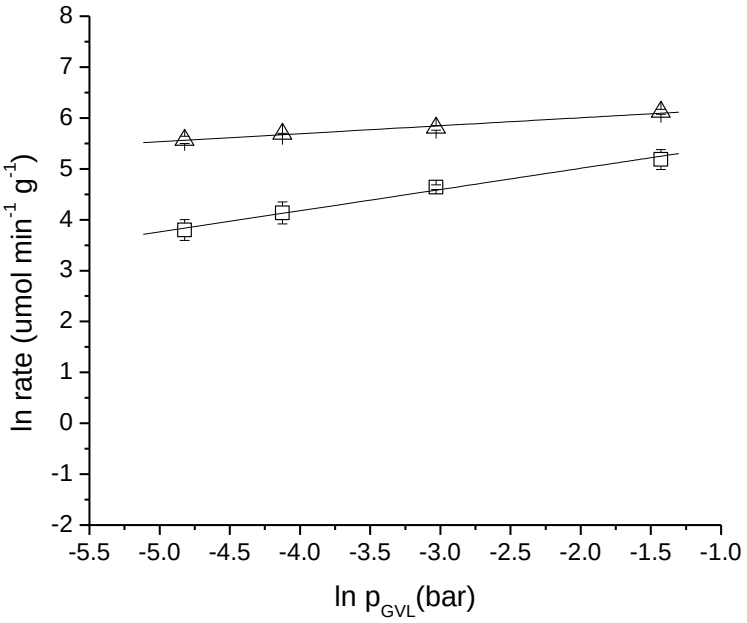

Figure 4.8 Rates of reaction for ring opening (Δ) and decarboxylation (□) of gamma-valerolactone at various partial pressures of GVL; T = 623 K, WHSV = 10 h^{-1}

It is apparent that increases in GVL concentration yield only modest enhancements in rates of reaction, particularly in ring opening, and this behavior could potentially be attributed to a strong interaction between GVL and the surface of SiO_2/Al_2O_3 which causes saturation of acid sites and a diminished response to GVL partial pressure at high concentrations**.** The observation of different reaction orders with respect to ring opening and decarboxylation suggests that GVL concentration contributes differently to each reaction.

4.4.5 Effect of PEA Partial Pressure

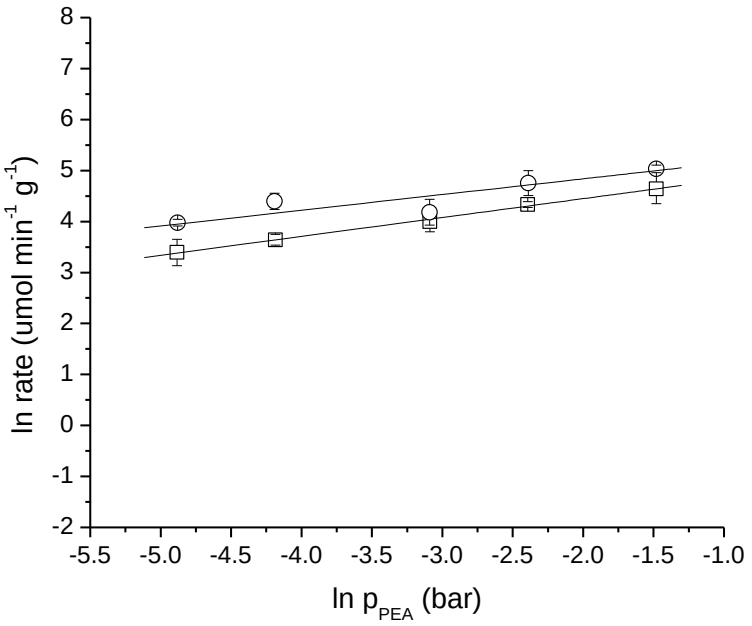

Figure 4.9 Rates of reaction for ring closure (○) and decarboxylation (□) of trans-2-pentenoic acid at various partial pressures of PEA; T = 623 K, WHSV = 10 h^{-1}.

Similar to the trends reported above with respect to changes in the GVL partial pressure, we observe in Figure 4.9 a slightly positive reaction order in both the rate of ring closure (0.31 +/- 0.07) and decarboxylation (0.37 +/- 0.07) for conversion of PEA over SiO_2/Al_2O_3. The observation of similar, fractional reaction orders for both ring closure and decarboxylation suggests that both reactions occur through a common coordination of PEA with the catalyst surface, which is likely indicative of a unimolecular surface reaction. PEA surface coverage has a strong effect on the overall rate of reaction, even at the low range of partial pressures described in this study, and its adsorption should be considered in governing rate expressions

4.4.6 Effect of Water Partial Pressure

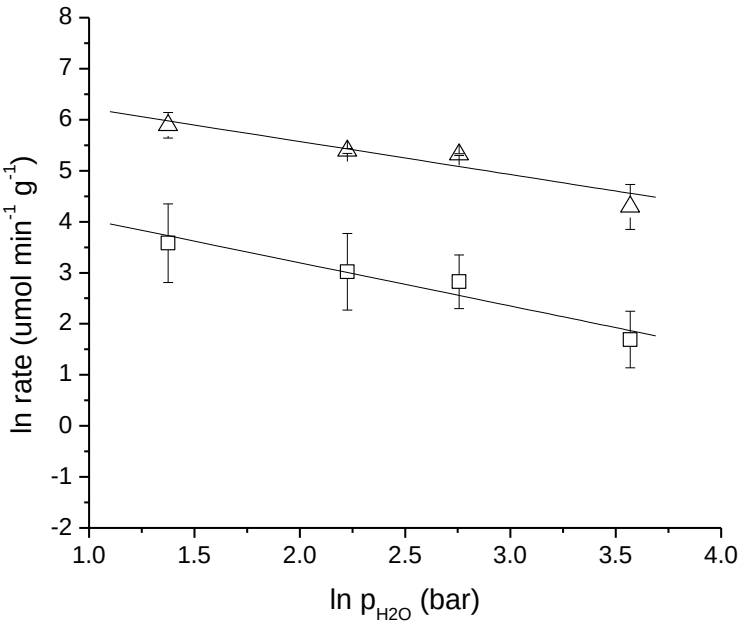

Figure 4.10 Rates of reaction for ring opening (Δ) and decarboxylation (□) of GVL at various partial pressures of water; T = 623 K, WHSV = 10 h^{-1}.

We have observed previously that the presence of water is necessary to minimize the extent of catalytic deactivation in the production of butene(4). Additionally, water is commonly considered to inhibit acid-catalyzed surface reactions by competing for adsorption at acid sites(10, 11). In Figure 4.10, the rates of GVL ring opening and decarboxylation are plotted against the partial pressure of water on a logarithmic scale. In both cases, we observe that the rate of reaction has a negative, fractional reaction order with respect to water, equal to -0.65 +/- 0.2 and -0.85 +/- 0.45 for ring opening and decarboxylation of GVL, respectively, which is consistent with competitive surface coordination of water molecules.

4.5 Decarboxylation Pathways

In Figure 4.4, we outline two possible pathways by which decarboxylation of GVL may occur. Pathway 1 illustrates direct GVL decarboxylation, which takes place upon initial protonation to open the lactone ring followed by a proton shift to form a beta-carbenium ion, which undergoes C-C cleavage to liberate 1-butene and CO_2. Pathway 2 suggests that decarboxylation may also occur, after ring opening, upon de-protonation (forming pentenoic acid) and re-protonation (forming a beta-carbenium ion). In this section, we analyze the extent to which both pathways contribute to the net rate of butene production from GVL. It is important to note that contributions of either pathway may be influenced by the degree of deactivation in the acid catalyst. For example, freshly calcined catalysts having stronger acidity and a higher active site density may promote direct decarboxylation (pathway 1 of Figure 4), whereas the dominant pathway may shift to indirect decarboxylation (pathway 2 of Figure 4) as the catalyst deactivates and loses acidity. Here, we have elected to study the behavior of partially deactivated SiO_2/Al_2O_3, because this state will ultimately be more relevant for long term industrial implementation.

The relative rates for production of butene by direct decarboxylation of GVL or indirect decarboxylation of PEA can be probed by examining both the concentration of PEA and the net production rate of butene and CO_2 as functions of space time. Specifically, the rate of decarboxylation achieved in the limit of infinite space velocity (where GVL conversion and PEA concentration are expected to approach zero) allows quantification of the rate of decarboxylation in the absence of PEA. The results of this experiment are summarized in Figure 4.11.

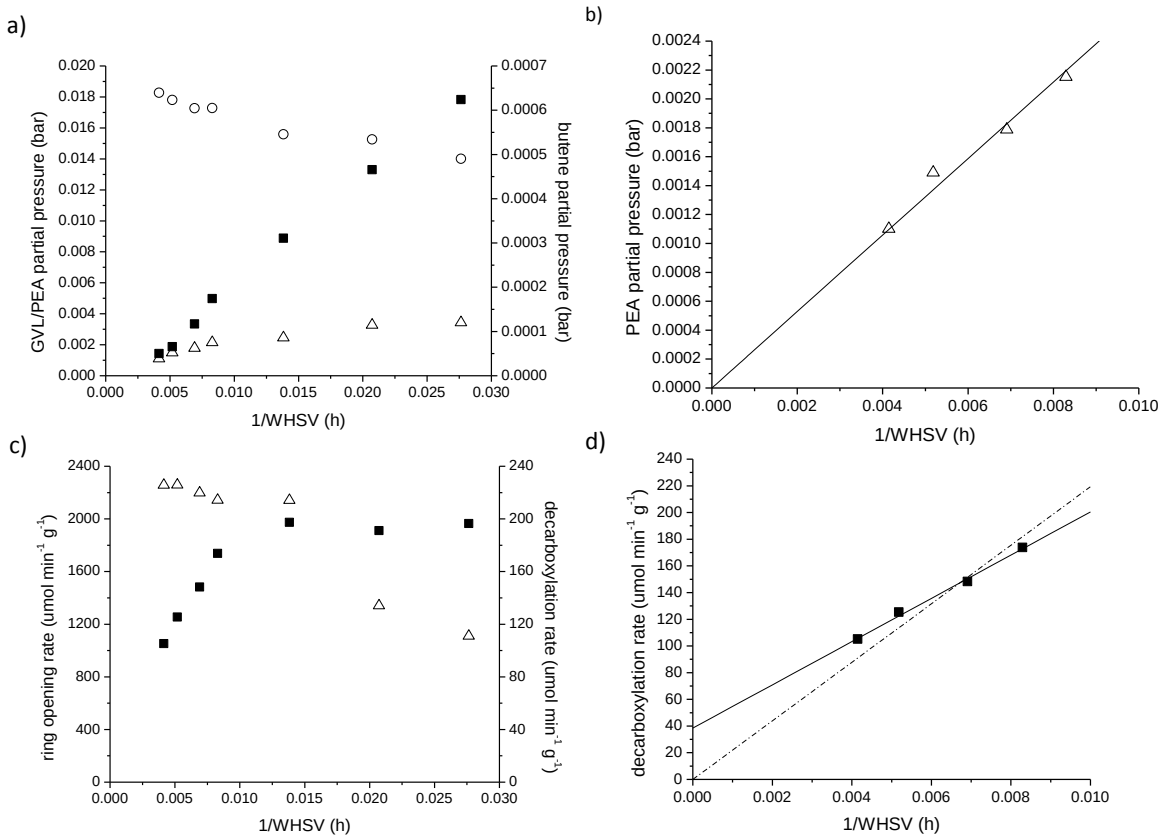

Figure 4.11 Summary of reaction kinetics data obtained at short space times. a) Outlet GVL (○), PEA (Δ), and butene (or CO_2) (■) partial pressures as a function of space time (1/WHSV). Butene (or CO_2) partial pressure (■) is plotted on the right hand axis. b) Extrapolation of PEA partial pressure (Δ) to the zero space time limit. c) Rates of ring opening (Δ) and decarboxylation (■) as a function of space time (1/WHSV). The decarboxylation rate is plotted on the right hand axis. d) Extrapolation of the decarboxylation rate to the zero space time limit. The solid line represents a linear regression of the measured data while the dashed line is included to illustrate the requisite decarboxylation trend in the absence of a direct pathway for GVL decarboxylation. Experimental conditions for a) – d) 10 wt% GVL in water, 633 K, WHSV of 36 to 240 h^{-1}

Figure 4.11 a) illustrates the effect of space time on the effluent partial pressures of pentenoic acid, GVL, and butene (plotted on the right hand axis) at 633 K using a 10 wt% solution of GVL in water. Note that the partial pressure of the CO_2 co-product was measured to

be equal to that of butene and is not reported in a separate data set. We observe that the partial pressures of PEA and decarboxylation products (butene and CO_2) decrease monotonically, ultimately approaching zero, with decreasing space time. The GVL partial pressure approaches that of the reactor feed (0.0198 bar) in the limit of zero space time. Figure 4.11 b) provides an expansion of the trend in PEA partial pressure as space time approaches zero, and we observe a trend that is well described by a linear model with a zero y-intercept. The rate of ring opening in this limit is also shown (Figure 4.11 c). Taken together, these results suggest that PEA is a primary product of GVL conversion.

Figure 4.11 c) shows rates of both ring opening and decarboxylation (plotted on the right hand axis) as a function of space time. The rate of decarboxylation reported here quantifies either the rate of butene or (equivalently) CO_2 production, and we observe the two products in a 1:1 ratio under all conditions reported. The net rate of GVL ring opening decreases with increasing space time, which can be attributed to the onset of PEA ring closure and eventually GVL/PEA equilibration at relatively long space times. Figure 4.11c) also shows that the rate of decarboxylation remains constant at relatively long space times (0.015~0.030 h) and begins to decrease only at shorter space times (<0.01 h). The long space time limit is informative regarding the total rate of decarboxylation attainable at these conditions (~200 umol min^{-1} g^{-1}). At shorter space times (<0.01 h), we observe a pronounced decrease in the partial pressure of PEA in the reactor effluent (Figures 4.11a and b), which parallels a decrease in the overall rate of decarboxylation. This behavior suggests that at sufficiently short space times, the total production rate of butene is limited by the concentration of PEA; however, it is unclear whether PEA is a necessary precursor for decarboxylation. Figure 4.11 d) provides an expansion of the

trend in decarboxylation rate observed at short space times. In the limit of infinite space velocity, we observe by extrapolation that the rate of decarboxylation is predicted to be 38 +/- 14 μmol min^{-1} g^{-1}, despite a clear indication that the partial pressure of PEA approaches zero under these conditions (Figure 4.11 b). The only species present in significant concentration at a space time of zero is GVL; therefore, the non-zero rate of decarboxylation can be attributed to a direct pathway for decarboxylation (pathway 1 of Figure 4.4).

Given the proximity of the estimated y-intercept to zero, we acknowledge that such an extrapolation is tenuous evidence of a direct pathway for GVL decarboxylation. To facilitate a direct comparison of the implications of either outcome, we additionally illustrate in Figure 4.11 d) the trend in decarboxylation predicted through a linear model with a y-intercept fixed at zero (dashed line). This model describes the necessary trend in the rate of butene production, as the partial pressure of PEA approaches zero, in the absence of a direct decarboxylation pathway. Although we cannot be absolutely confident in our estimate of the decarboxylation rate in the limiting case of infinite space velocity, the observed trend in Figure 4.11 d) is better described by allowing a positive y-intercept corresponding to a non-zero rate of butene production in the absence of PEA. In section 4.6, we show that inclusion of the direct decarboxylation pathway significantly increases the predictive capability of the kinetic model and is also justified by statistical critiera.

To summarize, the experimental data at short space times suggest the possibility of direct GVL decarboxylation, and our subsequent models have thus considered both of the proposed decarboxylation pathways. Quantitatively, we estimate that direct GVL decarboxylation could

contribute as much as 10 – 20% (38 umol min^{-1} g^{-1}) to the total rate of butene/CO_2 production (200 umol min^{-1} g^{-1}).

4.6 Kinetic Model

Over the range of partial pressures studied, we observe a positive, fractional order dependence with respect to the GVL and PEA concentrations on the rates of GVL ring opening and PEA cyclization, respectively. Thus, adsorption of both GVL and PEA appears to be favorable on the surface of SiO_2/Al_2O_3 and influences the rates of all important reactions. We have observed that decarboxylation of GVL proceeds with a higher apparent activation barrier than decarboxylation of PEA. As presented above, data collected at short space times suggest that consideration of both direct and indirect decarboxylation pathways may be necessary to accurately describe trends in reaction kinetics data. Indeed, we have observed enhanced predictive capabilities upon the inclusion of a direct pathway in governing kinetic models, as described in subsequent paragraphs. The rate of decarboxylation has a fractional order dependence with respect to the concentrations of both GVL and PEA, suggesting again that adsorption of these species is important in both pathways for decarboxylation. Finally, we have observed that water has an inhibiting effect on both ring opening and decarboxylation, which can be attributed to competitive binding at the active sites.

We assume that each of the three reactions in Figure 4.1 can be considered a unimolecular surface reaction, and that adsorption of water, PEA, GVL, and butene can contribute in each rate expression. In this study, experiments were typically carried out at elevated temperatures and low extents of reaction, which resulted in low partial pressures of butene in the reactor. Thus, adsorption of butene is not expected to compete with that of water,

GVL, and PEA, all of which have demonstrated significant interactions with the catalyst surface. This assumption is supported by our observation of products rich in 1-butene under the conditions studied, suggesting that butene adsorption/isomerization is not occurring rapidly in the presence of other, strongly adsorbed species. Additionally, we have not observed butene oligomers or cracking products in the reactor effluent. Therefore, butene adsorption is not considered in the governing rate expressions. The rates of all relevant reactions can be expressed as a product of rate constants (k_i) and surface coverages (θ_i) for each species, as summarized in equations 4 - 7. The surface coverage expressions are given by equation 7, the denominator of which includes coefficients and partial pressures dependencies for adsorption of water, GVL, and PEA. The effect of water has been isolated from that of GVL and PEA to decouple its influence and allow for more efficient capture of trends related to water partial pressure, and an exponent parameter (n, m) is included for each factor to assist in capturing disparate reaction orders observed experimentally in GVL, PEA, and water.

$$r_1 = k_1 \cdot \theta_{GVL} - k_{-1} \cdot \theta_{PEA} \quad (4)$$

$$r_2 = k_2 \cdot \theta_{GVL} \quad (5)$$

$$r_3 = k_3 \cdot \theta_{PEA} \quad (6)$$

$$\theta_i = \frac{K_i \cdot p_i}{\left(1 + K_{GVL} \cdot P_{GVL} + K_{PEA} \cdot P_{PEA}\right)^m \cdot \left(1 + K_{H_2O} \cdot P_{H_2O}\right)^n} \quad (7)$$

We note here that we do not have sufficient information (e.g., from density functional theory, microcalorimetry, *in situ* spectroscopy) to build a proper micro-kinetic model for this

surface chemistry. Therefore, we have employed a rather semi-empirical model to capture the trends in the reaction kinetics. We have found that the use of two site-blocking terms in the denominator is necessary to describe the experimental data, suggesting that two different types of sites are involved in the chemistry (e.g., Brønsted and Lewis acid site). This observation could now serve as the impetus for theoretical calculations. Because we are using a semi-empirical model, we express the rate constants in expressions 4 – 6 simply, according to the compensation effect(12), as the product of a rate constant estimated at the average temperature of the study (595 K) and an activation energy as given in equation 8, a construct which is effective in decoupling temperature effects and aids in the estimation of activation barriers(13).

$$k_i = k_{o_i} \cdot e^{\left(\frac{-E_A}{R}\cdot\left(\frac{1}{T}-\frac{1}{T_o}\right)\right)} \quad (8)$$

Adsorption parameters (K_i) can be expressed in a similar manner as dependent on binding energies, presented in equation 9.

$$K_i = K_{o_i} \cdot e^{\left(\frac{-\Delta H_{ads}}{R}\cdot\left(\frac{1}{T}-\frac{1}{T_o}\right)\right)} \quad (9)$$

In Figure 4.12, we demonstrate that the rate expressions given by equations 4-9 are sufficient to capture the experimental observations, particularly those of butene production rates, which are the most significant in the interest of fuel production.

a)

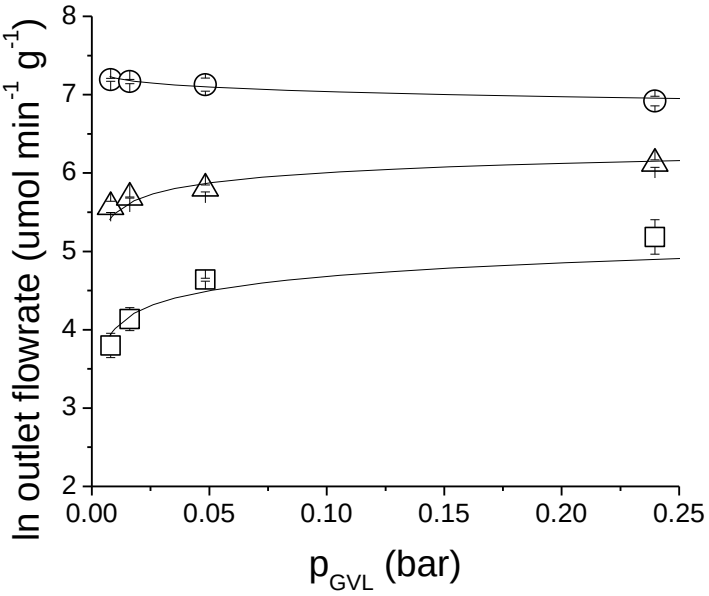
ln outlet flowrate (umol min-1 g-1)
8
7
6
5
4
3
2
0.00
0.05
0.10
0.15
0.20
0.25
pGVL (bar)

b)

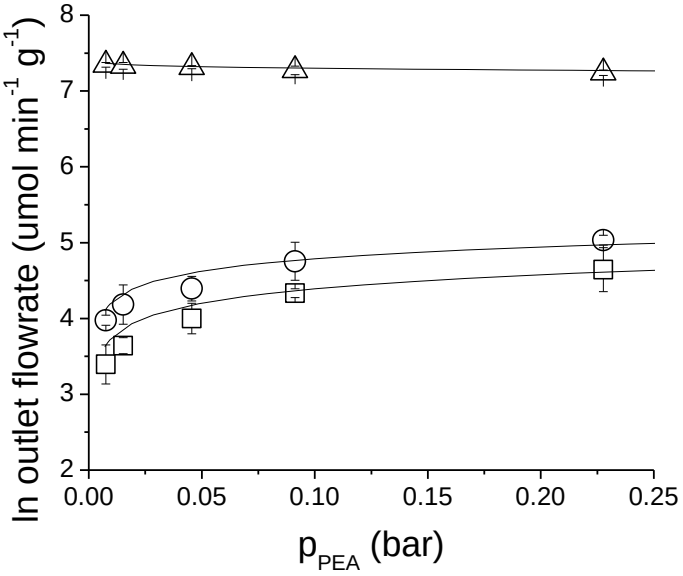
ln outlet flowrate (umol min-1 g-1)
8
7
6
5
4
3
2
0.00
0.05
0.10
0.15
0.20
0.25
pPEA (bar)

c)

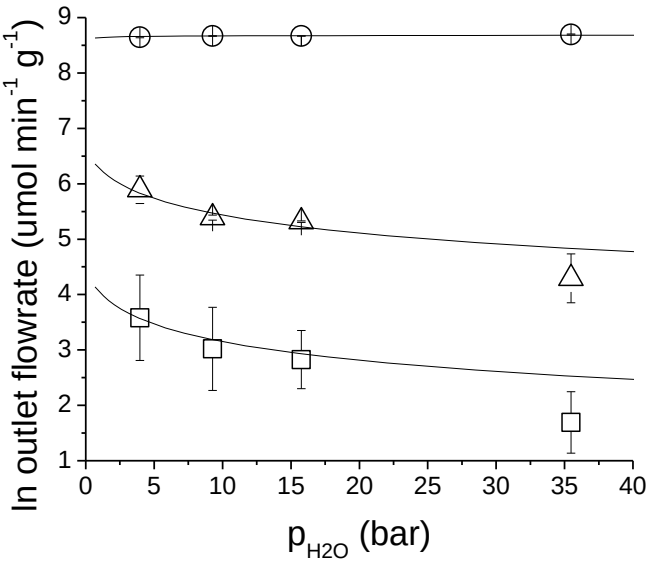
ln outlet flowrate (umol min-1 g-1)
9
8
7
6
5
4
3
2
1
0
5
10
15
20
25
30
35
40
pH2O (bar)

d)

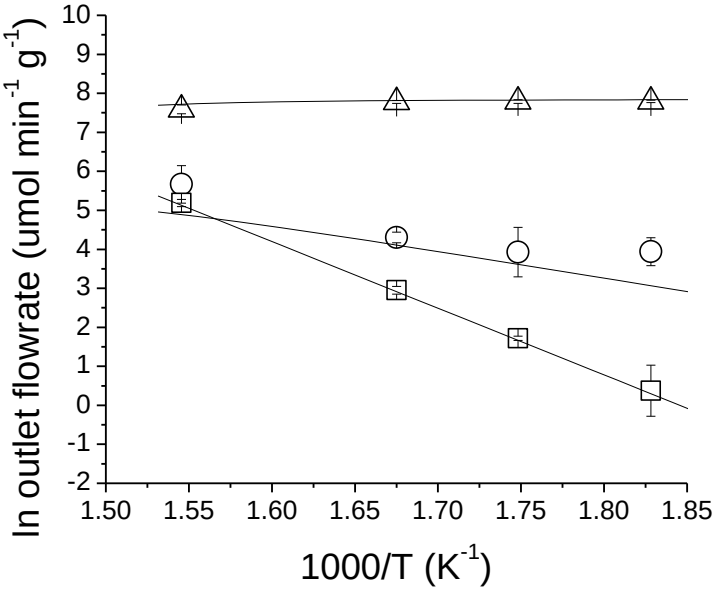
ln outlet flowrate (umol min-1 g-1)
10
9
8
7
6
5
4
3
2
1
0
-1
-2
1.50
1.55
1.60
1.65
1.70
1.75
1.80
1.85
1000/T (K-1)

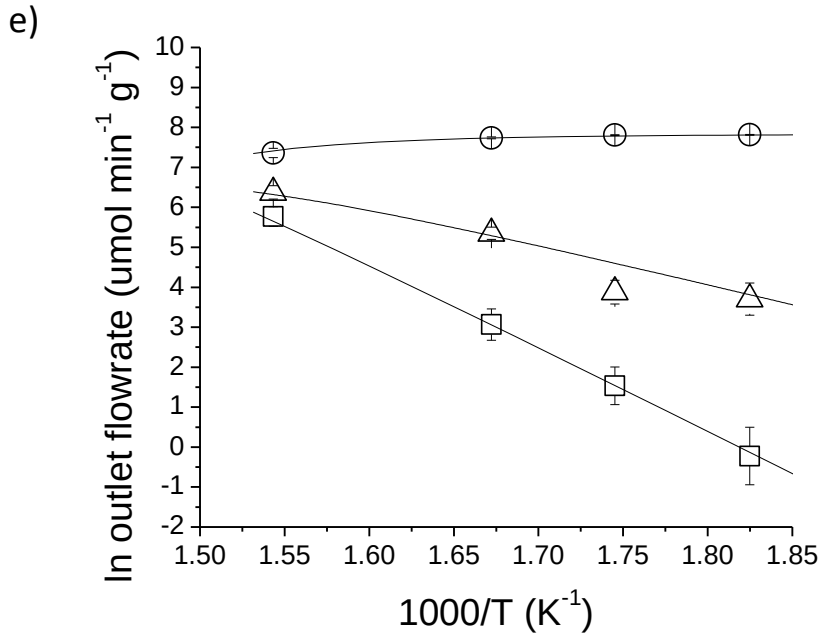

Figure 4.12 Comparison between model predicted trends (solid lines) and experimentally observed molar flow rates of GVL (○), PEA (Δ), and butene(or CO_2) (□) in the effluent of plug flow reactors operating at various conditions. a) describes the trends observed in the effluent molar flow rates versus the GVL partial pressure. b) describes the trends observed in the effluent molar flow rates versus the PEA partial pressure. c) describes the trends observed in the effluent molar flow rates versus the water partial pressure. d) describes the trends observed in the rates of GVL ring opening and decarboxylation at various reaction temperatures.e) describes trends observed in the rates of PEA cyclization and decarboxylation at various reaction temperatures.

Figures 4.12 a) and b) demonstrate good predictions by the model (in both GVL/PEA inter-conversion and decarboxylation) of the trends observed with varied partial pressures of both GVL and PEA. In addition, the model adequately describes the inhibitive effect of water on both GVL ring opening and decarboxylation, as illustrated in Figure 4.12c). The temperature dependencies for GVL ring opening/decarboxylation and PEA cyclization/decarboxylation are illustrated in Figures 4.12 d) and e), respectively. Estimated activation barriers are generally

sufficient to capture observed trends in the data. Estimates for kinetic parameters described in equations 4 - 9 are summarized in Table 4.1.

Table 4.1 Summary of kinetic parameters estimated by nonlinear least squares. (†) Parameter value fixed.

Parameter	Symbol	Optimized Value	Physical Contribution
1	K_{GVLo}	**590** +/- 13 bar^{-1}	Adsorption of GVL
2	K_{PAo}	**1.4E+03** +/- 510 bar^{-1}	Adsorption of PEA
3	K_{H2Oo}	**1.1** +/- 0.022bar^{-1}	Adsorption of Water
4	E_{A1}	**85**† kJ/mol	Activation barrier of GVL ring opening
5	E_{A-1}	**58**† kJ/mol	Activation barrier of PEA cyclization
6	E_{A2}	**175**† kJ/mol	Activation barrier for direct GVL
7	E_{A3}	**142**† kJ/mol	Activation barrier for PEA decarboxylation
8	k_{1o}	**0.27** +/- 0.006 min^{-1}	Average rate constant for GVL ring opening
9	k_{-1o}	**0.063** +/- 0.013 min^{-1}	Average rate constant for PEA cyclization
10	k_{20}	**0.024** +/- 0.0006 min^{-1}	Average rate constant for GVL decarboxylation
11	k_{30}	**0.017** +/- 0.003 min^{-1}	Average rate constant for PEA decarboxylation
12	m	**0.74 +/-** 0.003	Exponent for PEA and GVL adsorption
13	n	**0.52 +/-** 0.010	Exponent for Water adsorption

In the range of experimental conditions studied, we found that the binding energies for adsorption described in equation 9 were relatively insensitive; as such, the temperature dependence was eliminated and each constant was treated as a lumped parameter, K_o, at the average temperature. The activation barriers for the rate constants were fixed to the apparent values obtained through linear regression of temperature dependent reaction rates in the Arrhenius plots (section 4.4.3). This approximation was effective in capturing global trends in

rate of reaction while allowing a reduction in the total number of variable parameters without decreasing the predictive capabilities of the model. The kinetic model derived from equations 4 - 9 contains thirteen parameters, nine of which were varied in optimization studies to fit the data. The remaining four (activation barriers) were fixed at independently estimated values.

We have assessed the necessity of including both direct and indirect pathways (Figure 4.4) through consideration of the Akaike Information Criterion (AIC_c), calculated as in Equations 10 and 11, where k represents the number of parameters, n is the number of experimental observations, and RSS is the residual sum of squares calculated for the optimal parameter set(14).

$$AIC = 2k + n \cdot \left[\ln\left(\frac{2\pi RSS}{n} \right) + 1 \right] \qquad (10)$$

$$AIC_c = AIC + \frac{2k(k+1)}{n-k-1} \qquad (11)$$

The addition of a parameter is justified provided that any resultant decrease in residual error is sufficient to offset the positive contribution of an increased parameter number and yield an overall decrease in the value for AIC_c. Using a data set of 79 experimental points covering a range of temperatures and GVL and PEA partial pressures, the optimal 9-parameter set presented in Table 4.1 yields a residual square error of 3.10. In contrast, for an 8-parameter model (which did not include a direct pathway for GVL decarboxylation), the minimum residual achieved is 5.71. The corresponding AIC_c values are 34.7 and -11.1 for the 8- and 9-parameter models respectively. Because the variation of a 9th parameter (specifically, one governing direct GVL decarboxylation) decreases the value of AIC_c, its inclusion is statistically justified. Qualitatively,

we have observed that it is not possible to simultaneously capture trends in the rate of GVL ring opening and net decarboxylation without the consideration of a direct pathway.

In general, the parameter values obtained through least squares estimation agree with expectations from the qualitative analyses above. First, we observe that the adsorption coefficients (K_o) for GVL, PEA, and water are 590, 1400, and 1.1 respectively. These values suggest that the binding of both GVL and PEA is favorable on SiO_2/Al_2O_3, especially when compared to water. Assuming a common pre-exponential factor for adsorption and an average reaction temperature of 595 K, we estimate that a small difference in binding energy (<5 kJ/mol) can lead to the observed differences in K_o for GVL and PEA on SiO_2/Al_2O_3. The substantially smaller coefficient for water adsorption could be attributed to a binding energy that is weaker than that of GVL/PEA by roughly 35 kJ/mol. Typically, for experiments designed to assess reaction orders, the partial pressures of feed oxygenates were varied in the range of 0.01 – 0.2 bar while the partial pressure of water was fixed at 1.5 bar, at which conditions we observe that oxygenate adsorption occurs sufficiently strongly such that adsorbed GVL and PEA account for significant portions of the total surface coverage.

Employing an estimate of 85 kJ/mol for the activation barrier of GVL ring opening, we adequately capture trends in experimental data. Similarly, an estimated barrier of 58 kJ/mol for ring closure of PEA is a reasonable approximation, which is consistent with thermodynamic expectations that the conversion of GVL to PEA is an endothermic reaction. We consider this outcome in the context of equation 12, where the barrier to ring formation is expressed relative to that of ring opening, binding energies for GVL and PEA, and the enthalpy change between gas phase GVL and PEA, suggested by prior studies to be endothermic and dependent upon the

isomer of PEA considered. It has been demonstrated that the ring opening of GVL occurs with an enthalpy change of 17 to 40 kJ/mol in computational(9) and experimental studies(15). We expect that for comparable binding energies of GVL and PEA (as suggested by the magnitude of adsorption coefficients), the forward barrier would exceed that of the reverse barrier for this endothermic reaction, and the model is thus consistent with the expected thermodynamics of GVL ring opening.

$$E_{A_{-1}} = E_{A_1} + \Delta H_{GVL_{ads}} - \Delta H_{PEA_{ads}} - \Delta H_{rxn} \qquad (12)$$

Quantitatively, the difference in magnitude of forward and reverse activation barriers observed here (27 kJ/mol) is in the range suggested by previously reported reaction enthalpies. This result suggests that adsorptions of GVL and PEA occur with similar binding energies and supports observations that both species interact with the catalyst surface strongly and with comparable observed reaction orders.

Excellent agreement is achieved with respect to trends in butene production using activation barriers for decarboxylation of GVL and PEA of 175 and 142 kJ/mol, respectively, suggesting that butene production from PEA is the lower energy pathway; however, at typical temperatures of decarboxylation and within the precision of the estimate, we cannot eliminate the possibility of direct GVL decarboxylation, especially at short space times. Values of k_o are taken to be representative of the rate constant for each reaction considered at the average temperature of the data set, (595 K) and these values are estimated to be 0.274, 0.0631, 0.0241, and 0.0173 min^{-1} for GVL ring opening, PEA cyclization, GVL decarboxylation, and PEA decarboxylation, respectively. Thus, while the simple kinetic model outlined here is not intended as a definitive

description of reactions occurring during the decarboxylation of GVL, this lumped model is effective in describing the rate of butene production under reaction conditions that would be expected in most biomass applications.

4.7 Conclusion

In this chapter, we report results for the reaction kinetics of the decarboxylation of GVL and PEA and their inter-conversion over a SiO_2/Al_2O_3 catalyst. In addition to the catalytic decarboxylation of PEA, we consider that direct decarboxylation of GVL may also contribute to the total rate of butene production (corresponding to about 10-20% of the overall rate at typical reaction conditions). The increasing ratio of 1-butene:2-butenes in the product mixture with decreasing space time supports a mechanism where 1-butene is first formed via β-scission of intermediate carbenium ions. The simple kinetic model developed in this work provides a useful tool for predicting the rates of butene production for a wide range of reaction conditions. The results from this study can be used to aid in reactor design and process optimization studies to assess the techno-economic feasibility of producing liquid transportation fuels by the conversion of ligno-cellulosic biomass to GVL combined with catalytic decarboxylation to produce butene and alkene oligomers.

4.8 References

1. J. A. Dumesic, D. F. Rudd, L. M. Aparicio, J. E. Rekoske and A. A. Trevino, *The Microkinetics of Heterogeneous Catalysis*, American Chemical Society, Washington, D.C., 1993.
2. W. L. McCabe, J. C. Smith and P. Harriot, *Unit Operations of Chemical Engineering*, McGraw Hill, Boston, 2001.

3. M. A. Vannice, *Kinetics of Catalytic Reactions*, Springer, New York, 2005.
4. J. Q. Bond, D. M. Alonso, D. Wang, R. M. West and J. A. Dumesic, *Science*, **327**, 1110-1114.
5. H. H. Voge and N. C. May, *Journal of the American Chemical Society*, 1946, **68**, 550-553.
6. D. M. Golden, K. W. Egger and S. W. Benson, *Journal of the American Chemical Society*, 1964, **86**, 5416-5420.
7. D. S. Noyce, S. K. Brauman and F. B. Kirby, *Journal of the American Chemical Society*, 1965, **87**, 4335-4338.
8. D. S. Noyce and E. H. Banitt, *The Journal of Organic Chemistry*, 1966, **31**, 4043-4047.
9. J. Q. Bond, D. Martin Alonso, R. M. West and J. A. Dumesic, *Langmuir*, 2010, **26**, 16291-16298.
10. L. Smith, A. K. Cheetham, R. E. Morris, L. Marchese, J. M. Thomas, P. A. Wright and J. Chen, *Science*, 1996, **271**, 799-802.
11. T. Okuhara, *Chemical Reviews*, 2002, **102**, 3641-3666.
12. M. Boudart, *Kinetics of Chemical Processes*, Prentice-Hall, Inc., Englewood Cliffs, NJ, 1968.
13. T. Bligaard, K. Honkala, A. Logadottir, J. K. Norskov, S. r. Dahl and C. J. H. Jacobsen, *The Journal of Physical Chemistry B*, 2003, **107**, 9325-9331.
14. R. M. West, D. J. Braden and J. A. Dumesic, *Journal of Catalysis*, 2009, **262**, 134-143.
15. V. N. Emel'yanenko, S. P. Verevkin, E. N. Burakova, G. N. Roganov and M. K. Georgieva, *Russian Journal of Physical Chemistry A*, 2008, **82**, 1521-1526.

5. Selective Formation of Alpha Olefin via Decarboxylation of Lactones and Unsaturated Acids over Solid Lewis Acid Catalysts

5.1 Introduction

As outlined in Chapter 1, the use of biomass feedstocks is central to satisfy the long-term need for carbon-based commodity chemicals in a sustainable manner. Compared to the energy sector, suitable feedstock for the chemical industry is quite limited. While heat and electricity can be generally garnered from a variety of resources, most materials, especially polymer-based materials, can only be derived from carbon-based raw materials. A promising strategy for the conversion of biomass-derived carbohydrates to value-added chemicals is to take advantage of the synergies between the high chemo- and stereo-selectivity of biocatalysis and the high efficiency of chemical catalysis.(1) An example is polyketide/fatty acid biosynthesis, which offers flexibility to produce targeted molecules with specified carbon chain lengths and functionalities within a homologous series based on a single metabolic pathway.(2) The products assessabled through this route create a diverse platform, which can be subsequently upgraded by chemical catalysis to access families of commodity chemicals. In this chapter, we present a process that can efficiently convert unsaturated carboxylic acids and lactones (C_n) obtained by the above biological routes to selectively produce linear alpha olefins (LAOs) (C_{n-1}) by selective decarboxylation. This strategy uses inexpensive, robust heterogeneous solid acid catalysts, and it is suitable for a wide range of unsaturated carboxylic acids and their lactones.

LAOs form a family of valuable commodity chemicals featuring highly accessible terminal double bonds. LAOs are versatile building blocks for the manufacture of a broad range

of chemical products.(3) Short-chain LAOs (C_4-C_8) are used as co-monomers for producing high density polyethylene (HDPE) and linear low-density polyethylene (LLDPE). Higher LAOs are used as precursors to detergents (C_{12}-C_{14}), synthetic oils and plasticizers (C_6-C_{10}), and specialty chemicals such as oilfield fluids (C_{16}-C_{18}).(3) The linearity of LAOs gives rise to products with desirable mechanical properties, such as increased flexibility, strength and advantages such as biodegradability.(4) The global demand for LAO (C_4-C_{20+}) amounted to 3.4 million metric tons at the end of 2002 and has been growing rapidly.(5)

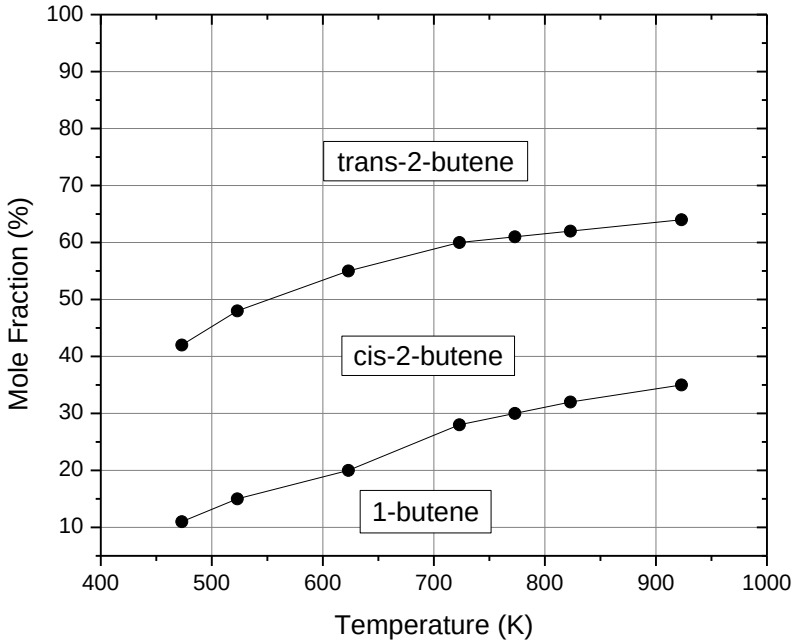

Figure 5.1 Distribution of isomeric n-butenes at equilibrium at various temperatures. (6)

The production of LAOs is inherently challenging due to the ease of migration of the terminal double bond to internal positions. For example, as can be seen in Figure 5.1, the thermodynamics of butene double bond isomerisation strongly favors the formation of *trans*- and

cis-2-butenes at elevated temperatures.(6) LAOs are manufactured commercially from fossil fuel feedstocks by two main routes, oligomerization of ethylene and cracking of Fischer-Tropsch products.(4) These processes necessarily lead to a distribution of LAOs with different chain lengths. Moreover, LAOs with odd carbon numbers cannot be produced by direct ethylene oligomerization. In addition, current processes overwhelmingly rely on fossil carbon and thus are not sustainable. In this regard, the development of processes for production of LAOs from renewable feedstocks has become of wide interest. For instance, a process has been demonstrated for LAO production by decarbonylation/dehydration of fatty acids over homogenous catalysts based on Pd.(7) Another process involves silver (II) mediated decarboxylation of fatty acids followed by ethenolysis over a commercial metathesis catalyst to produce renewable LAOs.(8) However, these processes entail expensive homogeneous catalysts, which present issues concerning separation and recyclability.

In Chapter 3, we describe the decarboxylation of gamma-velerolactone (GVL) as a highly efficient route to form a stream of butenes that can be integrated with a subsequent oligomerization step to produce long-chain hydrocarbons with molecular weights suitable as jet fuel or diesel precursors. The catalyst used in this case is amorphous SiO_2-Al_2O_3., which demonstrates high yield (>90%) to total butenes. We note that under typical operating conditions used to maximize the total butene yield from GVL (e.g., 30~60 wt% GVL in water, 648 K, 1 bar, WHSV = 0.18~0.90 h^{-1}),(9-11) the product stream is an equilibrium mixture of 1-butene, *trans*- and *cis*-2-butene (Figure 5.1). In kinetic studies carried out in Chapter 4, we further observe that when the reactor is operated at low conversion levels, the concentration of 1-butene in the final product stream is significantly higher than equilibrium values and increases drastically with

increasing space velocities,, which leads to the conclusion that 1-butene is the primary product of GVL or pentenoic acid decarboxylation.

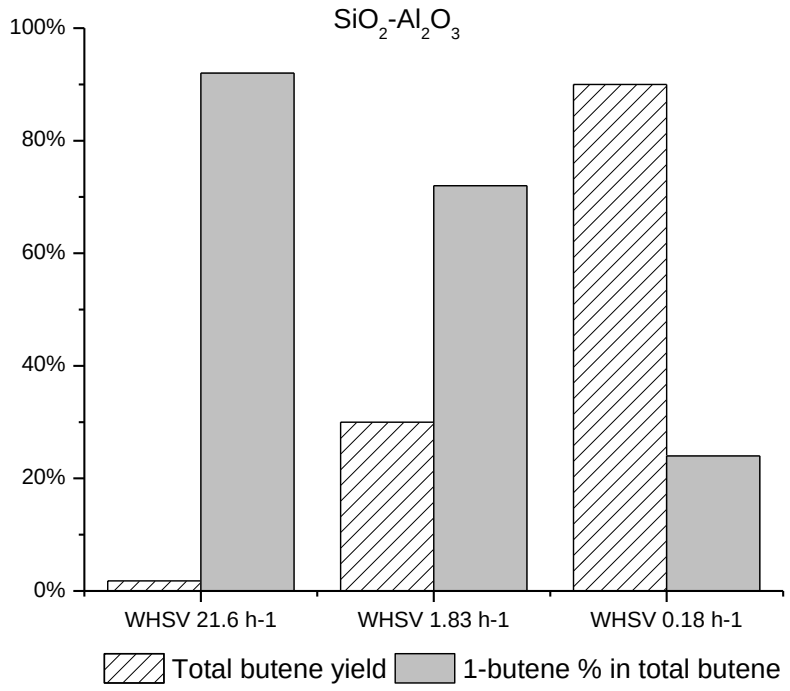

Figure 5.2 Butene production by decarboxylation of GVL over SiO_2-Al_2O_3. Reaction conditions: 30 wt% GVL in water, 648K, 1 bar at various WHSV.

We performed further optimization of reaction conditions to study whether 1-butene can be selectively produced over amorphous SiO_2-Al_2O_3. As shown in Figure 5.2, the Brønsted acid SiO_2-Al_2O_3 catalyst shows only 24% selectivity to 1-butene at 90% total butene yield, with a weight hourly space velocity (WHSV) of 0.18 h^{-1}. When the WHSV is increased to 21.6 h^{-1}, 92% of the product olefin stream can be retained as 1-butene using SiO_2-Al_2O_3 as catalyst, but only at 2% total butene yield. Increasing the total olefin yield only to 30% decreases the selectivity to 1-butene to 72%. Given the trade-off between 1-butene selectivity and total butene yield over

SiO_2-Al_2O_3, the maximum yield to 1-butene is limited to approximately 22%. If a stream of highly pure 1-butene (e.g. >90%) is desired for less-demanding downstream separation, the reactor needs to be operated at very low conversion levels, requiring separation of the butene product from GVL, and recycle of unreacted GVL to the reactor inlet. Therefore, it is challenging to selectively produce 1-butene or other alpha olefins using our previously-studied solid Brønsted acid catalysts such as SiO_2-Al_2O_3, because these catalysts exhibit high activity for both formation of 1-butene and its isomerization. Nevertheless, the decarboxylation of γ-lactones and the corresponding olefinic acids could provide a new route to terminal olefins, provided that the olefin isomerization reaction can be effectively suppressed

5.2 Seletive 1-Butene Formation over Gamma-Alumina

It is now clear that the challenge for the selective production of 1-butene from decarboxylation of GVL/pentenoic acids over solid Brønsted acid catalyst such as SiO_2-Al_2O_3 lies in their high activity for both formation of 1-butene and its isomerization. On the other hand, solid Lewis acid catalyst has been observed to catalyze olefin double bond isomerization at substantially lower rates as compared to that of Brønsted acid catalysts (12). Hence, we hypothesize that if the GVL decarboxylation can also be effectively catalyzed by solid Lewis acids, it is possible to obtain on these catalysts the desirable combination of high activity for 1-butene formation and low activity for its isomerization and thus leads to selective production of the alpha olefin.

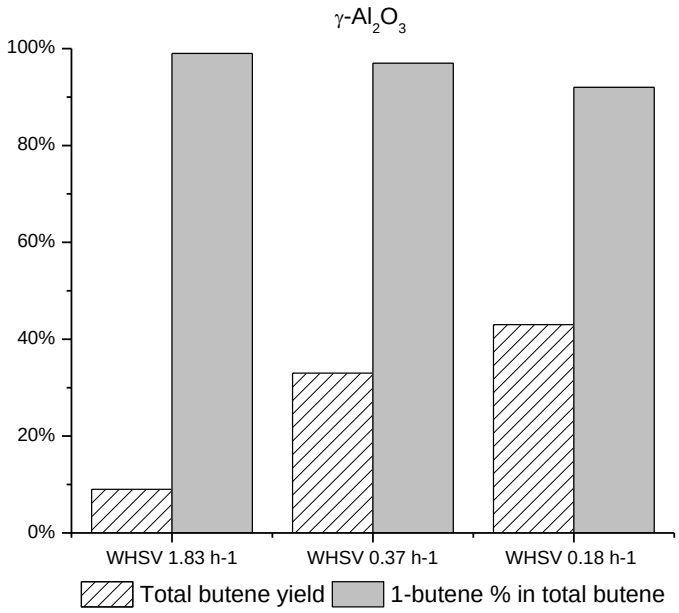

Figure 5.3 Butene production by decarboxylation of GVL over γ-Al_2O_3. Reaction conditions: 30 wt% GVL in water, 648K, 1 bar at various WHSV.

To test this hypothesis, we then investigated the decarboxylation of GVL over γ-Al_2O_3, an acidic oxide possessing predominantly Lewis acidity (13). Figure 5.3 shows that a stream of C_4 olefin containing unprecedentedly high levels of 1-butene can be produced in a single flow reactor using γ-Al_2O_3 as catalyst. Nearly pure 1-butene (>99% of C_4 stream) can be obtained (10% total butene yield). The yield to total butenes can be increased at longer space time, which also leads to a slight decrease in percentage of 1-butene in the butene product stream. However, over 92% selectivity to 1-butene can be achieved at 43% total butene yield.

While the high isomer selectivity to 1-butene is encouraging, additional side reactions were also observed with γ-Al_2O_3. In particular, equimolar amounts of acetic acid and propionaldehyde are formed as major by-products, with yields up to 16% of total GVL converted. In contrast, we note that the selectivity to acetic acid is very level (<1 %) over SiO_2-Al_2O_3. The

combined reaction network of GVL decarobxylation over these two catalysts is presented in Figure 5.4. We propose that acetic acid and propionaldehyde are formed via retro-aldol type mechanism through 3-hydroxypentanoic acid, which can be formed from hydration of 3-pentenoic acid and potentially 2-pentenoic acid.

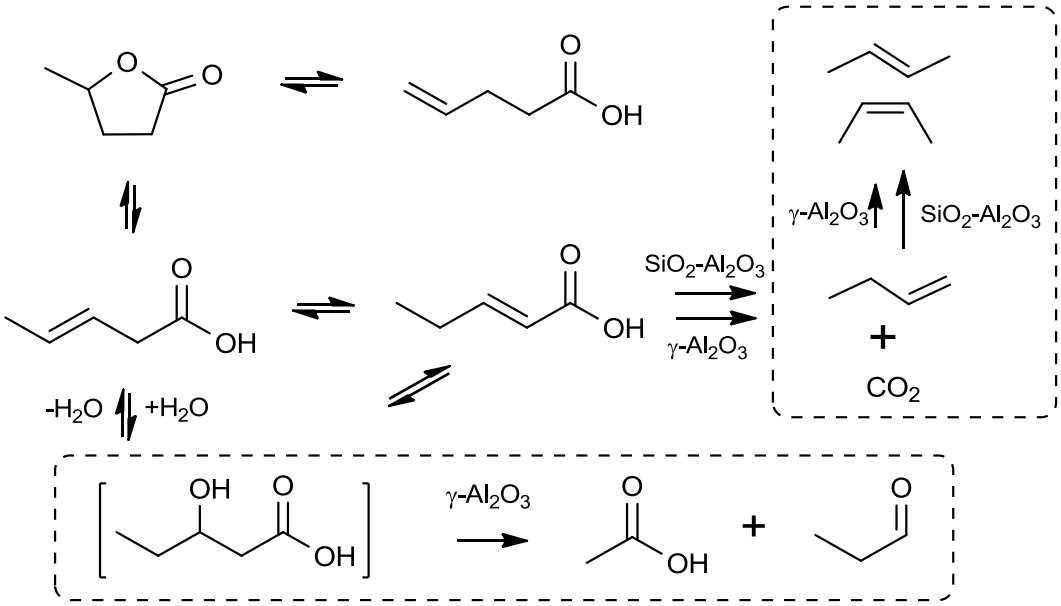

Figure 5.4 Pathway of gamma-valerolactone decarboxylation over γ-Al_2O_3 and SiO_2-Al_2O_3

Under the temperature ranges used for GVL decarboxylation, we did not collect the proposed intermediate 3-hydroxy-pentanoic acid in the final liquid product, presumably because the 3-hydroxy-pentanoic acid dehydrates to form the more stable pentenoic acids at these conditions. However, the validity of this proposed mechanism can be indirectly verified by studying the effect of water concentration in the feed on product selectivities, especially on that of acetic acid / propionaldehyde. As shown in Figure 5.5 (a), the selectivity to acetic acid formation clearly increases when more dilute aqueous solution of GVL is used as feed, which is consistent with the proposed mechanism where higher partial pressure of water increases the

concentration of the hydroxy-acid intermediate, thus increasing acetic acid production. With 10 wt% aqueous solution of GVL is used, acetic acid accounts for as high as 33% selectivity at complete conversion.

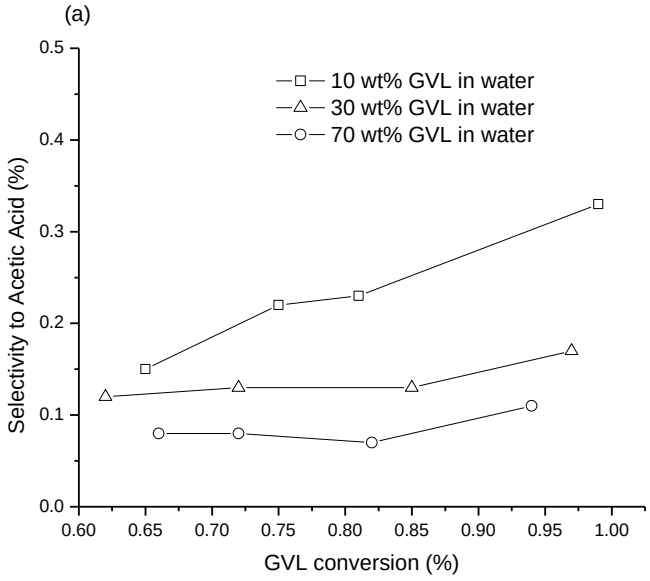

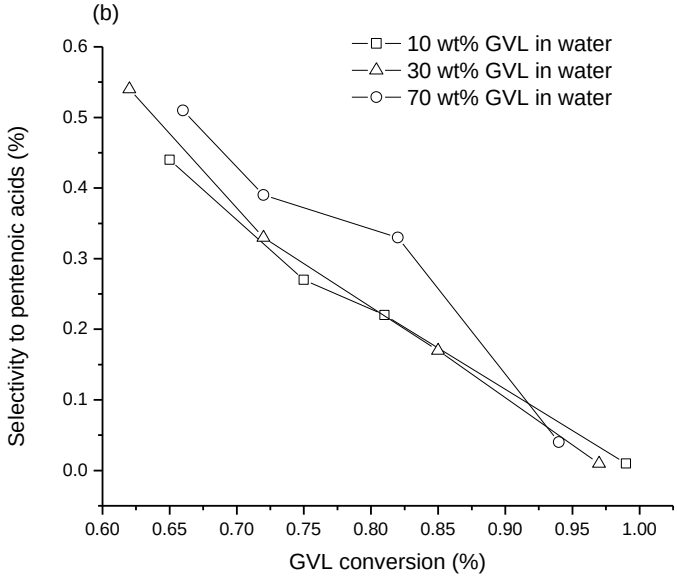

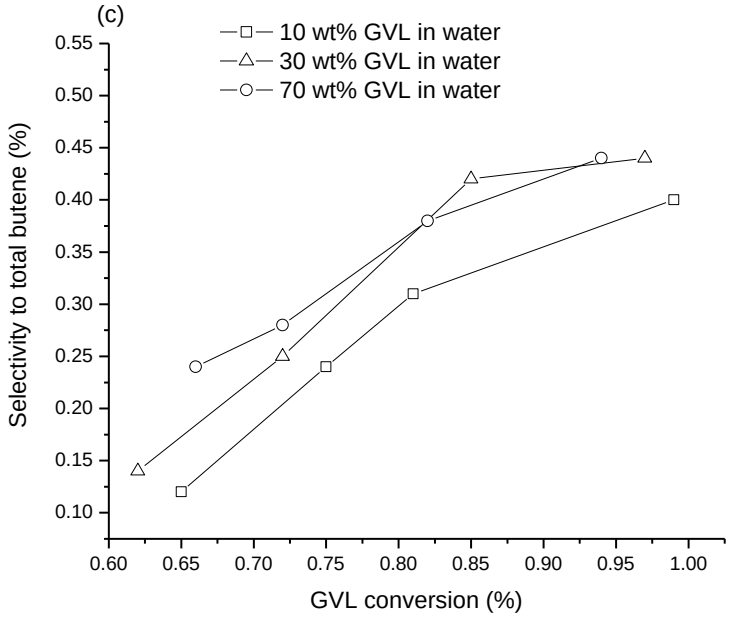

Figure 5.5 Effect of water concentration on the selectivity to acetic acid (a), pentenoic acids (b) and butenes (c) for GVL decarboxylation over γ-Al_2O_3. Reaction conditions: 648K, 1 bar, varying WHSV to achieve desired conversion levels.

Accordingly, the selectivity to pentenoic acid decreases (Figure 5.5 (b)) with increasing water partial pressure (as more dilute solutions are used as feed) due to the competitive formation of the hydroxy acid intermediate and eventually the formation of acetic acid. The decrese in the selectivity to pentenoic acids also leads to a corresponding decrease in selectivity to butene formation (Figure 5.5 (c)).

5.3 Role of Basic Sites and Improved 1-Butene Yields over Tungstated-Alumina

γ-Al_2O_3 is a well-known amphoteric oxide which possesses both Lewis acidic and basic sites.(14, 15) The surface model proposed by Konzinger et al (16) is generally accepted to well describe both the Lewis acidity and basicity of γ-Al_2O_3. As shown in Figure 5.6, a partially

dehydroxylated γ-Al_2O_3 surface constitutes of hydroxyl groups (-OH), oxide anions (O^{2-}) and coordinatively unsaturated Al^{3+} site with varying degrees of unsaturation.(17)

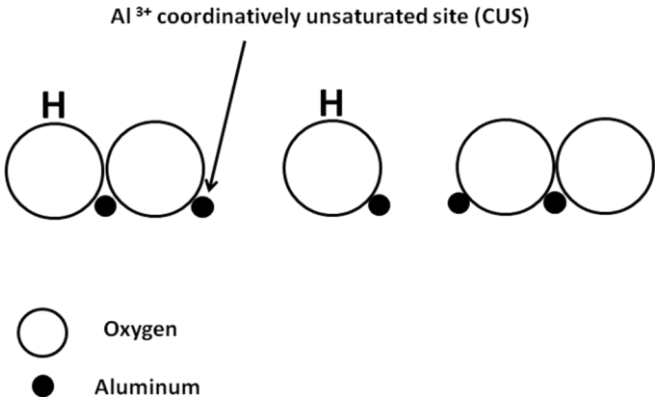

Figure 5.6. Schematic representation of partially dehydroxylated γ-Al_2O_3 surface

It has been determined based on extensive experimental measurements that the density of -OH groups on a fully hydroxylated γ-Al_2O_3 surface is on the order of 10^{14} cm^{-2}.(18-20) In contrast, the densities of catalytically active sites as measured by chemisorption are normally lower by one or two orders of magnitude, indicating that the surface -OH groups are unlikely to be catalytically active.(17) Infrared spectroscopic measurements also indicate no pyridinium ion foramtion on pure (hydroxylated) γ-Al_2O_3, confirming lack of intrinsic Brønsted acidity on this material.(16, 21) Indeed, protonation of basic probe molecules by surface -OH groups could not be observed except for very strong bases such as NH_3.(21) Accordingly, it has been proposed that defect sites with multiple vacancies account for the Lewis acidity on γ-Al_2O_3, while clusters of adjacent oxygen anions constitute the basic sites. (16)

To elucidate the respective role of Lewis acid sites and basic sites in the reaction network, we first investigated GVL decarboxylation using Sn-Beta zeolite, which is a purely Lewis acidic

zeotype that efficiently catalyzes the isomerization of glucose to fructose (22) and the conversion of mono- and disaccharides to methyl lactate.(23) The Sn-Beta zeolite was provided by Haldor Topose Research and Development Division. Our results show that over Sn-Beta zeolite, the main reaction pathway is very similar to that described in Figure 5.4, where GVL ring opens to form pentenoic acids that decarboxylate to form butene and carbon dioxide. However, acetic acid / propionaldehyde were not detected in the final liquid product, which suggests that the retro-aldol type reaction that leads to the formation of these by-products over γ-Al_2O_3 is likely to be catalyzed by its surface basic sites. We note that the results presented herein for Sn-Beta zeolite is qualitative since we observed that the GVL conversion obtained on this material was consistently lower than 5% (although the selectivity to total butene and isomer purity of 1-butene were high) and showed decreasing trends, likely due to disintegration of the material under the high-temperature, high-steam reaction conditions employed.

To explore further the role of active sites on γ-Al_2O_3, it was modified with varying loadings of tungsten oxide (WO_x). Table 5.1 compiles the physiochemical properties and catalytic activities for butene production over selected solid catalysts at high conversions of GVL. The densities of Brønsted and Lewis sites were measured by a combination of NH_3 temperature programmed desorption (TPD) (total number of acid sites) and infrared spectroscopy of adsorbed pyridine (ratio of Brønsted and Lewis sites).

Table 5.1 Physiochemical properties and catalytic activities of solid catalysts for GVL (30 wt% in water) decarboxylation at 648 K, 1bar.

Entry	Catalyst	S.A.(m^2/g)	CO_2 uptake (μmol/g)	BAS[c] / LAS (μmol/g)	GVL conv (%)	$C^{=}_4$ yield[d] (%)	AA[e] yield (%)	PEA[f] yield (%)	Carbon loss (%)	1-$C^{=}_4$[g] (%)
1	SiO_2/Al_2O_3	450	<1	546/136	98	92	<1	3	4	24.2
2	γ-Al_2O_3	200	55	0/219	97	43	16	1	40	92.2
3	γ-Al_2O_3[a]	200	55	0/219	99	59	8	2	31	82.4
4	4W-Al [b]	195	27	5/230	98	70	10	1	19	91.8
5	8W-Al	193	10	32/191	96	73	8	3	16	71.0
6	20W-Al	188	7	141/107	95	80	3	5	12	27.9
7	MgO	78	220	-	83	2	15	22	61	88.9

[a] 723K. [b] denotes 4 wt% WO_x-Al_2O_3. [c] Brønsted acid sites/Lewis acid sites. [d] denotes butene. [e]denotes acetic acid. [f] denotes pentenoic acid. [g] 1-butene percentage in total butenes.

It can be seen (entries 4-6) that increasing the loading of WO_x from 0 to 20 wt% progressively creates Brønsted acidity at the expense of Lewis acidity, consistent with a previous report by Stoled et al.(24) Consequently, the catalytic behaviour of WO_x-Al_2O_3 with increasing WO_x loading should approach that of SiO_2-Al_2O_3 (entry 1), whose activity is dominated by Brønsted acidity. This expected trend is clearly evidenced by the low 1-butene selectivity observed at high WO_x loading (entry 6). Remarkably, 4wt% WO_x-Al_2O_3 catalyst is able to retain 92% of total C_4 olefin as 1-butene at total butene yield of 70%, leading to 64% yield to 1-butene (entry 4).

Table 5.1 also summarizes basic site densities on these materials as titrated by CO_2-TPD. The extent of CO_2 uptake is negligible for SiO_2-Al_2O_3, whereas the CO_2 update for γ-Al_2O_3 is 55 μmol CO_2 /g. Importantly, the basic site density of γ-Al_2O_3 can be decreased by the progressive addition of WO_x (0 to 20 wt %), leading to a corresponding decrease in the yields to acetic acid and condensation products (entries 2-6). To further test this hypothesis, we studied the decarboxylation of GVL over magnesium oxide (MgO), a basic oxide. The MgO catalyst

produced over seven times more acetic acid than butene from GVL conversion, implicating the importance of basic sites in this pathway. Accordingly, we suggest that the formation of acetic acid and propionaldehyde on the γ-Al_2O_3 catalyst takes place by a retro-aldol type mechanism, which is known to be catalyzed by basic sites.(25) We have observed that doping γ-Al_2O_3 with small amount of acidic dopants, such as tungsten oxide, neutralizes surface basicity and suppresses by-products formation. However, higher loadings of tungsten oxide create Brønsted acidity that catalyzes 1-butene isomerisation.

5.4 Selective Production of Higher Linear Alpha Olefins

Having demonstrated high yields of 1-butene from GVL over our 4 wt% WO_x-Al_2O_3 catalyst, we then investigated the feasibility of accessing higher LAOs by decarboxylation of lactones with longer carbon chains, which can be derived from the polyketide/fatty acid synthesis. It is shown in Table 5.2 that γ-hexalactone (GHL), γ-octalactone (GOL) and γ-undecalactone (GUL) can be converted over 4 wt% WO_x-Al_2O_3 to form 1-pentene, 1-heptene and 1-decene, respectively. Remarkably high LAO percentages (>95%) can be obtained at moderate total olefin yields for the C6 and C8 lactones (entries 1, 3), although at higher total olefin yields (entries 2, 4), the LAO percentages decrease below 90%. We observe that maintaining a high LAO percentage at a high total olefin yield becomes challenging with GUL (entries 5, 6), whereas a high 1-decene percentage can be obtained at lower total decene yield.

Table 5.2 Production of LAO from various lactones on 4 wt % WO_x-Al_2O_3

Entry	Feed [a]	Lactone conv (%)	Olefin yield (%)	AA [d] yield (%)	Unsaturated acids yield (%)	Carbon loss (%)	LAO [e] %
1	5 wt% GHL [b]	82	54	8	12	26	97.1
2	5 wt% GHL [b]	98	61	13	2	24	88.3
3	30 wt% GOL [c]	91	16	<1	58	25	96.5
4	10 wt% GOL [c]	97	58	2	16	24	80.9
5	30 wt% GUL [c]	88	7	4	56	33	96.8
6	10 wt% GUL [c]	97	17	5	40	38	85.7

[a] co-fed with water using two syringe pumps. [b] Reaction T = 648K [c] Reaction T = 673K [d] denotes acetic acid. [e] LAO percentage in total olefins

In addition to the desirable decarboxylation reaction, we have also observed similar side reactions. Notably, acetic acid and aldehydes with two-fewer carbon atoms compared to the lactone reactant (i.e., butyraldehyde for GHL, hexanaldehyde for GOL and nonaldehyde for GUL) are produced as major by-products, regardless of the nature of the starting lactones. This behaviour further confirms that acetic acid is formed via a retro-aldol type mechanism through a common 3-hydroxy acid intermediate for different lactones, such as the 3-hydroxypentanoic acid in the case of GVL (Figure 5.4). Also, a portion of carbon goes to unidentified condensation products, likely formed between butene and GVL or pentenoic acids over γ-Al_2O_3. It appears that higher lactones and acids have lower reactivity towards decarboxylation and are more prone to side reactions. Indeed, thermogravimetric analysis (TGA) reveals that for the same mass of lactones processed, 50% more carbon is deposited on catalysts used to process GUL than that used for GHL. Thus, further optimization is needed to improve olefin yield from these feedstocks.

5.5 The Effect of Water: A Kinetic Phenomenon

It is interesting (and unexpected) that γ-Al_2O_3 and WO_x-Al_2O_3 can be used to selectively produce LAOs since both catalysts are known to have good activity for olefin double bond migration and skeletal isomerization at temperatures similar to those used in the present study (673 ~ 800 K).(12) The key role played by water, however, is that its presence significantly inhibits the undesirable isomerization of the alpha-olefins over Lewis acid sites, whereas this isomerization is rapid over Brønsted acid sites, even in the presence of water. Table 5.3 summarizes kinetic data on butene formation rate from 2-pentenoic acid decarboxylation and 1-butene isomerization rate both in the presence and in the absence of water over γ-Al_2O_3 and SiO_2-Al_2O_3. Initial rates of 2-pentenoic acid decarobxylation (deCO2) to form butenes (all isomers) and acid isomerization (acid iso) are measured in the same experiment, where the conversion of 2-pentenioc acid was kept well below 10% to maintain differential reactor assumption. To independently determine the rate of 1-butene isomerization, we carried out control experiments using 1-butene as the reactant. In these experiments, 1-butene (Airgas, 5% in helium) was diluted with helium to obtain the targeted partial pressure ($P_{1\text{-butene}}$= 0.005 bar) needed in the feed. Gas flow was regulated using a mass flow controller (Brooks 5850 model), and the system pressure was maintained at 1 bar. To eliminate any change in olefin isomerization rate due to variation in 1-butene partial pressure when cofeeding water, the flowrates of 1-butene, helium and water were adjusted accordingly to maintain 1-butene partial at 0.005 bar.

Table 5.3. Kinetic data on decarboxylation of 2-pentenoic acid and 1-butene isomerization reaction in the presence and in the absence of water

SiO_2-Al_2O_3			
Without water	Rate (μmol $min^{-1}g^{-1}$)	With water	Rate (μmol $min^{-1}g^{-1}$)
rate ($deCO_2$)[a]	476	rate ($deCO_2$)	528
rate (olefin iso) [b]	8775	rate (olefin iso)	4505
rate (acid iso) [c]	2854	rate (acid iso)	2669
γ-Al_2O_3			
Without water	Rate (μmol $min^{-1}g^{-1}$)	With water	Rate (μmol $min^{-1}g^{-1}$)
rate ($deCO_2$)	12	rate ($deCO_2$)	51
rate (olefin iso)	150	rate (olefin iso)	20
rate (acid iso)	391	rate (acid iso)	682

Reaction conditions : 648K, 1 bar; feed 2-pentenoic acid cofed with water (P_{acid} = 0.07 bar) to obtain rate ($deCO_2$) and rate (acid iso) with water; feed 2-pentenoic acid diluted with helium (P_{acid} = 0.07 bar) to obtain rate ($deCO_2$) and rate (acid iso) without water; feed 1-butene diluted with helium (P_{butene} = 0.005 bar) to obtain rate (olefin iso) without water; feed 1-butene cofed with water and helium (P_{butene} =0.005 bar) to obtain rate (olefin iso) with water. [a] denotes rate of decarboxylation; [b] denotes rate of 1-butene isomerization; [c] denotes rate of 2-pentenoic acid isomerization

The steady-state rates of 2-pentenoic acid decarboxylation and 1-butene isomerization over γ-Al_2O_3 are 0.012 (Feed: P_{total} = 1 bar, P_{PEA}= 0.07 bar, helium balance) and 0.15 mmol $min^{-1}g_{cat}^{-1}$ (P_{total} = 1 bar, $P_{1\text{-butene}}$= 0.005 bar, helium balance), respectively. However, when water was co-fed, the decarboxylation rate increased to 0.051 (P_{total} = 1 bar, P_{PEA}= 0.07 bar, P_{water}= 0.93 bar) while the 1-butene isomerization rate decreased to 0.020 mmol $min^{-1}g_{cat}^{-1}$ (P_{total} = 1 bar, $P_{1\text{-butene}}$= 0.005 bar, P_{water}= 0.90 bar, helium balance). Under the same conditions, the rates of decarboxylation and 1-butene isomerization over SiO_2-Al_2O_3 without water are 0.48 and 8.78 mmol $min^{-1}g_{cat}^{-1}$, respectively. When water was admitted into the system, the decarboxylation rate increased to 0.52 while the isomerization rate decreased only moderately to 4.50 mmol $min^{-1}g_{cat}^{-1}$. Hence, adding water decreases the 1-butene isomerization rate by a factor of 7.5 over γ-

Al_2O_3 and 1.9 over SiO_2-Al_2O_3. This finding thus represents an interesting case where the high water content commonly encountered in biomass processing can be utilized to positively influence product selectivity.

5.6 Conclusion

In summary, it is demonstrated in this chapter that it is possible to produce a stream of highly pure LAOs from lactones or unsaturated carboxylic acids in a single step using inexpensive, robust heterogeneous acid catalysts with no precious metal components. It is also shown that analogous decarboxylation chemistry exists for C_5 C_6, C_8 and C_{11} γ-lactones, which indicates the potential of this methodology as a general approach for the production of LAOs with varying chain lengths. The feedstock to this process can be derived from biological routes (e.g., polyketide/fatty acid biosynthesis), which thereby generates a series of homologous molecules for conversion to LAOs. Moreover, unlike the present ethylene-based route for production of LAOs, this new biological route is capable of targeting molecules with specified carbon chain length which after subsequent decarboxylation with the current technology, leads to a single LAO cut, thus offering additional manufacturing flexibility to meet market demand. This approach also allows for the production of both even and odd carbon number LAOs, depending on the number of carbons in the starting molecules. Such an integrated approach demonstrates the promise of a synergy between biocatalysis and chemical catalysis for efficiently converting biomass into value-added chemicals.

5.7 References

1. B. H. Shanks, *ACS Chem. Biol.*, 2007, **2**, 533-535.
2. B. J. Nikolau, M. A. D. N. Perera, L. Brachova and B. Shanks, *The Plant Journal*, 2008, **54**, 536-545.
3. D. Vogt, in *Applied Homogeneous Catalysis With Organometallic Compounds* 1996, vol. 1, pp. 245-258.
4. K. Weissermel and H.-J. Arpe, *Industrial Organic Chemistry*, 3rd edn., 1997.
5. *Alpha Olefins(02/03-4) PERP Report, Nexant Chemical Systems*, 2004.
6. H. H. Voge and N. C. May, *J. Am. Chem. Soc.*, 1946, **68**, 550-553.
7. G. A. Kraus and S. Riley, *Synthesis*, 2012, **44**, 3003-3005.
8. F. van der Klis, J. Le Nôtre, R. Blaauw, J. van Haveren and D. S. van Es, *Eur. J. Lipid Sci. Technol.*, 2012, **114**, 911-918.
9. J. Q. Bond, D. M. Alonso, D. Wang, R. M. West and J. A. Dumesic, *Science*, 2010, **327**, 1110-1114.
10. J. Q. Bond, D. Wang, D. M. Alonso and J. A. Dumesic, *J. Catal.*, 2011, **281**, 290-299.
11. J. Q. Bond, D. Martin Alonso, R. M. West and J. A. Dumesic, *Langmuir*, 2010, **26**, 16291-16298.
12. L. H. Gielgens, M. G. H. Vankampen, M. M. Broek, R. Vanhardeveld and V. Ponec, *J. Catal.*, 1995, **154**, 201-207.
13. A. Corma, *Chem. Rev. (Washington, DC, U. S.)*, 1995, **95**, 559-614.
14. V. R. Padmanabhan and F. J. Eastburn, *J. Catal.*, 1972, **24**, 88-91.
15. A. Gervasini, G. Bellussi, J. Fenyvesi and A. Auroux, *J. Phys. Chem.*, 1995, **99**, 5117-5125.
16. H. Knozinger and P. Ratnasamy, *Catalysis Reviews*, 1978, **17**, 31-70.
17. H. Knozinger, *Stud. Surf. Sci. Catal.*, 1985, **Volume 20**, 111-125.
18. D. S. Maciver, H. H. Tobin and R. T. Barth, *J. Catal.*, 1963, **2**, 485-497.
19. B. A. Hendriksen, D. R. Pearce and R. Rudham, *J. Catal.*, 1972, **24**, 82-87.
20. R. G. Haldeman and P. H. Emmett, *J. Am. Chem. Soc.*, 1956, **78**, 2917-2922.
21. H. Knozinger and C.-P. Kaerlein, *J. Catal.*, 1972, **25**, 436-438.
22. M. Moliner, Y. Roman-Leshkov and M. E. Davis, *Proc. Natl. Acad. Sci.*, 2010, **107**, 6164-6168.
23. M. S. Holm, S. Saravanamurugan and E. Taarning, *Science*, 2010, **328**, 602-605.
24. S. L. Soled, G. B. McVicker, L. L. Murrell, L. G. Sherman, N. C. Dispenziere Jr, S. L. Hsu and D. Waldman, *J. Catal.*, 1988, **111**, 286-295.
25. R. Mahrwald, *Modern Aldol Reactions*, WILEY-VCH 2004.

6. Bifunctional Pd/Nb_2O_5 Catalyst for the Conversion of γ-Valerolactone to Pentanoic Acid and its Ketonization to Nonanone

6.1 Introduction

As mentioned in Chapter 1, carbohydrates-derived molecules common possess an excess of functionality, hence making it difficult to control their reactivity and direct the conversion to targeted compounds. Consequently, one efficient strategy to catalytically convert these resources is based on an initial reduction of the oxygen content in the molecule, leading to the production of less-reactive intermediates that can be further upgraded to the desired products.(1) We have described in Chapter 3 and 5 the upgrading of GVL via its decarboxylation to form butene, where both oxygen atoms in the GVL molecule are removed in one step as CO_2. One major advantage associated with such strategies, in which complete removal of oxygen content is achieved, is that the resultant molecule can often be readily upgrading using well-established hydrocarbon chemistry and processes. Alternatively, oxygen can also be selectively removed or preserved, leaving certain degree of functionality that can be exploited for more specific chemical transformation. This approach has recently been applied to lactic acid (2-hydroxypropanoic acid), a prototypical over-functionalized biomass-derived molecule, using a water-stable bifunctional $Pt(0.1\%)/Nb_2O_5$ catalyst.(2) In this case, by combining dehydration/hydrogenation (to reduce the oxygen content) and C-C coupling reactions (to upgrade reactive intermediates), it is possible to transform, in a single reactor, concentrated aqueous solutions of lactic acid into an organic phase, that spontaneously separates from water and is rich in ketones in the C_4-C_7 range.(3) Following the same approach, we detail herein a

catalytic strategy (including dehydration/hydrogenation and C-C coupling reactions, Figure 6.1) to upgrade concentrated aqueous solutions of GVL into a set of valuable chemicals and fuels using a limited number of reaction and separation steps.

We discovered that if a metal component with hydrogenation / dehydrogenation activity is present in addition to a solid acid, decarboxylation of GVL is suppressed. Instead, the pentenoic acids, which form by GVL ring opern over solid acids, are rapidly hydrogenated into the saturated valeric acid (pentanoic acid). Control experiments using pentanoic acid using amorphous silica/alumina have shown that the extent of decarobxylation for pentanoic acid is negligible under conditions used for GVL or pentenoic acid decarboxylation. In this chapter, we study the formation of pentanoic acid from GVL using a bifunctional Pd/Nb_2O_5 catalyst in the presence of H_2. As a carboxylic acid, pentanoic acid can be upgraded via esterification reaction with an alcohol to produce alkyl valerate esters, which are reported to have acceptable energy densities and more suitable polarities than current biofuel molecules and showed superior performance in road tests.(4) The acid functionality also can be exploited in reactions that lead to C-C bond formation to form larger molecules. In this chapter, we also describe the catalytic upgrading of pentanoic acid via ketonization reaction over Ceria-Zirconia catalyst to form 5-nonanone, which can be further deoxygenated to form diesel precursor.

As mentioned in Chapter 1, one major concern of using most existing solid acids for aqueous biomass processing is their unsatisfactory performances under hydrothermal conditions. For example, niobia catalysts under hydrothermal conditions phase transforms from an amorphous to a crystalline phase (*TT*-phase), leading to a decrease in the surface area and catalytic activity.(5) Thus, novel solid acids with improved hydrothermal stability are highly

desirable for processing biomass-derived molecules in aqueous phase. In this Chapter, we demonstrate the synthesis of composite silica-niobia materials using conventional sol-gel technique as well as atomic layer deposition (ALD). These catalysts show superior stability compared to commerical niobia (CBMM, HY-340) when studied in the production of pentanoic acid from GVL.

6.2 Reaction Network

It is known in the literature that levulinic acid, in the presence of strong mineral or solid acids, dehydrates at moderate temperatures (573-623 K) yielding the corresponding cyclic product, alpha-angelica lactone (AL, Figure 6.1).(6) This substance polymerizes over acidic surfaces, (7) and we observed that upgrading routes involving this intermediate over acidic catalysts typically lead to deactivation of the catalyst and/or loss of carbon. As mentioned in section 3.7.3, by operating the reactor at lower temperatures (423 K) over a metal catalyst without the presence of acidic sites (Ru/C), concentrated aqueous solutions of levulinic acid were almost quantitatively converted to GVL (Table 6.1, entry1) through the intermediate 4-hydroxypentanoic acid (Figure 6.1), the presence of which was confirmed by GC-MS analysis. The catalytic reduction of levulinic acid to GVL has been previously carried out with high yields at high H_2 pressures (100 bar) and low levulinic acid concentrations (7 wt%)(8) or using solvents other than water.(9)We note that, in our case, nearly quantitative GVL yields can also be achieved for concentrated aqueous solutions of LA (50 wt %) at milder conditions (35 bar). The Ru/C catalyst showed high activity for the processing of concentrated solutions of LA, making it necessary to operate at high space velocities (WHSV=32 h^{-1}) to decrease the conversion below 100% to check for catalyst stability. At these conditions, the catalyst showed slow deactivation

with time on stream (from 90 to 68% conversion after 106 h), and treatment of the catalyst under flowing H_2 at 673 K for 2 h allowed for partial recovery of the initial catalytic activity (83% conversion).

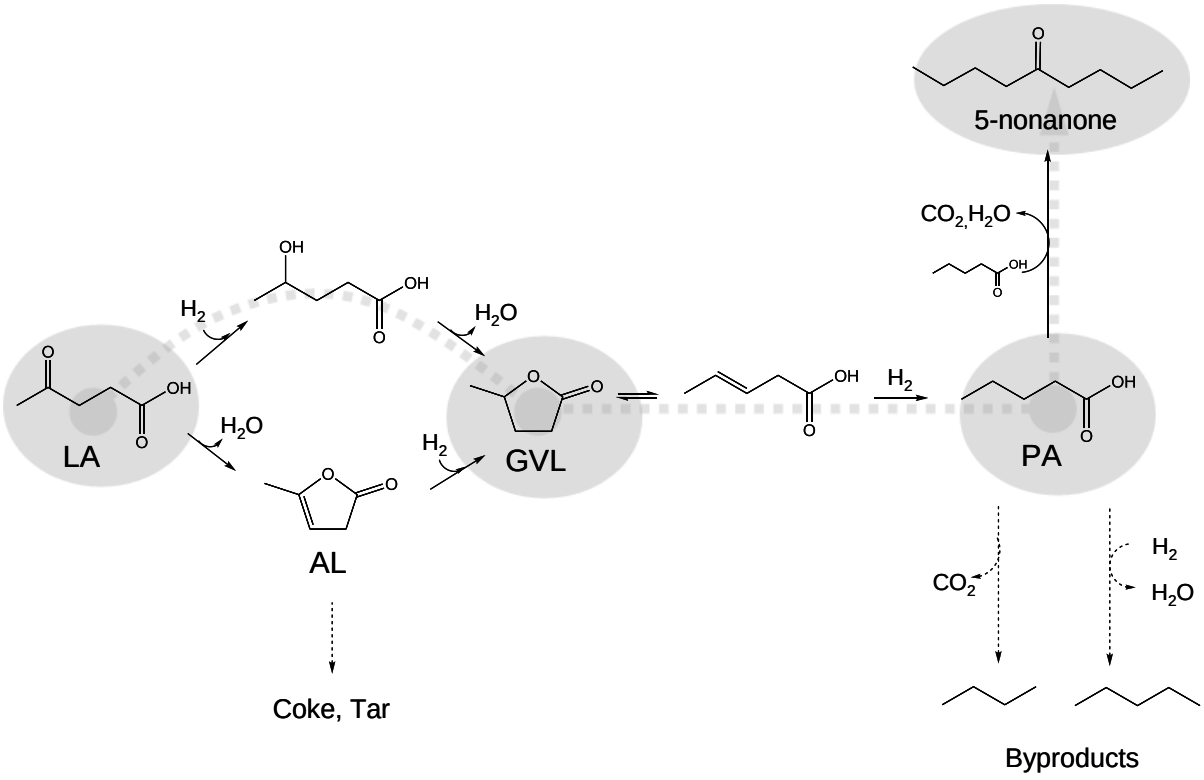

Figure 6.1. Catalytic approach used to upgrade levulinic acid by dehydration, hydrogenation and C-C coupling reactions.

6.3 Effect of Palladium Loading

Aqueous solutions of GVL is then converted to pentanoic acid (PA, Figure 6.1), by means of combined ring-opening (on acid sites) and hydrogenation reactions (on metal sites), over a water-stable bifunctional Pd/Nb_2O_5 catalyst at moderate temperatures and pressures (Table 6.1, entries 2-6). In the presence of H_2 and Pd/Nb_2O_5, the formation of n-butane is

observed from GVL, which is formed via Pd-assistied decarboxylation of pentanoic acid over metal sites,(10) with the release of stoichometric amounts of CO_x), along with n-pentane (as a result of successive hydrogenations and dehydrations of pentanoic acid over metal and acid sites, respectively). The formation of these unwanted products and the yield to pentanoic acid were found to be controlled by varying the metal loading of the catalyst. Thus, while a $Pd(1\%)/Nb_2O_5$ catalyst converted concentrated aqueous solutions of GVL into a mixture of C_4-C_5 alkanes, CO and CO_2 at 598 K and 35 bar (Table 6.1, entry 2), a decrease in the metal content by a factor of 10 caused a dramatic increase in the pentanoic acid yield (from 0 to 65%) at the same conditions of temperature and pressure (Table 6.1, entry 4). Remarkably, owing to its low solubility in water,(11) pentanoic acid was obtained in the separator at the effluent of the reactor, as an organic layer that spontaneously separated from water and accounted for almost 80% of the reacted carbon (see Table 6.1, entry 4). This liquid organic oil was enriched in pentanoic acid, with minor amounts butane and pentane dissolved in the liquid at the high system pressure. A decrease in the hydrogen partial pressure in the reactor also favored the formation of pentanoic acid versus hydrogenation and decarboxylation products (Table 6.1, entries 3 and 5). Therefore, proper choice of metal catalyst and reaction conditions leads to a yield of pentanoic acid equal to 92%, with 95% of the carbon being stored in the organic layer (Table 6.1, entry 5).

6.4 Integrated Dual-Bed Reactor for Upgrading γ-Valerolactone to 5-Nonanone

The formation of pentanoic acid achieves reduction of the oxygen content of levulinic acid, leading to a less-reactive, hydrophobic intermediate that is appropriate for new upgrading strategies to control reactivity (Table 6.1, entries 6-8). For example, pentanoic acid can be converted to 5-nonanone by means of ketonization reactions(12) with the release of

stoichiometric amounts of CO_2 and water (Figure 6.1). We found that, by increasing temperature and decreasing space velocity, this transformation can be carried out over Pd/Nb_2O_5, allowing the direct production of an organic stream enriched in 5-nonanone from aqueous GVL in a single catalytic bed (Table 6.1, entry 6). The C_9 ketone was produced with an optimized carbon yield of almost 60%, with unreacted pentanoic acid, C_{4-5} alkanes and lower ketones (produced by scission of 5-nonanone) accounting for the rest of the carbon stored in the effluent organic layer that spontaneously separates from water. Although this strategy is beneficial in that it minimizes the number of reactors involved (leading to reduction of capital and operating costs for the process), the number of reactions taking place in a single reactor is high, and control over the individual steps (from GVL to PA to 5-nonanone) is difficult, thus limiting the ultimate yield to the C_9 ketone. This limitation can be overcome by utilizing an additional bed of ceria-zirconia in a cascade approach.(1, 3) In this case, the reaction conditions in the first Pd/Nb_2O_5 reactor are adjusted to maximize the yield of pentanoic acid (Table 6.1, entry 5), which is then converted downstream to 5-nonanone over ceria-zirconia at higher temperatures (Table 6.1, entry 8). We note that the reaction conditions for the second bed were previously identified using pure pentanoic as feed to maximize the yield to 5-nonanone (Table 6.1, entry 7). The use of an additional reactor in this dual bed approach is justified by the improved yield to 5-nonanone (84 %), which is again obtained in a spontaneously-separating, high purity organic stream.

Table 6.1. Carbon distributions and carbon selectivities for levulinic acid and GVL conversion over different catalysts.

Entry	Catalyst	Feed	T (K)/P (bar)/ WHSV (h^{-1})	C distribution (%)[a]			C selectivity (%)[b]					
				Aq	Org	Gas	GVL	PA	C_9=O	CO_x	C_4+C_5 Alkanes	C_6-C_7 Ketones
1	Ru(5%)/C	50wt%LA[c]	423/35/4.8	100	-	-	96[d]	-	-	-	-	-
2	Pd(1%)/Nb_2O_5	50%wtGVL[c]	598/35/1.2[e]	-	37	63	-	-	-	13	83[f]	
3	Pd(1%)/Nb_2O_5	50%wtGVL[c]	598/35/1.2[g]	-	72	28	-	54[h]	2	6	35	-
4	Pd(0.1%)/Nb_2O_5	50%wtGVL[c]	598/35/1.2[e]	-	79	21	-	65	3	6	22	-
5	Pd(0.1%)/Nb_2O_5	50%wtGVL[c]	598/35/1.2[g]	-	95	5	-	92	-	1	5	-
6	Pd(0.1%)/Nb_2O_5	50%wtGVL[c]	623/35/0.1[g]	-	81	19	-	6	57[i]	12	6	7
7	$Ce_{0.5}Zr_{0.5}O_2$	Pure PA	698/20/1.1	-	86	14	-	1	82	11	3	3
8	$Ce_{0.5}Zr_{0.5}O_2$	Organic layer from entry 5	698/20/1.1	-	91	9	-	-	84	8	1	6

[a] C distribution % for a phase i is calculated as (moles of carbon detected in phase i divided by the sum of moles of carbon detected in the three phases) x 100. [b] C selectivity % for a product i is expressed as (moles of carbon as product i divided by the sum of moles of carbon for all the detected products) x 100. C_9=O: 5-nonanone; CO_x: CO and CO_2; C_4: n-butane; C_5: n-pentane; C_6-C_7 Ket.: 2-hexanone and 3-heptanone. [c] Aqueous solutions. [d] 4-hydroxypentanoic acid (3%) and 1,4-pentanediol (1%) accounted for the rest of carbon. [e] H_2 co-feed at 100 sccm. [f] Methane (4%) accounted for rest of carbon. [g] H_2 at 25 sccm and He at 25 sccm co-feed. [h] nonane (1%) and 1-pentyl pentanoate (2 %) accounted for rest of carbon. [i] Nonane (7%) and unidentified products (5%) accounted for rest of carbon.

6.5 Increasing Hydrothermal Stability of Niobia: Silica-Modified Niobia

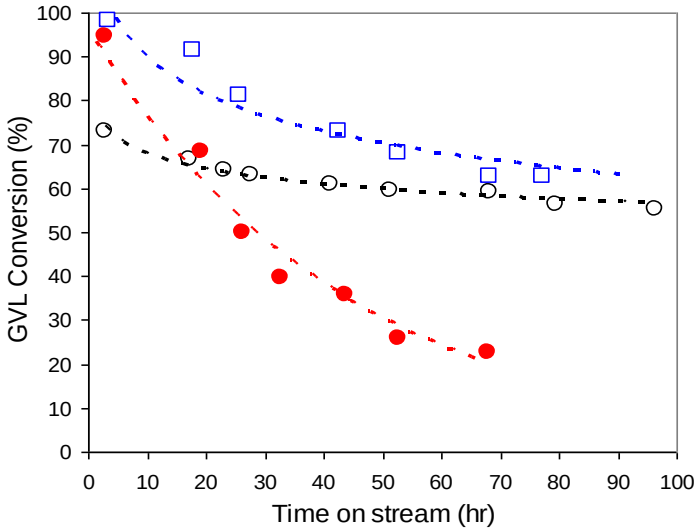

Figure 6.2. GVL conversion as a function of time on stream for a 50 wt% GVL in water feed at 573 K, 35 bar, WHSV=3.1 hr^{-1} and co-feed of both H_2 and He at 25 ml/min for the three niobia-supported Pd catalysts: (●) Pd(1%)/HY-340; (○) Pd(1%)/Nb-Si Oxide_ANO; (□) Pd(1%)/ Nb-Si Oxide_ETO.

A limitation of using commercial niobia (HY-340 supplied by CBMM) is that it transforms from an amorphous to a crystalline phase (*TT*-phase) under hydrothermal conditions, leading to a decrease in the surface area and catalytic activity.(5) This is consistent with our observation that the activity of the Pd(1%)/HY-340 catalyst decreases continuously with time on stream for the production of pentanoic acid from GVL(Figure 6.2). Surface area measurement using N_2 sorption reveals that the surface area of Pd(1%)/HY-340 before reaction was 150 m^2/g, which decreases drastically to 8 m^2/g after 68 hours on stream (Table 6.2). Thus, the synthesis of hydrothermally stable and catalytically active niobia with high surface area is essential in the development of more efficient catalytic systems for the production of pentanoic acid and in general, aqueous processing of biomass-derived molecules.

One approach that has been demonstrated to be effective in improving the hydrothermal stability of classical supports, such as silica, consists of doping the material with small amounts of alumina or zirconia, which assists to stabilize the silica framework under the hydrothermal conditions. (13) Following this approach, small amounts of silica (5%) were incorporated into niobia to prepare mixed oxides, which were then used to prepare supported Pd catalyst. The synthesis procedure is outlined in Chapter 2. Briefly, the sample prepared using ammonium niobium oxalate and sodium silicate is denoted Pd/ANO, while the sample prepared using tetraethyl orthosilicate (TEOS) as the silicon source and niobium(V) ethoxide ($Nb(EtO)_5$) (ETO) as the niobium source is denoted Pd/ETO.

In Figure 6.2, it can be seen that both Pd/ANO and Pd/ETO clearly demonstrated improved stability with time on stream compared to Pd/HY-340. The Pd/ANO showed lower initial activity compared to that of Pd/HY-340 and Pd/ETO. However, both catalysts supported on silica-modified niobia showed less severe deactivation with time on stream. After a slow initial deactivation during the first 15 h of reaction, the Pd/ANO catalyst showed remarkable stability for almost 100 h on stream (GVL conversion decreased to 55.5% from 64.2%). The tread of activity change can be partly rationalized by the less extent of surface area loss of the silica-modified niobia support. As shown in Table 6.2, Pd(1%)/ETO retained a surface area of 30 m^2/g after 80 hours on stream while the surface area of Pd(1%)/ANO was 31 m^2/g after nearly 100 hours on stream. The substantially lower surface area and acid site density per weight of catalyst of Pd(1%)/ANO is also consistent with the lower initial activity of this catalyst.

Table 6.2. Surface area and acid sites density of niobia-supported Pd catalysts (determined by NH_3-TPD)

Catalyst	Surface Area m^2/g		Acid Site Density μmol/g		Acid Site Density μmol/m^2	
	Fresh	Spent	Fresh	Spent	Fresh	Spent
Pd(1%)/HY-340	150	8	213	76	1.4	9.5
Pd(1%)/ETO	112	30	221	135	2.0	4.5
Pd(1%)/ANO	81	31	90	98	1.1	3.2

Besides loss of surface area due to crystallization of the niobia support, another potential mode of deactivation of the all the three types of bifunctional Pd/Nb_2O_5 catalysts involves the sintering of Pd nanoparticles at elevated temperatures in reducing atmosphere. The sintering of Pd nanoparticles can be monitored by chemisorption technique. CO is selected as the chemisorption probe molecule since another commonly employed probe molecule, H_2, is known to form bulk hydride with Pd (i.e., $PdH_{0.6}$)and complicates the choice of chemisorption stoichiometry and data analysis.(14)

Table 6.3. CO chemisorption for the niobia-supported Pd catalysts

Catalyst	CO uptake mmol/g		Dispersion %		Calculated particle size nm	
	Fresh	Spent	Fresh	Spent	Fresh	Spent
Pd(1%)/HY-340	0.014	0.004	15.3	4.4	7.2	25
Pd(1%)/ETO	0.017	0.005	17.9	5.8	6.1	19
Pd(1%)/ANO	0.016	0.006	17	6.4	6.5	17

The density of surface adsorption sites and Pd dispersion for three catalysts prior to and post reaction are compiled in Table 6.3. All three catalysts showed significant decrease in CO uptake after reaction, indicating increase of Pd particle size. Pd dispersions were calculated on

the basis of a Pd/CO stoichiometry of 2:1. The Pd particle sizes can also be calculated from dispersion values using the following formula.(15)

$$\text{Dispersion}\,(\%) = \frac{\text{moles of surface atom}}{\text{moles of total atom}} \times 100\%$$

$$\text{d}\,(\text{nm}) = \frac{1.1\,(\text{nm})}{\text{Dispersion}}$$

The particle sizes so calculated are summarized in Table 6.3.

Independently, the Pd particle size distribution was also studied by HAADF-STEM and HRTEM (Figure 6.3-6.5). No discernible Pd nanoparticles were observed in the freshly prepared Pd/HY-340 catalyst (Figure 6.3 a-b), indicating that the Pd nanoparticles were well-dispersed in this sample. However, after the GVL reaction, the Pd nanoparticles were found to have aggregated to form larger particles (Figures 6. 3 c-d). The same trend was observed for Pd/ETO, where Pd was well-dispersed initially and no particles could be discerned (Figure 6.4 a-b) but after reaction the particle size also increase in (Figure. 6.4 e-f). In contrast to Pd/HY-340, a significant fraction of the Pd particles in Pd/ETO remained small and well-dispersed after reaction (Figure 6.4 c-d), particularly those found in the region of the niobia support that still remained amorphous after reaction. In the case of Pd/ANO, Pd particles were observed in the freshly-prepared catalyst (Figure 6.5 a-b), indicating that the Pd nanoparticles were larger in this material (>5 nm) compared to Pd/HY-340 and Pd/ETO. However, it is remarkable that the growth of Pd particles after reaction was not as significant as on the other supports, as a large fraction of them remained well-dispersed in the amorphous niobia region (Figure 6.5 c-d).

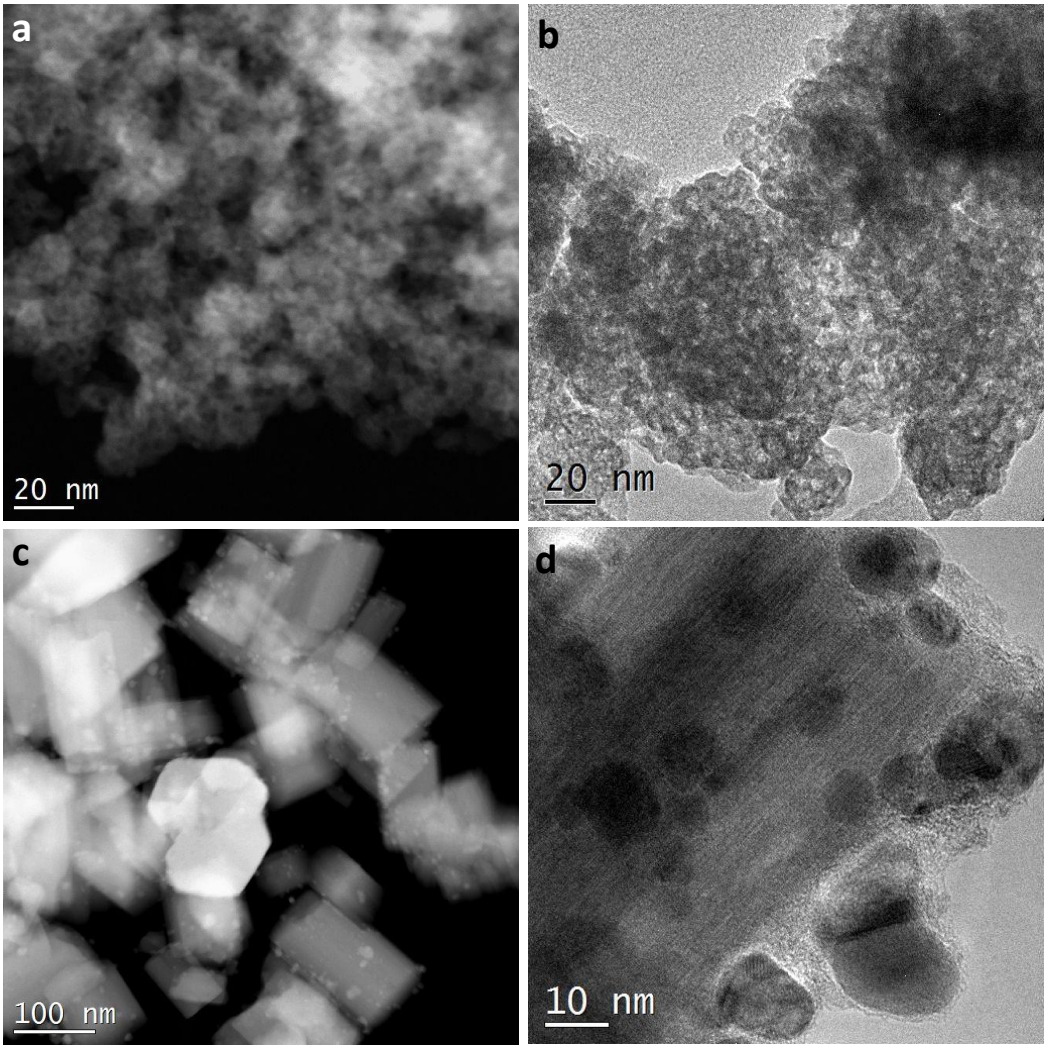

Figure 6.3. HAADF image a) and HRTEM image b) of 1 wt% Pd/HY-340, as-prepared, with well-dispersed Pd nanoparticles (not visible). After GVL reaction, HAADF image c) and HRTEM image d) show that Pd nanoparticles have sintered to form larger particles and the support has transformed from mesoporous, amorphous niobia into crystalline Nb_2O_5

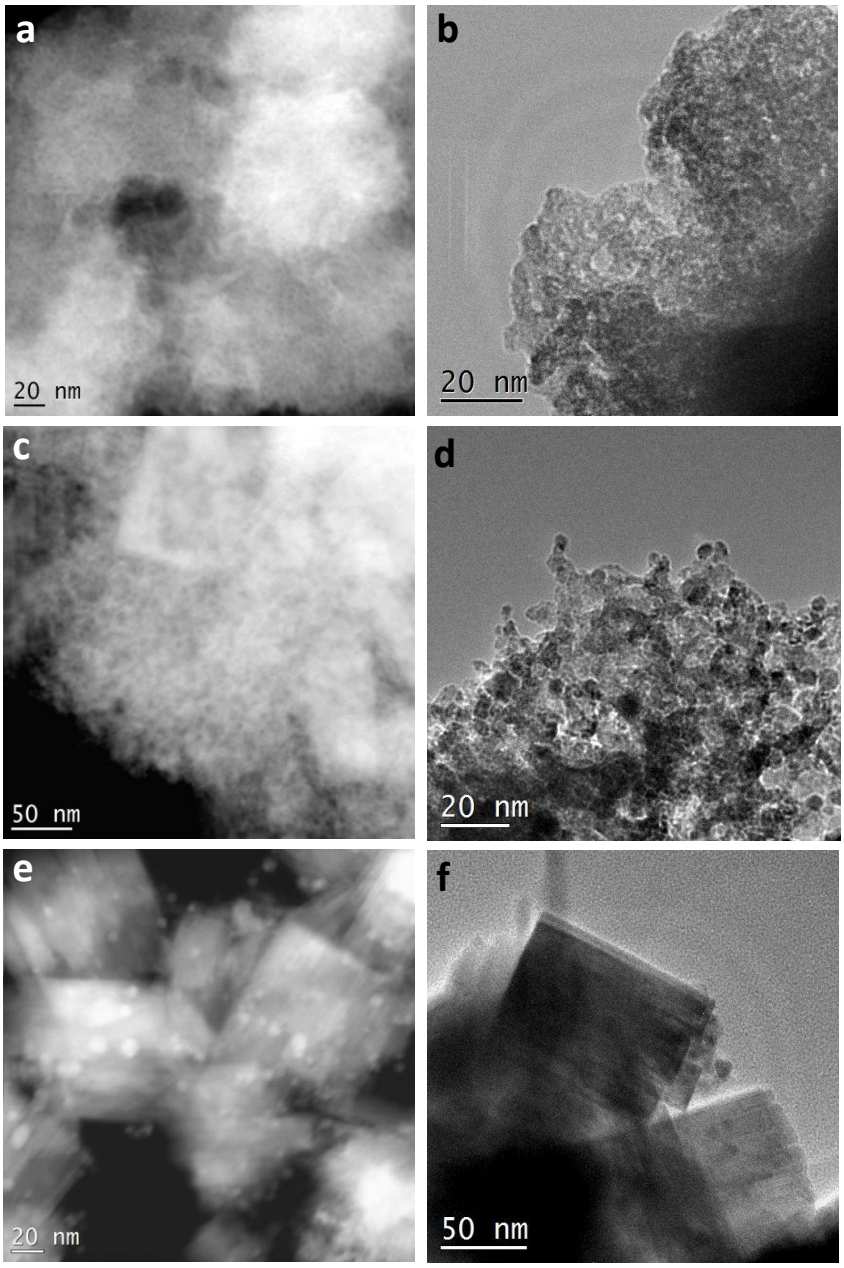

Figure 6.4. a) HAADF image and b) HRTEM image of 1 wt% Pd/ETO, as-prepared, with well-dispersed Pd nanoparticles (not visible). After GVL reaction, c) and e) HAADF image, d) and f) HRTEM images show the presence of Pd nanoparticles and two morphologies of niobia: mesoporous amorphous niobia (c-d) and crystalline niobia (e-f).

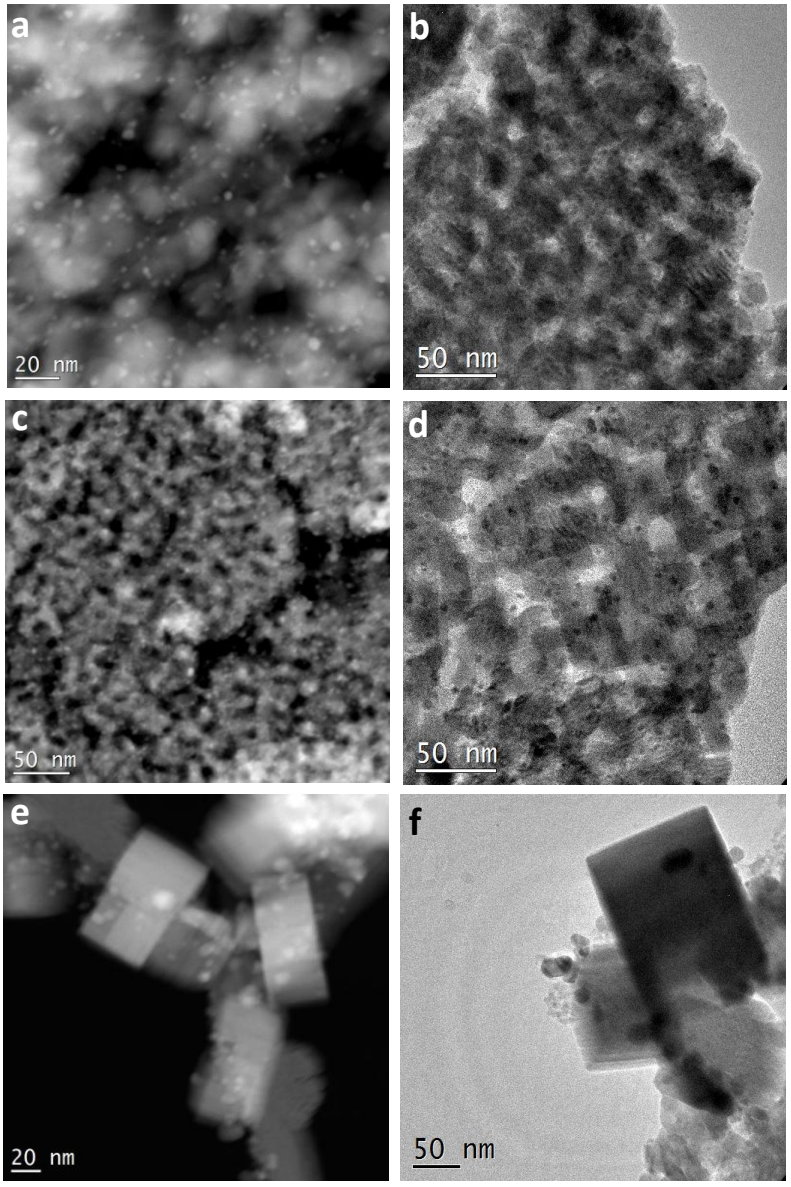

Figure 6.5. a) HAADF image b) HRTEM image of 1 wt% Pd/ANO, as-prepared, with small, dispersed Pd nanoparticles. After GVL reaction, c) and e) HAADF image, d) and f) HRTEM images show the presence of Pd nanoparticles and two morphologies of niobia: mesoporous amorphous niobia (c-d) and crystalline niobia (e-f).

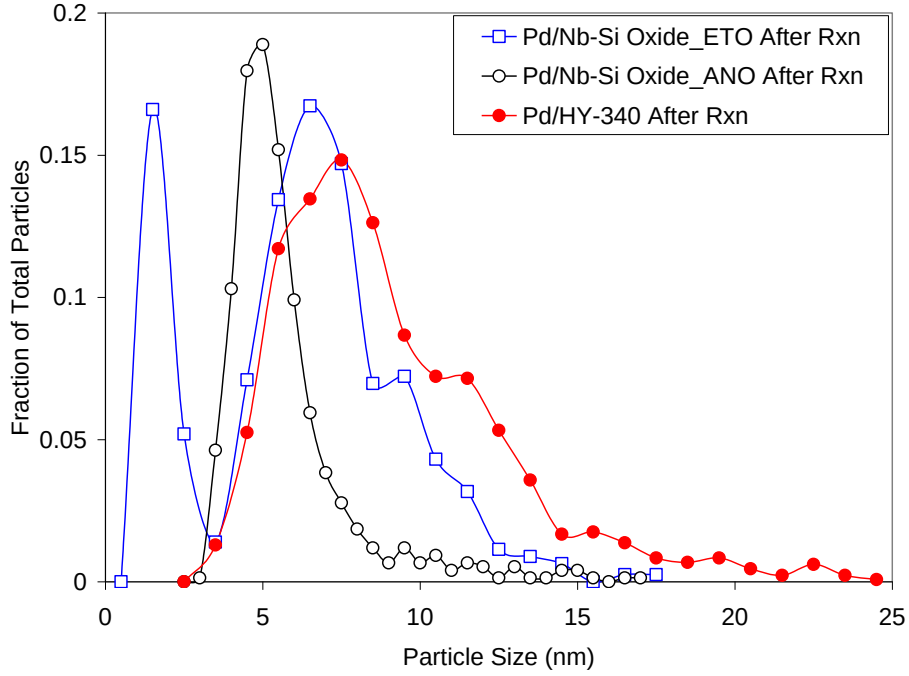

Figure 6.6 Pd particle size distributions for the three niobia-supported Pd catalysts after GVL reaction.

Figure 6.6 summarizes the particle size distribution as measured by TEM. Surface average diameters are 12 nm, 8.6 nm and 7.9 nm for the Pd/HY-340, Pd/ETO and Pd/ANO samples, respectively. Comparing results from Figure 6.6 and Table 6.2 suggests a correlation between the extent of hydrothermal Nb_2O_5 crystallization and Pd sintering. Specifically, the number of Pd particles with size larger than 10 nm followed the trend: Pd/HY-340 > Pd/ETO > Pd/ANO, which is in good agreement with the trend for extent of surface area loss observed for these samples (Table 6.2). Interestingly, Pd/ETO shows a bimodal particle size distribution, indicating distinct extents of Pd sintering across different regions of the underlying niobia support. Combined with the observation that two morphologies of niobia exist on spent Pd/ETO catalyst, these results strongly suggest that Pd sintering is likely to be less severe in amorphous niobia regions where the structure is porous and open as compared to regions where the niobia

support is largely crystalline. Remarkably, the Pd/ANO catalyst does not exhibit a bimodal Pd particle size distribution, suggesting lower overall extent of crystallization of the niobia. Qualitatively, the Pd particle sizes determined by CO chemisoprtion (Table 6.3) agree well with the trends measured by TEM for these samples (Pd/HY-340 > Pd/ETO > Pd/ANO). However, we note that values obtained by CO chemisorption are consistently larger than those measured by TEM. This apparent discrepancy can be rationalized by possible encapsulation of Pd nanoparticle by the niobia support as it crystallizes and a potential strong-metal support interaction (SMSI) (16, 17) between Pd and niobia that might suppress CO chemisorption. Nevertheless, results obtained by N_2 sorption, CO Chemisorption and TEM clearly demonstrate that doping niobia with small amount of silica leads to lower extent of surface area loss of the niobia support as well as sintering of the supported Pd nanoparticles, thus improving the stability of the bifunctional niobia-supported Pd catalyst under hydrothermal conditions. The mechanism for surface area stabilization due to added silica is not yet fully understood. It has been reported that niobia-silica microporous membranes show improved hydrothermal stability compared to silica membranes.(18) It is also known that the presence of dopants in silica can cause an increase in the viscosity of the silica.Therefore it is suggested that the addition of small amounts of silica (e.g. 5 wt%) retards the diffusive transport of niobia, thereby inhibiting crystallization of niobia.

The control over Pd sintering, which affects the reactivity, is strongly affected by the nature of the niobia (amorphous or crystalline) on which Pd is located. It appears that crystallization of niobia induces Pd sintering and encapsulation, both of them leading to loss of activity, as in the case of Pd/HY-340. However, it has been demonstrated in Chapter 4 that the

acid-catalyzed ring opening of GVL to pentenoic acid is a reversible reaction. Hydrogenation to pentanoic acid (PA) is irreversible at the reaction conditions of the present study.(19) Consequently, irreversible hydrogenation of pentenoic acid achieves continuous shifting of the pentenoic acid/GVL equilibrium to the right. Based on this, we suspect that metal functionality is the limiting factor in this bifunctional reaction (although a minimum number of acid sites is necessary to initiate reaction). This conclusion is supported by examination of the number of acid sites on these samples (Table 6.2). The samples that showed the highest stability, Pd/ANO, did not lose any acid sites, but did suffer a loss in GVL reactivity as well as CO chemisorption uptake. And the sample that lost 90% of its GVL reactivity, Pd/HY-340, only lost 65% of its acid sites, and its acid site density per unit surface area actually increased with time on stream.

6.6 Increasing Hydrothermal Stability of Niobia: Atomic Layer Deposition of Niobia on SBA-15

Taken alone, neither niobia nor silica possesses good hydrothermal stability. However, in section 6.5, we have successfully demonstrated that doping commercial niobia (HY-340) with small amount of silica produces a material with superior hydrothermal stability. Therefore, the fundamental message emerges from this approach seems to be that the formation of Si-O-Nb bond during the synthesis of the silica-modified niobia imparts extraordinary resistance against hydrothermal conditions. Indeed, it has been reported that the siloxane bridge (Si-O-Si) as well as surface silanol groups (-OH) are weak links most susceptible to hydrolytic attack by water.(20, 21) In this section, we describe a facile one-pot coating method for the synthesis of mesoporous niobia employing atomic layer deposition (ALD) of niobia within the pores of a mesoporous silica scaffold, SBA-15. The application of atomic layer deposition with selected precursors offers atomic-level control over the composition and structure of the surface niobium oxide

species created. The self-limiting nature of the gas-phase reactions occurring during ALD allows for the uniform coating of all exposed surfaces of SBA-15 with monolayer thickness control. (22) (23)Details on synthesis procedure can be found in Chapter 2.

Although ALD adopts alternating precursor pulses to ensure self-limiting growth mode, one ALD cycle does not necessarily lead to the formation of a monolayer of the coating material on the substrate. The surface coverage resulting from a single ALD cycle on a high surface- area, nanoporous support depends on a number of kinetic, geometric, and thermodyamic parameters, including (i) the ALD conditions used (temperature, flow, time of exposure, specific reactor configuration); (ii) the reactivity of the metal precursor toward the support surface; (iii) the diffusion coefficient and size of the precursor molecule; (iv) the surface area, particle size, and pore size of the support. Ultimately, the saturated (maximum) growth rate per ALD cycle is constrained by geometric factors including density of surface anchoring sites and the projected size of the metal precursor. (24, 25)

It is expected that optimum hydrothermal stability of the mesoporous niobia material will be achieved when all the exposed surface silanol -OH groups on the silica scaffold are capped by niobia precursor to form the more stable Si-O-Nb bond. Hence, it is crucial to establish upfront the number of niobia ALD cycles required to form a monolayer of niobia. FTIR was used to monitor the progressive consumption of surface silanol groups after 1, 10, 19, and 30 ALD cycles, denoted as SBA-15-ALD-y, with y being the number of ALD cycles used to synthesize the material (Figure 6.7).

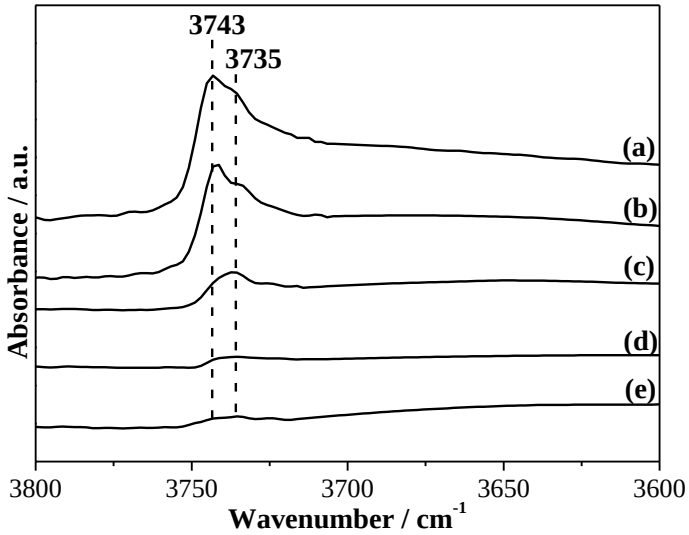

Figure 6.7. FTIR spectra of (a) SBA-15, (b) SBA-15-ALD-1, (c) SBA-15-ALD-10, (d) SBA-15-ALD-19 and (e) SBA-15-ALD-30.

In the region between 3800 and 3600 cm^{-1}, the FTIR spectrum of SBA-15 (Figure 6.7 a) is characterized by a band at 3743 cm^{-1} due to isolated silanol groups and a band at 3735 cm^{-1} attributed to weakly perturbed silanol groups.(26) A small decrease in the silanol bands is observed in the spectrum for SBA-15-ALD-1 (Figure 6.7 b) due to reaction of these groups with the niobium precursor. After 10 ALD cycles (Figure 6.7c), almost all the silanol groups have reacted. At this point, it is possible that a monolayer of niobium oxide is formed and that the remaining silanols could be located in the defects of this monolayer. The silanol band decreases further after 19 ALD cycles (Figure 6.7d). The remaining silanol groups are probably unavailable for reaction (in blocked defects or micropores), because no additional decrease in the surface silanol IR band is observed in the sample after 30 ALD cycles (Figure 6.7e).

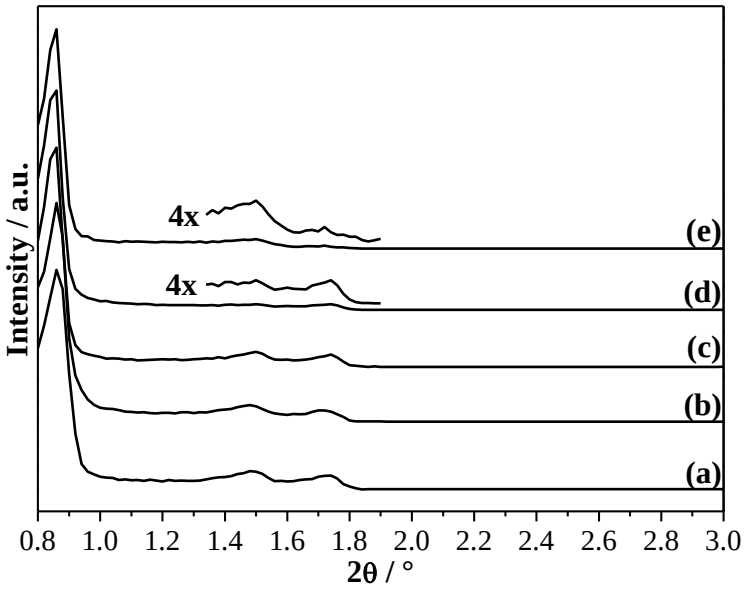

Figure 6.8. X-ray diffraction for (a) SBA-15, (b) SBA-15-ALD-1, (c) SBA-15-ALD-10, (d) SBA-15-ALD-19 and (e) SBA-15-ALD-30.

XRD patterns were collected to confirm the initial formation of the SBA-15 structure and to study the stability of this structure after ALD cycles (Figure 6.8). The structure of SBA-15 displays hexagonal P6mm symmetry (ref), and thus, three characteristic XRD peaks due to the (100) (most intense), (110), and (200) planes are expected at relative 2θ values of X,(√3)X and 2X, respectively.(27) The XRD pattern of the SBA-15 synthesized in this work (Figure 6.8 a) showed all three expected peaks, confirming the formation of the structure. Importantly, after the ALD cycles, the same XRD pattern (Figure 6.8 b-e). However, the relative intensities of the (110) and (200) peaks with respect to the (100) peak decrease, mainly for SBA-15-ALD-19 and SBA-15-ALD-30, due to the formation of niobia layers over the silica walls. Schuth and co-workers reported that for materials with the same unit cell parameter, increasing wall thickness leads to a decrease in the relative intensity of the (110) and (200) peaks. No further XRD peaks were

observed for SBA-15 or SBA-15- ALD samples at $2\theta > 3^{o}$, indicating no crystalline phase formation.

Table 6.4. Chemical composition, surface area and porosity properties of SBA-15 and SBA-15-ALD-y materials.

Sample	Nb_2O_5[a]	S_{BET}[b]	Expected S_{BET}[c]	S_{Microp}[d]	V_P	$V_{P\text{-}Microp}$[d]	D_P[e]	W[f]	Nb_2O_5 thickness
	[mol %]	[m^2g^{-1}]	[m^2g^{-1}]	[m^2g^{-1}]	[cm^3g^{-1}]	[cm^3g^{-1}]	[nm]	[nm]	[nm]
HY-340	100	118	-	-		-	-	-	-
SBA-15	-	930	930	162	1.11	0.078	6.49	5.36	-
SBA-15-ALD-1	3.30	671	687	90	0.78	0.034	5.80	6.05	0.35
SBA-15-ALD-10	16.8	326	351	0	0.46	0	5.60	6.25	0.45
SBA-15-ALD-19	22.2	246	247	0	0.32	0	4.75	7.10	0.87
SBA-15-ALD-30	32.3	126	142	0	0.14	0	3.74	8.11	1.38

[a] Determined by ICP-AES analysis. [b] BET specific surface area [c] Expected BET specific surface area based on the measured weight gain and reduction of pore diameter as niobia is deposited. [d] Micropore surface area and volume determined by the t-plot method. [e] Calculated by BJH method. [f] Wall thickness determined by a_0-D_P.

Measurements of N_2 physisorption were conducted to monitor the evolving structural properties of SBA-15-ALD-*y* materials at various niobia loadings. Table 6.4 summarizes the compositional and structural properties of these materials. As expected, the loading of niobium (measured by ICP-AES) increasing with number of ALD cycles, while the surface area (determined by BET equation) and diameter and volume of the mesopores (determined by BJH model) and micropores (determined by t-plot) decrease as more niobia is deposited. The "expected surface areas" after the niobia depositions were calculated based solely on geometric considerations of surface area reduction due to reduction of pore diameter, assuming that the growth of niobia layer follows the cylindrical shape of the pores of SBA-15. The values obtained are in good agreement with experimental measurements (Table 6.4), suggesting the growth of niobia layer is likely to be conformal.

For SBA-15-ALD-10, the pore diameter was 5.60 nm, which suggests an increase of 0.89 nm in the SBA-15 wall thickness due to the niobia layer. According to previous studies, the

density of niobium atoms in a monolayer covering amorphous silica is 6.3 niobium atoms/nm^2. For SBA-15-ALD-10, it was determined that the density of the deposited layer is 6.4 niobium atoms/nm^2. Shirai, et al.(28) studied the niobium oxide bond on a silica surface and determined bond lengths for the species at the interface between the silica and the niobium oxide. According to the bond length values, a monolayer of niobia would have a thickness of approximately 0.4 nm and hence, for a monolayer of niobia in a SBA-15 channel, this would suggest a reduction of 0.8 nm in the pore diameter. Furthermore, Du, et al. estimated a 0.7 nm increase in the wall thickness due to the formation of a monolayer of vanadium oxide grafted on SBA-15. This value is relatively close to the one found for SBA-15-ALD-10, considering the difference in the bond length and in the methods used for pore size determination. Combing results from FTIR measurements, it is thus concluded that a complete monolayer of niobia was formed for the SBA-15-ALD-10 sample. For SBA-15-ALD-19 and SBA-15-ALD-30, the pore diameters were 4.75 and 3.74 nm, respectively. The niobia layer thicknesses for these materials correspond to 0.87 and 1.38 nm, representing the deposition of 2 and 3 monolayers, respectively.

SBA-15-ALD-19 was further supported with Pd nanoparticles to study its activity and hydrothermal stability for the conversions of GVL to pentanoic acid. Figure 6.9 shows the conversion of GVL versus time-on-stream for Pd impregnated on SBA-15-ALD-19 and on HY-340. It is evident that the Pd/SBA-15-ALD-19 catalyst showed superior stability for at least 70 hours of time-on-stream.

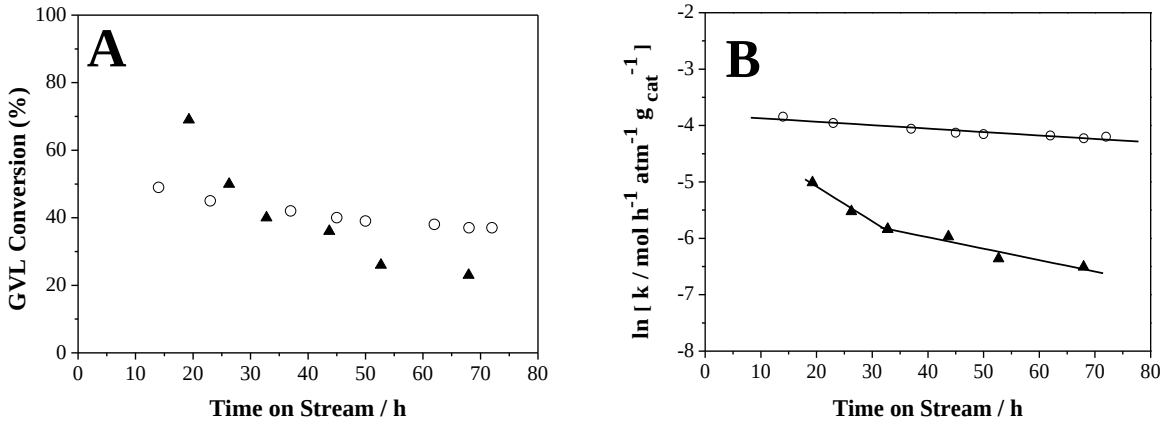

Figure 6.9. (A) GVL conversion as a function of time-on-stream for (▲) Pd/ HY-340 at 573 K and 35 bar, WHSV 3 h^{-1} and (○) Pd/ SBA-15-ALD-19 at 573 K and 35 bar, WHSV 17 h^{-1}. (B) Estimation of deactivation rate constants assuming pseudo first-order reaction (with a rate constant, k) and first-order deactivation for (▲) Pd/ HY-340 and (○) Pd/ SBA-15-ALD-19.

Deactivation rate constants were obtained from the data of Figure 6.9 to provide a quantitative comparison of the rate of deactivation between these two catalysts. The GVL conversion was modeled as a pseudo first-order reaction and the reactor as an integral packed bed plug flow reactor. The decay in catalytic activity was described by a first-order exponential law. The deactivation rate constant, k_d, can be determined from the slope of the straight line when ln (*k*) is plotted against *t*, where *k* is the pseudo first-order rate constant with units of mol h^{-1} atm^{-1} g_{cat}^{-1} and *t* represents time on stream in hours, as shown in Figure 6.9B. It can be seen from Figure 6.9B that Pd/HY-340 exhibited rapid deactivation during the initial 32 hours on stream, followed by a stage where the activity decreased less steeply. The values of deactivation constants for both stages are 0.0597 and 0.0203 h^{-1}, respectively. In contrast, the Pd/SBA-15-ALD-19 catalyst showed a substantially slower deactivation over the entire time-on-stream period investigated, giving a deactivation constant of 0.0061 h^{-1}.

6.7 Conclusion

In this Chapter, we first demonstrated that a concentrated aqueous stream of gamma-valerolactone (GVL) can be obtained by hydrogenation of levulinic acid in aqueous solution over Ru/C with almost quantitative yield. The GVL can then be ring opened and hydrogenated over a bifunctional Pd/Nb_2O_5 catalyst to afford pentanoic acid. In contrast to the formation of butene via decarboxylation of GVL / pentenoic acid as described in Chapter 3, 4 and 5, hydrogenation of the pentenoic acid intermediate to form the saturated pentanoic acid preserves the two oxygen atoms in the feed molecule, which allows the coupling of two pentanoic acid molecules via efficient ketonization reaction to form a C_9 ketone. Hence, work presented this chapter further expands the possible pool of molecules that can be efficiently derived from the GVL, thus increasing the processing flexibility of this important platform chemical. It is also shown in this chapter that improvements in the hydrothermal stability of the niobia support for the Pd/Nb_2O_5 catalyst can be achieved by addition of small amounts of silica, which retards crystallization of the niobia support and indirectly, the sintering of the Pd particles, leading to catalysts with superior stabilities under hydrothermal reaction conditions. Realizing the beneficial effect of the Si-O-Nb linkage for the stability of niobia, atomic layer deposition was used to synthesize a new class of mesoporous niobia that combines the highly-ordered porous structure of SBA-15 with the surface properties of niobia, which also demonstrates excellent hydrothermal stability for the production of pentanoic acid from GVL. These results have important implications for the development of catalysts for biorenewable conversions that operate under aqueous conditions at elevated temperatures.

6.8 References

1. E. L. Kunkes, D. A. Simonetti, R. M. West, J. C. Serrano-Ruiz, C. A. GÃ¤rtner and J. A. Dumesic, *Science*, 2008, 322, 417-421.
2. J. C. Serrano-Ruiz and J. A. Dumesic, *ChemSusChem*, 2009, 2, 581-586.
3. J. C. Serrano-Ruiz and J. A. Dumesic, *Green Chemistry*, 2009, 11, 1101.
4. J.-P. Lange, R. Price, P. M. Ayoub, J. Louis, L. Petrus, L. Clarke and H. Gosselink, *Angewandte Chemie International Edition*, 49, 4479-4483.
5. I. Nowak and M. Ziolek, *Chemical Reviews*, 1999, 99, 3603-3624.
6. B. V. Timokhin, V. A. Baransky and G. D. Eliseeva, *Russian Chemical Reviews*, 1999, 68, 73-84.
7. P. M. A. and J. P. Lange, *Shell Internationale.*, WO 2008/142127
8. H. Mehdi, V. r. FÃ¡bos, R. b. Tuba, A. Bodor, L. s. T. Mika and I. n. HorvÃ¡th, *Topics in Catalysis*, 2008, 48, 49-54.
9. L. E. Manzer, *Applied Catalysis A: General*, 2004, 272, 249-256.
10. W. F. Maier, W. Roth, I. Thies and P. V. R. Schleyer, *Chemische Berichte*, 1982, 115, 808-812.
11. J. A. Dean, in *Lange's Handbook of Chemistry, 15th edition*, McGraw-Hill,, 1999, vol. section: 1.292.
12. M. Renz, *European Journal of Organic Chemistry*, 2005, 2005, 979-988.
13. M. T. Bore, R. F. Marzke, T. L. Ward and A. K. Datye, *Journal of Materials Chemistry*, 2005, 15, 5022-5028.
14. N. K. Nag, *The Journal of Physical Chemistry B*, 2001, 105, 5945-5949.
15. M. A. Vannice, *Kinetics of Catalytic Reactions* Springer, 2005 edition.
16. T. Uchijima, *Catalysis Today*, 1996, 28, 105-117.
17. F. B. Noronha, M. Schmal, M. Primet and R. Frety, *Applied Catalysis*, 1991, 78, 125-139.
18. V. Boffa, D. H. A. Blank and J. E. ten Elshof, *Journal of Membrane Science*, 2008, 319, 256-263.
19. J. Q. Bond, D. Martin Alonso, R. M. West and J. A. Dumesic, *Langmuir*, 26, 16291-16298.
20. E. A. Sosnov, A. A. Malkov and A. A. Malygin, *Russian Journal of General Chemistry*, 80, 1176-1182.
21. Evgeni A Sosnov, *Russian Chemical Reviews*, 79, 907.
22. J. W. Elam, D. Routkevitch, P. P. Mardilovich and S. M. George, *Chemistry of Materials*, 2003, 15, 3507-3517.
23. M. Leskelo¤ and M. Ritala, *Thin Solid Films*, 2002, 409, 138-146.
24. R. L. Puurunen, *Chemical Vapor Deposition*, 2005, 11, 79-90.
25. R. L. Puurunen, *Chemical Vapor Deposition*, 2003, 9, 249-257.
26. J. M. R. Gallo, C. Bisio, G. Gatti, L. Marchese and H. O. Pastore, *Langmuir*, 26, 5791-5800.
27. P. Alexandridis, U. Olsson and B. r. Lindman, *Langmuir*, 1998, 14, 2627-2638.
28. M. Shirai, K. Asakura and Y. Iwasawa, *The Journal of Physical Chemistry*, 1991, 95, 9999-10004.

7. Selective Production of Aromatics from Alkylfurans over Solid Acid Catalysts

7.1 Introduction

Development of processes that convert biomass and biomass-derived molecules into bulk chemicals is essential to ensure continued supply of feedstocks for the chemical industry in an era of diminishing fossil fuel reserves.(1-4) In this respect, the production of key platform aromatic compounds, such as benzene, toluene and the xylenes (BTX compounds), has received increasing attention. (5-7) Interesting approaches have recently been demonstrated for the production of *p*-xylene.(8-11) Shiramizu and Toste reported the conversion of 2,5-dimethylfuran (DMF) and acrolein into terephthalic acid via a route consisting of Diels-Alder cycloaddition,(8) oxidation, dehydrative aromatization and decarboxylation. Williams et al. described the one-pot catalytic conversion of DMF and ethylene to *p*-xylene with good selectivity by combined cycloaddition and dehydration reactions over acidic zeolites, including H-Y, H-ZSM-5 and H-BEA.(9) Substituting DMF with 2-methylfuran (2-MF) or furan, which are also readily obtained from lignocellulosic biomass,(12-15) would allow for the production of toluene and benzene, respectively. However, the presence of substituent groups significantly affects the reactivity of furans towards the desired [4+2] cycloaddition reaction as well as competing side reactions, such as opening of the furan ring.(16-18) Therefore, a comparative study of substrates differing in the degree of substitution is necessary to provide insight into the essential factors that control the reactivity and selectivity of these systems to desired aromatic compounds. In addition, it is necessary to identify more active and selective catalysts to further improve the efficiency of BTX production.

In this chapter, we investigate the combination of cycloaddition and dehydration reactions between ethylene and furan, 2-MF or DMF for the selective production of BTX compounds. Reaction networks are proposed with key reaction intermediates identified for all three substrates. We show that acidic oxides such as tungstated zirconia (WO_x-ZrO_2) and niobic acid demonstrate superior activity and selectivity for the production of aromatics as compared to zeolites. A series of WO_x-ZrO_2 catalysts with different surface compositions are further investigated, and the observed catalytic properties suggest that the reason for the higher activity of these materials is at least partly associated with enhanced strength of the Brønsted acid sites

7.2 *Para*-Xylene Formation from 2,5-Dimethylfuran (DMF) and Ethylene

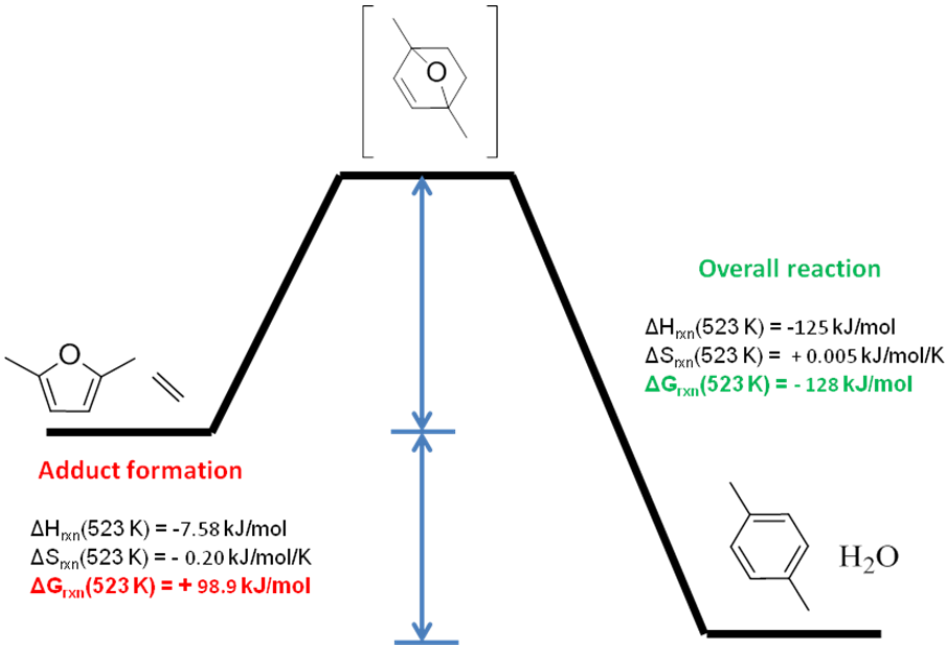

Scheme 7.1 Reaction scheme and thermochemistry (at 523K) for the conversion of 2,5-dimethylfuran DMF and ethylene to *p*-xylene

7.2.1 Activities of Selected Solid Acid Catalysts for *Para*-xylene Formation from DMF and Ethylene

The conversion of DMF to *p*-xylene by reaction with ethylene proceeds by initially forming a 7-oxabicyclo[2.2.1]hept-2-ene type adduct, as depicted in Scheme 7.1. The adduct is thermally unstable due to ring strain in the bicyclic system, and it decomposes into DMF and ethylene unless refrigerated conditions are maintained.(8, 19). In scheme 7.1, it can be seen that the Gibbs free energy for formation of the cycloadduct from DMF and ethylene is calculated to be +98.9 kJ/mol. However, significant decrease in free energy (enthalpy driven) for the aromatization of the cylcoadduct to produce *p*-xylene and water renders the thermodynamics favorable for the overall reaction, with a Gibbs free energy change of -128 kJ/mol. Hence, the strategy to obtain good *p*-xylene yield is through kinetic coupling of the two steps shown in Scheme 7.1 by use of an efficient catalyst to promote the dehydration step. Both Brønsted acid and Lewis acid catalysts have been demonstrate to promote the dehydrative aromatization of the cycloadduct.(20, 21)

Figure 7.1 shows the selectivity for the production of *p*-xylene from DMF measured at 523 K over seven solid acid catalysts at 60% DMF conversion. γ-Al_2O_3 and TiO_2, which possess predominantly Lewis acidity, exhibited low selectivity of 10% and 17% towards *p*-xylene, respectively. A homogenous Brønsted acid, trifluoroacetic acid (TFA), showed 40% selectivity to *p*-xylene. A selectivity of 40% was also obtained over amorphous SiO_2/Al_2O_3, which has both Brønsted and Lewis acid sites, but lacks a crystalline microporous structure. H-Y zeolite, which was studied as a catalyst for this reaction in a previous study(9), exhibited an increased selectivity of 52%. The *p*-xylene selectivity increased slightly to 57% over niobic acid, an amorphous acidic oxide. The highest selectivity was observed with tungstated zirconia (WO_x-

ZrO_2, calcined at 923 K), which displayed a remarkable selectivity of 77% towards the desired product. Major byproducts formed included 2,5-hexanedione, dimethyl-cyclohexenone and uncharacterized soluble oligomers.

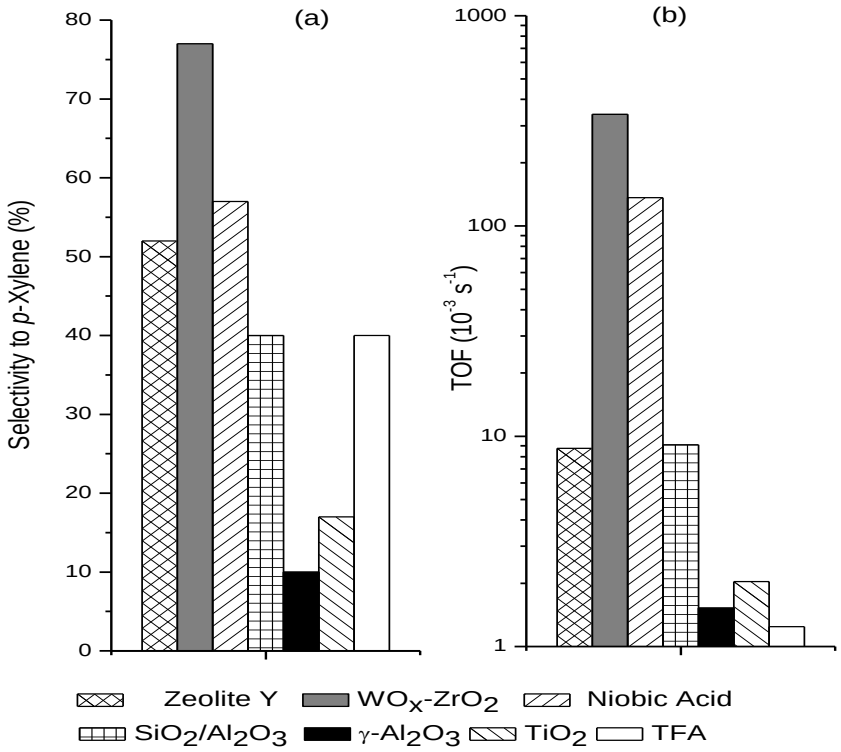

Figure 7.1 (a) Selectivity towards *p*-xylene, calculated at 60% DMF conversion, in the reaction with ethylene. (b)Turnover frequency (TOF) defined as the number of *p*-xylene molecules formed per Brønsted acid site (except for γ-Al_2O_3 and TiO_2) per second. TOF values are calculated at 25~30% DMF conversion.

The turnover frequency (TOF) for production of *p*-xylene on each catalyst was calculated by normalizing the rate by the number of acid sites, as determined by NH_3-TPD and FTIR spectroscopy of adsorbed pyridine (Table 7.1).

Table 7.1 Physiochemical properties and activity of catalysts.

Catalyst	$\rho_{Brønsted}$[a] (μmol g^{-1})	ρ_{Lewis}[a] (μmol g^{-1})	$S_2A.$ (m^2 g^{-1})	DMF Conv (%)	Sel to PX (%)	Sel to 2,5-HDO[b] (%)	Sel to DMCHO[c] (%)	Unidentified oligomers[d] (%)
γ-Al_2O_3	-	210	200	60	10	5	38	47
TiO_2 (P25)	-	40	50	60	17	6	23	54
SiO_2/Al_2O_3	546	136	450	60	40	7	5	48
Zeolite Y	692	132	732	60	52	6	13	29
WO_x-ZrO_2-923	72	46	116	60	77	5	7	11
Niobic Acid	51	77	118	60	57	11	11	21
TFA	8770	-	-	60	40	6	7	47

[a] The number of acid sites was determined by combining the total acid sites determined by NH_3-TPD and the Lewis/Brønsted acid ratio determined by FTIR spectroscopy of adsorbed pyridine. [b] 2,5-hexanedione. [c] 3,6-dimethyl-2-cyclohexenone [d] carbon loss

The Lewis acid sites on γ-Al_2O_3 and TiO_2 showed low selectivity and activity towards *p*-xylene production, with TOF values of 0.0015 s^{-1} and 0.0020 s^{-1} which are significantly lower than all other considered catalysts (panel b, Figure 7.1). Thus, it appears that Lewis acid sites are very inefficient at catalyzing the dehydrative aromatization compared to Brønsted acids, and the TOF values for aromatics production will be reported only with respect to the number of Brønsted acid sites. The TOF values for WO_x-ZrO_2 and niobic acid are 0.34 and 0.14 s^{-1}, respectively, which are substantially higher than the rates observed over zeolite Y and SiO_2/Al_2O_3 (0.0088 s^{-1} and 0.0090 s^{-1}). The effect of reaction temperature on the rate of *p*-xylene production from DMF and ethylene was investigated over WO_x-ZrO_2, which was the most promising catalyst identified (see Arrhenius plot in Figure 7.4). The rate of *p*-xylene formation increases monotonically with increasing temperature, which indicates that the promoting effect

of higher temperatures on the dehydration of the cycloadduct intermediate outweighs the lowering of the concentration of the adduct due to its thermal instability, within the considered temperature range (453 to 548 K). The apparent activation energy for *p*-xylene formation was determined to be 76 kJ mol^{-1}.

7.2.2 Catalyst Stability for *Para*-xylene Production

The stability of tungstated zirconia, niobic acid and zeolite Y was further investigated for *p*-xylene production from DMF and ethylene. The reactions were run to 60% DMF conversion over fresh catalysts. The spent catalysts were then recovered by centrifugation and washed with isopropanol before drying in an oven. Without further calcination, these catalysts were reused in the reaction for the same reaction time as the previous runs with the fresh catalysts. In a third run, spent catalysts from the second run were washed, dried and calcined under flowing air at 923 K for 3 h before they were reused in the reaction. As shown in Figure 7.3, zeolite Y deactivated significantly after the first run and simple washing was not able to recover its activity. In contrast, WO_x-ZrO_2 and niobic acid retained 83% and 60% of their initial activity, respectively. Upon high-temperature calcination, however, both zeolite Y and WO_x-ZrO_2 recovered essentially all of the catalytic activity, whereas niobic acid, known to crystallize and lose most of its surface area after high temperature treatment, became even less active (showing 15% of its initial activity). These results suggest that the mesoporosity of WO_x-ZrO_2 (Table 7.1) offers higher resistance to deactivation by carbon deposition compared to microporous materials such as zeolites, thus requiring less frequent regeneration in a continuous process.

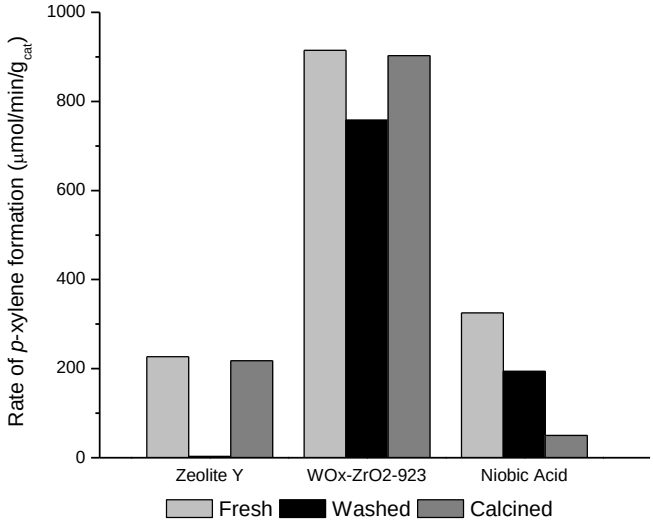

Figure 7.2 Stability of catalysts for *p*-xylene production in three consecutive recycle runs. Fresh: all three catalysts were subjected to 60% DMF conversion; Washed: catalysts were washed with isopropanol and dried before reuse; Calcined: catalysts were washed with isopropanol, dried and calcined in air for 3 hours at 923 K. The same reaction time was allowed in three runs for the same catalyst.

7.3 Toluene and Benzene Production from 2-Methylfuran and Furan

Substituting DMF with 2-MF or furan allows for the production of toluene and benzene, respectively. The combined reaction network for the conversion of all three substrates into aromatics is presented in Scheme 7.2.

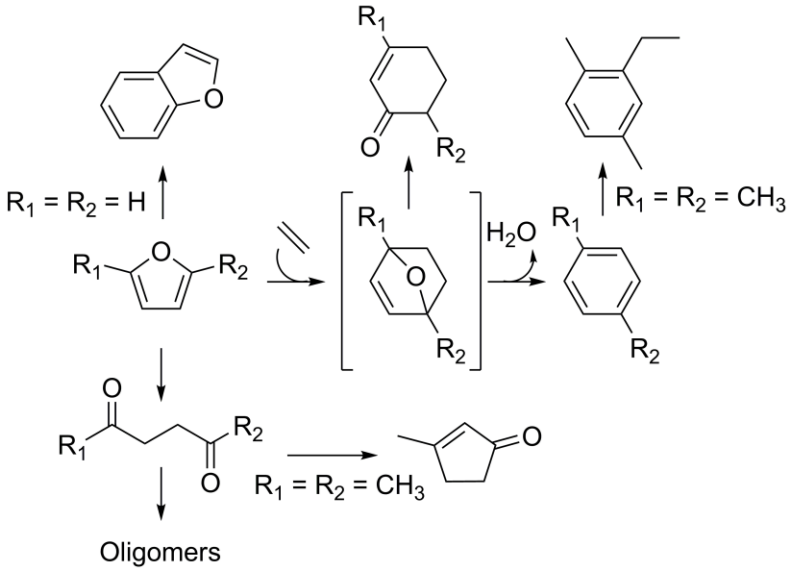

Scheme 7.2. Reaction network for the conversion of furanoic substrates to aromatics, where R_1 and R_2 are either -H or -CH_3.

It has been shown that the presence of methyl substituents enhances the reactivity of the furan ring towards [4+2] cycloaddition reactions.(18, 22) Furthermore, the methyl groups stabilize charged intermediates in the dehydration of the bicyclic adduct, thus facilitating the dehydration step.(21) Combining these effects, the overall production rate of aromatics is expected to decrease moving from two methyl substituents (DMF) to zero (furan). In addition, side reactions can take place that lower the selectivity to aromatic products, such as opening of the furan ring to form γ-dicarbonyl compounds and the subsequent degradation of these species, e.g., by oligomerization.(16, 23) Although the ring opening of DMF occurs more readily than either 2-MF or furan,(16, 18) the product, 2,5-hexanedione, is stable leading to an equilibrium situation (the diketone is observed with a yield of approximately 5% at 60% conversion). Intramolecular aldol reaction of 2,5-hexanedione yields 3-methyl-2-cyclopentenone, as observed in small quantities at high conversions. On the other hand, the ring opening products from furan and 2-MF are more reactive and are known to oligomerize rapidly,(16, 18) thereby lowering the

carbon balance. (Because of their high reactivity, these compounds were not observed in experiments starting from 2-MF or furan.) In addition to the desired dehydration reaction to produce the aromatic ring, the adduct can react through an isomerization step to form an unsaturated cyclohexanone. Formation of 1-ethyl-2,5-dimethylbenzene by alkylation of *p*-xylene with ethylene is also observed to small extents at high conversions. Finally, two furan molecules can undergo Diels-Alder cycloaddition to form benzofuran in the presence of solid acid catalysts, such as zeolites.(24)

Figure 7.3 shows the rates of formation of aromatics and major byproducts for reaction of ethylene with DMF, 2-MF and furan over zeolite Y, WO_x-ZrO_2, niobic acid and γ-Al_2O_3. The rate of aromatic production significantly decreases moving from two methyl substituents in DMF to zero in furan (left panel) over all four catalysts. In contrast, the formation rates of cyclohexenone-type compounds (middel panel) are highest for 2-MF, followed by DMF and furan. For both DMF and 2-MF, we suggest that the formation rate of the cycloadduct intermediate is sufficiently high to lead to high rates of aromatics production. The higher rate of cyclohexenone compound formation for 2-MF can be explained by its lower rate of aromatization due to the lower extent of alkyl substitution, as noted above. In the case of furan, the formation rate of the cycloadduct becomes the limiting factor, which leads to low rates for benzene and cyclohexenone formation. These trends suggest that the aromatics and cyclohexenones are formed via the same cycloadduct intermediate.

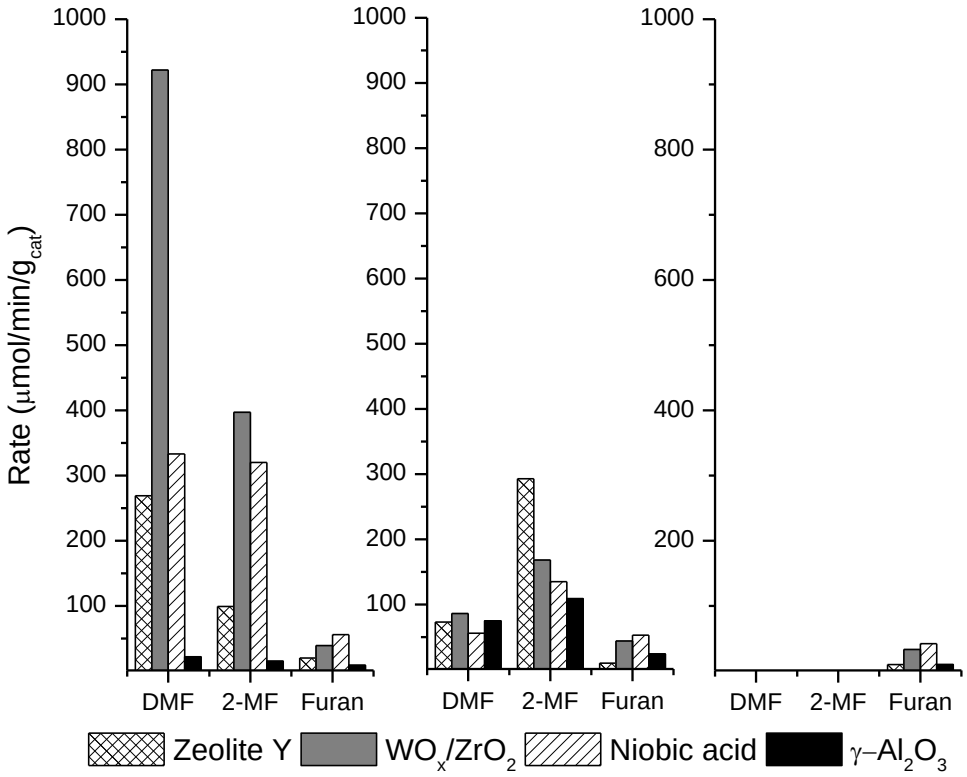

Figure 7.3 Formation rates of aromatics, cyclohexenone and benzofuran type compounds from different furanoic substrates. Left panel: rates for benzene, toluene and *p*-xylene formation; middle panel: rates for cyclohexenone type compunds; right panel: rates for benzofuran type compounds. (Reaction conditions: 10 wt% dienes in anhydrous hexadecane, 0.15 g catalyst, 523 K, 20 bar ethylene charged at 298 K in 50 mL batch reactor)

With DMF, the apparent activation energy for cyclohexenone formation was determined to be 56 kJ mol^{-1}, as compared to 76 kJ mol^{-1} for *p*-xylene formation (Figure 7.4).

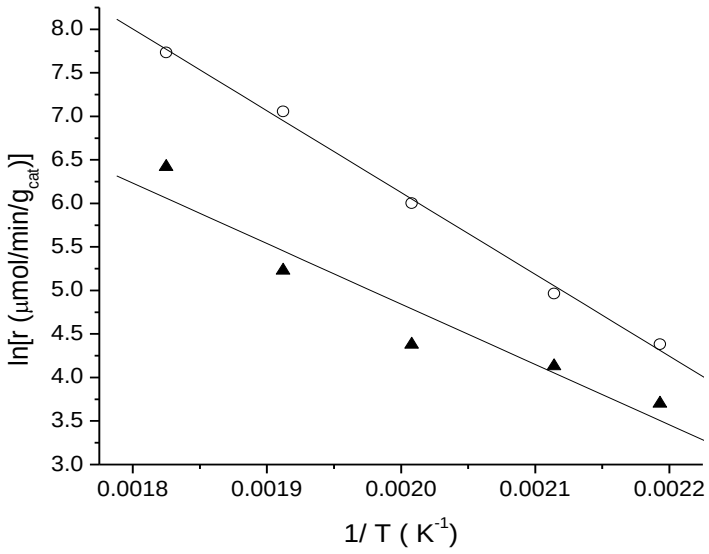

Figure 7.4 Effect of reaction temperature on the rates of p-xylene (○) and dimethylcyclohexenone (▲) formation over WO_X-ZrO_2-923. (Reaction conditions; 10 wt% DMF in anhydrous hexadecane, 0.15 g catalyst, 453 to 548 K,20 bar ethylene charged at 298 K in 50 mL batch reactor, DMF conversions < 35%)

Catalysts that are more active for DMF conversion also exhibit higher activity for conversion of 2-MF and furan, reflecting analogous reaction pathways for all three substrates, as depicted in Scheme 7.2. It is interesting to note that the rate of cyclohexenone formation (middle panel) is lower than dehydration over all catalysts except for γ-Al_2O_3. Since γ-Al_2O_3 only possesses Lewis acidity, this trend could suggest that the rearrangement reaction to form cyclohexenone derivatives is more effectively catalyzed by Lewis acid sites. It is possible that Brønsted acid sites catalyze dehydration of the adduct more efficiently, shifting the selectivity towards the dehydration direction when Brønsted acidity is introduced in addition to Lewis acidity. It is also observed that zeolite Y shows a higher rearrangement rate than dehydration.

Formation of benzofuran type compounds was not detected for DMF and 2-MF. However, when furan was reacted, it displayed similar rates for the formation of benzene, 2-cyclohexen-1-one and benzofuran. This result shows that the steric hindrance imposed by the substituent groups on the furan ring effectively prevents the coupling between furan rings to form benzofuran.

The high rates for production of aromatics observed with WO_x-ZrO_2 and niobic acid allow for efficient use of these catalysts. Interestingly, despite the fact that WO_x-ZrO_2 is significantly more active than niobic acid for *p*-xylene productions, the activities for production of toluene and benzene are similar, with niobic acid displaying a slightly higher activity than WO_x-ZrO_2 for benzene production. The conversions of DMF, 2-MF and furan were run to completion over the most active catalyst, WO_x-ZrO_2-923, and yields of 80%, 34% and 18% were obtained for *p*-xylene, toluene and benzene, respectively at 523 K and 20 bar ethylene charged at room temperature

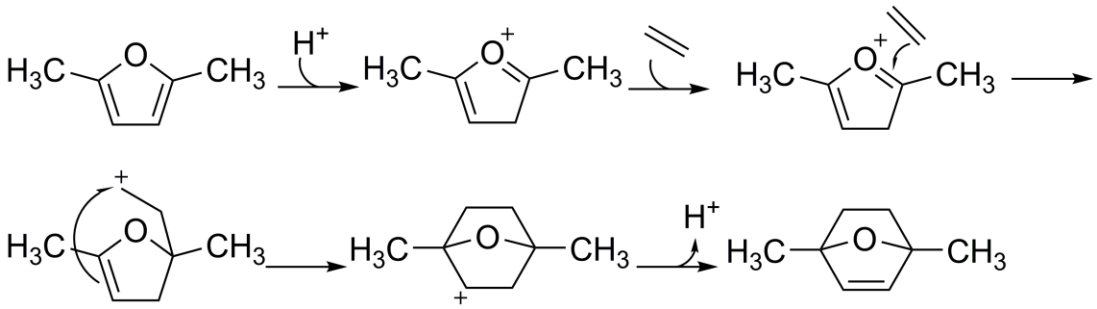

Scheme 7.3 Proposed reaction mechanism for the formation of a bicyclic adduct from DMF and ethylene catalyzed by Brønsted acids.

Our finding that the presence of Brønsted acidity is essential for dehydration of the adduct is consistent with previous reports using acidic zeolites.(9) It has been reported that the

formation of the bicyclic adduct is promoted by the confinement imposed by the microporous structure of zeolites, with the cage structure of zeolite Y giving the highest reaction rate.(9) Both niobic acid and WO_x-ZrO_2 exhibit enhanced activity towards *p*-xylene production compared to zeolite Y.(9) However, neither of these catalysts possesses a microporous structure. Furthermore, the TOF observed with SiO_2/Al_2O_3, which also lacks a microporous structure, is comparable to that of zeolite Y. Thus, the confinement effect does not seem to be a likely explanation in the present case. Instead, the higher rates over the WO_x-ZrO_2 and niobic acid catalysts could be caused by higher rates of dehydration over these materials. The reaction order with respect to ethylene partial pressure is essentially unity (i.e. 0.97) at 523 K within the pressure range studied (27 to 60 bar at 523 K). In contrast, the reaction order for DMF is 0.19, suggesting that the formation of the cycloadduct is also kinetically important. It is possible that this step is catalyzed by Brønsted acids as well, which relies on the ability of the catalyst to protonate the diene substrate as shown in Scheme 7.3. The adduct is then formed by a stepwise mechanism instead of the concerted mechanism of the Diels-Alder cycloaddition.

7.4 Effect of Tungsten Surface Density on Catalyst Activity

Tungstated zirconia is generally agreed to possess stronger Brønsted acidity compared to zeolites.(25, 26) For example, it has been previously reported that WO_x-ZrO_2 is more active than acidic zeolites for reactions including hydration,(27) isomerization(28) and esterification.(29) Using n-hexane isomerization as probe reaction, the deprotonation energy (DPE), which provides a reliable metric of Brønsted acid site strength,(30, 31) is determined to be 1120 kJ mol^{-1} and 1185 kJ mol^{-1} for WO_x-ZrO_2 and zeolite Beta,(32) respectively, indicating stronger acid strength of the former, hence its superior activity.

Table 7.2 Physiochemical and catalytic properties of WO_x-ZrO_2 with varying W surface densities for *p*-xylene production

Sample[a]	S.A. ($m^2\ g^{-1}$)	D_p (nm)	$\rho_{w,s}$ ($W\ nm^{-2}$)	$\rho_{Brønsted}$ ($\mu mol\ g^{-1}$)	ρ_{Lewis} ($\mu mol\ g^{-1}$)	TOF[b] ($10^{-3}s^{-1}$)
WO_x-ZrO_2-723	240	3.2	1.6	97	251	32
WO_x-ZrO_2-773	182	3.7	2.1	75	160	152
WO_x-ZrO_2-923	116	5.0	3.4	72	46	212
WO_x-ZrO_2-1023	85	6.4	4.6	77	44	182
WO_x-ZrO_2-1123	50	9.4	7.8	91	41	134
WO_x-ZrO_2-1223	20	23.2	19.5	15	27	6

[a] WO_x-ZrO_2-723 denotes the sample calcined at 723 K; all samples have an initial loading of 15 wt% WO_3 [b] Normalized by Brønsted acid site density.

Tungstated zirconia is generally agreed to possess stronger Brønsted acidity compared to zeolites.(25, 26) For example, it has been previously reported that WO_x-ZrO_2 is more active than acidic zeolites for reactions including hydration,(27) isomerization(28) and esterification.(29) Using n-hexane isomerization as probe reaction, the deprotonation energy (DPE), which provides a reliable metric of Brønsted acid site strength,(30, 31) is determined to be 1120 kJ mol^{-1} and 1185 kJ mol^{-1} for WO_x-ZrO_2 and zeolite Beta,(32) respectively, indicating stronger acid strength of the former, hence its superior activity.

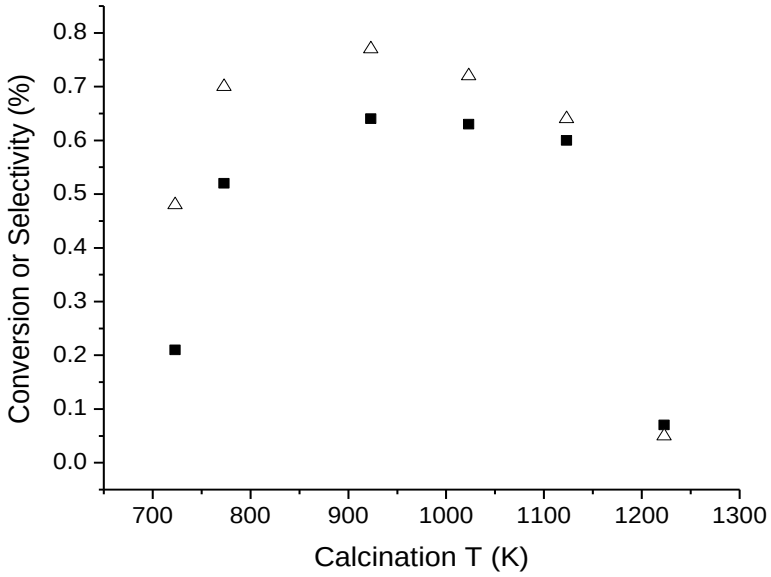

Figure 7.5 Effect of calcination temperature on conversion of DMF and selectivity to *p*-xylene. (Δ *p*-xylene selectivity ■ DMF conversion, reaction conditions: 10 wt% dienes in anhydrous hexadecane, 0.15 g catalyst, 523 K, 20 bar ethylene charged at 298 K in 50 mL batch reactor)

It has been generally recognized that the surface density of WO_x species, expressed as the average number of W atoms per unit area, is a key parameter that controls the surface morphology, surface acidity and the catalytic properties of these materials.(33-36) To further investigate the nature of active sites and the acidity requirement to achieve high selectivity to aromatics, we prepared a series of WO_x-ZrO_2 catalysts with a representative range of W surface densities by varying the calcination temperatures (723 to 1223 K) for materials with the same initial tungsten loading (15 wt% WO_3). It can been seen from Table 7.2 that higher calcination temperatures lead to a progressive decrease in total surface area and a corresponding increase in pore size and tungsten surface density, as previously reported. (35) Figure 7.5 shows that the

most active catalyst for *p*-xylene formation is produced by calcination at 923 K, which is consistent with the range previously found for other acid-catalyzed reactions.(35)

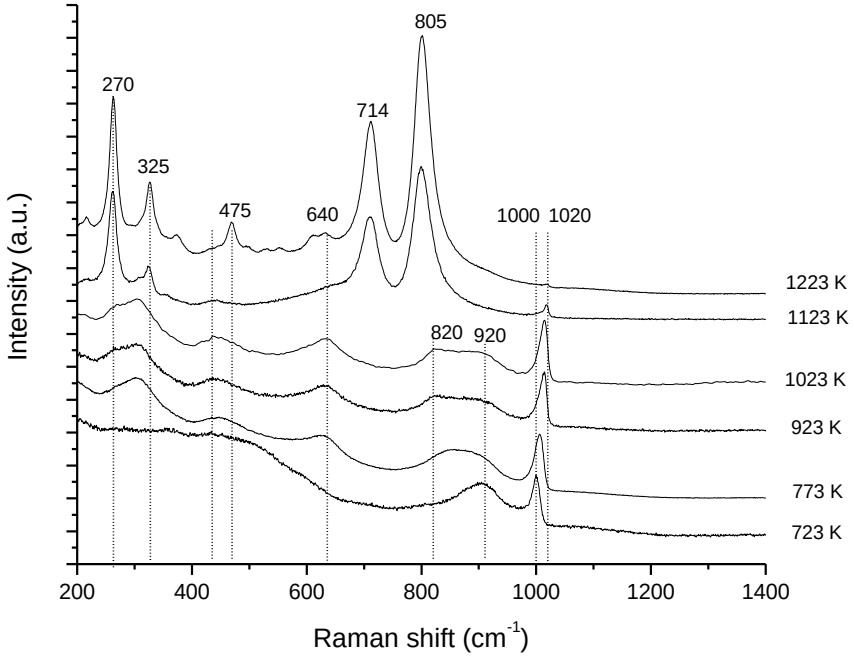

Figure 7.6 In situ Raman spectra of WOx-ZrO2 catalysts calcined at different temperatures acquired under dehydrated conditions

Raman spectroscopic measurements were performed to probe the nature of surface WO_x species. Both t-ZrO_2 and m-ZrO_2 have strong Raman vibrations below 700 cm^{-1}.(37, 38) It is known, however, that the presence of WO_x species on the surface of zirconium hydroxide retards the crystallization of the latter.(38, 39) As can be seen with the sample calcined at 450 ^oC, characteristic Raman bands due to crystalline t-ZrO_2 or m-ZrO_2 are not observed for this material. However, a sharp peak at 1000 cm^{-1} is observed, which corresponds to the symmetric stretching mode of the terminal W=O stretch of monotungstate species revealed only under dehydrated conditions.(40) The broad band at 820-920 cm^{-1} is assigned to distorted WO_x subnanometer

clusters intermixed with Zr,(35) which starts to form at the lowest treatment temperature. The zirconium hydroxide support starts to crystallize with increasing calcination temperature (500-750 ^{o}C), as evidenced by the appearance of broad t-ZrO_2 Raman bands at 320, 470 and 640 cm^{-1}. The broad band between 820-920 cm^{-1} becomes more pronounced while the sharp band originally at 1000cm^{-1} gradually shifts towards higher frequencies as calcination temperature rises, which reflects the progressive polymerization of the monotungstate species to form polytungstate species as tungsten surface density increases, as previously reported.(40) At higher calcination temperatures, surface tungsten species further aggregate to form well-ordered crystallites of WO_3, as evidenced by the sharp, characteristic bands at 270, 714 and 805 cm^{-1}.(41) The mono- or polytungstate bands at 1000-1020 cm^{-1} become completely invisible for the sample treated at 950 ^{o}C, indicating a significant extent of crystallization of surface WO_x species. A distinctive band from these species can still be observed for the sample treated at 850 ^{o}C, suggesting a lower degree of aggregation.

In situ Raman spectroscopy measurements thus reveal the presence of distorted Zr-containing WO_x clusters ranging 0.8-1 nm in size (Raman bands 820-920 cm^{-1}) on the most active WO_x-ZrO_2 materials. These clusters have been identified as the most acidic surface tungsten species that exhibit high activity for methanol dehydration, and they reach maximum surface concentration at intermediate tungsten coverage as a result of the aggregation of monotungstates and the increasing extent of Zr migration.(35, 42) It has also been suggested that these WO_x clusters are more effective in dispersing the electron density transferred to the catalyst surface during catalysis, thus stabilizing the transition states, leading to higher reaction rates.(43) At higher calcination temperatures (1123 K and 1223 K), the concentration of these clusters

decreases as surface tungsten species further aggregate to form well-ordered WO_3 nanocrystalites (strong Raman bands at 270, 714 and 805 cm^{-1}). The density of Lewis acid sites decreases significantly with increasing calcination temperature, as reported previously.(43) The increase in TOF is not likely caused by the decrease in Lewis sites density, because the TOF value displays a maximum while the Lewis site density decreases monotonically. Brønsted acid sites with varying strengths are collectively titrated by NH_3-TPD, thus giving similar densities of total Brønsted sites (Table 7.2). The overall acid strengths of materials calcined at different temperatures, however, can be distinguished by the TOF values. It can be seen from Table 7.2 that the TOF for *p*-xylene increases initially, reflecting an increase in the acid strength of surface tungsten species with increasing surface concentration of Zr-containing subnaometer WO_x clusters. The TOF reaches a maximum at a surface density of approximately 4 W atom nm^{-2}, and then decreases as the surface density of tungsten increases further, consistent with the disappearance of Zr-containing WO_x clusters due to formation of WO_3 crystallites see in Raman spectra.

7.5 Product Analysis: Isomeric Purity of *Para*-xylene

Currently, almost all *p*-xylene are oxidized to produce terephthalic acid (TPA), which are used to manufacture polyesters, such as polyethylene terephthalate (PET).(44) The *p*-xylene feedstock for the production of TPA requires the purity of the para isomer to be around 99.6-99.8% .(45) Commercially, mixed xylenes are obtained from catalytic reformate, pyrolysis gasoline, toluene disproportionation product, and to a less extent coke-oven light oil.(46)

Table 7.3 Physical properties of xylene isomers

	Boiling point (^{o}C)	Freezing point (^{o}C)
p-xylene	138	13.3
m-xylene	139	-47.9
o-xylene	144	-25.2

It can be seen from Table 7.3 that the boiling points of all three xylene isomers are rather similar, which makes it difficult to completely separate them from each other via conventional distillation.(47) *o*-xylene is the easiest to separate from a mixture as its boiling point differs from *m*-xylene and *p*-xylene by 5 and 6 ^{o}C, respectively. However, *p*-xylene and *m*-xylene cannot be separated via simple distillation because their boiling points are too close. Instead, current separation technologies exploit the differences in freezing points and adsorption characteristics.(47) Two major methods that are currently used commercially to separate and manufacture high purity *p*-xylene: (1) crystallization and (2) adsorption. These special separation processes are quite complex and are often costly. One example is the Amoco PX crystallization process shown in Figure 7.7. (47)

One major potential benefit of producing *p*-xylene using the approach presented here is that only *p*-xylene is formed as the primary product due to the inherently high stereo-selectivity of the Diels-Alder reaction. However, it is also well-known that migration of the methyl groups of xylenes can be catalyzed by acid catalysts.(28) In the presence of the WO_x-ZrO_2 catalyst, if the secondary isomerization reaction is rapid and proceeds close to equilibrium at the reaction temperature (523K), then only 22% of *p*-xylene can be obtained, while 50% of the xylene will

exist as *m*-xylene (Figure 7.8). In fact, as long as the purity of *p*-xylene is significantly lower than the specification of most commercial products (i.e. 99.7%), the crystallization / adsorption unit still needs to be installed and operated to further purify the *p*-xylene, thus increasing production cost.

Therefore, it is important to study whether the *p*-xylene is being isomerized into *m*- and *o*-xylenes under the reaction conditions. To this end, the liquid product is diluted with ethanol and analyzed with a J&W HP-INNOWax column. The chromatogram is shown in Figure 7.9 and the concentration of each isomer is calculated in Table 7.4.

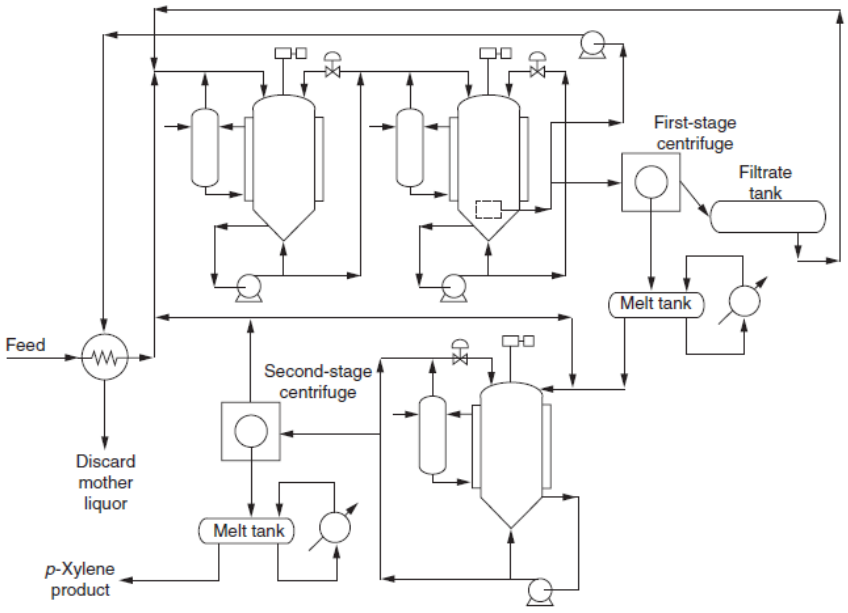

Figure 7.7 Amoco PX crystallization process

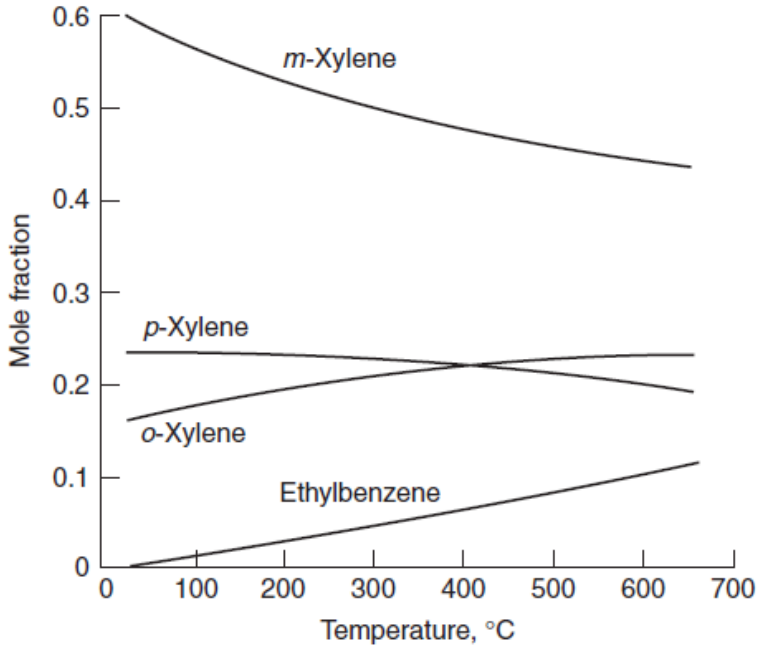

Figure 7.8 Equilibrium concentrations for C_8 aromatic compounds.

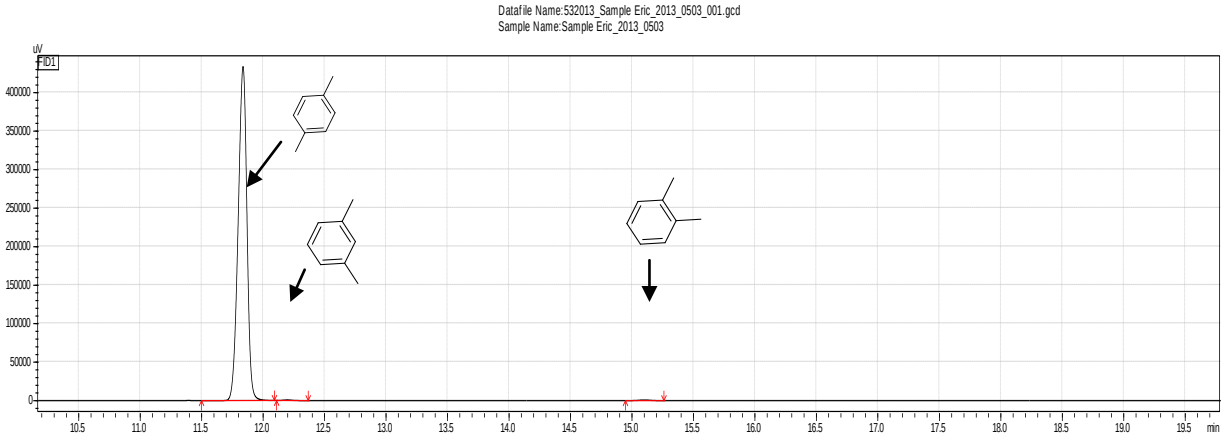

Figure 7.9 Chromatogram showing the relative concentrations of three xylene isomers.

Table 7.4 Comparison between specifications of commercial *p*-xylene product and *p*-xylene stream obtained in this work

	Typical % in commercial product	% in the xylene stream obtained in this work
p-xylene	99.60%	99.59%
m-xylene	0.20%	0.17%
o-xylene	0.10%	0.24%

From Table 7.4, it can be seen that in the liquid product obtained using the Diels-Alder cycloaddition followed by dehydrative aromatization, the isomeric purity of *p*-xylene is 99.59%, which meets the specifications stipulated in commercial products. Therefore, the process described in this chapter represents a truly selective route to *p*-xylene production from DMF, thus eliminating the need for further purification by the costly crystallization/adsorption process. Control experiments using 10 wt% *p*-xylene dissolved in hexadecane as reactant and WO_x-ZrO_2 as catalyst also showed negligible isomerization under the reaction conditions. Existing xylene isomerization technologies using amorphous silica/alumina typically operate at temperatures ranging from 370^{o}C to 470^{o}C. In ZSM-5 based xylene isomerization processes commercialized by Mobil (now ExxonMobil), the preferred operating temperatures are all above 350^{o}C.(47) Low-temperature (around 250^{o}C) *o*-xylene isomerzation requires the presence of H_2, and in some cases is catalyzed by a bifunctional catalyst with a metal component.(47) Therefore, we believe that the negligible extent of *p*-xylene isomerization is likely due to the low reaction temperature used in our process.

7.6 Conclusion

We have shown in this chapter that Brønsted acid sites are particularly active for the production of benzene, toluene and *p*-xylene by the reaction of ethylene with furan, 2-methylfuran (2-MF) and 2,5-dimethylfuran (DMF), respectively, by the combination of cycloaddition and dehydrative aromatization reactions. Microporous catalysts are not required for these reactions, as amorphous solid acids and homogeneous Brønsted acids also demonstrate significant activity for *p*-xylene formation. In particular, WO_x-ZrO_2 exhibits a TOF frequency for *p*-xylene formation that is 35 times higher than zeolite Y. Mesoporous materials such as WO_x-ZrO_2 offer higher resistance to deactivation by carbon deposition compared to microporous materials. In addition, the process described in this chapter represents a highly selective route to produce *p*-xylene with an isomer purity of 99.59%, thus eliminating the need for further purification by the costly crystallization/adsorption process. Results from Raman spectroscopy and the changes in TOF caused by varying the W surface density for a series of WO_x-ZrO_2 catalysts are consistent with the conclusion from previous investigations that the high activity of WO_x-ZrO_2 is mainly associated with the presence of subnanometer WO_x clusters mixed with Zr, which reach maximum surface concentration at intermediate tungsten coverage. Accordingly, the development of new catalysts for the production of aromatic compounds from biomass-derived furans can be guided by the fundamental concepts of Brønsted acidity developed for petroleum chemistry.

7.7 References

1. P. N. R. Vennestrøm, C. M. Osmundsen, C. H. Christensen and E. Taarning, *Angewandte Chemie International Edition*, 2008, **50**, 10502-10509.
2. C. H. Christensen, J. Rass-Hansen, C. C. Marsden, E. Taarning and K. Egeblad, *ChemSusChem*, 2008, **1**, 283-289.
3. J. v. Haveren, E. L. Scott and J. Sanders, *Biofuels, Bioproducts and Biorefining*, 2008, **2**, 41-57.
4. A. Corma, S. Iborra and A. Velty, *Chemical Reviews*, 2007, **107**, 2411-2502.
5. T. P. Vispute, H. Zhang, A. Sanna, R. Xiao and G. W. Huber, *Science*, 2010, **330**, 1222-1227.
6. Y.-T. Cheng, J. Jae, J. Shi, W. Fan and G. W. Huber, *Angewandte Chemie International Edition*, 2012, **51**, 1387-1390.
7. T. Carlson, G. Tompsett, W. Conner and G. Huber, *Topics in Catalysis*, 2009, **52**, 241-252.
8. M. Shiramizu and F. D. Toste, *Chemistry – A European Journal*, 2011, **17**, 12452-12457.
9. C. L. Williams, C.-C. Chang, P. Do, N. Nikbin, S. Caratzoulas, D. G. Vlachos, R. F. Lobo, W. Fan and P. J. Dauenhauer, *ACS Catalysis*, 2012, **2**, 935-939.
10. T.Brandvold, *UOP LLC, USA Patent.*, 20100331568, 2010.
11. S. S. K.Takanishi, *Toray Industries, Tokyo, Japan*, WO 2009110402A1, 2009.
12. Y. Roman-Leshkov, C. J. Barrett, Z. Y. Liu and J. A. Dumesic, *Nature*, 2007, **447**, 982-985.
13. J.-P. Lange, E. van der Heide, J. van Buijtenen and R. Price, *ChemSusChem*, 2012, **5**, 150-166.
14. T. Thananatthanachon and T. B. Rauchfuss, *Angewandte Chemie*, 2010, **122**, 6766-6768.
15. J. B. Binder and R. T. Raines, *Journal of the American Chemical Society*, 2009, **131**, 1979-1985.
16. G. Piancatelli, M. D'Auria and F. D'Onofrio, *Synthesis*, 1994, **1994**, 867-889.
17. E. J. Stamhuis, W. Drenth and H. van den Berg, *Recueil des Travaux Chimiques des Pays-Bas*, 1964, **83**, 167-176.
18. F. M. Dean and A. R. Katritzky, in *Advances in Heterocyclic Chemistry*, Academic Press, 1982, vol. Volume 30, pp. 167-238.
19. J. A. Moore and E. M. Partain, *The Journal of Organic Chemistry*, 1983, **48**, 1105-1106.
20. E. V. Adamskaya and A. F. Oleinik, *Chemistry of Heterocyclic Compounds*, 1985, **21**, 1063-1076.
21. José M. Fraile, José I. García, María A. Gómez, A. de la Hoz, José A. Mayoral, A. Moreno, P. Prieto, L. Salvatella and E. Vázquez, *European Journal of Organic Chemistry*, 2001, **2001**, 2891-2899.
22. J. Sauer, *Angewandte Chemie International Edition in English*, 1967, **6**, 16-33.
23. P. M. Hardy, A. C. Nicholls and H. N. Rydon, *Journal of the Chemical Society, Perkin Transactions 2*, 1972, 2270-2278.
24. Y.-T. Cheng and G. W. Huber, *ACS Catalysis*, 2011, **1**, 611-628.
25. M. Hino and K. Arata, *Journal of the Chemical Society, Chemical Communications*, 1988, 1259-1260.

26. K. Arata, *Applied Catalysis A: General*, 1996, **146**, 3-32.
27. W. Chu, T. Echizen, Y. Kamiya and T. Okuhara, *Applied Catalysis A: General*, 2004, **259**, 199-205.
28. R. D. Wilson, D. G. Barton, C. D. Baertsch and E. Iglesia, *Journal of Catalysis*, 2000, **194**, 175-187.
29. Y.-M. Park, D.-W. Lee, D.-K. Kim, J.-S. Lee and K.-Y. Lee, *Catalysis Today*, 2008, **131**, 238-243.
30. J. Macht, R. T. Carr and E. Iglesia, *Journal of the American Chemical Society*, 2009, **131**, 6554-6565.
31. M. J. Janik, J. Macht, E. Iglesia and M. Neurock, *Journal of Physical Chemistry C*, 2009, **113**, 1872-1885.
32. J. Macht, R. T. Carr and E. Iglesia, *Journal of Catalysis*, 2009, **264**, 54-66.
33. J. G. Santiesteban, J. C. Vartuli, S. Han, R. D. Bastian and C. D. Chang, *Journal of Catalysis*, 1997, **168**, 431-441.
34. C. D. Baertsch, S. L. Soled and E. Iglesia, *The Journal of Physical Chemistry B*, 2001, **105**, 1320-1330.
35. E. I. Ross-Medgaarden, W. V. Knowles, T. Kim, M. S. Wong, W. Zhou, C. J. Kiely and I. E. Wachs, *Journal of Catalysis*, 2008, **256**, 108-125.
36. M. Valigi, D. Gazzoli, I. Pettiti, G. Mattei, S. Colonna, S. De Rossi and G. Ferraris, *Applied Catalysis A: General*, 2002, **231**, 159-172.
37. V. G. Keramidas and W. B. White, *Journal of the American Ceramic Society*, 1974, **57**, 22-24.
38. M. Scheithauer, R. K. Grasselli and H. Knozinger, *Langmuir*, 1998, **14**, 3019-3029.
39. K. Arata and M. Hino, *Materials Chemistry and Physics*, 1990, **26**, 213-237.
40. D. S. Kim, M. Ostromecki and I. E. Wachs, *Journal of Molecular Catalysis A: Chemical*, 1996, **106**, 93-102.
41. M. A. Vuurman and I. E. Wachs, *The Journal of Physical Chemistry*, 1992, **96**, 5008-5016.
42. W. Zhou, E. I. Ross-Medgaarden, W. V. Knowles, M. S. Wong, I. E. Wachs and C. J. Kiely, *Nat Chem*, 2009, **1**, 722-728.
43. D. G. Barton, S. L. Soled, G. D. Meitzner, G. A. Fuentes and E. Iglesia, *Journal of Catalysis*, 1999, **181**, 57-72.
44. K. Weissermel and H.-J. Arpe, *Industrial Organic Chemistry*, 3rd edn., 1997.
45. W. W. Kaeding, C. Chu, L. B. Young, B. Weinstein and S. A. Butter, *Journal of Catalysis*, 1981, **67**, 159-174.
46. W. A. Sweeney and P. F. Bryan, in *Kirk-Othmer Encyclopedia of Chemical Technology*, John Wiley & Sons, Inc., 2000.
47. W. J. Cannella, in *Kirk-Othmer Encyclopedia of Chemical Technology*, John Wiley & Sons, Inc., 2000.

8. Conclusions and Recommendations

8.1 Summary of Conclusions

In developing strategies for utilizing biomass resource, priority needs to be given to technologies that utilize abundant and non-edible lignocellulose over other forms of biomass that can also serve as food supply. However, the conversion of the recalcitrant lignocellulose into consumable fuels and chemicals requires a set of technologies to break lignocellulose into chemical platforms that are more amenable for further biological or catalytic upgrading. One such strategy starts with fractionation of lignocellulose into cellulose, hemicellulose and lignin followed by aqueous-phase processing of each fraction under optimized conditions to produce a handful of simple platform molecules (e.g. acids, furanics, ketones and alcohols) with high yields, thereby allowing for highly efficient utilization of the whole lignocellulose. In this sense, the aqueous-processing approach resembles the refining of petroleum. Analogous to the evolution of the petroleum refinery, the success of a biorefinery also hinges on the availability of highly efficient processes to produce fuels and commodity chemicals. The field of catalysis hence plays a pivotal role in the development of these conversion processes.

The use of solid acids is indispensable in aqueous-processing of lignocellulose due to the need to reduce oxygen content of bio-based feedstock through various acid-catalyzed reactions such as dehydration, decarboxylation or decarbonylation to form hydrocarbon-like products. The need to expand the existing network of molecules that can be efficiently obtained from the important HMF-LA-GVL platform (outlined in section 1.4.4) motivated us to develop four solid-

acid based catalytic strategies to produce hydrocarbon fuels or commodity chemicals with wide industrial applications.

Chapter 3 develops a novel catalytic route that converts an aqueous solution of gamma-valerolactone (GVL) into a stream of butene mixture, which is then oligomerized to produce liquid hydrocarbons with molecular weights suitable as jet and diesel fuel precursors. The decarboxylation of GVL is highly efficient and leads to nearly quantitative yields to butenes (>96%). The transformation of GVL to a simple olefin allows for the use of well-known olefin oligomerization chemistry to form C-C bond and potentially offers good control over the chain lengths, degree of branching and aromaticity in the fuel product. The overall yields to C_{8+} hydrocarbons are greater than 60%. The last part of this chapter presents a concerted effort that converts raw lignocellulosic biomass to produces C_8 and higher hydrocarbon fuels in liter quantities. In this manner, common practical issues encountered in process scaling up including sulfuric acid management, solid residue (e.g., gypsum) removal and catalyst stability over extended period of time have been explored, which provides guidance for future design and development of catalytic routes for biomass conversion. The two-reactor process has been demonstrated to be sufficiently robust to handle GVL derived from maple wood over 200 hours on stream.

In chapter 4, a detailed kinetic study of the interconversion between GVL and pentenioc acid (PEA) and their decarboxylation was conducted. In addition to the catalytic decarboxylation of PEA, we consider that direct decarboxylation of GVL may also contribute to the total rate of butene production (corresponding to about 10-20% of the overall rate at typical reaction conditions). The increasing ratio of 1-butene:2-butenes in the product mixture with decreasing

space time supports a mechanism where 1-butene is first formed via β-scission of intermediate carbenium ions. The simple kinetic model developed in this work provides a useful tool for predicting the rates of butene production for a wide range of reaction conditions. The results from this study can be a useful tool in reactor design and process optimization studies to assess the techno-economic feasibility of producing liquid transportation fuels from GVL. Since it is identified in chapter 4 that 1-butene is the primary decarboxylation product, this chapter also provides the incentive for chapter 5 to study the selective production of 1-butene and other alpha olefins via lactone decarboxylation by identifying catalysts and reaction conditions that can suppress olefin isomerization.

Chapter 5 demonstrates the production of a stream of highly pure (e.g., 1-butene isomeric purity >99% at 10% total butene yield) linear alpha olefins (LAOs) from lactones or unsaturated carboxylic acids in a single step using Lewis acid-based catalysts. Using a WO_x-Al_2O_3 (4% WO_x loading), 70% yield to total butene can be obtained, of which 92% is retained as 1-butene. It is also shown that analogous decarboxylation chemistry exists for C_5 C_6, C_8 and C_{11} γ-lactones, which demonstrates the potential of this method as a general route for the production of LAOs with varying chain lengths. The feedstock to this process can be potentially derived from biological routes (e.g., polyketide/fatty acid biosynthesis). Compared to the present ethylene-based route for production of LAOs, the biological sythetic route is capable of targeting molecules with specified carbon chain length which after subsequent decarboxylation with the technology presented in this chapter, leads to a single LAO cut, thus offering additional manufacturing flexibility to meet market demand. This approach also allows for the production

of both even and odd carbon number LAOs, depending on the number of carbons in the starting molecules. As an example, 1-heptene was produced from the C_8 lactone.

In Chapter 6, we demonstrated the ring opening and hydrogenation of GVL over a bifunctional Pd/Nb_2O_5 catalyst to produce pentanoic acid with yields around 92%. Compared to the production of butene via decarboxylation of GVL/pentenoic acid as described above, hydrogenation of the pentenoic acid intermediate forms the saturated pentanoic acid and preserves the two oxygen atoms in the feed molecule, which allows for the coupling of two pentanoic acid molecules via ketonization reaction to produce a C_9 ketone with 84% yield. In chapter 6, It is also shown that improvements in the hydrothermal stability of the niobia support for the Pd/Nb_2O_5 catalyst can be achieved by addition of small amounts of silica, which retards crystallization of the niobia support and indirectly, the sintering of the Pd particles, leading to catalysts with superior stabilities under hydrothermal reaction conditions. Realizing the beneficial effect of the Si-O-Nb linkage for stabilizing niobia, atomic layer deposition was used to synthesize a new class of mesoporous niobia that combines the highly-ordered porous structure of SBA-15 with the surface properties of niobia, which also demonstrates excellent hydrothermal stability for the production of pentanoic acid from GVL. These results have important implications for the development of catalysts for biorenewable conversions that operate under aqueous conditions at elevated temperatures.

Chapter 7 investigates the production of benzene, toluene and *p*-xylene by the reaction of ethylene with furan, 2-methylfuran (2-MF) and 2,5-dimethylfuran (DMF), respectively, by consecutive cycloaddition and dehydratioin reactions. Using a WO_x-ZrO_2 (15 wt% WO_x loading) catalyst calcined at 923K, 80%, 34% and 18% yield to *p*-xylene, toluene and benzene are

obtained, respectively. Remarkably, the isomeric purity of *p*-xylene in the xylene product stream is as high as 99.6%, thus completely eliminating the need to separate *p*-xylene from *o*-xylene and *m*-xylene by adsorption / crystallization process. We have shown in this chapter that Brønsted acid sites are particularly active for the formation of aromatics. Microporous catalysts are not required for these reactions, as amorphous solid acids and homogeneous Brønsted acids also demonstrate significant activity for *p*-xylene formation. In particular, WO_x-ZrO_2 exhibits a TOF frequency for *p*-xylene formation that is 35 times higher than zeolite Y. In addition, mesoporous materials such as WO_x-ZrO_2 offer higher resistance to deactivation by carbon deposition compared to microporous materials. Results from Raman spectroscopy and the changes in TOF caused by varying the W surface density for a series of WO_x-ZrO_2 catalysts are consistent with the conclusion from previous investigations that the high activity of WO_x-ZrO_2 is mainly associated with the presence of subnanometer WO_x clusters mixed with Zr, which reach maximum surface concentration at intermediate tungsten coverage. Accordingly, the development of new catalysts for the production of aromatic compounds from biomass-derived furans can be guided by the fundamental concepts of Brønsted acidity developed for petroleum chemistry.

8.2 Recommendations

8.2.1 Synthesis of Solid Lewis Acid Catalysts that Withstand Harsh Hydrothermal Conditions

Identification and synthesis of solid acid catalysts with superior activity, selectivity and stability have formed an important theme in this thesis. In Chapter 5, γ-Al_2O_3 initially displayed promising selectivity for LAO formation. However, it also possesses surface basic sites that catalyze side reactions. We have shown that by impregnating acidic tungsten oxide (WO_x) onto

the surface of γ-Al_2O_3, these basic sites can be progressively titrated, thus decreasing carbon loss due to side reactions and lead to improved olefin yields. However, we have also found that higher loadings of WO_x introduce Brønsted acidity and lead to increasing extent of LAO isomerization. Sn-Beta zeolite possesses only Lewis acidity and has demonstrated excellent selectivity to 1-butene and no by-product formation by our preliminary results. Nevertheless, we have also observed rapid loss of activity with time on stream, likely due to the disintegration of the zeolitic structure under the harsh reaction conditions employed (648K in the presence of steam). In this respect, it is suggested that future research should explore the synthesis of a water-tolerant solid acid catalysts bearing predominantly Lewis acidity with minimal Brønsted acidity and basicity, which would be ideal for the selective production of LAOs via lactone or unsaturated acid decarboxylation.

8.2.2. Tailor-Make Liquid Hydrocarbon Fuels that Meet Fuel Specifications

The continuous process developed in chapter 3 efficiently converts GVL into liquid hydrocarbons with molecular weights suitable for jet fuel and diesel applications. The transformation of GVL to a simple alkene allows access to well-established olefin oligomerization chemistry. Therefore, the characteristics of molecules in the fuel including molecular weights, degree of branching and aromaticity can be controlled by using different solid acid catalysts and by tuning reaction conditions (e.g., temperature, pressure, space velocity) in both reactors. In this manner, the composition and molecular characteristics of the fuel product can be further refined by designing catalysts and process parameters in order to generate fuels that potentially directly meet specifications of gasoline, jet or diesel fuel.